Computer-Aided Drug Design for Discovery of Novel Adenosine A_3 Receptor Antagonists - Investigation of the Orthosteric Binding Area and Functional Activity of the Antagonists

Panagiotis Lagarias
Department of Pharmacy, Section of Pharmaceutical Chemistry, School of Health Sciences, National and Kapodistrian University of Athens

A thesis submitted for the degree of
Doctor of Philosophy
Yet to be decided

I would like to dedicate this thesis to my family (John, Vassiliki and Adeline) and my aunt Penelope (Notsi).

Acknowledgements

I would like to express my deep gratitude for IKY Foundation, which was my sole source of funding throughout the years I spend in Athens for *my PhD thesis work. Then I would like to acknowledge the following people whose contribution was crucial for the successful completion of my PhD thesis:*
My special thanks to Prof Antonios Kolocouris for trusting me, and his guidance all of these years. Our meetings and discussion helped me learn the basics of drug design and the theoretical background of a variety of computational methods.

Extended Synopsis

Pharmaceutical companies and academic research laboratories are involved in intense efforts to identify antagonists with selectivity for each adenosine receptor (AR) subtype as potential clinical candidates for "soft" treatment of different diseases. All AR sub-types play distinct roles throughout the body. $A_{2A}R$ antagonists can be useful for treating cancer, central nervous system (CNS) disorders; A_1R antagonists can provide kidney-protective agents, anti-asthmatic and CNS agents; A_3R antagonists are promising for therapeutic applications in asthma, glaucoma and $A_{2B}R$ antagonists for diabetes, asthma and chronic obstructive pulmonary disease. The reported crystal structures of $A_{2A}R$ in complex with agonists or antagonists and of A_1R with an antagonist, along with other advances attributed to the progress of GPCR crystallography have made structure-based approaches an attractive strategy for drug design against adenosine receptors which are pharmaceutically important targets. The $A_{2A}R$ is one of the best studied receptors of all class A GPCRs. Additionally, among the 688 known GPCRs, class A is the 7th more intensely investigated. The application of virtual screening and medicinal chemistry studies for a few decades now has resulted in a high number of bioactive compounds (~ 11000) against $A_{2A}R$ as was retrieved from ChEMBL20. An introduction to GPCRs and ARs is the subject of first Chapter.

In the second Chapter of the thesis, is presented the virtual screening (VS) results of the small Maybridge HitFinder library of 14,400 compounds against $A_{2A}R$, using its crystallographic structure in complex with the antagonist ZM241385, through a combination of structure-based and ligand-based procedures. This is one of the few VS against ARs reported in the literature which however use the ZINC library of millions compounds . The docking poses were re-scored by applying energy minimization using CHARMM software with CHARMM19 ff of the ligand inside rigid receptor and consideration of desolvation energy electrostatics using the Poisson-Boltzmann equation, i.e., using Molecular Mechanics-Poisson Boltzmann Surface Area (MM-PBSA) method reduced to include only energy minimization. Out of the eight selected and tested compounds, three showed micromolar affinity for the A_{2A} and A_3Rs and two were low micromolar binders only to the A_3R receptor using radiolabelled assays. Thus, although initially targeting the $A_{2A}R$, the project resulted in the following percent of successful binder hits: 25% for A_{2A} and 63% for A_3R. Of particular interest for futher exploration as novel chemical probes, are the synthetically feasible **K1** and **K5** with a 2-amino-thiophene-3-carboxamide and a carbonyloxycarboximidamide structure, respectively. Given the similarity between ARs orthosteric binding sites, obtaining highly selective receptor antagonists is a challenging but critical task.

In a second step, described in Chapter 3 of the thesis, based on the structure of mainly two promising active hits, possessing a 2-amino -3-carboxamide-thiophene and a carbonyloxycarboximidamide chemotype respectively, 19 more compounds were selected by similarity for testing. For this second series of 19 compounds, 17 were found to bind to the ARs using radiolabelled assays. Eight of those revealed A_3-selective affinity with K_i values in the micromolar to low micromolar regime. Along with 2-amino-thiophene-3-carboxamide and carbonyloxycarboximidamide derivatives we identified a new class of ligands, the 3-acylamino-5-aryl-thiophene-2-carboxamides.

These three classes of compounds have novel chemotypes with low T_c values (< 0.17) compared to the known ARs ligands have been identified: (a) The 2-amino thiophene-3-carboxamide (2-NH_2 and 3-CONHR; class A) thiophenes with low micromolar affibity to A_{2A}R and A_3R. (b) The 3-acylamino-5-aryl-thiophene-2-carboxamides (class B) including the new substitution pattern (2-$CONH_2$ and 3-NHCOR) of the thiophene ring, which -compared to 2-NH_2 and 3-CONHR' substitution pattern- enhances the affinity for A_1R and A_3R. (c) The carbonyloxycarboximidamide derivatives (class D), many having selective A_3R affinity. The selective A_3R ligands with micromolar affinity and novel chemotypes found here, may contribute to the treatment of the A_3R-related human pathologies.

Compound **K18** (O4-{[3-(2,6-dichlorophenyl)-5-methylisoxazol-4-yl]carbonyl}-2-methyl-1,3-thiazole-4-carbohydroximamide) with the carbonyloxycarboximidamide chemotype have the lowest micromolar binding affinity to A_3R (K_d=0.898 μM) between the discovered lead compounds. We focused on the selective A_3R ligand **K18** with the lowest micromolar binding affinity to A_3R and purchased and measured the binding affinity of 12 new carbonyloxycarboximidamide analogs including mainly compounds that bear a biphenyl instead of 3-phenyl-isoxazole for additional structure-activity relationship (SAR) studies.

The 39 tested molecules resulted in similar docking poses against A_1, A_{2A}, A_{2B} or A_3Rs. The experimental structures of A_1, A_{2A}Rs, after completion of missing loops, were used for the simulations. Since A_{2B} or A_3Rs are unsolved, homology models were applied. Using the docking poses of the ligands as starting structures, the performance of hundreds of 20ns-molecular dynamics (MD) simulations, using Desmond software with OPLS2005 force field (ff), allow the differentiation of stable and unstable docking poses based on the RMSD values for the displacement of the ligand from its starting docking pose inside the orthosteric binding area. Generally, stable or unstable docking poses agree with the experimental results of radiolabelled values of binding affinity. The stability of the stable complexes were further tested using 100ns-MD simulations using Desmond software with OPLS2005ff and Amber software with amberff14sb provided the basic features of the binding interactions with A_1, A_{2A}, and A_3Rs for compounds exhibiting affinity.

The MD simulations show the basic features of the binding interactions with A_1, A_{2A}, and A_3Rs for compounds exhibiting affinity. The complexes with A_{2A} and A_1Rs were stabilized through hydrogen bonding interactions between an amino or amido group of the ligand and N(6.55) of the AR. E(5.30) can be involved also in hydrogen bonding interactions with the bound ligand. A_{2A}R ligands include a lipophilic bulky substituent which was oriented towards the extracellular area, close to EL2 and TM7, and a smaller lipophilic group which was fitted deep in the binding region, close to L(6.51) and H(6.52). Similar interactions have been described in the X-ray structures between antagonists and A_{2A}R. Interestingly, for the A_1R ligands the ligand covers a larger space between TM5/TM6 and TM1/TM2, as shown in the recent X-ray structure between an antagonist and A_1R. **(Glukhova et al. 2017c)** Many of the ligands studied in this report, i.e. **K1, K2 K5-K7, K9-K14, K16, K18, K20-K27, K31, K32, K35**, bind to A_3R. We suggest that selectivity against A_3R is boosted by increasing the size and lipophilicity of a suitable substituent reflecting a better fit with V(5.30). Compounds **K6**, **K7, K10, K12-K15, K17, K18, K25, K27, K31, K32** are selective binders to A_3R. These findings are in line with previously published results from our group on the description of the orthosteric binding area of highly selective A_3R agonists with a bulky group in a compatible position, like the 3-iodo-benzyl group in N^6-position in **N^6-(3-iodobenzyl)-adenosine-5′-N-**

methyluronamide (IB-MECA) which has increased binding affinity for A_3R. In partcular we applied MD simulations and Molecular Mechanics-Generalized Born (MM-GBSA) in combination with mutagenesis data.

A_3R antagonists have been described as potential treatments for numerous diseases including asthma. In Chapter 4, it is described that the 39 potential A_3R antagonists were screened using agonist-induced inhibition of cAMP. Positive hits were assessed for AR subtype selectivity through cAMP accumulation assays. The antagonist affinity was determined using Schild analysis (pA_2 values) and fluorescent ligand binding using the bioluminescence resonance energy transfer (BRET) method. Further, a likely binding pose of the most potent antagonist **K18** was determined through MD simulations using an homology model of A_3R, combined with mutagenesis studies.

Eventually it was suggested that **K18**, which contains a 3-(dichlorophenyl)-isoxazole group connected through carbonyloxycarboximidamide fragment with a 1,3-thiazole ring, is a specific A_3R (<1 μM) competitive antagonist. Structure-activity relationship investigations revealed that loss of the 3-(dichlorophenyl)-isoxazole group significantly attenuated **K18** antagonistic potency. Mutagenic studies supported by MD simulations identified the residues important for binding in the A_3R orthosteric site.

We also introduce a model that enables estimates of the equilibrium binding affinity for rapidly dissociating compounds from real-time fluorescent ligand-binding studies. These results demonstrate the pharmacological characterization of a selective competitive A_3R antagonist and the description of its orthosteric binding mode.

In Chapter 5, the binding profile of the selective **K18** inside the orthosteric binding site of A_3R was further investigated and a computational model was also suggested for A_3R in complex with antagonists by applying detailed simulations.

The A_3R is currently an important drug target,(Liang and Jacobson 2002; Okamura et al. 2004) and there is a lack of available structures. In this work using experimental pA_2 values from mutagenesis experiments, a computational model for the description of a specific antagonist binding with orthosteric binding area of A_3R is approved. In particular, we generated a computational model based on: (a) An homology model of A_3R in complex with **K18** and the most likely binding conformation of **K18** inside WT A_3R orthosteric binding area which was investigated using, MD simulations with amber99sb, and MM-PBSA and MM-GBSA calculations. (b) The effect of point-mutations of residues in the orthosteric binding area to **K18** activity.

We first tested if the amber ff99sb can describe the conformational change from active to inactive form of $A_{2A}R$ when the active form is complexed with ZM213485 in hydrated POPE bilayers. Since, we observed the characteristic reduction in distance between TM3 and TM6 from ca 11 to 7.5 Å we used ff99sb as appropriate for the MD simulations of the complexes between **K18** and WT or mutant A_3Rs.

In a previous study, it was found experimentally and confirmed computationally using the same model that critical interactions for IB-MECA activity to A_3R include residues at the TM5, TM6 and EL2. These are $F168^{5.29}$, $L246^{6.51}$, $V169^{5.30}$, $N250^{6.55}$ forming direct

interactions with agonist and M177$^{5.38}$, L90$^{3.32}$ at the bottom of the orthosteric binding area which include indirect interactions. Other critical direct interactions for IB-MECA activity include the additional residues at the bottom of the binding area, T94$^{3.36}$, S271$^{7.42}$, H272$^{7.43}$ and I268$^{7.39}$.

Three likely different docking poses of **K18** and its congeners **K5**, **K17** differing in conformation and orientation inside the binding area were examined by molecular dynamics (MD) simulations with amber and MM-PBSA calculations. Two of them have equal energies with thiazole ring oriented deep in the receptor and dichlorophenyl of **K18** oriented towards either TM5, TM6 or TM1, TM2. The significance of these conformations was investigated using the site-directed mutagenesis experiments and biological activities results of mutant A_3Rs in complex with **K18** which suggested that the dichlorophenyl ring of **K18** is oriented towards TM5, TM6.

Thus, according to our computational model the competitive antagonist **K18** is stabilized inside the A_3R orthosteric binding area through an "up TM5, TM6" conformer which interacts directly with some common residues with the agonist. It forms a π-π interaction with F168$^{5.29}$, van der Waals interactions with L90$^{3.32}$, V169$^{5.30}$, L246$^{6.51}$, and hydrogen bond interactions with N250$^{6.55}$. In the middle region of the A_3R, **K18** makes contacts with residues M177$^{5.38}$, I249$^{6.54}$ which are not in contact with IB-MECA. To add further contrast, IB-MECA contacts residue W185$^{5.46}$ whereas **K18** does not. From these residues M177$^{5.38}$ causes a negation of both agonists and antagonist potency when mutated to alanine. L90$^{3.32}$ is a residue in contact with **K18** but not in contact with the agonists suggesting that **K18** sits higher in the orthosteric binding region. L90$^{3.32}$A mutation causes correspondingly an increase in the potency of K18 and a reduction in the potency of agonists. Our calculations describe why the majority of mutated residues to alanine, which are in contact with **K18** antagonist in the WT receptor, reduce or eliminate potency, i.e. correspondingly V169$^{5.30}$, M177$^{5.38}$ or L246$^{6.51}$, F168$^{5.29}$, N250$^{6.55}$. Additionally, the computational model shows that the selectivity of **K18** is not only due to direct interactions with the binding area residues. Remote residues which are positioned at the edges of the binding area in EL2, TM5 and TM6, like M174$^{5.35}$ at 4 Å may act by modulating the structure of the pocket. Residue M174$^{5.35}$ is important for NECA and K18 activity since its mutation to alanine reduce potency. The results produced experimental pA_2 values which were used as experimental probes for MD simulations and binding free energy MM-GBSA calculations for of **K18** in complex with 14 mutant A_3Rs. Using the MM-GBSA calculated ΔG_{eff} values it was possible to distinguish three sets of mutant receptors, i.e. those that reduce or negate **K18** potency at the A_3R, those that bind stably and maintain potency and those that increase potency compared to WT A_3R. The calculated ΔG_{eff} values for **K18** and experimentally determined pA_2 values displayed very good correlation, with r = -0.81. In our previous work investigating IB-MECA and NECA agonists binding to A_3R, the correlation between calculated ΔG_{eff} values and experimental pIC_{50} values was also fair (correspondingly r = -0.69 and r = -0.76).

The characterization of the area TM6-EL2-TM5 in A_3R which includes lipophilic residues is very important for structure-based drug design of selective ligands. Although this area is considered to be occupied from the lipophilic groups of selective ligands, like the iodo-benzyl group in IB-MECA, the experimental results show and the computational model supports that the mutation V169$^{5.30}$E causes an increase in IB-MECA and NECA activity, rather than the expected reduction, and that I253$^{6.58}$ is not an important residue of this region. We also show

here that I253$^{6.58}$ and V169$^{5.30}$E maintains **K18** antagonistic potency. It is also interesting that the potency of **K18** is enhanced by the mutations of L90$^{3.32}$A in the low region or L264$^{7.35}$A in the middle/upper region which are directly interacting residues with **K18**, suggesting an empty space in the orthosteric area available for increasing antagonist potency. These findings could have significant impact on the design of potent and selective ligands targeting A_3R.

Table of Contents

List of Figures

Nomenclature

AC	Adenylyl Cyclase
ADP	adenosine diphosphate
Ado	adenosine
AMBER	Assisted Model Building with Energy Refinement
AR	adenosine receptor
A_1R	alpha-1 adenosine receptor
$A_{2A}R$	alpha-2-alpha receptor
$A_{2B}R$	alpha-2-beta receptor
A_3R	alpha-3 receptor
ASP	Astex statistical potential
ATP	adenosine triphosphate
BRET	bioluminescence resonance energy transfer
cAMP	cyclic adenosine monophosphate
CD	cavity and dispersion
CG	coarse-grained
CHARMM	chemistry at Harvard molecular mechanics
ChemPLP	chemistry Piecewise linear potential
CHO	Chinese hamster ovary
CNS	central nervous system
COPD	chronic obstructive pulmonary disease
DMPC	1,2-Dimyristoyl-sn-glycero-3-phosphocholine (Phosphatidylcholine)
DMSO	Dimethyl sulfoxide
DPCPX	8-cyclopentyl-1,3-dipropylxanthine
ECCC	european collection of cell culture
ECFP4	extended chemical (radial) fingerprints for four atoms
EDTA	Ethylene diamine tetra-acetic acid
EL	extra-cellular loop
ERK	extracellular signal-regulated kinase
FDA	food and drug administration
FBS	foetal bovine serum
FD	finite difference
FEP	free energy perturbation
FRET	Förster/ fluorescence resonance energy transfer
GAFF	generalized amber force field
GB	Generalized Born
GOLD	Genetic Optimization for Ligand Docking
GPCR	G protein-coupled receptor
GPU	graphics processing unit
GTP	guanosine triphosphate
HTRF	homogeneous time resolved fluorescence
HEMADO	2-(1-hexynyl)N6-methyladenosine
IB-MECA	1-deoxy-1-[6-[[(3iodophenyl)methyl]amino]-9H-purin-9-yl]-N-methyl-β-D-ribofuranuronamide

IL	intra-cellular loop
LIE	linear interaction method
MD	molecular dynamics
MM	molecular mechanics
MMFF94	molecular mechanics force field 94
MM-GBSA	molecular mechanics - generalized Born surface area
MM-PBSA	molecular mechanics - Poisson Boltzmann surface area
ND	no difference
NECA	1-(6-amino-9*H*-purin-9-yl)-1-deoxy-*N*-ethyl-β-D-ribofuranuronamide or 5′-(N-ethylcarboxamido)adenos
NMR	nuclear magnetic resonance
NPT	constant number of particles, pressure, and temperature
NR	no response
ns	nano-second
NVT	constant number of particles, volume, and temperature
OPM	orientations of proteins in membranes
OPLS	optimized Potentials for Liquid Simulations
PAINS	pan-assay interference
PB	Poisson-Boltzmann
PBC	periodic boundary conditions
PBEQ	Poisson-Boltzmann equation
PCM	polarizable continuum model
PDB	protein data bank
PKC	protein kinase C
PME	particle mesh Ewald
POPC	1-Palmitoyl-2-oleoyl-sn-glycero-3-phosphocholine (Phosphatidylcholine)
POPE	1-Palmitoyl-2-oleoyl-sn-glycero-3-phosphoethanolamine (Phosphatidylethanolamine)
PTX	pertussis toxin
QSAR	quantitative structure activity relationship
RESP	restrained electrostatic potential
RMSD	root mean square deviation
ROCS	rapid overlay of chemical structures
RTK	receptor tyrosine kinase
SANDER	simulated annealing with NMR-derived energy restraints
SAR	structure activity relationship
SASA	solvent-accessible surface area
SBDD	structure-based drug design
SD	standard deviation
SEM	standard error of mean
SID	simulation interactions diagram
SP	standard precision
TI	thermodynamics integration
TM	trans-membrane (helix)
TR	time-resolved measurement
TR-FRET	time-resolved Förster/ fluorescence resonance energy transfer

UCSF	university of California and San Francisco
vdW	van der Waals interactions
VMD	visual molecular dynamics
VS	virtual screenings
WT	wild-type
XAC	xanthine amine congener
XP	extra precision
ZM241385	4-{2-[(7-amino-2-furan-2-yl[1,2,4]triazolo[1,5-a][1,3,5]triazin-5-yl)amino]ethyl}phenol

Chapter 1

G-protein coupled receptors and Adenosine receptors

1.1 G-protein coupled receptor family

One of the most common response pathways in the cell is formed by the guanine nucleotide-binding proteins (G proteins), which are involved in second-messenger cascades triggered by the G-protein-coupled receptors (GPCRs), which are membrane proteins with seven-transmembrane helices denoted as TM I through TM VII [1].
Major targets for drug discovery and development, proteins of the GPCRs family are involved in recognition of a great variety of extracellular signals including ions, small molecules, peptides and globular proteins [2,3]. Despite the diversity of natural GPCRs ligands, there exist several receptor subfamilies in which all proteins respond to a single endogenous agonist: for example, all GPCRs in the adrenergic subfamily are activated by epinephrine while all muscarinic receptors naturally bind acetylcholine and its derivatives. GPCR subtypes within a subfamily usually have distinct amino acid sequences, tissue distributions, effect or coupling, and/or functional and pharmacological profiles; however, their ligand binding pockets are highly conserved within the subfamily. The similarity of the orthosteric binding pockets poses a challenge for design of subtype selective ligands which remains one of the main hurdles in development of safe and effective medications targeting GPCRs [4].

1.2 The GPCR cascade

G protein-coupled receptors (GPCRs) are the largest group of cell surface proteins, which translate chemical information of various extracellular stimuli to a specific biological response in cells. Clinically, GPCR ligands regulate many physiological and pathological conditions and represent a remarkable class of pharmaceutical agents, with 26.8% of FDA approved drugs targeting group A of GPCRs.[5] Classically, the binding of an agonist to an inactive state of a GPCR causes conformational changes that lead to an active state of a GPCR, which is capable of activating a heterotrimeric G protein. The discoveries of the past 40 years have transformed GPCR receptors from abstract physiological concepts into physicochemical entities. They have revealed pervasive, even universal, principles concerning their structure, function and regulation. [6] The GPCRs modulate an enormous variety of physiological and behavioral signaling pathways causing functional changes that include dynamic interactions with regulatory molecules and trafficking to various cellular compartments at various stages of the life cycle of a GPCR, leading to the generation of second messengers [7] Termination of the signal, which is known as receptor desensitization, results in uncoupling of the receptor from the G protein through phosphorylation of the receptor C terminus and recruitment of β-arrestin to the phosphorylated C terminus of GPCRs, where β-arrestin binding stimulates receptor endocytosis.[89]
The first second-messenger molecule that was identified is cyclic 3′,5′-adenosine monophosphate (cAMP), which was discovered by Sutherland and Rall in the late 1950 [10]. Changes in cellular

cAMP levels can occur from increase or decrease in its biosynthesis, caused corresondingly by the catalytic conversion of ATP to cAMP that takes place due to the enzyme adenylyl cyclase. Adenylyl cyclase is an enzyme whose activity can be stimulated and inhibited by different GTP-bound proteins, like the GPCR receptors. $A_{2A}R$ and $A_{2B}R$ stimulate adenylyc cyclase, through a G_s mediated response, and increase cAMP but A_1R or A_3R inhibited adenyl cyclase and reduce cAMP in cells through a $G_{i/o}$ mediated response. The α-subunit of the stimulatory G protein, $G\alpha_s$, enhances the activity of every adenylyl cyclase isoform whereas, the α-subunit of the inhibitory G protein, $G\alpha_i$ has been shown to directly inhibit this enzyme [11].

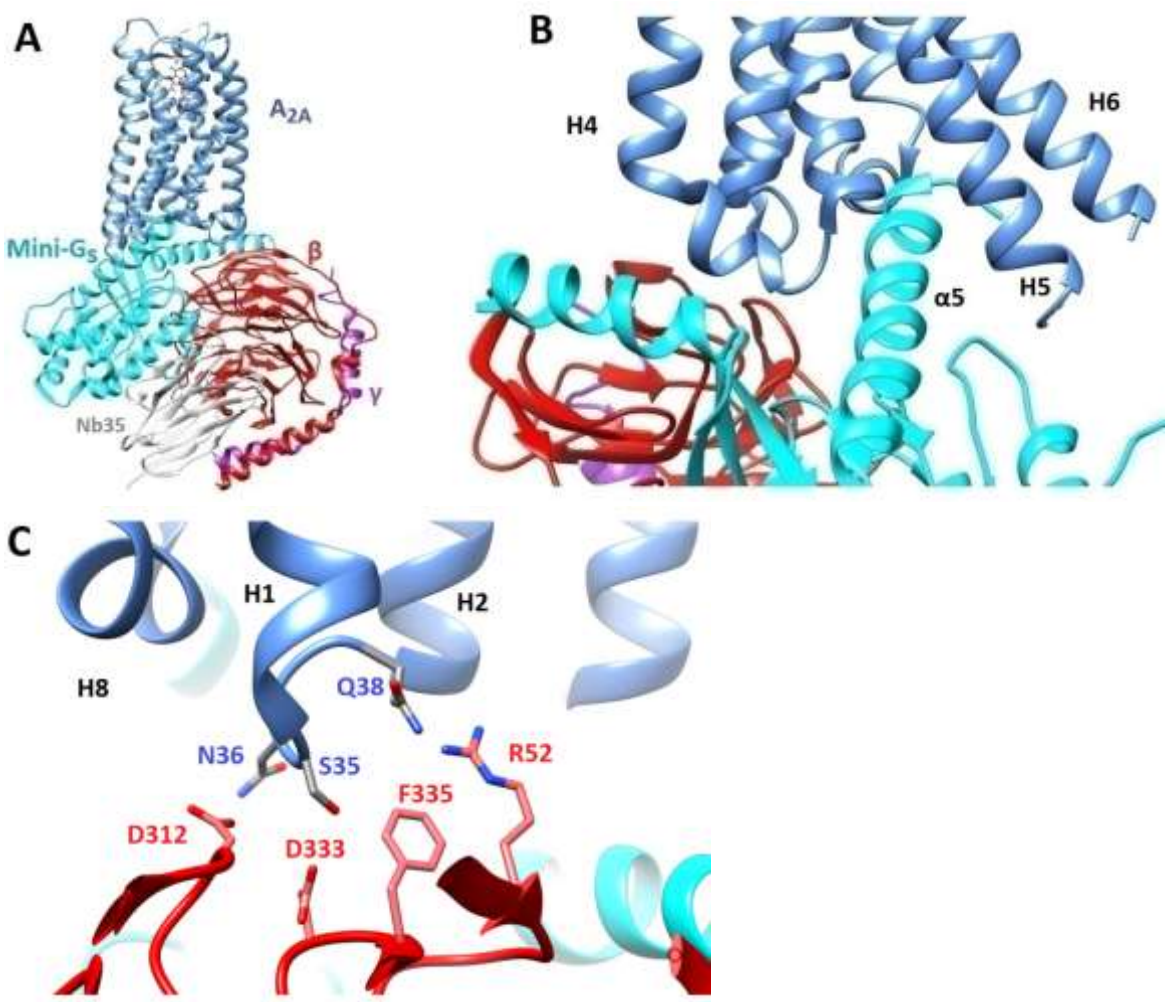

Figure 1.1 The figure presents the GPCR typical structure (here A_{2A} in complex with Gs via cryo-EM. PDB ID: 6GDG). a5 helix and the N36, S35, Q38 of the $A_{2A}R$ seem to contribute with D312, D333, F335 and R52 of the Gs subunit to the complex's formation.

1.3 The GPCRs-G complex

Adenosine receptors ($A_{2A}R$) is a good example of a prototypical G protein-coupled receptor (GPCR) that couples to the heterotrimeric G protein G_S**,** the GTPase domain of the α subunit β and γ sub-units **(Figure 1.1a)**. $A_{2A}R$ is activated by the endogenous agonist adenosine and plays a

prominent role in cardiac function, the immune system and central nervous system, including the release of the major excitatory neurotransmitter glutamate [12]. An active intermediate state bound to agonists[13] [14,15] and the fully active state bound to an agonist and coupled to an engineered G protein, mini-G_S [16].

So far the main choice in how to determine the structure of a GPCR coupled to a heterotrimeric G protein, was the X-ray crystallography [17]. However, the disadvantage of the X-ray crystallography lies in the difficulty of producing good quality crystals of a GPCR coupled to a heterotrimeric G protein, and new methods, such as lipidic cubic phase and cryo-EM microscopy in order to determine the structures of the GPCRs. The latter even the low resolution structures it provides, determines the regions are characterized by high flexibility, in contrast with the X-ray crystallography [17]**.**

A significant number of studies showed that the interactions between a heterotrimeric G protein and a Class A GPCR, the vast majority of interactions are made by the α subunit, in particular the C-terminal α5 helix [17,18]. The roles for the βγ subunits could not be described. However, there was an interaction between the β subunit and the β_2-adrenoceptor [18] and also between the β subunit and the class B receptors for calcitonin and glucagon-like peptide [17]. In addition, there is mutagenesis data suggesting that the α2-adrenergic receptor directly interacts with the β subunit [17]**.**

There are two Class A receptors whose structures have been determined coupled to heterotrimeric G_S, β_2AR [18] and A_{2A}R and two Class B structures coupled to G_S were published. All the receptor structures coupled to G_S show the majority of the contacts between the α5 helix of the α subunit and H3, H5 and H6 of the receptor, with receptor-dependent contacts in H1, H2 and H8 [17]. **(Figure 1.1bc)** The overall architecture of the receptors coupled to G_S are conserved. The interactions observed here between A_{2A}R and the β subunit are also observed in the Class B receptors, but are absent from the crystal structure of the β_2AR-G_S structure, although a shift of the β subunit by only a few ångstroms would be sufficient for interactions to occur [17].

1.4 Common structural elements of the GPCR A family

In the past years the field of GPCRs structural biology has enjoyed a renaissance, with a big number of new members yielding to crystallization [19–23]. These efforts represent examples of what is sure to be a blossoming of information for this important class of membrane proteins. I will report what insights might be gained from a structural comparison of the different regions of the GPCRs after introducing the structures themselves [24].

The class A receptors can be divided into four groups termed α, β, γ, and δ. The α group is divided into, opsins, melatonin, prostaglandin, and MECA (melatonin/EDG/cannabinoid/adenosine) receptors. The β group contains peptide receptors, and the γ group contains the chemokine melanin concentrating hormone (MCH) receptors and SOG (somatostatin/opioid/galanin) receptors. Finally, the δ group contains the Mas proto-oncogene and Mas proto-oncogene-related receptors, purine binding receptors, and the glycoprotein receptors [1,25].

For A GPCRs after the X-ray structure of A_{2A} adenosine receptor (A_{2A}R) in complex with the antagonist(4-[2-[7-amino-2-(2-furyl)-1,2,4-triazolo-[1,5-a][1,3,5]triazin-5-ylamino]ethyl]phenol) (ZM241385, see **Figure 1.5**) was published in 2008 considerable progress in methodology of membrane proteins crystallization and structural biology methods led

to the experimental determination of the complex between $A_{2A}R$ and $A_1R$with antagonist using X-ray [7,26–32], the complex of $A_{2A}R$-Gs with agonist using cryo-em [16,17,33].

Analysis of the structure of three representative subclasses of A GPCRs family, i.e., rhodopsin, adrenergic, adenosine receptors, eveals many common structural elements. The most important common feauture consists of seven TM α-helices that surround the orthosteric binding cavity **(Figure 1.2)**. Thus, alignment of the TM regions of the five GPCRs, with PDB ID 1U19, 3CAP, 2RH1, 2VT4, and 3EML, corresponding to opsin, adrenergic (β1, β2) and adenosine A_{2A} receptor, respectively, identified a common structural core of 97 residues with an average RMSD of Cα carbons 1.3 Å [1]. Also, the three common broad extracellular loops EL1 EL2 and EL3 **(Figure 1.3)** and the three intracellular loop regions IL, IL2 and & IL3 were identified **(Figure 1.4)**. The length of these loops varies between the members of the GPCR family.
Based on a big number of solved structures of GPCRs receptors with ligands using X-ray crystallography [34] or cryo-em [35] and the initial solved bovine rhodopsin structure the role of one highly conserved between GPCRs stretch of residues, the amino acids glutamate acid/aspartic acid–arginine–tyrosine, i.e., the E/DRY motif, has significant role to regulate GPCR conformational states. The E/DRY motif at the intracellular base of TM3 is found in most class A GPCRs, has a conserved interaction with a glutamate residue at the base of TM4 [36–38]. More specifically, interactions between the cytoplasmic end of TM3 ($Asp^{3.49}$-$Arg^{3.50}$-$Tyr^{3.60}$) and TM6 ($Glu^{6.30}$) forming the conserved E/DRY sequence motif Asp/Glu-Arg-Tyr have been proposed to constitute an "ionic lock" that may play a role in restraining the fully in active conformation of the class A receptors. As in β_1AR and β_2AR, the E/DRY motif in the A_{2A}AR adenosine receptor participates in interactions that restrain the conformation of IL2. In the A_{2A} adenosine receptor, $Asp^{3.49}$ forms a hydrogen bond with $Tyr^{3.60}$ in IL2 and $Thr^{2.39}$ at the base of TM 2. $Arg102^{3.50}$ may play also a role in stabilizing the deprotonated state of the adjacent $Asp101^{3.49}$ to allow this residue to make stronger hydrogen-bonding interactions with TM2 and IL2[20]. In **Figure 1.3** the ionic lock is formed in β_1AR and rhodopsin but not in $A_{2A}R$ and β_2AR.

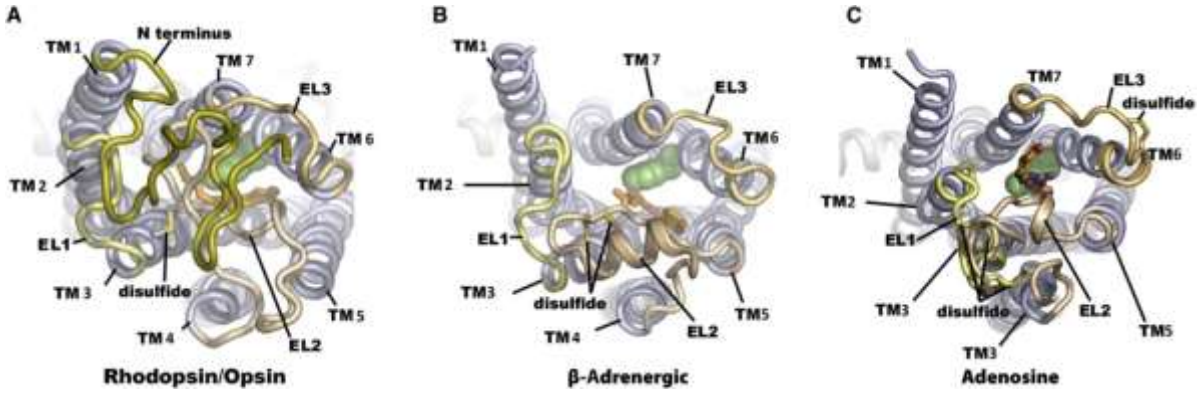

Figure 1.2 Top view from the extracellular domain of (A) Rhodopsin R, (B) β-Adrenergic R, (C) $A_{2A}R$. The extracellular domain is highly constrained and held away from the ligand binding pocket opening [1]. The binding cavity is surrounded by seven TM helices and is positioned

in the middle of the protein, where here is presented by the Trp $246^{6.48}$ in green van der Waals spheres.

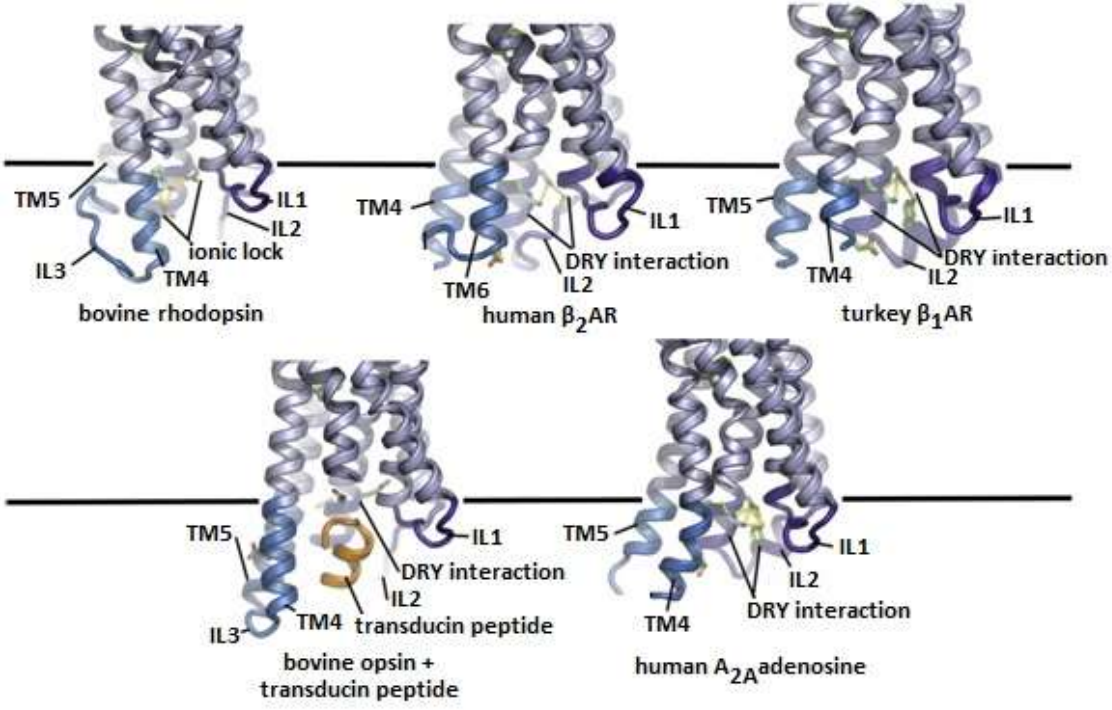

Figure 1.3 Panel of intracellular interactions across the family of experimentally solved Class A GPCRs. Top panel includes the bovine rhodopsin and the adrenergic receptors. Bottom panel includes opsin receptor and $A_{2A}R$. [1]

Bovine rhodopsin is the only receptor with an intact ionic lock interaction between arginine in **TM 3** and glutamate in **TM 6** since it exists in the inactive state. However, in the opsin structures (both bound with the agonist transducin peptide of rhodopsin or without its presence), the ionic lock is broken in the active state and the a-helical section of **TM 5** moves part from **TM 3** considerably relative to the inactive bovine rhodopsin. Human β_2AR has a similar length **TM 5** as bovine opsin, turkey β_1AR, and human A_{2A}Rs, all of which have a disrupted ionic lock being in the active sate. With the exception of opsin and rhodopsin, the DRY motif interacts with IL2 through a hydrogen bonded interaction between the aspartate residue and either a serine or tyrosine residue on IL2 [1].

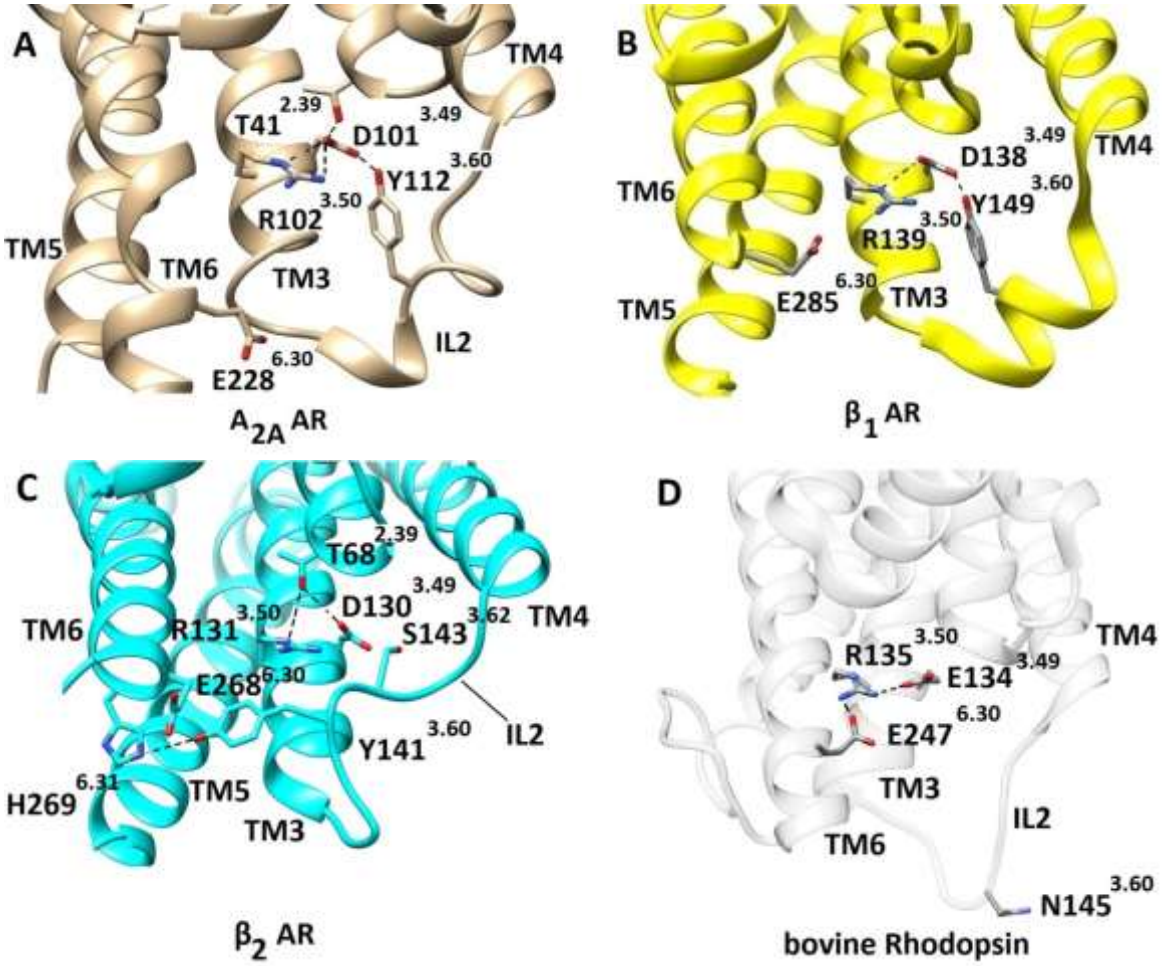

Figure 1.4 Comparison of interactions between TM3 and IL2, i.e. the E/DRY ($Asp^{3.49}$/$Glu^{6.30}$-$Arg3^{.50}$-$Tyr^{3.60}$) motif for human A_{2A}AR (PDB ID 3EML), human β_2AR (PDB ID 2RH1), turkey β_1AR (PDB ID 2VT4) and bovine rhodopsin (PDB ID 1U19). (A), (C) In A_{2A}R the DRY-motif does not participate in any stabilizing ionic interactions, similarly to β_2AR. It has been proposed that the "ionic lock" $Glu^{6.30}$-$Arg^{3.50}$ of E/DRY motif may play a role in restraining the fully inactive conformation of rhodopsin and other class A receptors [20]. β_2AR and rhodopsin does not contain a helical segment in IL2. (B), (D) Turkey β_1AR participates in interactions similar to canonical ionic lock in rhodopsin without the hydrogen bond to TM3 (Tyr3.60). Noteworthy, there is no Tyr3.60 in bovine rhodopsin, but Asn instead; relatively away from the motif.

1.5 Adenosine Receptors

Adenosine (Ado, (**1**)) (**Figure 5**) a naturally occurring purine nucleoside, is the endogenous agonist of adenosine receptors (ARs) and can influence a wide range of physiological functions [39]. Ado (**1**) is involved through its ARs in the regulation of various biological functions in different tissues and organ systems, including cardiovascular, liver, renal, respiratory and central nervous system (CNS). [29,40]. In **Figure 5** are shown also the structures of other agonists, like the 1-(6-amino-9*H*-purin-9-yl)-1-deoxy-*N*-ethyl-β-D-ribofuranuronamide or 5′-(N-ethylcarboxamido)adenosine (NECA, (**3**)), the 1-deoxy-1-[6-[[(3iodophenyl)methyl]amino]-9H-purin-9-yl]-N-methyl-β-D-ribofuranuronamide (IB-MECA, (**5**)), the 2-(1-hexynyl)N6-

methyladenosine (HEMADO, (**8**)) etc and antagonists **9** and **10** which will be discussed later in this thesis.

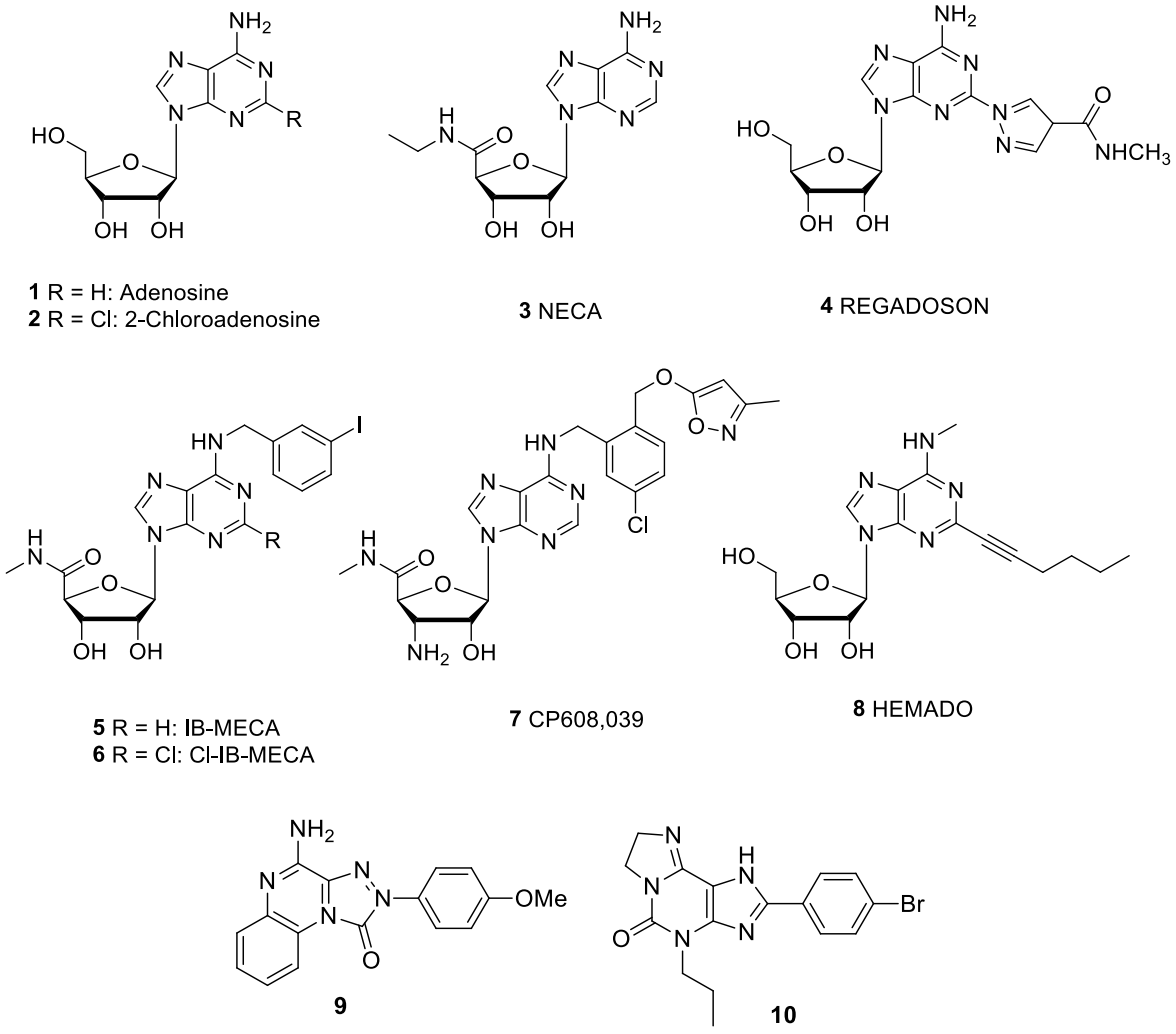

Figure 1.5 The structures of Ado (**1**), 2-Cl-Ado (**2**) (1). The non-selective A_3R agonist NECA (**3)** and the A_3R-selective agonist IB-MECA (**5**), Cl-IB-MECA (**6**), HEMADO (**8**) and CP608,039 (**7**). The structures of A_3R selective antagonists **9,10** are shown. Also is shown the new generation $A_{2A}R$ selective agonist regadenoson (**4**) which was approved by FDA as a coronary vasodilator for use in myocardial perfusion imaging **(4)**. [41,42]

ARs are G protein-coupled receptors (GPCRs), which are expressed in both the CNS and the periphery, and comprise four subtypes; A_1, A_{2A}, A_{2B} and A_3. The four AR subtypes (A_1, A_{2A}, A_{2B}, and A_3) are responsible for a wide range of physiological processes by acting upon different signaling pathways. In particular, $A_{2A}R$ and $A_{2B}R$ subtypes are activated by Ado (**1**) and coupled through G_s resulting in the stimulation of adenylyl cyclase, and therefore, the increase of 3′,5′-cyclic adenosine monophosphate (cAMP) levels. In contrast, A_1R and A_3R subtypes, when activated by Ado (**1**), inhibit adenylyl cyclase and decrease cAMP levels within cells by coupling to the $G_{i/o}$ family of G proteins.[43–45]

A breakthrough in the AR field was the publication of a crystal structure for the $A_{2A}R$ subtype, which revealed the binding mode of the antagonist 4-[2-[7-amino-2-(2-furyl)-1,2,4-triazolo-[1,5-a][1,3,5]triazin-5-ylamino]ethyl]phenol (ZM241385)[20], see **Figure 1.6**. The ZM241385 antagonist of Astra Zeneca also bind to the human $A_{2B}R$ with moderate affinity. The structure of $A_{2A}R$-ZM241385 complex enabled the use of remarkably successful structure-based approaches in ligand discovery providing high hit rates and novel ligands using $A_{2A}R$ and homology models of A_3AR. and have been used as a radioligand at that subtype. [46]

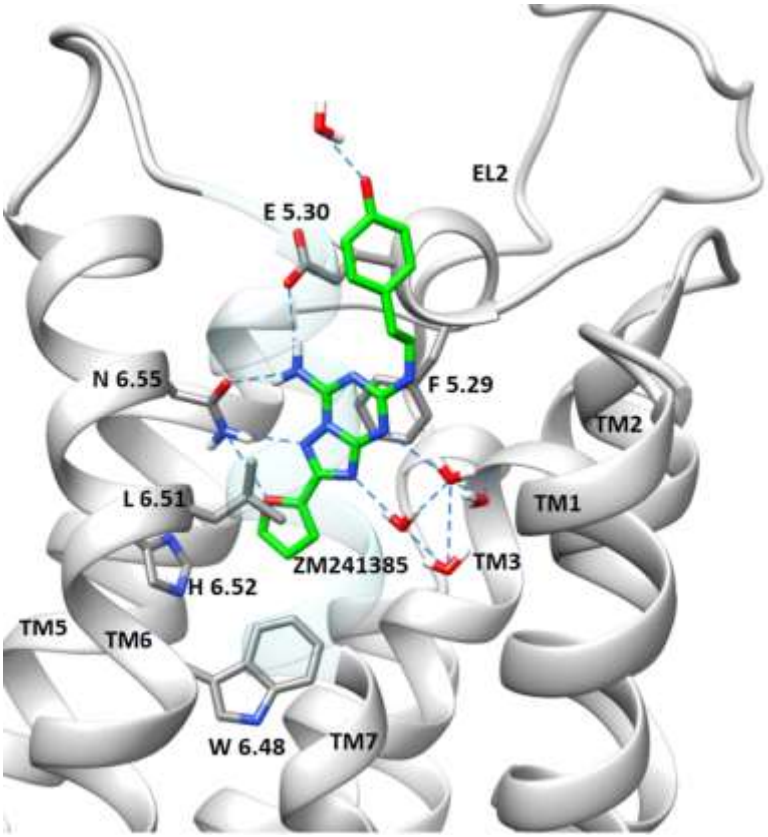

Figure 1.6 Binding mode of ZM241385 at the $hA_{2A}AR$ binding site (PDB ID 3EML). [20] The complex is viewed from the membrane side facing helices TM6 and TM7 with the view of TM7 partially omitted. Side chains of the amino acids crucial for ligand binding are displayed as gray sticks. Hydrogen atoms are not displayed, whereas hydrogen bond interactions are highlighted as blue dashed lines.

$A_{2A}R$ had been, until recently, the only AR subtype structure that had been determined in various activation and coupling states. The binding mode of agonists like Ado (**1**) and NECA (**2**) (**Figure 1.5**) were resolved using X-ray crystallography [32 35 14 15 47 48 49] or cryo-EM.[50]**,** respectively.
The binding mode of several antagonists, i.e., CGS-21689, [12] UK-432097, [15] ZM241385, [20] PSB36, caffeine and theophylline[51 30 34 52] inside the $A_{2A}R$ and one bound to an engineered G protein [47] have been determined since 2008. [17] Experimental structures show also the binding of A_1R with the antagonists DU172 [32] and PSB36 [53 35] and the adenosine-bound A_1R-G_i complex. [54]

These experimental structures of $A_{2A}R$ and A_1R complexes can be utilized for structure-based drug design. To date, no experimental structure for A_3R and $A_{2B}R$ has been released, most likely due to difficulties in crystallization, compared to A_1 and $A_{2A}Rs$, and therefore, homology modeling must be realized to study these receptors in complex with ligands.

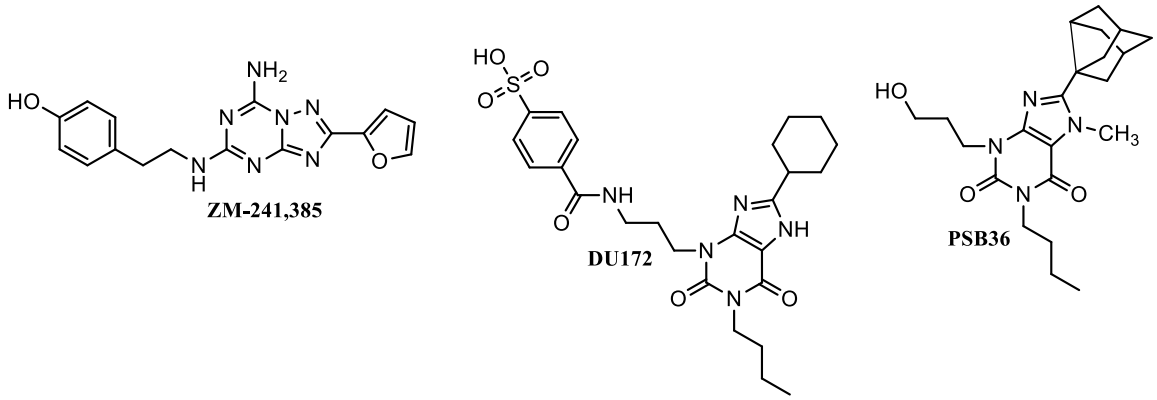

Figure 1.7 Chemical structures of ARs antagonists ZM-241385, DU172 and PSB36 which formed complexes with A_{2A} and A_1 receptors respectively analyzed with X-ray crystallography.

It has been reported that the EL2 may orchestrate a network of interactions which may stabilize the inactive conformation of the receptor and/or kinetically control the receptor-ligand recognition [55,56]. $A_{2B}Rs$ are characterized by the longest EL2 (≥38 amino acids) while in A_3 subtype, EL2 is the shortest (≥28 amino acids). [57] Despite the high degree of structural diversity with respect to EL2 in family A GPCRs, there is one feature that is conserved in the vast majority of GPCRs i.e. a disulfide bond between EL2 and the top of TM3 (Cys3.25). This disulfide bond effectively tethers EL2 on the top of the TM helical bundle and provides a very important conformational constraint of the EL2. Some GPCRs have additional disulfide bonds between different ELs such as for example between EL2-EL1 in all $A_{2A}R$ receptors. Additionally, the $A_{2A}R$ subtype also possesses an additional intra-loop disulfide bond within EL3, in common with melanocortin receptors and human histamine receptor 1. These "additional" disulfide bonds contribute to reduce the flexibility of ELs and, consequently, they peculiarly sculpt the topography of the extracellular portion of the receptor in proximity of the orthosteric binding cleft. Finally, only one cysteine-bridge, linking TM3 to EL2 in $A_{2B}R$ models, is detectable.

If the orthosteric binding area is compared for the ARs, the A_1 subtype has a much closer homology to $A_{2A}R$. Although A_1R differs from $A_{2A}R$ by only four residue changes in the periphery of the binding pocket, the shape of the binding area differs according to the recently published X-ray structure of A_1R in complex with the covalently bound antagonist DU172 [32]**.** It was showed that due to movements of TM1,TM2,TM3 and TM7 and EL3 in A_1R. A_1R binding cavity is very wide and open compared to $A_{2A}R$ which is elongated and narrower. The $A_{2A}R$ pocket is narrower with Met(7.35) acting as a gatekeeper (see **Figure 1a**) and preventing entry and binding of bulky substituents.The compact structure of the TM bundle of the $A_{2A}R$ is consistent with its unique disulphide bond, C74-C146, through which the beginning of TM3 is tightly connected with the end of EL2 allowing for shifts in 1, 2, and 3 TMs as suggested in this work. Both A_1 and A_3Rs lack this disulphide bond. According to ref. [32], TM7 also tilts towards TM6, possibly as a result of a shorter EL3 in the A_1R due to the deletion of one amino acid; EL3 is also shorter by one amino acid in A_3R. These differences in ELs tethering resulted in the different shape of binding site and influence especially the approach of the ligand **(Figure 1.8).**

A_1R binding area includes a common orthosteric binding region and a secondary one, i.e., there is a common region covered by ZM241385 inside A_{2A}R or DU172 inside A_1R despite their different orientation and height into the cavity and the different shape and extension of the binding area **(Figure 1.8)**.

A_1, A_{2A}, A_{2B}Rs contain the E(5.30) residue, except A_3R which have a valine in (5.30) position. This glutamate acid residue in (5.30) position may play an important role in high affinity ligand binding through the formation of a strong hydrogen bond, for example, with an unsubstituted exocyclic amine. Instead, the valine in (5.30) position of A_3R may allow bulky substitutents fitting, for example, bulky substituents on amino group or other lipophilic moieties at this region.

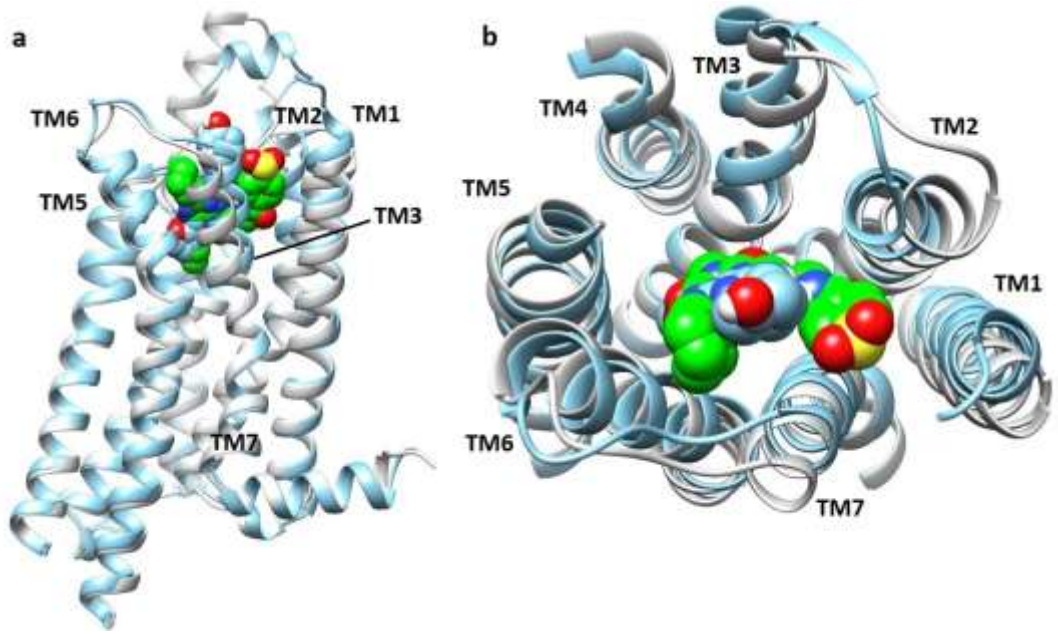

Figure 1.8 Comparison of the experimetally resolved orthosteric binding area in A_1, A_{2A}Rs. PDB ID 4EIY A_{2A}AR is colored blue; Light gray for the PDB ID 5UEN A_1.

1.6 Adenosine Receptor Agonists and Antagonists

1.6.1 General

Ado (**1**) is involved in the regulation of various biological functions in different tissues and organ systems, including cardiovascular, liver, renal, respiratory and CNS through its receptors. The biological and biochemical activities of adenosine are energy transfer in the form of ATP and ADP, signal transduction, depressant effect on heart rate and atrioventricular conduction etc. [58]. Ado (**1**) is the natural ligand for the ARs. It is an endogenous purine nucleoside that acts as an agonist with a high affinity for the human A_1, A_{2A} and A_3Rs (hA_1 Ki = 310 nM , hA_{2A} Ki = 700

nM, hA_3 Ki = 290 nM) and with considerably lower affinity for the A_{2B} receptor (hA_{2B} Ki ≥ 10 μM) [59].

$A_{2A}R$ antagonists have emerged as an attractive approach to treat Parkinson, sickle cell and infectious diseases, cancer, ischemia reperfusion injury, diabetic nephropathy, cognition, and other CNS disorders [60] [61]. $A_{2B}R$ antagonists may be useful for the treatment of asthma, chronic obstructive pulmonary disease (COPD), and inflammation. A_1R is an attractive pharmacological target, since its antagonists have been explored as kidney-protective agents, cognitive enhancers, and antiasthmatic and CNS agents.

A_3R is a target for a number of inflammatory diseases, including asthma, glaucoma, COPD, rheumatoid arthritis and ischemic injury [58] In addition, evidence is emerging to suggest that the A_3R is over-expressed in various tumor cells compared to normal cells, presenting the possibility that A_3R may be a viable drug target against cancer cell proliferation.[62–69].

Functional importance of different AR subtypes in various body functions and tissues imposes very high requirements on subtype selectivity of AR antagonists and agonists as candidate drugs [70–72] and leads to significant challenges in clinical development of the candidate drugs.

It has been showed that Ado acts as a cardiac anti-arrhythmic agent.[29] [73] However, Ado (**1**), as well as 2-Cl-Ado (**2**) and NECA (**3**) (**Figure 1.5**), are non-selective AR agonists and their side effects include chest pain, flushing, dyspnea and low blood pressure through the activation or inhibition of other AR subtypes**.** [74] Thus, the development of more selective AR agonists with fewer adverse effects is needed. Despite early setbacks, 2008 has been marked by successful FDA approval of the new generation $A_{2A}R$ selective agonist regadenoson (**4**) as a coronary vasodilator for use in myocardial perfusion imaging (**Figure 1.5**). This breakthrough, along with other advances in preclinical and clinical studies [72] boosts interest to development of a new generation of bio-available and safe agonists and antagonists for adenosine receptors [4].

1.6.2 Agonists and antagonists to A_3R

Therapeutic modulation of the adenosine system could offer the possibility of a "soft" treatment of different diseases, but due to the ubiquitous distribution of adenosine and its receptors, the challenge in ligand development depends on the specificity for the different receptor subtypes.

Optimization of Ado (**1**) has been achieved after structural modifications of the ribose moiety and by substitutions on the adenine ring and few structure are swhown in **Figure 1.5**. [75] However, NECA (**2**) and analogues are non-selective AR agonists and their side effects include chest pain, flushing, dyspnea and low blood pressure through the activation or inhibition of different AR subtypes.[74] Among the developed agonists [76–80] IB-MECA (CF101, Piclidenoson, (**5**)) **(Figure 1.4)** and its 2-chloro analogue, Cl-IB-MECA (**6**) (CF102, Namodenoson) are the most potent, subtype-selective and widely used A_3R agonists that have progressed to advanced clinical trials for inflammation and cancer, respectively.[81,82] Both compounds [75] inhibit tumor cell growth according to *in vitro* and *in vivo* tumor models.[83–85]. Other potent and selective A_3R agonists, which have been synthesized as analogues of NECA (**3**) and IB-MECA (**5**), include CP-608,039 (**7**) [76], HEMADO (**8**) [78], etc (**Figure 1.5**).

Only few selective antagonists have been developed like compounds **9, 10** and most of them are heterocyclic derivatives with a non-purine structure (**Figure 1.5**). Cyclized derivatives of xanthines, such as PSB-11, are A_3R-selective [72]. Selective A_3R antagonists are used for studies of several diseases, such as the heterocyclic derivatives OT-7999 which has been used for the

treatment of glaucoma studies [86], and other such antagonists are under consideration for treatment of cancer, stroke, and inflammation [71,87]. MRS5147 and its 3-iodo analog MRS5127 are highly selective A_3R antagonists in human, based on a conformationally constrained ribose-like ring that is truncated at the 5′ position [88]. No selective A_3R antagonists have yet reached human trials.

Chapter 2

Drug Design of Adenosine Receptors Antagonists

2.1 Theoretical Background

2.1.1 Structure-based Drug Design: Molecular Docking and Scoring functions

Docking in the field of molecular modeling is a method that makes predictions for the most preferable placement of a molecule within a second one when they bound to each other to form a stable complex [89]. Molecular docking is one of the most widely applied techniques in the field of drug design, because of its ability to give predictions about the possible binding mode of a small molecule ligand within a protein target binding site. [90]

In most of cases, molecular docking method can be described to handle a problem of "lock-and-key" nature in which the correct relative orientation of the "key" (small molecule ligand) will fit within the "lock" (protein receptor) resulting in a docking pose. In the common rigid molecular docking method only the ligand is flexible. However, both the ligand and protein are characterized by flexibility. Thus a "hand-in-glove" analogy is more realistic and precise than "lock-and-key" model for rigid molecular docking [91]. More sophisticated and computationally demanding model correspond to the "induced fit" method, where both the ligand and the protein adjust their structures to achieve an overall "best-fit" [92]. Molecular docking applied on structural complementarity taking into account receptor's molecular surface which is described in terms of its solvent-accessible surface area and ligand's molecular surface. Most algorithms include also the protein and the ligand separation by some physical distance, and the ligand finds the best conformation and orientation, i.e., docking pose to fit into the protein's binding site after a certain number of "moves". The "moves" are structural changes of the ligand and after the placement the energy between the protein and the ligand in the possible complex is calculated usually with a force field function. To the resulting docking pose another estimating function, the scoring function, is usually applied. The scoring function may be a force field function, an empirical funstion or a knowledge-based function.
Every docking program includes two steps components for its normal execution. A search docking algorithm and at least one scoring function.

Genetic Algorithms for Generation of Docking Poses. A genetic algorithm is a search algorithm that is inspired by Charles Darwin's theory of natural evolution as described in his book "The origin of species". This algorithm reflects the process of natural selection where the fittest offsprings are selected for reproduction. If parents have better fitness, their offsprings will be better than the parents and they will have a better chance for surviving. This process keeps on iterating and at the end, a generation with the fittest individuals will be found.

This could also be applied as an algorithm for searching of docking poses. Such an algorithm, includes an initial population of conformations, a fitness function, selections, cross-overs and mutations of parameters which change the conformations. The initial population consists of a group of individuals (conformations). Each individual consists of a set of parameters (variables) known as Genes; the latter are joined together to form a string which is called Chromosome corresponding to solution, i.e., a docking pose. The fitness function determines how fit an individual conformation is (the ability of an individual to compete with other individuals) and it is the measure of the probability for an individual to be selected for reproduction. Selection is the procedure where the fittest individuals pass their genes to the next generation. Then cross-over follows where the chromosomes of the selected individuals combined to produce the next generation of individuals. After that, in some offsprings, some of their genes can be subjected to a mutation with a low random probability and eventually mutations maximize the diversity and eventually the chance to produce the best-fitted individual, i.e., the best docking solution.

Docking softwares. GOLD. GOLD, is world-wide distributed software, which applied a genetic algorithm for conformational sampling of the ligand inside the binding cavity. There many other common softwares like DOCK AutoDock etc. [93]

Scoring functions. Scoring functions are functions that are utilized for the binding affinity calculation between two molecules after they have been complexed using docking calculations. In the majority of the cases the docking problem includes a small organic molecule within a binding cavity of a protein. Scoring functions have also been developed to the affinity interaction between two proteins [94] and between protein and DNA [95]. Representative scoring functions are physics-based scoring functions, i.e., molecular mechanics force fields equations that estimate the energy of the docking solution within the binding site. For these scoring functions the various contributions to the overall Gibbs binding free energy (ΔG_{bind}) can be written according to ~~as~~ the equation below:

$\Delta G_{bind} = \Delta G_{prot\text{-}lig}$ (vdW) + $\Delta G_{prot\text{-}lig}$ (electrostatic) + $\Delta G_{conf} + \Delta G_{rot} + \Delta G_{vib} + \Delta G_{solvation}$

The major components of ΔG_{bind} consist of the van der Waals and electrostatic protein-ligand interactions (usually calculated in the gas phase), conformational changes in the protein and ligand, restrictions of internal rotations upon binding, hanges in vibrational modes, desolvation of receptor and ligand upon association [96].

Gold software has available four scoring functions, all of which produce dimensionless fitness scores. The higher the value of the fitness score, the better the produced docking solution according to GOLD estimations. The scoring functions ~~se~~ are GoldScore, ChemScore, ASP and ChemPLP. In this work GOLD software and [93] GoldScore, ChemScore, and ChemPLP scoring functions were used for the Molecular Docking calculations.

GoldScore function. The GoldScore fitness function is the original scoring function provided with GOLD. It has been optimized for the prediction of ligand binding positions and takes into account factors such as hydrogen bonding energy, van der Waals energy, metal interaction and ligand torsion strain. [93]

ChemPLP function. The ChemPLP scoring function uses an empirical hydrogen bonding term and multiple linear potentials to model van der Waals and repulsive terms. It is fast to calculate

(4x faster than GoldScore) and recent validation tests have shown it to be generally more effective than the other GOLD software scoring functions for both pose prediction andscreening (VS).[93]

ChemScore function. The ChemScore fitness function use ΔG to define the total free energy change occurred on ligand binding and was trained against binding affinity data for 82 complexes. The ChemScore also incorporates a protein-ligand atom clash term and an internal energy term. ChemScore takes into account the hydrogen bonding, ligand flexibility, metal interactions and also the hydrophobic-hydrophobic contact area. [93]

ASP function. The ASP (Astex Statistical Potential) scoring function is an atom-atom distance potential derived from a database of protein-ligand complexes. [93]

2.1.2 Ligand-based Drug Design: Cheminformatics and structural fingerprints

Cheminformatics is the field of computer science that includes techniques applied to a variety of problems in the field of chemistry, i.e. it focuses on storing, indexing, searching, retrieving, and applying information about chemical compounds. These methods are widely used in chemical and allied industries in various other forms [97]. Thus, cheminformatics combines chemistry and computer science in the areas of topology, information retrieval and data mining in the chemical space [98] [99]. The term cheminformatics was defined by F.K. Brown**.** [100] [101]
3D paremeters can be used, for example the RMSD value of the compounds library when are overlayed with a reference compound (query) using various softwares like ROCS (OpenEye.Inc) as it is the experimental conformation of an antagonist inside an adenosine receptor for example the coordinates of ZM241385 inside the A_{2A}R (PDB ID 3EML, 2YDV).
Cheminformarics are usually connected with 2D molecular fingerprints as the most common representations of chemical structures for diversity analysis and molecular similarity searching. [102] [103] Representations of this type are simplifications of the chemical information contained in any chemical entity through binary vectors. **Figure 2.1** represents a binary fingerprint example of a chemical structure. [102]
The fingerprint methods **(Figure 2.1)** are widely used so far and include Linear, Dendritic, Radial (ECFP), MACCS, MOLPRINT2D, Pairwise, Triplet, and Torsion. [103]
For the purpose of the current thesis, both the 3D parameter, RMSD and radial ECFP4 fingerprints **(Figure 2.2)** were used to measure the molecular similarity. The first was used for virtual screening purposes, i.e., for filtering the highest scored 20000 docking poses, generated with GOLD and scored with ChemPLP, from 200000 conformations of compounds from HifFinder Maybridge Library**.** The 2D ECFP4 fingerprint was applied to validate the novelty of 27 hits as regards the structure of antagonists of A_1 A_{2A} A_{2B} and A_3 receptors available in ChEMBL database.

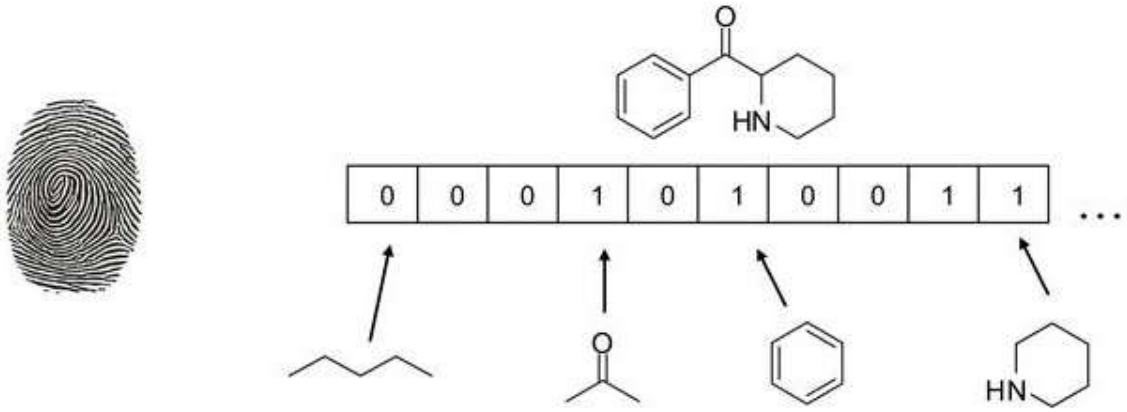

Figure 2.1 Fingerprint (left). Schematic representation of a binary and dictionary-based molecular fingerprint (right) [102].

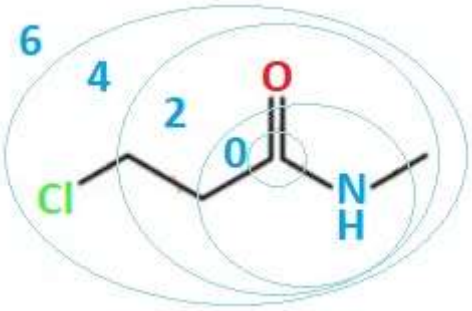

Figure 2.2 ECFP fingerprints divide the molecule in fragments, based on the distances. For example ECFP4 divides the molecule in every 4Å distances, ECFP6 in every 6Å and so on. These fragments are translated in binary fingerprints that are compared with the binary fingerprints stored in the dataset intended to be examined for molecular searching.

While most fingerprints are similar into the drug-like molecules each fingerprint has special characteristics so different query molecules and ligand sets can be distinguished [103]. For example, the performance of the ECFP4 fingerprint type is the best or among the best [104].
MOLPRINT2D was shown to behave similarly but was more effective and retrieves a higher number of active compounds, when the dataset is characterized by lack of knowledge about the active ligands of the dataset [103]. For significantly decreased feature numbers of a dataset, the calculation of Tanimoto similarity that ECFP gives was found to be much less effective than the bit density metric [105]. All the 2D fingerprints tools can be used for calculation of the structural similarity between molecules, using the Tanimoto coefficient for the comparison measurement. The Tanimoto coefficient is calculated according to the equation:

$$\mathbf{T_c = c / (a + b - c)}$$

With a: features of compound A, b: features of compound B and c: features common to A and B. Two molecules with value $T_c = 1$ are identical and $T_c = 0$ value means similarity absence.

2.1.3 MD simulations and MM-PBSA calculations

Molecular docking calculations using suitable scoring functions have been successful in certian cases**.** [106] However, end-point bindig free energy methods methods which account for solvation of the ligand and the protein before and after binding like Linear Interaction Method (LIE) or using an implicit solvation model [107], like Molecular Mechanics - Generalized Born Surface Area (MM-GBSA) or the Molecular Mechanics - Poisson Boltzmann Surface Area (MM-PBSA) methods, may improve scoring significantly. [108 109]
Scoring functions can dock high affinity ligands properly, but they likely give plausible docked conformations for ligands that do not bind. This results in a large number of false positive hits, i.e., similar docking poses for both active and inactive. One way to reduce the number of false positives is to perform MD simulations and check the stability of the docking pose.
Even if the docking pose for an inactive compound is stable during the MD simulations the mean binding free energy can be calculated using snapshots from the MD simulation trajectory and compared to the mean binding free energy of a reference active compound using the Molecular Mechanics - Generalized Born Surface Area (MM-GBSA) or the Molecular Mechanics - Poisson Boltzmann Surface Area (MM-PBSA) methods [110]. Essentials for the background for MD simulations are described in Chapter 3 and for MM-MBSA or MM-GBSA method in 5.1.1.
While using MM-MMBSA the molecular docking orientations derived from structure-based virtual screening are usually improved with short MD simulation [111] , this can be accomplished even in the cases where sampling by MD simulations is reduced to molecular mechanics (MM) minimization of the binding partners in MM-PBSA or LIE methods [112 113]

2.1.4 Binding affinity assays of ligands against ARs

2.1.4.1 Radiolabelled assays

Radioligands are used to measure the ligand binding to receptors and should ideally have high affinity, low non-specific binding, high specific activity to detect low receptor densities, and receptor specificity. [114] The most common, that is also applied in the current thesis is the Competition binding radioligand assay, which is used to determine the presence of selectivity for a particular ligand for receptor sub-types, which allows the determination of the density and proportion of each sub-type in the sample. [114] A typical competition radioligand assay is followed by plotting analysis that gives the percentage of the total binding, against the concentration log of the competing ligand.[115] A steep competition curve is usually indicative of binding to a single population of receptors, whereas a shallow curve, or a curve with clear inflection points, is indicative of multiple populations of binding sites. [114]

2.1.4.2 Adenylyl Cyclase activity assay

Adenylyl cyclase is an enzyme whose activity can be stimulated and inhibited by different GTP-bound proteins, like the GPCR receptors. Changes in cellular cAMP concentration within the cell can occur from increase s or decrease s in its biosynthesis, caused by the catalytic conversion of ATP to cAMP that takes place due to the enzyme adenylyl cyclase. $A_{2A}R$ and $A_{2B}R$ stimulate

adenylyc cyclase, through a G_s mediated response, and increase cAMP but A_1R or A_3R inhibited adenyl cyclase and reduce cAMP in cells through a $G_{i/o}$ mediated response.

Intracellular cAMP produced by whole cells or membrane receptors stimulated with GPCR agonists and antagonists can be measured using FRET method with red-shifted Alexa® Fluor dye chemistry for maximum excitation/emission discrimination.
Other methods measurements of the intra-cellular cAMP concentration include protein kinase A activation, competitive binding assays, and immunoassays. Alternatively, the adenine nucleotides (including ATP) of whole cells can be radio-labeled by their incubation with [3H]-adenine and the amount of radio-labeled cAMP that is located within the cell is measured [116,117] or the conversion of added radio-labeled ATP (commonly ^{32}P) to cAMP is measured.

2.1.5 Ballesteros-Weinstein for the aminoacid residues numbering of the A_1, A_{2A}, A_3Rs

The GPCR structures and especially the AR subptypes are characterized by concensus structural elements. However, many local modifications and slight structural variations between the AR subtypes, can cause confusion when a certain area of the ARs, for example the orthosteric binding area, is compared based on amino acid residues numbering description between two or more receptors. This kind of difficulties are overcome by using the Ballesteros-Weinstein numbering [118]. According to this amino acid numbering, the position of the residues is described by two numbers and the full-stop character between the numbers. The first number on the left describes the TM helix I-VII, and the second one, its position within the helix. Additionally, the most conserved residue in a given helix, X, is assigned the index X.50 and the other residues of the helix are numbered relative to the 50 position. In Table 2.1 is shown the Ballesteros-Weinstein (see 1st collumn from left) and common numbering (see 3rd, 4th, 5th column) for aminoacid residues of the orthosteric binding area for A_1, $A_{2A}$and A_3Rs.

Table 2.1 Ballesteros-Weinstein numbering of the orthosteric binding area for A_1, $A_{2A}$and A_3Rs

B-W	**A_1R**	**A_{2A}**	**A_3R**
2.66	I69	I66	V72
3.32	V87	V84	L90
3.33	L88	L85	L91
5.28	E170	L167	Q167
5.29	F171	F168	F168
5.30	E172	E169	V169
5.35	M177	M174	M174
5.38	M180	M177	M177
5.42	N184	N181	S181
6.48	W247	W246	W243
6.51	L250	L249	L246
6.52	H251	H250	S247

6.55	N254	N253	N250
6.58	T257	T256	I253
7.32	S267	L267	Q261
7.35	T270	M270	L264
7.39	I274	I274	I268
7.43	H278	H278	H272

2.2 Purpose of the work

Adenosine receptors (ARs) belong to the family of G protein-coupled receptors (GPCRs) and are expressed in both the CNS and the periphery. Adenosine is involved in the regulation of several biological functions in different organs and tissues, including the CNS, the cardiovascular system and the airways; many pathophysiological states are associated with changes of adenosine levels [29]. For these reasons, selective agonists, antagonists and allosteric enhancers [119] provide promising clinical candidates.

A breakthrough in the AR field was the publication of a crystal structure for the A_{2A} subtype, which revealed the binding mode of the antagonist ZM241385 (**Figure 1.5**). [20,52] This enabled the use of remarkably successful structure-based approaches in ligand discovery providing high hit rates and novel ligands using **A_{2A}AR** [7,26,28,30,31,120–124] and homology models of A_1 and A_3AR derived therefrom. [125,126]

In these studies, the ligand recognition occurs in the upper region of the transmembrane (TM) bundle, and the bound ligand is surrounded by TM3, 5, 6, and 7 and occasionally by TM2. The bound ligands are anchored inside the same binding cleft for all AR subtypes and can form up to two stabilizing hydrogen bonds with the side chain amide group of the N(6.55) [127,128] in TM6 (numbers in parentheses refer to the Ballesteros–Weinstein numbering [129]). The importance of interactions with N(6.55) was identified early in docking screenings. [120] N(6.55) and L(6.51) are key-to-recognition and highly conserved residues in all four AR subtypes and have been found to be crucial interaction partners for both agonists and antagonists in mutagenesis studies. [127] The ligands can occasionally form a tight hydrogen bond with the carboxylate group of E(5.30) in the extracellular loop 2 (EL2) in A_1, A_{2A} and A_{2B}ARs (see **Figure S1**).

Although the docking campaigns applying convenient scoring functions are often successful, [106] molecular mechanics Poisson-Boltzmann surface area **(**MM-PBSA) methods which account for ligand and the protein solvation before and after binding using an implicit solvation model [107] improved scoring significantly. [108,109,113,130]

Here, we explored the *in silico* screening of 14400 compounds included by Maybridge HitFinder library [131] against the X-ray structure of A_{2A}R complexed with ZM241385 using a combination of structure-based and ligand-based approaches. The re-scoring of a subset of docking poses was performed with CHARMM-PBSA energy minimization to further account for desolvation energy. Eight compounds were selected and tested and five of them were identified as positive hits. Compounds **K1** and **K5** exerted low micromolar affinities against A_{2A}/A_{3A}Rs (Table 1). Compound **K2** exhibited micromolar affinity against A_3AR and a very weak affinity against A_{2A}AR and compounds **K6** and **K7** micromolar affinity against A_3AR.

2.3 Methods

2.3.1 Virtual Screening of a Commercial Library against $A_{2A}R$

2.3.1.1 Ligand Preparation

Prior to the docking calculations, the Maybridge HitFinder library [131] was prepared using the LigPrep workflow as implemented on Maestro 10.3 [132]. The initial 14400 structures gave 19229 tautomers. Those tautomers were subjected to conformational analysis using OMEGA software **(OpenEye .Inc)** [133,134] resulting in 1655368 conformers which were used for virtual screening.

2.3.1.2 Structure-Based Virtual Screening: Molecular Docking and Scoring Calculations

Our molecular docking calculations were carried out using the 2.6 Å resolution crystal structure of the human $hA_{2A}R$ in complex with the antagonist ZM241385 (PDB ID 3EML). [20] The complex $hA_{2A}R$ - ZM241385 was prepared for the calculations by removing all non protein atoms and the intracellular T4-lysozyme insertion. The protonation states of ionizable residues (Asp, Glu, Arg, and Lys) were set to the most probable in aqueous solution at pH 7 using Maestro [135] The protonation states of the histidines in the binding region were set according to literature data in order to contribute to the stabilization of complexes. His7.43 was protonated at epsilon position to form H-bonds with the ligands (see for example **Figures 4c, 6b**). His6.52 was protonated at the epsilon position so as to form possible interactions with waters according to the literature. His6.66, at the top of the ligand binding site, was doubly protonated to form a salt-bridge with Glu5.30 in A_{2A} and A_1AR subtypes; in A_3AR it was protonated at the delta position to avoid repulsive interactions since A_3AR has a Val instead of Glu5.30. The N- and C-termini of the protein were capped by acetyl and methylamino groups, respectively, after applying the protein preparation module of Maestro [135] All hydrogens atoms of the protein-ZM241385 complex were minimized with the AMBER* force field by means of Maestro/Macromodel 9.6 using a distance-dependent dielectric constant of 4.0. The MM minimizations were performed with a conjugate gradient (CG) method and a root mean square of the energy gradient (threshold) value of 0.0001 kJ $Å^{-1}$ mol^{-1} was used as the convergence criterion. The *apo*-protein and ZM241385 structures were saved separately and used for the subsequent docking calculations. Molecular docking was performed with GOLD 5.2. [136,137] The ligand binding site was defined within 15 Å of the native ligand in the receptor structure. Comparison of the best docking poses obtained with GoldScore, [136] ChemScore [138] and ChemPLP [139] afforded an RMSD of of 1.1 Å, 4 Å and 0.80 Å respectively for ZM241385, relative to the X-ray coordinates [20]**.** Therefore, further docking calculations were performed using the ChemPLP [139] scoring function. The energy minimized ligands structures were submitted to ten genetic algorithm runs which is the default value used by the GOLD program. The "allow early termination" command was activated (which terminates searching for a ligand if the top three solutions have an RMSD difference in their coordinates smaller than 1.5 Å) and the docking poses were clustered using an RMSD difference criterion of

1.5 Å. All other parameters were set to their default values. In total, 48230 clusters and representative docking poses (Scheme 1) were selected.

2.3.1.3 3D Similarity Calculations

The ligand-based virtual screening tool Rapid Overlay of Chemical Structures (ROCS) [140] was used to predict structures that were similar to ZM241385 (molecular query). In brief, the docking poses of each compound were superimposed and scored on the basis of their overlap with the query in terms of shape (ShapeTanimoto) and functional groups (ColorTanimoto). All of the 3D similarity calculations were ranked according to the TanimotoCombo metric, which is the sum of the ShapeTanimoto and ColorTanimoto scores and thus ranges from 0 to 2. The top 6000 solutions (TanimotoCombo coefficient > 0.65) were selected for re-scoring using the MM-PBSA method as follows.

2.3.1.4 2D Similarity Calculations

Similarity calculations for ligands were carried out using the Canvas program by Schrödinger. [141] In order to investigate the novelty of the discovered hits, we calculated the maximum pairwise Tanimoto similarity of each hit in respect to the thousands of known AR ligands in the ChEMBL22 database using the extended chemical fingerprints for four atoms (ECFP4). [142,143] (see Table S4). The Tanimoto coefficient (Tc) quantifies the two-dimensional chemical similarity between two molecules by adopting a value between 0 and 1.

2.3.1.5 CHARMM-PBSA re-scoring

The theoretical background for MM-MBSA method is described in 5.1.1. Here, we applied instead of MD simulation for sampling, CHARMM-PBSA energy minimization in the docking pose for each of 5000 compounds. The result is a molecular mechanics-based calculated energy which includes the contribution of the desolvation energy term, i.e., the energy required for transferring the ligand from the water solution inside the binding cavity. When MD simulation is applied for sampling of the conformational space, instead of a single energy minimization, the mean energy from the MD simulation trajectory snapshots is obtained.

Energy minimization. Complexes of 6000 docking poses with A_2AR were subjected to MM-PBSA calculations using the CHARMM program [144,145] after applying a software for fragment-based molecular docking and protein structure preparation created by the A. Caflisch group. [146] All ligand-protein complexes were minimized with the CHARMM27 force field by the CG algorithm to a threshold value of 0.001 kcal mol^{-1} $Å^{-1}$. During minimization, the electrostatic energy term was screened by a distance-dependent dielectric of 4r to prevent artificial deviations due to vacuum effects and the default nonbonding cutoff of 14 Å was used. Protein atoms were

kept fixed. The minimized structures were used for evaluating the van der Waals and Coulomb energy, and solvation energies using finite-difference Poisson calculations.

Binding Energy Calculations. The van der Waals and electrostatic interaction energies were calculated by subtracting the values of the isolated components from the energy of the complex. The van der Waals energy was calculated with CHARMM27 force field using the default cutoff of 14 Å. The electrostatic energy is the sum of the Coulomb energy in vacuum and the solvation energy. The electrostatic energy was calculated with CHARMM [145] using infinite cutoff and neglecting interactions between pairs of atoms separated by one or two covalent bonds. The electrostatic solvation energy was calculated by the finite-difference Poisson approach [147] using the PBEQ (Poisson-Boltzmann equation) module [148] in CHARMM and a focusing procedure with a final grid spacing of 0.3 Å. The size of the initial grid was determined by considering a layer of at least 20 Å around the solute. The dielectric discontinuity was delimited by the molecular surface spanned by a rolling probe of 1.4 Å. The ionic strength was set to zero, and the temperature to 300 K. Two finite-difference Poisson calculations were performed for each of the three systems (ligand, protein, and ligand-protein complex). The solvation energy is the difference between the values from calculations between ligand-protein complex and ligand and protein alone. The exterior dielectric constant was set to 78.5 and 1.0 in the first and second calculation, respectively, while the solute dielectric constant was set to 1.0, which is consistent with the value used for the parameterization of the charges and the membrane-protein environment. Eight compounds were selected for testing based on their synthetic feasibility and structural availability of which five were identified to be positive hits.

2.3.1.6 Radioligand Binding Studies at human A_1, A_{2A} and A_3Rs

All pharmacological methods followed the procedures as described in the litarature. [115] In brief, membranes for radioligand binding were prepared from CHO cells stably transfected with hAR subtypes in a two-step procedure. In the first step, cell fragments and nuclei were removed at 1000 x g and then the crude membrane fraction was sedimented from the supernatant at 100000 x g. The membrane pellet was resuspended in the buffer used for the respective binding experiments and it was frozen in liquid nitrogen and stored at -80 ºC. For radioligand binding at the hA_1AR, 1 nM [^{3}H]CCPA was used, for hA_{2A}AR 10 nM [^{3}H]NECA and for hA_3AR 1 nM [^{3}H]HEMADO. Non specific binding of [^{3}H]CCPA was determined in the presence of 1 mM theophylline and in the case of [^{3}H]NECA and [^{3}H]HEMADO 100 μM R-PIA was used**.** [149] K_i values from competition experiments were calculated using the program Prism [150] assuming competitive interaction with a single binding site. The curve fitting results (see **Figure 8**) showed R^2 values ≥ 0.99 for all compounds and receptors, indicating that the used one-site competition model assuming a Hill slope of n=1 was appropriate. The affinity of the ligands is depicted in Table 1.

2.3.1.7 Adenylyl cyclase activity

The potency of antagonists at the hA_{2B}AR was determined by adenylyl cyclase experiments. The procedure was carried out as described previously with minor modifications. [115,151] Membranes were prepared from CHO cells stably transfected with hA_{2B}AR using only one high speed

centrifugation of the homogenate. The resulting crude membrane pellet was resuspended in 50 mM Tris/HCl, pH 7.4 and immediately used for the cyclase assay. Membranes were incubated with about 150000 cpm of [a-32P]ATP for 20 min in the incubation mixture as described without using EDTA and NaCl. [151] None of the compounds showed measurable interaction with A_{2B}AR, as the IC_{50}-values for concentration-dependent inhibition of NECA-stimulated adenylyl cyclase were all > 30 µM.

2.4 Results and Discussion

2.4.1 Virtual Screening to A_{2A}R

2.4.1.1 Binding interactions in the experimental structure of ZM241385-A_{2A} and molecular docking calculations results

ZM241385 contains an aminotriazolotriazine with a furyl group and a $(CH_2)_2$Ph(OH fragment connected at opposite sides of the central aromatic ring. In the experimental structure of ZM241385-A_{2A} complex the central aromatic ring has an aromatic π-π stacking interaction with the side chain of the conserved Phe(5.29) located in the EL2 and additional hydrophobic contacts with Leu(6.51) (**Figure 2.3** and other van der Waals interactions in the same area including for example Ile(7.39) (numbers in parentheses refer to the Ballesteros–Weinstein numbering [129]. The furan ring, is positioned deep in the ligand-binding cavity towards TM5 and TM7 forming hydrophobic interactions with His(6.52), Leu(6.51) and Trp(6.48) (**Figure 1.6**). The oxygen acceptor atom of the furan ring forms a hydrogen bond to the amide NH_2 group of Asn(6.55) and this ring have been implicated in both antagonist and agonist binding from mutagenesis experiments.[152,153] The $(CH_2)_2$Ph(OH) fragment a can be oriented either at the solvent-exposed part of the open binding cavity [20] or at the extracellular ends of TM1, TM2 and TM7.[52] In this area of the receptor which is close to a more solvent exposed region (EL2 and EL3) a high flexibility of the ligand is allowed compared to the transmembrane domain.[20] These two orientations is observed for $(CH_2)_2$Ph(OH) in the two X-ray structures of A_{2A}-ZM241385 complex forming hydrophobic interactions with Leu(7.32) and Met(7.35) and other additional residues. [20,52] The interaction of the phenol ring of the ZM241385 ligand with TM2 is observed in the A_{2A}-StaR2 structure [52] and has been calculated by several of the top scoring groups in GPCR Dock 2008 modeling competition [120] These differences in the position of this portion of ZM241385 between the two A_{2A}R experimental structures [20,52] reflect the difficulty of accurately calculating the binding pose of small molecule ligands in GPCR structures as well as the inherent flexibility of this portion of the molecule.

We chose ChemPLP which calculated the binding interactions conformation of ZM241385 in the binding site with an RMSD of 0.8 Å, compared to 1.1 Å and 4 Å of GoldScore [136] and ChemScore [138] respectively.

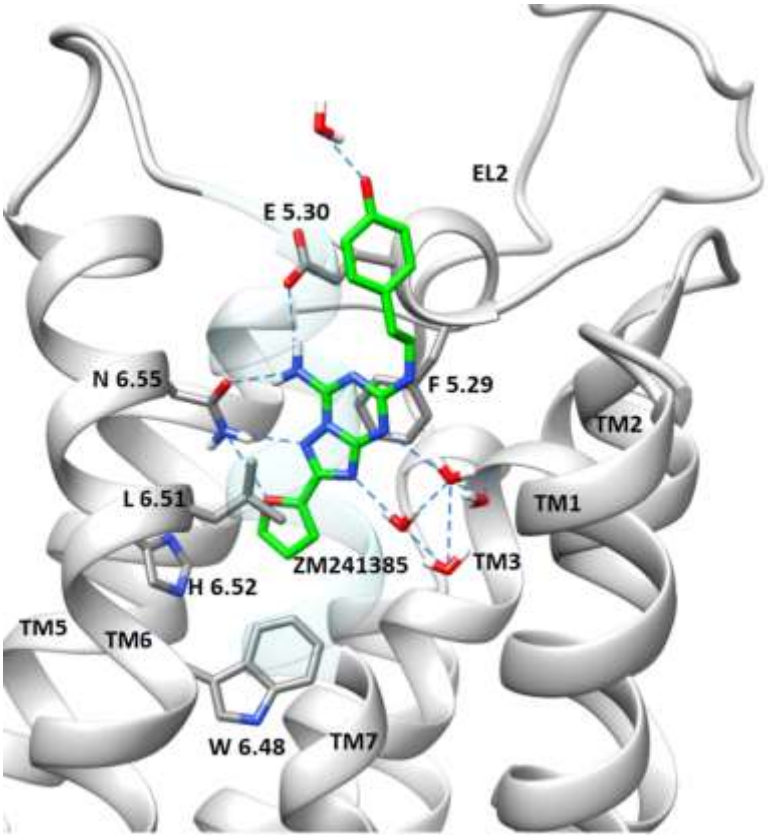

Figure 2.3 Binding mode of ZM241385 at the hA_{2A}AR binding site (PDB ID 3EML) [20] The complex is viewed from the membrane side facing helices TM6 and TM7 with the view of TM7 partially omitted. Side chains of the amino acids crucial for ligand binding are displayed as gray sticks. Hydrogen atoms are not displayed, whereas hydrogen bond interactions are highlighted as blue dashed lines.

2.4.1.2 Structure- and ligand-based drug design methodology

Decades of screening and medicinal chemistry studies have increased-the number of bioactivities (10184) in ChEMBL20 for A_{2A}R which ranks at number 7 of the 688 class A GPCRs. However, advances in GPCR crystallography [154] have made structure-based approaches an attractive strategy for drug design against adenosine receptors which are pharmaceutically important targets. A_{2A}R is one of the best studied receptors of all class A GPCRs and the crystal structures of A_{2A}R in complex with agonists or antagonists have been unveiled [20,30,34,52,155,156]. Between ARs, A_1R structure has also been resolved and three experimental structures with both antagonists and agonists [35,54] have been published.

We applied molecular docking calculations to 14400 compounds (included in the HitFinder collection of Maybridge) against the A_{2A}R crystal structure PDB ID 3EML [20] after generating 200 conformations for each ligand using the program OMEGA (see Scheme 2.5 and Materials and Methods Section) [157]. The docking calculations were performed on the resulting library (1655368 conformers) with GOLD5.2 [136,137] and ChemPLP [139] was used as the scoring function to produce 48230 clusters of docking poses.

The resulting docking poses were overlaid onto the crystallographic ZM241385 conformation adopted inside the crystal structure of $A_{2A}AR$ [20] using ROCS [158], which relies on the detection of molecules with 3D properties similar to those of the reference compound using a TanimotoCombo value of 0.65. [140]
The top 6000 conformers were re-scored by a CHARMM-PBSA minimization (see Table 2.1). This last filtering was very important since the docking poses from the previous step had similar polar and vdW contacts. Using MM-PBSA method the electrostatic energy is computed as the sum of the Coulombic energy and the electrostatic solvation energy calculated by the finite-difference Poisson approach [147] to account for the desolvation of the ligand and protein binding site during binding.

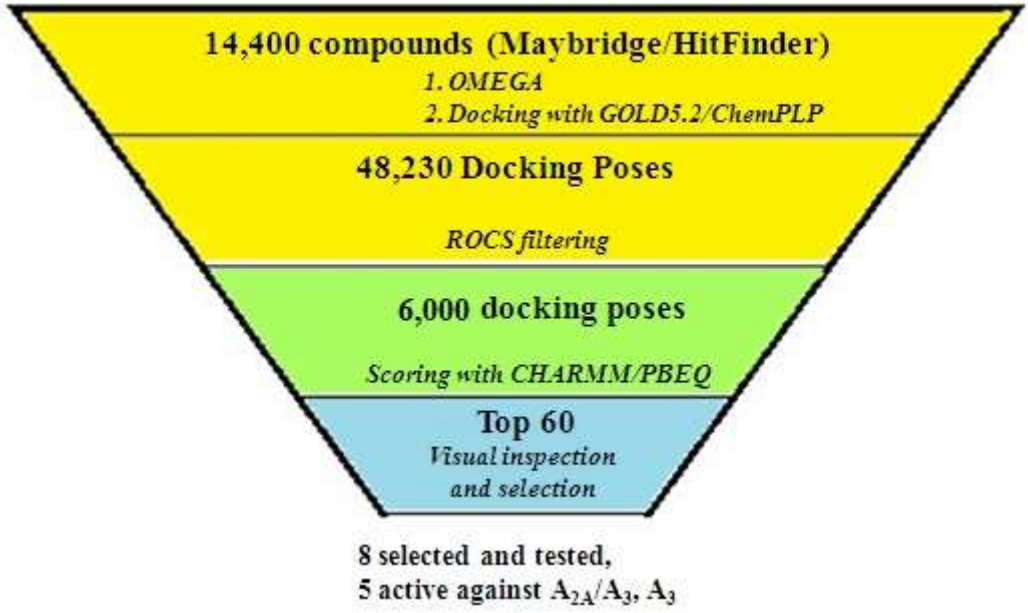

Figure 2.4 Workflow used for the discovery of ligands from docking screen.

2.4.1.3 Results of Virtual Screening

Selected hits for affinity and radio-labelled binding affinity results to ARs. The top 60 docking poses from 60 different compounds were selected and eight compounds were purchased based on the structural versatility and synthetic feasibility. From the eight compounds tested (**Figure 2.4**, five were found to be positive hits (62.5% success) showing mixed antagonistic activity against ARs with affinities ≤ 20-30 μM. Three of them were A_{2A}/A_3R ligands, i.e., compound **K1, K5** exhibited low micromolar affinity against A_{2A} and A_3R and compound K**2** have a moderate affinity for these receptors. Compounds **K6**, **K7** exhibited a moderate to good selective affinity against A_3R. Compounds **K3, K4** and **K8** did not bind to any of the ARs **(Table 2.2)**.

Table 2.2 Binding affinities from radioligand binding assays and structures of the eight hits (compounds K**1**-**K8**) from the docking screen against the A_1, A_{2A}, A_{2B} [a] and A_3Rs.

Compound number	**Ranking** [d]	**Chemical structure**	***K*$_i$ (*μ*M)** [b]			T_c [c]
			A_1R	**A_{2A}R**	**A_3R**	
K1	10	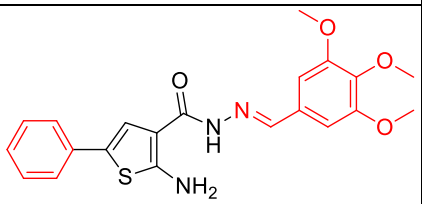	>100	**2.67** (2.26-3.15)[e]	**3.10** (2.48-3.88)	0.22
K2	3	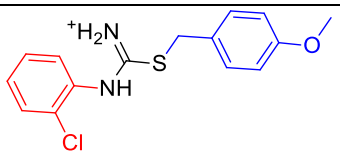	≥100	**61.3 (**52.6-71.5)	**16.6** (11.5-23.9)	0.17
K3	54	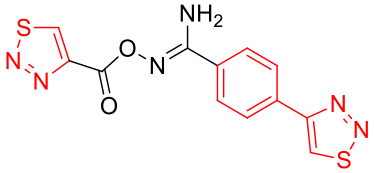	>100	>100	>100	0.13
K4	44	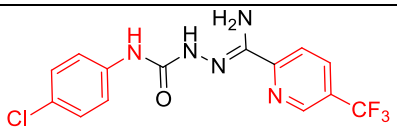	≥100	>100	>100	0.14
K5	32	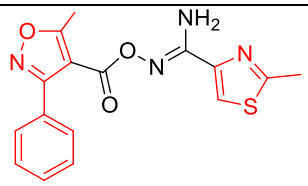	>100	**21.8** (18.1-26.2)	**9.45** (8.75-10.2)	0.16
K6	20	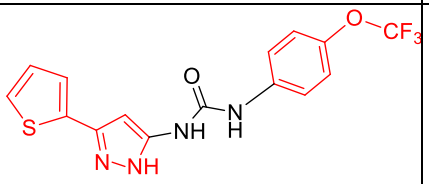	>100	>100	**30.6** (17-55)	0.21
K7	14	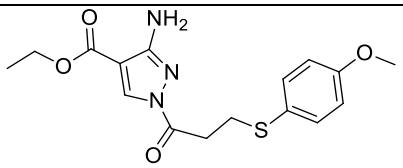	>100	>100	**18.3** (10.3-32.7)	0.21
K8	58	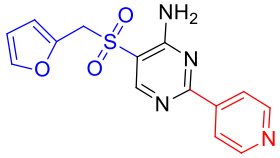	>100	≥100	>100	0.15

[a] All compounds did not exhibit binding evidence to $A_{2B}R$. [b] Measured in three independent experiments. [c] Tanimoto similarity coefficient to the closest annotated AR ligand from ChEMBL (see also Table 2.2). [d] Ranking of compounds in the screened library using CHARMM-PBSA.

Filtering efficiency of the virtual screening. Remarkably, none of these eight positive hits was among the 60 after just applying: a) docking with GOLD program and scoring with ChemPLP, and b) filtering with ROCS using scoring based on the T_c (**Table 2.3**). Thus, the CHARMM-PBSA re-scoring step which accounts for the desolvation energy needed in order the ligand to reach the receptor binding area was significant for ligands filtering.

Table 2.3 Ranking of compounds **K1-K8** after docking and scoring with ChemPLP and ROCS.

	CHEMPLP		ROCS (T_c)
Compound	Rank	Score	Rank
K3	5465	66.6	496 (0.944)
K7	4963	67.8	1759 (0.975)
K1	2792	73.1	3429 (0.932)
K4	7448	62.0	4552 (0.911)
K8	5595	66.3	5791 (0.893)
K2	7241	62.5	5843 (0.892)
K5	5427	66.67	420(1.065)
K6	4383	69.2	2206 (0.960)

Several other approaches have been applied in previous virtual screening attempts for improving ligand enrichment. These works include a combination of scoring tools for filtering. In the first campaigns, an optimized docking protocol was applied [120] or a docking and scoring using DOCK program which also accounted for the desolvation penalty.[26] Other groups applied also a docking/scoring using DOCK which accounted for the desolvation penalty [124,125] or applied GlideSP/XP and other tools like induced fit docking.[121] In a recent effort after docking and scoring with Glide/SP, REOS/Knime filtering was applied and then MM-GBSA calculations were performed which account for the desolvation penalty; in this particular effort after testing 79 compounds only two were found to meet the criterion of approximately 50 % radioligand displacement at a concentration of 10 μM. [123]

Further, it was rewarding for us to find active compounds with novel structures after previous successful virtual screening efforts including docking of million compounds from ZINC library from Shoichet, Katritch - Abayan, Itzstein, Carlsson **etc** [26,28,30,31,120–124,126]**.** In particular, a half to 4 million commercially available compounds from ZINC database were docked to $A_{2A}R$ and after testing 20-70 compounds, i.e., 10^{-5}-10^{-4} % of the compounds set, 1/30 - 1/3 were proved to be active in the micromolar to nanomolar regime, i.e. that hit rate was 10-41%

[4,28,30,31,121,123,125,126,154,159,160]. The percentage of the compounds tested from our compounds library is $3.5x10^{-4}$ %, i.e. it is similar to the previous big campaigns. In that sense, our attempt provide a representative example of a virtual screening of a small number of compounds to the experimental structure of a receptor starting from a small library, which led to novel hits after careful scoring methodology.

ARs are not easy targets for achieving selectivity since they have broad and similar orthosteric binding sites (**Figure 2.5**. Thus, it is not a surprise the fact that a research targeting a particular AR subtype can lead to antagonists of another AR subtype. A characteristic example that illustrate this point, is the virtual screening campaign starting with four separate homology models of the human A_1R and docking of 2.2 million compounds to all four models. Thirty-nine (39) hits were selected and tested for their binding in three AR subtypes. They were found to bind to two or three AR subtypes resulting in 21% A_1, 38% A_{2A} and 36% A_3R successful antagonist hits**.** [125].

Residues	**3.33**	**5.20**	**5.30**	**5.38**	**5.42**	**6.48**	**6.51**	**6.52**	**6.55**	**6.66**	**6.67**	**7.32**	**7.35**	**7.36**	**7.39**
A_{2A}	L	F	E	M	N	W	L	H	N	A	A	L	M	Y	I
A_1	L	F	E	M	N	W	L	H	N	K	K	S	T	Y	I
A_3	L	F	V	M	S	W	L	S	N	V	V	Q	L	Y	I

Figure 2.5 Sequence alignment based of the residues surrounding the binding site of A_1, A_{2A} and A_3Rs.

Influence of the starting experimental receptor structure. Among the crystal structures of $A_{2A}R$-antagonist complexes released after 3EML, PBD ID 4EIY [34] contained also co-crystallized ZM241385 possessed the highest 1.8 Å resolution. Both the desolvation energy for inserting a compound into the receptor and its attractive interactions with the orthosteric binding area of $A_{2A}R$ were used as contributions to energy during hit selection. In this context, the shape and coordinates of the critical amino acid side chains participating to interactions with the ligands inside the binding site, do not differ essentially between 3EML and the other newer released structures, for example 3PWH (3.3 Å), or the highest in resolution 4EIY. **Figure 2.6** hows the superposition of 3EML, 4EIY and 3PWH. The highest resolution receptor structure 4EIY is nearly identical to the original 2.6 Å resolution crystal structure 3EML with an all-atom RMSD of 0.45 Å to 81% of $A_{2A}R$. Recently, it was reported that a virtual screening performed against $A_{2A}AR$ using two different X-ray structures (PDB ID 4EIY, 3PWH) resulted in 11 ligands with affinity to $A_{2A}AR$. [7] Five were identified from docking using Glide and structure 4EIY and six were identified by the Glide docking based on structure 3PWH, i.e., the virtual screening based on the two crystal structures produced different hits. Nevertheless, we did not test a second virtual screening using 4EIY or other protein co-crystallized structure of AR with a ligand.

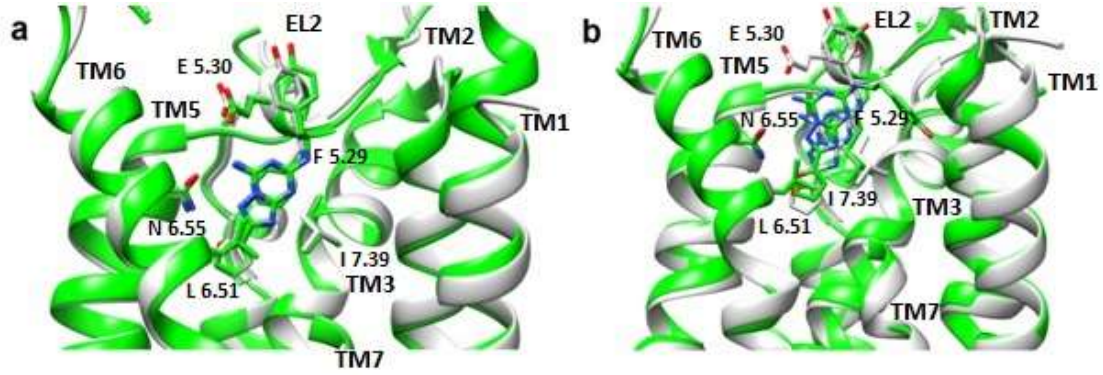

Figure 2.6 Superposition of 3EML with (a) 4EIY and (b) 3PWH. The highest resolution receptor structure 4EIY (1.8 Å resolution) is nearly identical to the 2.6 Å resolution crystal structure 3EML with an all-atom RMSD of 0.45 Å over 81% of A_{2A}AR or an RMSD of 1.3 Å for all heavy atoms. The 3PWH has an RMSD of 1.5 Å for all heavy atoms; the structures differ mainly to EL2 loop coordinates. There is a visible difference in the position of E(5.30) side chain between 3EML and 3PWH that may affect differently polar interactions with potential binders. In both figures the complex is viewed from the membrane side facing helices TM6 and TM7 with the view of TM7 partially omitted. Side chains of the amino acids crucial for ligand binding [E(5.30), F(5.29), L(6.51), I(7.39), N(6.55)] are displayed as gray sticks. Hydrogen atoms are not displayed.

2.4.2 Novelty of the tested ligands

The number of scaffolds resulting from decades of screening and medicinal chemistry studies is high for A_{2A} or A_3R. Structure-based methods still appear to be more affordable than ligand-based methods for identifying novel structures binding to targets that have been well explored, since the latter methods are generally designed to find compounds similar to known binders.
Here we applied a combination of structure-based and ligand-based procedures which identified five compounds with affinity, i.e., compounds K**1**, K**2**, K**5-7** of the eight compounds tested. The chemical novelty of these compounds was assessed based on their two-dimensional similarities to any known compound tested for binding to ARs, such a comparison was realized in previous successful virtual screening efforts [26,28,30,31,120–124,126]. We calculated the pairwise Tanimoto similarity, with extended chemical fingerprints for four atoms (ECFP4), for each of the compounds **K1-K8** to the thousands of known AR ligands in the ChEMBL22 [142 143] database using the Canvas program (radial fingerprints) by Schrodinger [141]. For each of the ligands K**1-K8**, the highest T_c value compared to all previously characterized AR ligands (**Table 2.4**). A T_c value close to zero suggests no chemical similarity between a pair of molecules, whereas a value equal to one represents two identical molecules. **K1-K8** corresponding to novel chemotypes as ligands for the ARs as reflected by the low Tanimoto coefficients (T_c = 0.14-0.33) for the most similar compounds identified. A detailed discusion is included in subsection 3.3.3.

Table 2.4 Results from 2D similarity using ECFP4 fingerprints for ligands **K1-K8.** It is shown, the chemical structure of the antagonist under investigation and the chemical structure of the most similar AR ligand found in the ChEMBL22 database. The similarity is described with the corresponding maximum Tanimoto coefficient.

Ligand		Most similar Ligand Structure	Tc	Reference
K1	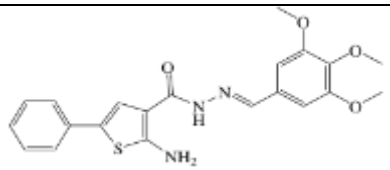 $K_i(A_1)$=2.67μM, $K_i(A_3)$=3.10μM	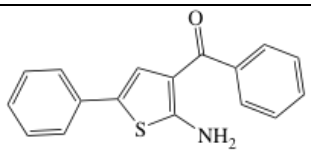 CHEMBL1241077 hA_1AR pK_b (A_1)=6.36 inhib. activity (A_1)=12% $K_i(A_1)$=209μM	0.22	Aurelio L et al., J. Med. Chem. (2010) 53:6550-6559
K2	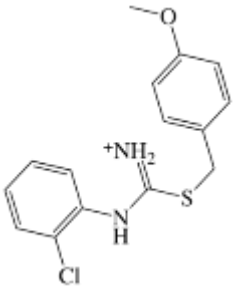 $K_i(A_{2A})$=61.3μM, $K_i(A_3)$=16.6μM	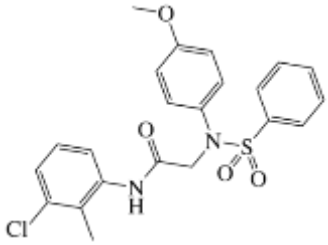 CHEMBL114302 hA_3AR inhib. activity (A_3)=65%	0.17	Webb TR et al., Bioorg. Med. Chem. Lett. (2000) 10:31-34
K3	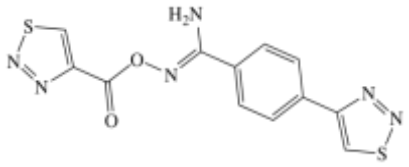 Inactive	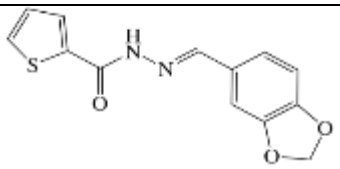 CHEMBL2171381 hA_1R, hA_{2A}R, hA_3R inhib. activity (A_3)=67% inhib. activity (A_1)=30% inhib. activity (A_{2A})=47.5%	0.13	Leal CM et al., Eur. J. Med. Chem. (2012) 55:49-57
K4		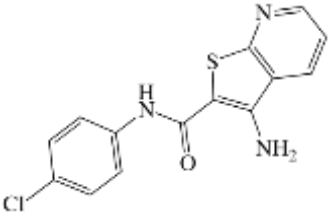	0.14	Katritch et al., J. Med. Chem. (2010) 53:1799-1809

	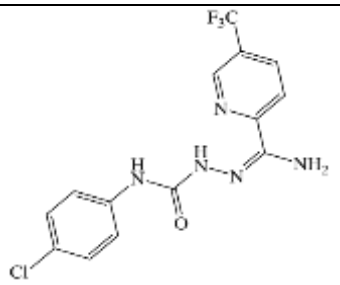 Inactive	CHEMBL599481 $hA_{2A}R$ inhib. activity (A_{2A})=51% K_i(A_{2A})=6.9μM		
K5	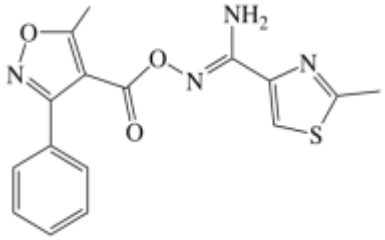 K_i(A_3)=9.45μM	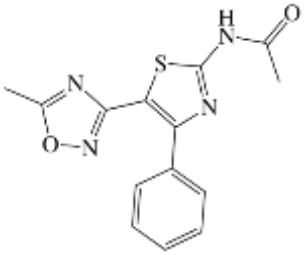 CHEMBL1222302 hA_1R, $hA_{2A}R$ inhib. activity (A_1)=76%, K_i(A_{2A})=110nM, K_i(A_{2A}) (2nd_value)=190nM	0.16	Sams AG et al., Bioorg. Med. Chem. Lett. (2010) 20:5241-5244
K6	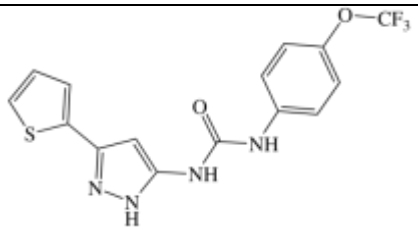 K_i(A_3)=30.6μM	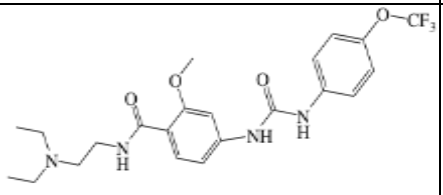 CHEMBL365055 hA_1R inhib. activity (A_3)=36%	0.205	Receveur JM et al., Bioorg. Med. Chem. Lett. (2004) 14:5075-5080
K7	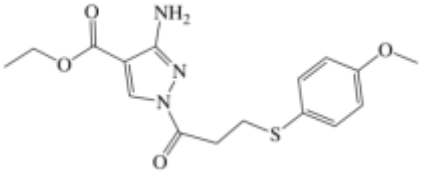 K_i(A_3)=18.3μM	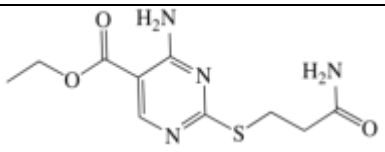 CHEMBL591926 $hA_{2A}R$ inhib. activity (A_{2A})=38%	0.212	Katritch et al., J. Med. Chem. (2010) 53:1799-1809
		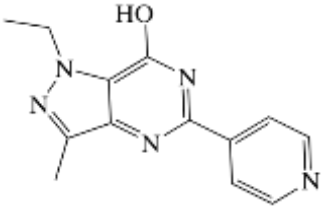	0.151	Hamilton HW et al., J. Med. Chem. (1987) 30:91-96

K8	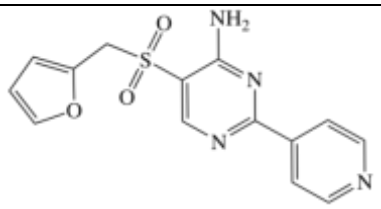 Inactive	CHEMBL366461 rA_1R $K_i(A_1)$=0.25μM		

2.5 Conclusions

In silico screening of vast compound libraries against receptor structures, offers huge potential in the development of highly selective ligands [123]. We explored the *in silico* screening of 14400 compounds of the Maybridge HitFinder library [131] to the X-ray structure of A_{2A}R complexed with ZM241385 using a combination of structure-based and ligand-based approach. The re-scoring of a subset of docking poses was performed with molecular mechanics (CHARMM) Poisson-Boltzmann surface area (MM-PBSA) energy minimization to account also for desolvation energy. Eight compounds were selected and tested. We identified three compounds with sub-micromolar affinity against A_{2A}/A_3Rs and two with selective sub-micromolar affinity to A_3R. Of particular interest for futher exploration as promising hits, are the synthetically feasible **K1** and **K5** with a 2-amino-thiophene-3-carboxamide and a carbonyloxycarboximidamide structure, respectively.

Chapter 3

Structure Activity Relationships and Simulations of the Complexes between A_1, A_{2A}, A_3Rs and Antagonists

3.1 Theoretical Background

3.1.1 Molecular Dynamics simulations

MDsimulations are performed aiming at understanding the evolution of the system through time based on the intramolecular and intermolecular interactions of the studied system. Using MD simulations the position $\mathbf{r}^N = (\mathbf{r}_1,\mathbf{r}_2,...\mathbf{r}_N)$ and velocity $\mathbf{u}^N = (\mathbf{u}_1,\mathbf{u}_2,...\mathbf{u}_N)$ of each of the N atoms of the system through time can be calculated using a convenient potential $V(\mathbf{r}^N)$ and integration of the Newtonian equations motion [161]

$$m_i \mathbf{a}_i = \mathbf{F}_i(t) = \sum_{i \neq j}^{N} \mathbf{F}_j \quad (3.1)$$

$$\frac{d\mathbf{p}_i(t)}{dt} = \frac{\partial V(\mathbf{r}_i,...,\mathbf{r}_N)}{\partial \mathbf{r}_i} \quad (3.2)$$

Equation (3.2) can be transformed to equation (3.3)

$$\frac{d^2\mathbf{r}_i(t)}{dt^2} = \frac{1}{m_i}\frac{\partial V(\mathbf{r}_i,...,\mathbf{r}_M)}{\partial \mathbf{r}_i} \quad (3.3)$$

For this purpose we calculate the forces $\mathbf{F}_i$ acting on each atom i from the other atoms N-1 atoms of the system using the applied potential of the system according to equation (3.2). Numerical integration through a convenient integration algorithm leads to the complete set of momentums $\mathbf{p}^N$ or equally velocities $\mathbf{u}^N$ and positions $\mathbf{r}^N$ ($3N$ atomic coordinates) i.e. the trajectory of the system **(Figure 3.1)** after a time step Δt if the velocities and positions and know in time t

$$\mathbf{r}_1(t),...,\mathbf{r}_N(t) \rightarrow \mathbf{r}_1(t+\Delta t),...,\mathbf{r}_N(t+\Delta t) \quad (3.4)$$
$$\mathbf{p}_1(t),...,\mathbf{p}_N(t) \rightarrow \mathbf{p}_1(t+\Delta t),...,\mathbf{p}_N(t+\Delta t) \quad (3.5)$$

At t=0 arbitrary velocities $\mathbf{u}^N$ can be assigned according to the temperature T of the system according to the equation (3.6)

$$\sum_{i=1}^{N}\frac{m_i v_i^2}{2} = \frac{3}{2}Nk_{\mathrm{B}}T \text{ or}$$

$$\Delta T = \frac{1}{2}\sum_{i=1}^{N}\frac{2}{3}\frac{m_i v_i^{\,2}}{Nk_{\mathrm{B}}} \quad (3.6)$$

and coordinates correspond to an experimental or potental energy minimized protein structure, using a steepest-descent or conjugate gradient algorithm. Time step or integration step Δt is in the range of 1 fs = 10^{-14} s in atomistic simulations.

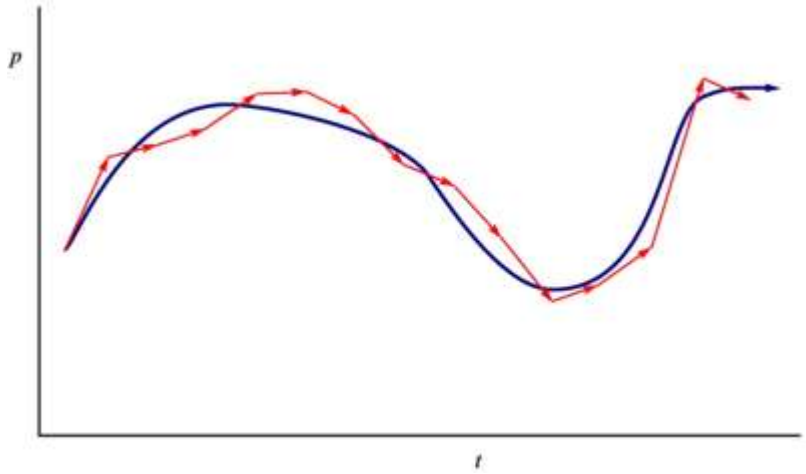

Figure 3.1 Accurate (in blue) trajectory of one atom of a *N*-atoms system and approximate trajectory (in red) the resulted after integration of the Newtonian equation of motions. Read arrows follow the accurate trajectory depending the size of the time step and the accuracy of the potential energy $V(\mathbf{r}^N)$ describing the forces between the atoms. Time step is always the same but the size Δp can be significantly changed after a time step.

A common integrator is the Verlet algorithm ref which is based on the equations (3.7), (3.8)

$$\mathbf{r}(t + \Delta t) = 2\mathbf{r}(t) - \mathbf{r}(t - \Delta t) + \mathbf{a}(t)(\Delta t)^2 \quad (3.7)$$

$$\mathbf{v}(t) = \frac{\mathbf{r}(t + \Delta t) - \mathbf{r}(t - \Delta t)}{2\Delta t} \quad (3.8)$$

Periodic boundary conditions (PBCs) are a set of boundary conditions which are used for approximating a large (or infinite) system by using a small part called a unit cell. The geometry of the unit cell satisfies perfect two-dimensional tiling, and when an object passes through one side of the unit cell, it re-appears on the opposite side with the same velocity. The large systems approximated by PBCs consist of an infinite number of unit cells. In computer simulations, one of these is the original simulation box, and others are copies called images. During the simulation, only the properties of the original simulation box need to be recorded and propagated. The minimum-image convention is a common form of PBC particle book keeping in which each individual particle in the simulation interacts with the closest image of the remaining particles in the system. [161]

A flow scheme for MD simulations is presented in **Figure 3.2**.

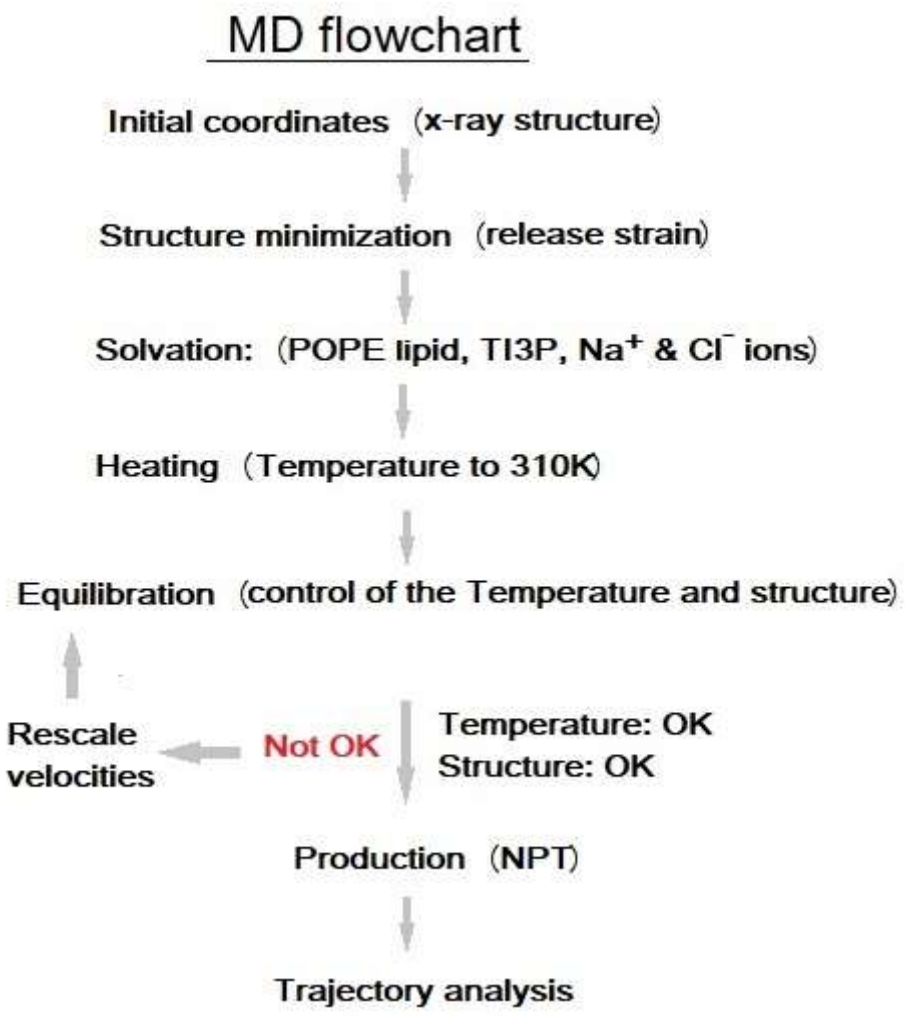

Figure 3.2 The flow scheme for the molecular dynamics simulations applied.

3.1.2 The potential energy function and force fields

The potential energy function in MD simulations, is a set of equations that estimate the total potential energy of the system. It contains energetic terms that are associated with the angle values and the bond lengths deviation from their equilibrium values and terms that described the non-bonded interactions of the system (Coulomb and van der Waals interactions). A number of parameters are used for the equilibrium values of bond lengths, angles, bond, angle and dihedral potential constants etc and atom types that descibed the connectivity of the atoms in the molecules. The set of equations, parameters and atom-types is known as force field. It is often that the during an evolution of a force field to descibe more accurately, for example, the proteins the equations remain the same but the parameters set is changed. For example the functional form of the OPLS 2005 and AMBER force are shown in equations (3.9) and (3.10), respectively.

$$V_{MM} = V_{stretch} + V_{bend} + V_{torsn} + V_{vdW} + V_{el} = \sum^{r\ bonds} \frac{k_r}{2}(r \quad r_{eq})^2 + \sum^{b\ angles} k_\theta(\theta \quad \theta_{eq})^2$$

$$+ \sum^{t\ dihedrals} \frac{V_1}{2}(1+\cos\varphi) + \frac{V_2}{2}(1+\cos 2\varphi) + \frac{V_3}{2}(1+\cos 3\varphi) + \frac{V_4}{2}[(1+\cos 4\varphi)$$

$$+ \sum_i^a \sum_j^b \left[\frac{q_i q_j}{\varepsilon r_{ij}} + 4\varepsilon_{ij} \left(\frac{\sigma_{ij}^{12}}{r_{ij}^{12}} - \frac{\sigma_{ij}^{6}}{r_{ij}^{6}} \right) \right] \qquad (3.9)$$

$$V_{MM} = V_{stretch} + V_{bend} + V_{torsn} + V_{vdW} + V_{el} = \sum^{r\ bonds} \frac{k_r}{2}(r - r_{eq})^2 + \sum^{b\ angles} k_\theta(\theta - \theta_{eq})^2$$

$$+ \sum^{t\ dihedrals} \frac{V_n}{2}\left[1+\cos(n\varphi - \gamma)\right] + \sum_i^a \sum_j^b \left[\frac{q_i q_j}{\varepsilon r_{ij}} + 4\varepsilon_{ij} \left(\frac{\sigma_{ij}^{12}}{r_{ij}^{12}} - \frac{\sigma_{ij}^{6}}{r_{ij}^{6}} \right) \right] \qquad (3.10)$$

3.2 Purpose of the work

Based on the structure mostly of two promising active hits against A_{2A}/A_3R, which include a 2-amino-thiophene-3-carboxamide in compound **K1** and a carbonyloxycarboximidamide in compound **K5**, 19 compounds were selected from e-molecules search engine using a 2D similarity index 0.9, purchased and biologically tested. Only two compounds were selected based on similarity with compound **K2**.

In particular compounds **K12-K14, K16, K20-K23, K25** were selected based on the structure of **K1**. Compounds **K1**, **K12-K14, K21, K22** have an amino group at 2-thiophene position and an amido group CONHR at 3-thiophene position. Compared to **K1**, **K12-K14, K21, K22** compounds **K16, K20, K23 K25** were selected to have the $CONH_2$ group at 2-thiophene position and the NHCOR' group at 3-thiophene position. Compound **K19** was selected to have a similar structure with **K2.** Compounds **K9-K11, K15, K17, K18, K24, K26, K27** were selected based on the structure of **K5**

The results from testing of compounds K**9-K27** (**Table 3.1**), showed that 16 compounds, over the additional 17 tested, were binders with K_i values ranging from 37 μM to low micromolar or sub-micromolar against ARs (with the exception of compound **19** which lack of affinity). Overall, of all the twenty five compounds only four compounds lack of affinity against all ARs.

Then, compounds **K28, K35** with a $CONH_2$ group at 2-thiophene position and **K29-K34, K36-K39** with a carbonyloxycarboximidamide moiety but a diphenyl instead of phanyl-isoxazole were also selected, purchased and tested for including in the project new structure-activity relationships (SARs).

Molecular docking and MD simulations of numerous complexes (which are possible only using supercomputers), have been applied to investigate further the basic binding interactions of the active compounds. In particular, over two hundreds short (10 ns) MD simulations were performed with Desmond [162,163] using OPLS 2005 [164,165,166] force field to relax ligand-receptor interactions. When the MD simulations resulted in a binding orientation similar to the docking pose ($RMSD_{lig}$ < 1.5 Å) the stability of the AR-ligands complexes was verified by performing longer (100 ns)

MD simulations with Desmond [162,163] using OPLS 2005 [164–166] force field and with Amber [167] using ff14SB [168] to model all protein and ligand interactions.

3.3 Methods

3.3.1 Models for A_1, A_{2A}, A_3 and A_{2B}Rs

Our molecular docking calculations were carried out using the 2.6 Å resolution crystal structure of $hA_{2A}R$ in complex with the antagonist ZM241385 (PDB ID 3EML) [20] and the 3.2Å resolution crystal structure of A_1R with the antagonist DU172 (PDB ID 5UEN)[32]. For having structures of AR-ligand complexes suitable for performing MD simulations we added the missing portions in the structures of $A_{2A}R$ in complex with ZM241385. The missing residues in the crystal structure (PDB ID 3EML [20] were added, i.e., M1-I3 (N-terminus), P149−H155 (extracellular loop 2 or second extracellular loop, EL2), and K209-A221 (intracellular loop 3, IL3) using software MODELLER [169,170]. The final structure did not include the C-terminus and contained only residues 1 to 310. The seven structural waters in the binding site of $A_{2A}R$-ZM241385 complex were kept in MD simulations The experimental structure of A_1R in complex with DU172 (PDB ID 5UEN [32] did not need any additions.

No crystal structures for A_{2B} and A_3Rs are available. Therefore, for the calculations the homology models of A_{2B} and A_3Rs developed by Katritch and Abagyan [4] were applied or were taken from Adenosiland of Moro [171] which were built using the crystal structure of the $hA_{2A}R$ (PDB ID 3EML [20] as a template. Structures in Adenosiland of Moro [171] include all residues 1 to 310 and do not need any additions. In Katritch-Abagyan [4] structures of the hA_3R and $hA_{2B}R$ the portion of the EL2 between positions Leu141(4.62) and Cys166(5.27) of the $hA_{2A}R$ is missing. We prepared also a model of hA_3R starting from the experimental structure of hA_1R.

The Katritch and Abagyan [4] structures take into account the selectivity of ligands by comparing differences between the predicted binding energies using scoring functions from molecular docking calculations for the three subtypes [4,171]. The most obvious difference in residues between ARs structures inside the orthosteric binding site is a Val residue in position 5.30 in A_3R. In all other subtypes this position is occupied by a Glu residue that may play an important role in high affinity ligand binding by forming a hydrogen bond, for example with an un-substituted exocyclic amine. With Val in this position, the A_3R may lose this interaction and therefore allows bulky amine substitutions or neighboring lipophilic fragments of ligand protruding towards the extracellular opening of the pocket. Katritch and Abagyan reported [4] that some Val rotamer conformations can also partially block this opening, so using an optimized conformational model of the receptor may be required for specific ligand binding investigation against A_3R. We applied this conformer for Val5.30 in our calculations.

The structures of the complexes between A_3R and $A_{2B}R$ in complex with ZM241385, used as templates for docking **K1-K39 to** A_3R and $A_{2B}R$, were prepared by ovelay the models of $A_{2A}R$-ZM241385 and A_3R, prepared as previously described, and deleting $A_{2A}R$ structure.

3.3.2 Molecular Docking calculations

The structures of the ligands **K1-K39 (Table 3.2)** were gennerated by means of Maestro 8.5 and were subsequently minimized by means of MacroModel 9.6 and the MMFF94 force field [172,173] using the CG method and a distance-dependent dielectric constant of 4.0 until a convergence value of 0.0001 kJ $Å^{-1}$ mol^{-1} was reached. The 39 ligands depicted in Table 3.2 were subjected to docking calculations with Gold5.2 [93,136,137] using PDB IDs 3EML [20] and 5UEN [50] [32] for $A_{2A}R$ and A_1R, respectively, and GoldScore [136] or ChemPLP [139] as scoring functions. Moro and Katritch-Abagyan models were used for the A_3 and A_{2B}Rs and the position of ZM241385 in $A_{2A}R$ (PDB ID 3EML [32] as reference ligand for the docking calculations with the same scoring functions. The receptor models were generated as previously described. Ligands were submitted to 10 genetic algorithm runs. Docking poses for each ligand were visually inspected using the UCSF Chimera package. [174]

3.3.3 2D Similarity calculations

Similarity calculations for 25 ligands in **Table 3.3** were carried out using the Canvas program by Schrodinger. [141] In order to investigate the novelty of the discovered hits, we calculated for each hit the maximum pairwise Tanimoto similarity, with extended chemical fingerprints to four atoms (ECFP4), to the thousands known AR ligands included in the ChEMBL22 database. [142,143] **(Table 3.3)**. The Tanimoto coefficient (Tc) quantifies the two dimensional chemical similarity between two molecules by a value between 0 and 1.

3.3.4 MD simulations

MD simulations were carried out to the complexes of the 39 compounds with ARs using the experimental structure of $hA_{2A}R$ (PDB ID 3EML) [20], of hA_1R (PDB ID 5UEN) [32] and the homology model of A_3R developed by Katritch and Abagyan [4] or from Moro [171] and modified as previously described. Since none of the compounds have affinity to $A_{2B}R$ and the molecular docking calculations show that most of the compounds bind as well as to hA_1, hA_{2A}, hA_3Rs, we did not perform MD simulations with $A_{2B}R$ to reduce the computational cost.
N- and C-termini of the protein model systems were capped by acetyl and methylamino groups, respectively, after applying the protein preparation module of Maestro. Each AR complex was embedded in a POPE lipid bilayer extending 15 Å beyond the solute. For the MD simulations of $A_{2A}R$ complex in different lipids the complex was embedded in a DMPC or POPE or POPC lipid bilayer. The total number of atoms was 81770 for POPE, 76860 for POPC and 77245 for DMPC. The $A_{2A}R$ complex in different lipidsm The ligand-receptor complex was placed into the membrane according to the orientation with respect to the membrane plane (x,y plane) calculated by the "Orientations of Proteins in Membranes (OPM)" server [175]. Membrane creation and system solvation were conducted with the "System Builder" utility of [162,163]. The resulting systems were solvated using the TIP3P [176] water model. Na^+ and Cl^- ions were placed in the water phase to neutralize the systems and to reach the experimental salt concentration of 0.150 M NaCl. The total number of atoms of each complex was c.a. 61770; 151 lipid molecules, 12997 water molecules and approximately and 85 ions. The OPLS 2005 force field [164,166,177] was used to model all protein and ligand interactions and lipids. The particle mesh Ewald method (PME) [178,179] was employed to calculate long-range electrostatic interactions with a grid spacing of 0.8 Å. Van der Waals and

short range electrostatic interactions were smoothly truncated at 9.0 Å. The Nosé-Hoover thermostat [180] was utilized to maintain a constant temperature in all simulations, and the Martyna-Tobias-Klein method [180] was used to control the pressure. Periodic boundary conditions were applied (80×95×110) $Å^3$. The equations of motion were integrated using the multistep RESPA integrator [181] with an inner time step of 2 fs for bonded interactions and non-bonded interactions within a cutoff of 9 Å. An outer time step of 6.0 fs was used for non-bonded interactions beyond the cut-off. Each system was equilibrated in MD simulations with a modification of the default protocol provided in Desmond, which consists of a series of restrained minimizations and MD simulations designed to relax the system, while not deviating substantially from the initial coordinates. First, two rounds of steepest descent minimization were performed with a maximum of 2000 steps with harmonic restraints of 50 kcal mol $Å^{-2}$ applied on all solute atoms, followed by 10000 steps of minimization without restraints. The first simulation was run for 200 ps at a temperature of 10 K in the NVT (constant number of particles, volume, and temperature) ensemble with solute heavy atoms restrained with a force constant of 50 kcal mol $Å^{-2}$. The temperature was then raised during a 200 ps MD simulation to 310 K in the NVT ensemble with the force constant retained. The temperature of 310 K was used for POPE and POPC bilayers in the MD simulations in order to ensure that the membrane state is above the melting temperature state of 271 K for POPC, 298 K for POPE, 297 K for DPMC. [182]**.** The heating was followed by equilibration simulations. First, two stages of NPT equilibration (constant number of particles, pressure, and temperature) were performed. One with the heavy atoms of the system restrained for 1 ns with a force constant of 10 kcal mol $Å^{-2}$ for the harmonic constraints and one with the heavy atoms of the protein-ligand complex restrained for 1 ns with a force constant of 2 kcal mol $Å^{-2}$ for the harmonic constraints to equilibrate solvent and lipids. A NPT simulation followed with the C_α atoms restrained for 1 ns with a force constant of 2 kcal mol $Å^{-2}$. The above-mentioned equilibration was followed by 10ns simulation without restrains. We extended the unrestrained NPT simulation to 100 ns when the ligand remained stable inside the cavity in order to test the stability of the complex in a longer simulation period. In certain cases we also followed the stability of the complex inserted as described previously in POPC hydrated bilayers for 100 ns unrestrained MD simulation.

We also tested the stability of these complexes using Amber ff14SB force field implemented with Amber14 software inserted in POPC bilayers as described previously. The systems were processed by the LEaP module in AmberTools14 [167]. Amber ff14SB force field parameters [168] were applied to the protein, lipid14 [183] to the POPC lipids, GAFF to the ligands [184] and for the ligands, we used the atomic charges calculated using the R.E.D. Server development [185] along with PARM10 parameters**.** [186]**.** TIP3P [176] for the water molecules for the calculation of bonded, vdW parameters and electrostatic interactions. and to the water molecules.

MD simulations were performed using the SANDER module and the new implementation PMEMD. SANDER is the basic MD engine of Amber and was for energy minimization, while PMEMD is the high performance implementation of the MD engine that contains a subset of features of sander and was used for the next steps of MD simulations**.** [167] MD simulation protocol consists of five stages: (a) Minimization, (b) Heating, (c) Adjustment of density, (d) Equilibration and (e) Production. The systems were minimized in SANDER by 2500 steps of steepest descent to remove bad contacts and 7500 steps of conjugated gradient minimization in the presence of a harmonic restraint with a force constant of 5 kcal mol^{-1} $Å^{-2}$ on all atoms of protein and ligand and non-bonded cutoff of 8.0 Å. The next stage in MD simulation protocol is to allow the system to heat up from 0 K to 310 K. Langevin thermostat [187] as implemented in Amber14 [167] was used for

temperature control employing a Langevin collision frequency of 2.0 ps^{-1}. The system in two consecutive steps to 310 K in the presence of a harmonic restraint with a force constant of 10 kcal mol^{-1} $Å^{-2}$ on all membrane, protein, and ligand atoms. In the first step, systems were heated to 100 K in a NVT of 50 ps length where the adjustment of the density was realized using the Berendsen barostat [188] with a 2 ps coupling time. In the second step, the temperature was raised to 310 K in a NPTγ (with γ = 10 dyn cm^{-1}) simulation of 500 ps length. Subsequently, the systems were equilibrated without restraints in a NPTγ simulation of 1 ns length with T = 310 K and γ = 10 dyn cm^{-1}. The equilibration phase was followed by production simulation for 100 ns with system-specific lengths using the same protocol as in the final equilibration step. The simulation temperature of 310 K was well above the gel to liquid crystalline phase transition temperature of POPC lipids of 298 K. [182] In the NPTγ simulations semiisotropic pressure scaling to p = 1 bar was applied using a pressure relaxation time of 1.0 ps. For the treatment of long-range electrostatic interactions the Particle-mesh Ewald summation method [178,179] was used, and short-range non-bonding interactions were truncated with an 8 Å cutoff. Bonds involving hydrogen atoms were constrained by the SHAKE algorithm [189] and a time step of 2 fs was used for the integration of the equations of motion. Snapshots recorded every 20 ps during the production MD simulations were considered for analysis. Properties and dynamics of the protein and ligand systems as well as of the membrane were analyzed with the *ptraj* and *cpptraj* modules of AmberTools12 [167] In the production phase, the relaxed systems were simulated in the NPT ensemble conditions for 100 ns. Within this simulation time, the total energy and the RMSD of the protein's backbone Cα atoms reached a plateau, therefore the systems were considered equilibrated and suitable for statistical analysis.

We measured the area per lipid, based on a combination of the two-dimensional Voronoi tessellation and the Monte Carlo integration method**.** [190]

The visualization of produced trajectories and structures was performed using the programs Chimera [174] and VMD. [191] All the MD simulations were run on ARIS and CyTERA Supercomputing Systems or in workstations using the GPU implementation of the MD simulations codes.

3.3.5 Radioligand Binding Affinity Studies at hA_1, hA_{2A} and hA_3Rs

The radioligand binding measurements were performed with the procedures described in subsections 2.2.1.6 and 2.2.1.5

3.3.6 2D similarity calculations

2D similarity calculations were performed according to subsection 2.2.1.3.

3.4 Results and Discussion

3.4.1 Classification of the selected molecules

The affinity of first 8 compounds is depicted in **Table 2.2** and the affinity of the 31 additional compounds is included in **Table 3.1**. The novelty of all the compounds for AR affinity of activity was accessed in ChEMBL database using CANVAS. Then the compounds were subjected in molecular docking calculations and MD simulation to investigate their binding profile based on the experimental binding affinities. The work flow of all the compounds is depicted in **Scheme 3.3**.

The 39 compounds are categorized in five classes A-E based on similar structural features and in four classes according to receptor selectivity, i.e., ligands with affinity only against A_3 or affinity for A_{2A},A_3Rs, A_1,A_3Rs, or A_1,A_{2A},A_3Rs. Class A includes the 2-amino-thiophene-3-carboxamide derivatives **K12-K14,** and 2-amino-5-phenyl-3-thiophenecarbohydrazide derivatives **K1**, **K21, K22**. Class B have the 3-acylamino-thiophene-2-carboxamide **K16** and the 5-aryl-3-acylamino-thiophene-2-carboxamide derivatives (aryl is phenyl or 3-thiophenyl) **K20, K23 K25, K28, K35**. Class C includes the methanimidothioate derivatives **K2** and **K19** and the urea derivative **K6**. Members of class D are compounds **K3, K5, K9-K11, K15, K17, K18, K24, K26, K27** bearing a carbonyloxycarboximidamide fragment and **K4** with an ureacarboximidamide fragment. Also compounds **K29-K34, K36-K39**. In most of Class D compounds' the carbonyl group is connected with 3-phenyl-isoxazole at 4-position and the carboximidamide carbon with an aromatic group like substituted phenyl, pyridinyl or 4-thiazolyl. In the inactive derivative **K3** the carbonyl group is connected with a thiadiazolyl and the carboximidamide carbon with thiadiazolephenyl group. In the inactive analogue **K4** the carboxy group has been replaced with an urea fragment. Class E contains molecules than cannot be classified in any of the above classes, i.e. the ethyl 3-amino-1-{3-[(4-methoxyphenyl)sulfanyl]propanoyl}-1H-pyrazole-4-carboxylate **K7** and 5-[(2-furylmethyl)sulfonyl]-2-(4-pyridyl)pyrimidin-4-amine **K8**.

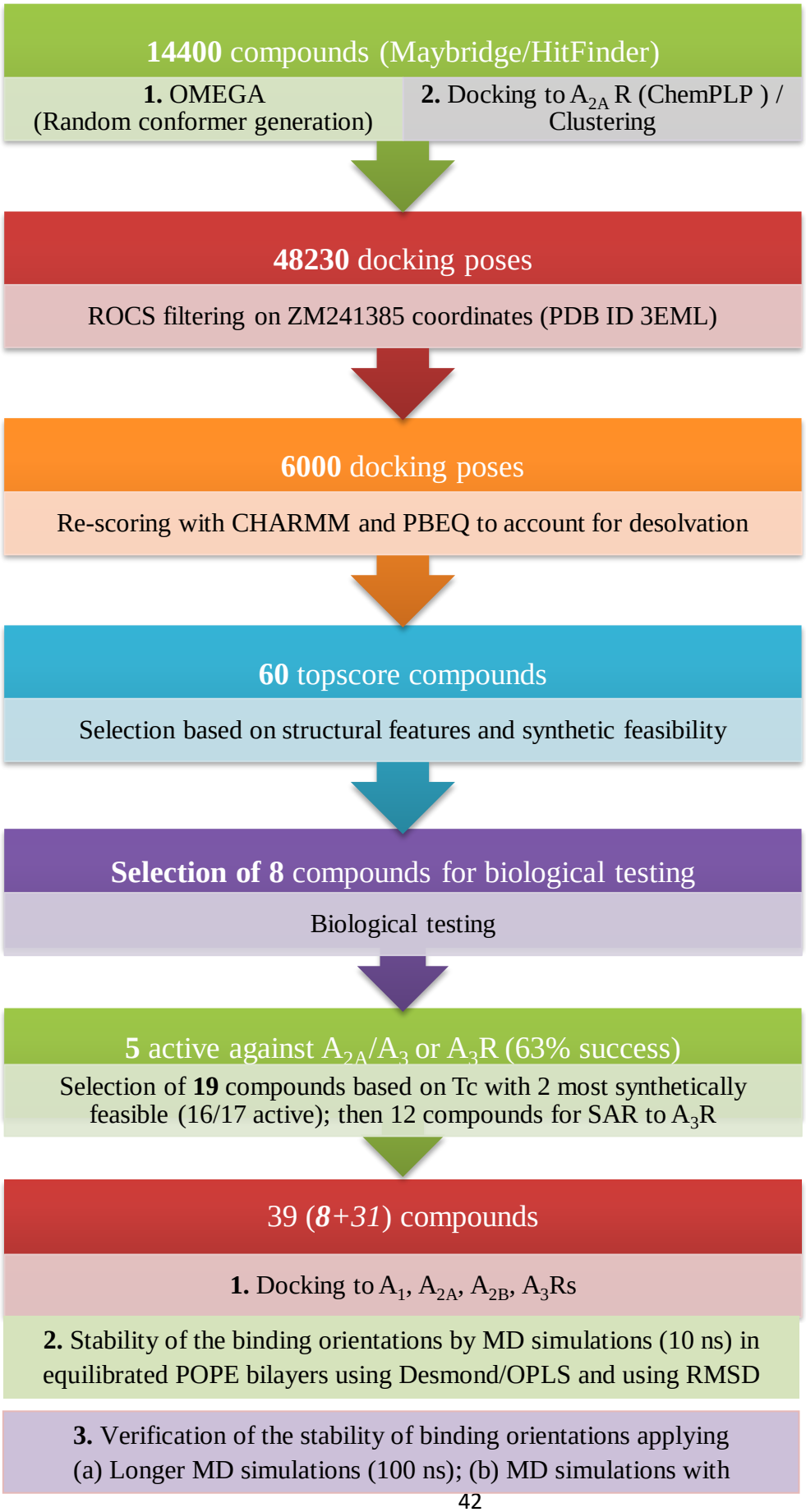
14400 compounds (Maybridge/HitFinder)
1. OMEGA (Random conformer generation)
2. Docking to A_{2A} R (ChemPLP) / Clustering
48230 docking poses
ROCS filtering on ZM241385 coordinates (PDB ID 3EML)
6000 docking poses
Re-scoring with CHARMM and PBEQ to account for desolvation
60 topscore compounds
Selection based on structural features and synthetic feasibility
Selection of 8 compounds for biological testing
Biological testing
5 active against A_{2A}/A_3 or A_3R (63% success)
Selection of **19** compounds based on Tc with 2 most synthetically feasible (16/17 active); then 12 compounds for SAR to A_3R
39 (***8***+*31*) compounds
1. Docking to A_1, A_{2A}, A_{2B}, A_3Rs
2. Stability of the binding orientations by MD simulations (10 ns) in equilibrated POPE bilayers using Desmond/OPLS and using RMSD
3. Verification of the stability of binding orientations applying (a) Longer MD simulations (100 ns); (b) MD simulations with

Figure 3.3 Workflow used for the discovery of ligands from docking screen.

3.4.2 Binding affinities of the selected molecules

Class A: The 2-amino-thiophene-3-carboxamide derivatives **K12**, **K13** and **K14** have binding affinity only to A_3R with K_i values 37.1, 16.5, 14.8 μM respectively. Compared to **K12** which is only a mediocre for A_3R, compounds **K13** and **K14** have a condensed cyclopentane or cyclohexane ring to thiophene ring, respectively, and c.a. two-fold increased affinity **(Table 3.2)**. Compared to **K12**, compounds **K21** and **K1** have a 3-phenyl substituent to the thiophene ring. The 2-amino-5-phenyl-3-thiophenecarbohydrazide derivatives **K21** and **K1** have affinity for A_{2A}/A_3R with K_i values 3.93, 5.77 μM and 2.67, 3.10 μM, and K22 binds to A_1, A_{2A}, A_3Rs with affinity 15.2, 4.59, 5.16 μM.

Class B: The 3-acylamino-5-aryl-thiophene-2-carboxamides (aryl: phenyl or 3-thiophenyl) **K23** **K20** bind to A_1, A_{2A}, A_3Rs with K_i values 1.18, 4.69, 1.65 μM and 1.09, 7.29, 0.918 μM, respectively. In **K25** the 3-acylamino is sizeable and this compound is A_3R selective with a K_i = 1.55 μM. Noteworthy, **K24** lacks 5-aryl substituent and do not of $A_{2A}R$ affinity, i.e., **15** exhibited an A_1, A_3Rs affinity with K_i values 7.48, 5.39 μM. In **K16** the 3-amino group lipophilic is not linked with an acyl substituent and the molecule has A_{2A}/A_3R affinity with K_i values 31.7, 19.7 μM, i.e., the A_1R affinity is abolished.

Class C: Compound **K19** lacks of affinity for ARs compared to the other methanimidothioate derivative **K2** which has A_{2A}, A_3Rs affinity with K_i values 61.3, 16.6 μM. It seems that the aryl substitution pattern is important for the affinity profile and this may trigger additional SAR studies in the future. Compound **K6** is an urea derivative and has a medium affinity against A_3R with a K_i value 30.6 μM.

Class D: The carbonyloxycarboximidamide derivatives **K15**, **K10**, **K17** and **K18** have selective A_3R affinity with K_i values 30.9, 4.49, 4.16, 0.899 μM. As discussed before the carbonyl group of this fragment is connected with a 3-phenyl-isoxazole at 4-position and the carboximidamide carbon with an aromatic group like substituted phenyl, pyridinyl or 4-thiazolyl. Compared to **K15** the presence of the bulky iodine connected with phenyl group in **K9** increases A_3R affinity and adds A_1R affinity. The K_i values for A_1, A_3Rs are 6.90, 4.13 μM. Considering the structure of **K5**, **K17**, **K18,** with all having 2-methyl-1,3-thiazole linked with the carboximidamide carbon, the presence of the chloro substituents in the phenyl ring of 3-phenyl-isoxazole favor A_3R selectivity. The K_i values of **K5** are 21.8 and 9.45 μM for A_1, A_3Rs while **24** and **25** exhibited A_3R selectivity with K_i values 4.16 and 0.899 μM respectively. The change of pyridinyl nitrogen from 3-position in **K10** to 4-position in **K11** leads to $A_{2A}R$ affinity in addition to A_3R affinity, i.e., **K11** has for A_{2A}, A_3Rs K_i values of 30, 5.15 μM, respectively. The aminomethylidenehydrazine-1-carboxamide derivative **K4** has no detectable affinity for ARs.

Class E: Compounds that cannot be included in classes A-D are the 5-[(2-furylmethyl)sulfonyl]-2-(4-pyridyl)pyrimidin-4-amine **K8** which showed no AR binding. The ethyl 3-amino-1-{3-[(4-methoxyphenyl)sulfanyl]propanoyl}-1H-pyrazole-4-carboxylate **K7** bound only to A_3R with a K_i of 18.3 μM.

Table 3.1 Binding affinities obtained from radioligand binding assays and chemical structures of the eight hits (compounds **1-8**) from the docking screen and the 31 compounds (**9-39**) selected based on their similarity structures mainly with compounds **K1** and **K5**, purchased and tested based against the A_1, A_{2A}, A_{2B} ,[a] A_3Rs.

No	Compound	Class	Compound code	Chemical structure	K_i (μM) [b]			T_c [c]
					A_1R	**A_{2A}R**	**A_3R**	
1	**K1**	**A**	HTS12884SC	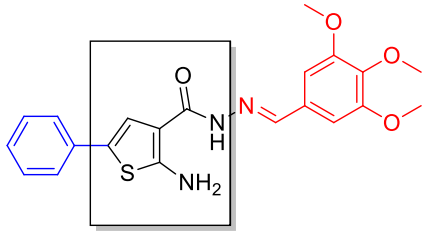	>100	**2.67** (2.26-3.15)[e]	**3.10** (2.48-3.88)	0.22
2	**K12**	**A**	STK441862	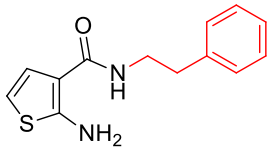	>100	>60	**37.1** (23.0-60.0)[d]	0.32
3	**K13**	**A**	STK448949	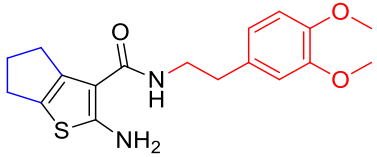	>30	>60	**16.5** (11.2-24.3)	0.34
4	**K14**	**A**	STK450213	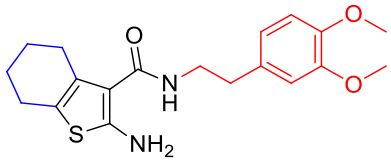	>30	>60	**14.8** (12.3-17.8)	0.34

5	**K21**	**A**	HTS13009	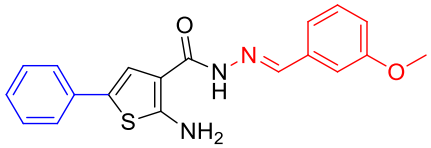	>100	**3.93** (2.85-5.42)	**5.77** (5.34-6.23)	0.21
6	**K22**	**A**	HTS12882	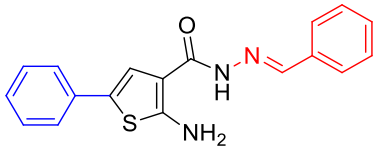	**15.2** (10.5-22)	**4.59** (3.18-6.63)	**5.16** (4.77-5.57)	0.24
7	**K16**	**B**	Z56987720	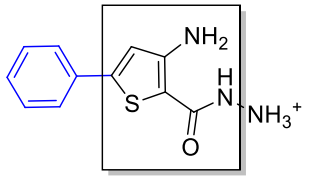	>30	**31.7** (24.9-40.3)	**19.7** (11.6-33.4)	0.25
8	**K24**	**B**		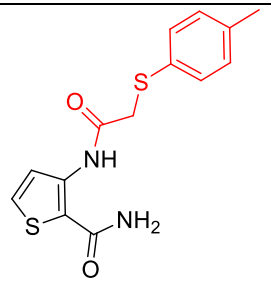	**7.48** (5.72-9.78)	>100	**5.39** (4.72-6.15)	0.16
9	**K23**	**B**	GK01176	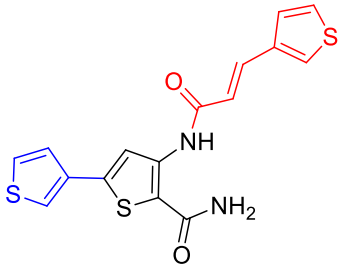	**1.18** (1.09-1.28)	**4.69** (3.98-5.52)	**1.65** (1.24-2.21)	0.14

10	**K20**	**B**	GK03725	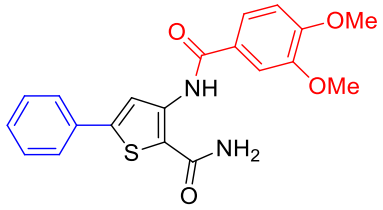	**1.09** (1.0-1.17)	**7.29** (6.86-7.76)	**0.918** (0.813-1.04)	0.19
11	**K25**	**B**	GK01513	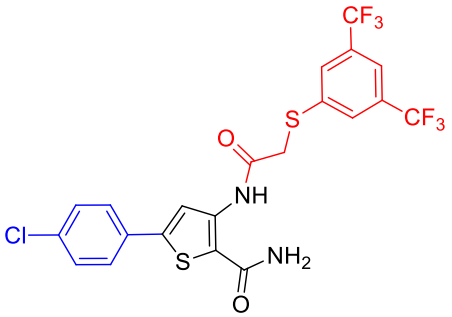	>100	>100	**1.55** (1.25-1.93)	0.17
12	**K35**	**B**	Z1848163164	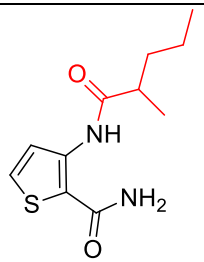	**7.33** (6.80-7.70)	>100	**27.4** (20.1-32.5)	0.20
13	**K28**	**B**	GK00478	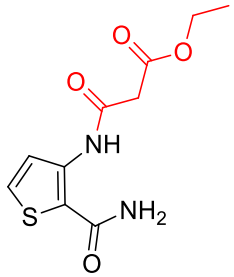	**18.0** (13.0-21.2)	>100	>100	0.18

14	**K2**	**C**	S05993	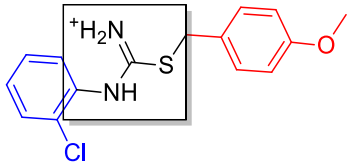	≥100	**61.3** (52.6-71.5)	**16.6** (11.5-23.9)	0.17
15	**K19**	**C**	RDR01677	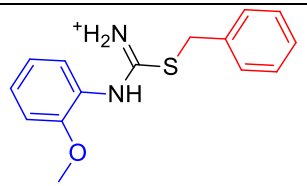	>100	>100	>100	0.20
16	**K3**	**D**	SEW01061	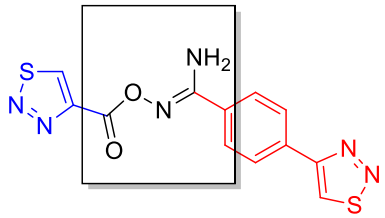	>100	>100	>100	0.13
17	**K4**	**D**	SPB06895	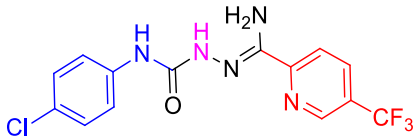	≥100	>100	>100	0.14
18	**K5**	**D**	SPB02733	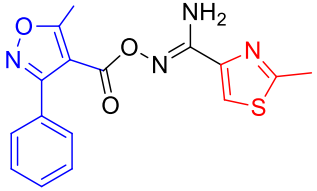	>100	**21.8** (18.1-26.2)	**9.45** (8.75-10.2)	0.16

19	**K15**	**D**	STK106598	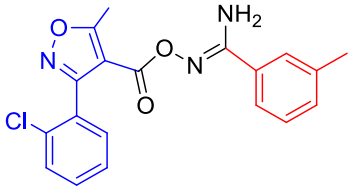	>100	>100	**30.9** (20.8-45.8)	0.16
20	**K9**	**D**	STK323059	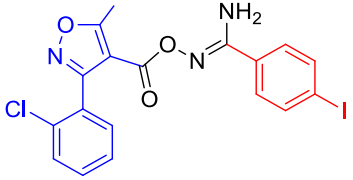	**6.91** (6.36-7.52)	>100	**4.13** (3.38-5.04)	0.15
21	**K10**	**D**	STK300529	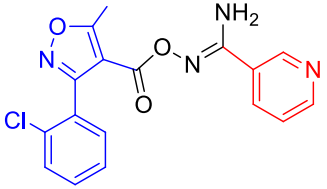	>60	>60	**4.49** (4.13-4.88)	0.16
22	**K11**	**D**	STK323144	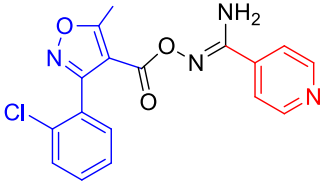	>60	**30** (26.7-33.8)	**5.15** (4.51-5.88)	0.17
23	**K17**	**D**	SPB02734	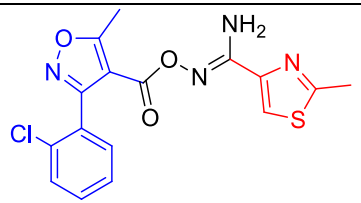	>30	>60	**4.16** (3.56-4.87)	0.16

24	**K18**	**D**	SPB02735	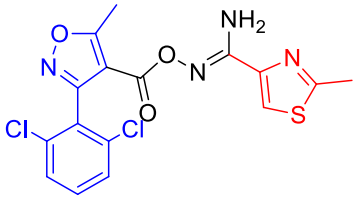	>100	>100	**0.899** (0.766-1.060)	0.14
25	**K26**	**D**	7709975	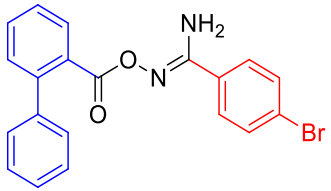	>30	**25.1**	**5.07**	0.22
26	**K27**	**D**	7709775	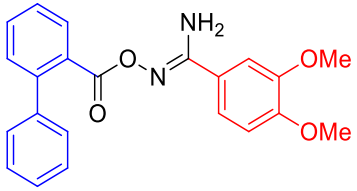	>30	30.0	**11.9**	0.32
27	**K29**	**D**	5687250	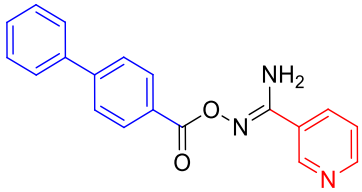	>100	>100	>100	0.34
28	**K30**	**D**	6169223	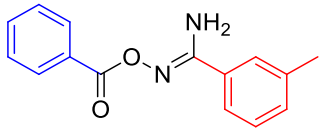	>100	>100	>30	0.34

29	**K31**	**D**	7721356	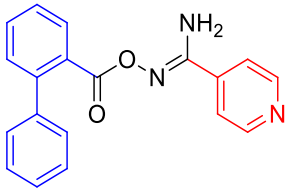	>100	>30	**44.3**	0.21
30	**K32**	**D**	STK323544	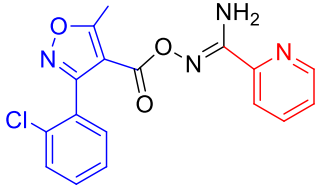	>60	>60	**2.40**	0.16

31	**K33**	**D**	STK300607	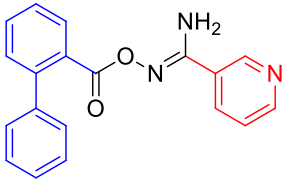	>30	>100	>100	0.21
32	**K34**	**D**	7713195	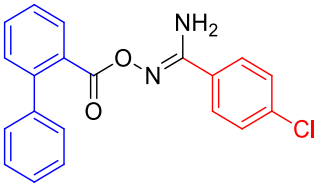	**7.53**	>100	>100	0.18
33	**K36**	**D**	STK710194	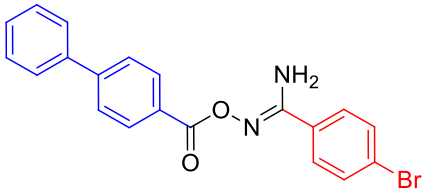	>100	>100	>100	0.17

34	**K37**	**D**	5685368	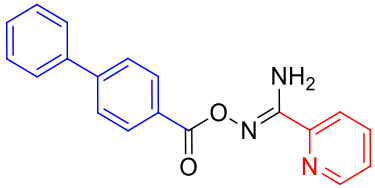	>100	>100	>100	0.20
35	**K38**	**D**	5685368	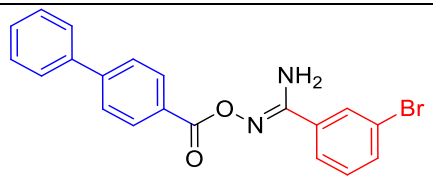	>100	>100	>100	0.16
36	**K39**	**D**	7712234	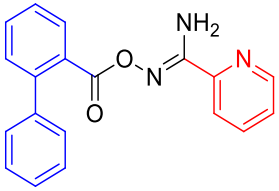	**22.9**	>100	>30	0.22

37	**K6**	**E**	KM08495	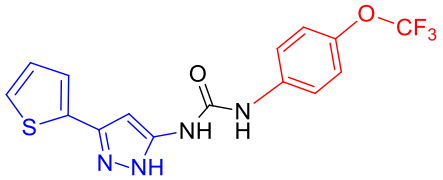	>100	>100	**30.6** (17-55)	0.21
38	**K7**	**E**	HTS06244	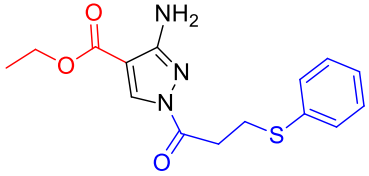	>100	>100	**18.3** (10.3-32.7)	0.21

39	**K8**	**E**	KM03338	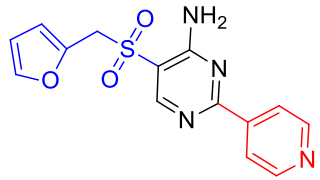	>100	≥100	>100	0.15

[a] All compounds did not exhibit binding evidence to $A_{2B}R$. [b] Measured in three independent experiments. [c] Tanimoto similarity coefficient to the closest annotated AR ligand from ChEMBL (see **Table 3.3**).

3.4.3 Novelty of the tested ligands

The chemical novelty of the compounds was assessed based on their two-dimensional similarity to any known compound tested for binding to ARs. [26,28,30,31,120–124,126] We calculated the pairwise Tanimoto similarity, with extended chemical radial fingerprints for four atoms (ECFP4), for each of the compounds K**9-K39** to the thousands of known AR ligands in the ChEMBL22 [142,143] database using the Canvas program [141]. For each of the K**9-K39** , the highest T_c value compared to all previously characterized AR ligands (**Table 3.2**). A T_c value close to zero suggests no chemical similarity between a pair of molecules, whereas a value equal to one represents two identical molecules.

Novel chemotypes for the ARs corresponding to binders **K9-K39** were identidied as reflected by their low Tanimoto coefficients (T_c = 0.14-0.33). Compounds of class B and D differ the most from previously known structures with T_c < 0.17 (**Tables 3.1, 3.2**).

Compounds **K12-K14, K21, K22** in class A which have mainly A_{2A}/A_3R affinity include the 2-amino-thiophene scaffol. Compounds **K21**, **K22** include a 5-phenyl substitution while compounds **K13**, **K14** contain the 2-amino-5,6,7-trihydro-2*H*-cyclohexa[*b*]thiophene and 2-amino-5,6,7,8-tetrahydro-4*H*-cyclohepta[*b*]thiophene, respectively. In these molecules a carbamide moiety (CONHR) is attached at 3-thiophene position, where R a substituted phenyl at the end of the substituent chain. The most similar compounds in ChEMBL22 with A_{2A}/A_3R ligands of class A (T_c = 0.22-0.34) are 2-amino-3-aroyl-thiophenes [56,192–197] and 2-amino-3-aroyl-5,6,7,8-tetrahydro-4*H*-cyclohepta[*b*]thiophene derivatives [197] which are allosteric agonists and antagonists, respectively, to A_1R [197,198]. However, compounds **K1, K12-K14, K21, K22** include at 3-thiophene position a carbonyl group in an carbamido moitey branched with a lipophilic fragment and have A_{2A}/A_3R affinity instead of the aroyl group in the allosteric agonists or antagonists to A_1R.

Compounds **K16, K20, K23-K25, K28, K35** of class B contain also a thiophene ring but have a $CONH_2$ group at 2-thiophene position and a NHCOR' group at 3-thiophene position, where R' is a lipophilic group with a substituted phenyl at the end of the chain; **K16**, **K20, K23, K25** have an aryl substituent at 5-thiophene positiont. Compound **K24** have $A_{1/}A_3$ affinity, **K20**, **K23** have $A_1/A_{2A}/A_3R$ affinity and **K25** have A_3R affinity. All compounds of class B have low similarity with known active ARs ligands found in ChEMBL22 (Tables 3.2, 3.3, T_c = 0.14-0.17). The similar compounds in ChEMBL22 fall into three types of compounds: (a) Compounds with a thiophene ring, a substituted carbamido group CONHPh at 2-thiophene position and the $CONH_2$ group at 4-position compared with **K25**. These compounds have A_1R allosteric agonistic binding. [198] (b) Compounds with one aryl group [196] or two aryl groups [199], which are common structural features with compounds **K20**, **K23**, **K25** connected in a central ring. These compounds are A_1R allosteric agonists or A_3R antagonists, respectively. (c) Compounds with a benzamido group $NHCOPh(OMe)_2$, as compound **K20**, connected in a central ring. These compounds are A_3R antagonists. [200]

Compounds of class D, **K3-K5, K9, K10, K11, K15, K17, K18, K26-K39**, incude few compounds with selective A_3R affinity. The diaryl-pyridinyl or diaryl-pyrazinyl $A_{2B}R$ antagonists with a NHCOR group (R = Me, cyclopropyl) attached in an heterocyclic ring **(Eastwood et al. 2010)** with low similarity (**Table s 3.1 3.2**, T_c = 0.14-0.17) to class D molecules are the most similar compounds identified in ChEMBL22. We identified a carbonyl-urea antagonist, with a low similarity to **K5** (T_c = 0.071). The former compound has a good affinity to $A_{2A}R$ as published in the results of one of the leading virtual-screening campaigns against $A_{2A}R$ [26]**.**

For compounds **K2, K19** with A_{2A}/A_3R affinity the compounds found in ChEMBL22 have a low similarity (**Tables 3.1, 3.2**, T_c = 0.17, 0.19). These latter compounds include either a substituted amide or urea group and similar to **K2, K19** aryl groups [26,203] and they A_{2A}/A_3R affinity. Some urea derivatives with low similarity for **K2** (T_c = 0.17) have a considerable binding against $A_{2A}R$ and low affinity to A_1 and A_3R according to the results from a virtual-screening campaign [26]. For **K7** with an A_3R affinity, the compounds found in ChEMBL22 have moderate A_3R affinity [204] and low similarity (T_c = 0.21) and include an amino and an ester group linked with an aromatic ring (**Tables 3.1, 3.2**, T_c = 0.21).
Overall, these results indicate that the basic classes A, B, D of identified compounds are ARs ligands with novel structure, since they are not ever experimentally confirmed as binders to ARs.

Table 3.2 Results from 2D similarity using ECFP4 fingerprints for ligands **K9-K39.** It is shown, the chemical structure of the compound under investigation and the chemical structure of the most similar AR ligand found in the ChEMBL22 database. The similarity is described with the corresponding maximum Tanimoto coefficient.

Ligand	Chemical Structure	Most Similar Ligand Structure	Tc	Reference
K12	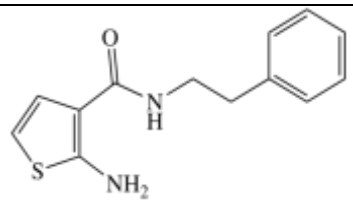 $K_i(A_3)$=37μM	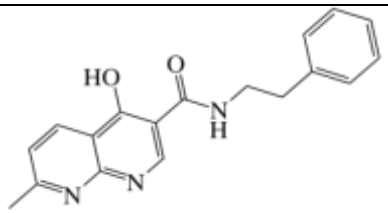 CHEMBL371131 hA_1R, hA_{2A}R bosA_1R, bosA_{2A}R K_i (hA_1)=0.73μM, K_i(bosA_1R)=6.8μM K_i(hA_{2A})=0.15μM, K_i(bosA_{2A}R)=0.14μM	0.32	Manera C et al., Bioorg. Med. Chem. Lett. (2005) 15:4604-4610
K13	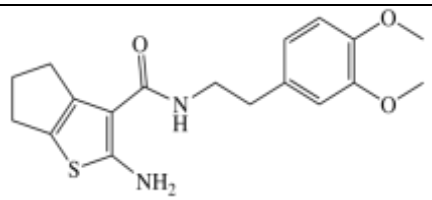 $K_i(A_3)$=16.5μM	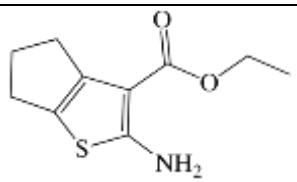 CHEMBL341097 hA_1AR antag. activity (A_1)=58%	0.34	Tranberg CE et al., J. Med. Chem. (2002) 45:382-389
K14	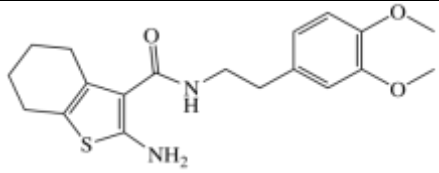 $K_i(A_3)$= 14.8μM	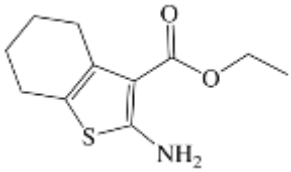 CHEMBL338479 hA_1R antag. activity (A_1)=53%	0.338	Tranberg CE et al., J. Med. Chem. (2002) 45:382-389
K21	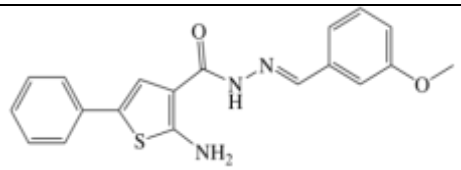 $K_i(A_{2A})$=3.93μM, $K_i(A_3)$=5.7μM	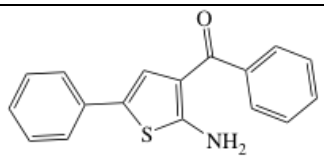 CHEMBL1241077 hA_1R p$K_b(A_1)$=6.36, antag. activity (A_1)=12%, $K_i(A_1)$=209μM	0.214	Aurelio L et al., J. Med. Chem. (2010) 53:6550-6559

K22	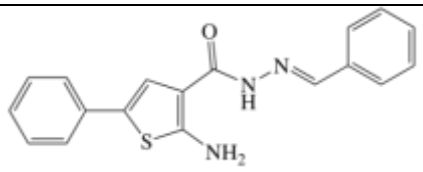 $K_i(A_1)$=15.2μM, $K_i(A_{2A})$=4.59μM, $K_i(A_3)$=5.16μM	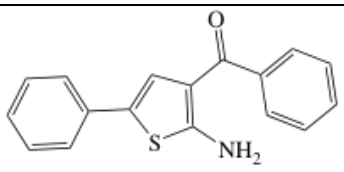 CHEMBL1241077 hA_1R p$K_b(A_1)$=6.36, antag. activity (A_1)=12%, $K_i(A_1)$=209μM	0.24	Aurelio L et al., J. Med. Chem. (2010) 53:6550-6559
K16	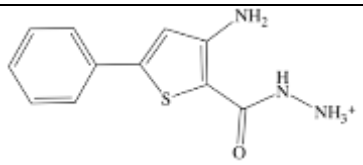 $K_i(A_{2A})$=31.7μM, K_i (A_3)=19.7μM	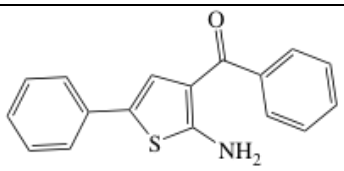 CHEMBL1241077 hA_1R p$K_b(A_1)$=6.36, antag. activity (A_1)=12%, K_d (A_1)=209 µM	0.251	Aurelio L et al., J. Med. Chem. (2010) 53:6550-6559
K24	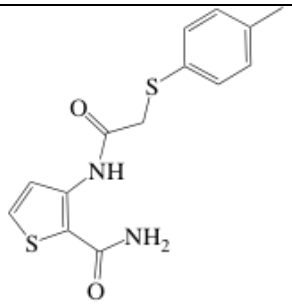 $K_i(A_1)$=7.48μM, $K_i(A_3)$= 5.39μM	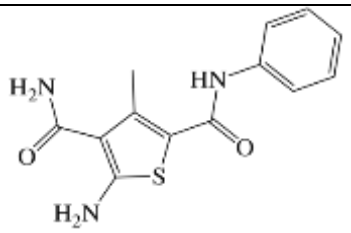 CHEMBL494292 hA_1R antag. activity (A_1)=80.3%	0.163	Ferguson GN et al., J. Med. Chem. (2008) 51:6165-6172
K23	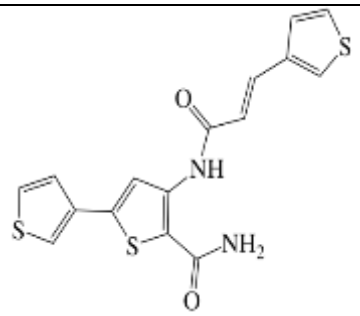 $K_i(A_1)$=1.18μM, $K_i(A_{2A})$=4.69μM, $K_i(A_3)$=1.65μM	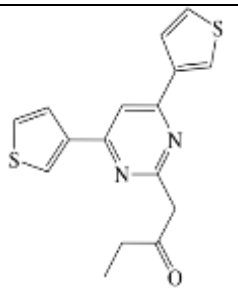 CHEMBL1650347 hA_1R, hA_{2A}R, hA_{2B}R, hA_3R $K_i(A_1)$=0.347μM $K_i(A_{2A})$=1.93μM $K_i(A_{2B})$=3.25μM $K_i(A_3)$=1.270μM	0.144	Yaziji V et al., J. Med. Chem. (2011) 54:457-471

K20	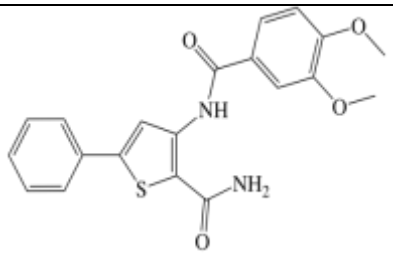 $K_i(A_1)$=1.09μM, $K_i(A_{2A})$=7.29μM, $K_i(A_3)$=0.918μM	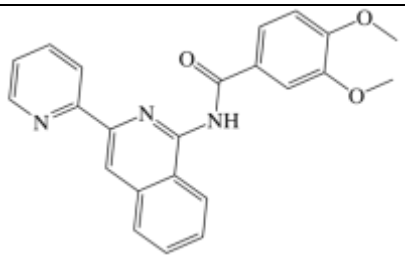 CHEMBL130130 hA_3R, rA_1AR, $rA_{2A}R$ $K_i(A_3)$=0.3μM, antag. activity (rA_1)=41%, antag. activity (A_{2A})=20%	0.19	van Muijlwijk-Koezen JE et al., J. Med. Chem. (1998) 41:3994-4000
K25	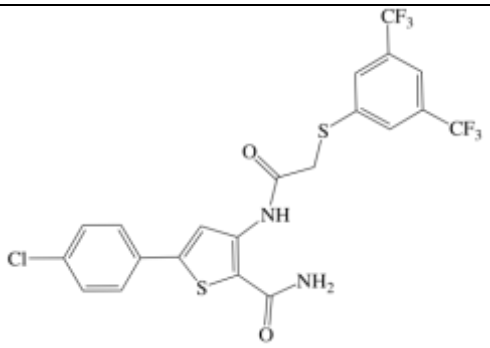 $K_i(A_3)$=1.55μM	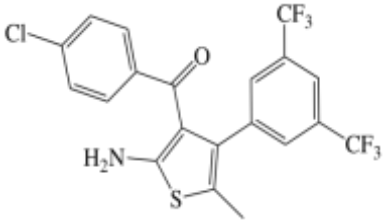 CHEMBL2086980 hA_1R antag. activity (A_1)=88% antag. activity (A_1)=84% (2nd value)	0.165	Valant C et al., J. Med. Chem. (2012) 55:2367-2375
K19	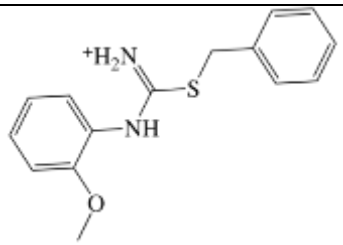 Inactive	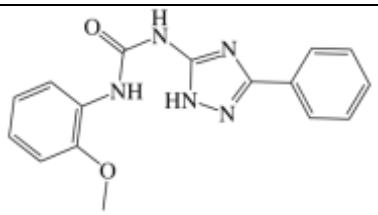 CHEMBL2151132 hA_1R, $hA_{2A}R$, $hA_{2B}R$, hA_3R antag. activity (A_1)=22% K_i (A_{2A})=0.2μM antag. activity (A_{2B})=10% K_i (A_3)=0.3μM	0.195	Carlsson et al. ACS Med Chem Lett (2012) 3:715-720.
K15	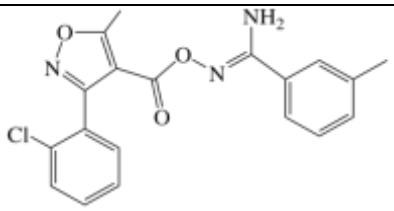 $K_i(A_3)$=30.9μM	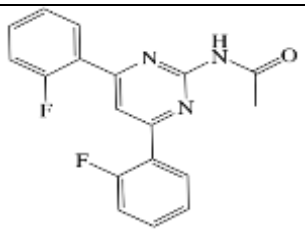 CHEMBL1650163 hA_1R, $hA_{2A}R$, $hA_{2B}R$, hA_3R	0.160	Yaziji V et al., J. Med. Chem. (2011) 54:457-471

		antag. activity (A_1)=8% antag. activity (A_{2A})=12% antag. activity (A_{2B})=10% antag. activity (A_3)=15%		
K9	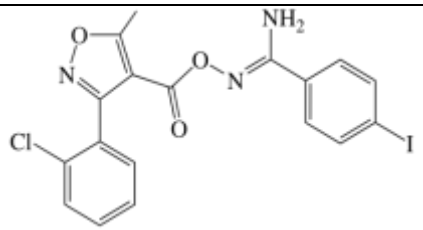 $K_i(A_1)$=6.91μM, $K_i(A_3)$=4.13μM	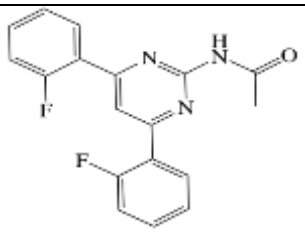 CHEMBL1650163 hA_1R, $hA_{2A}R$, $hA_{2B}R$, hA_3R antag. activity (A_1)=8% antag. activity (A_{2A})=12%, antag. activity (A_{2B})=10% antag. activity (A_3)=15%	0.150	Eastwood et al. ACS Med Chem Lett (2011) 2:213-218.
K10	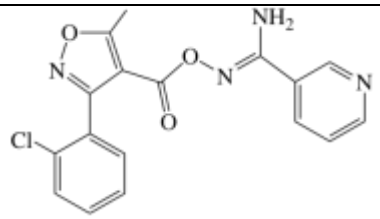 $K_i(A_3)$=4.49μM	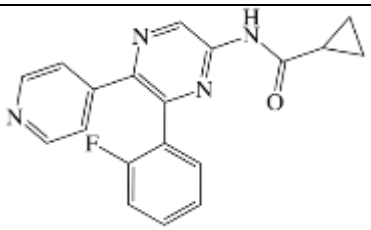 CHEMBL1672623 hA_1R, $hA_{2A}R$, $hA_{2B}R$, hA_3R $K_i(A_1)$=0.025μM $K_i(A_{2A})$=0.051μM $K_i(A_{2B})$=0.001μM $K_i(A_3)$=0.326μM	0.165	Eastwood et al. ACS Med Chem Lett (2011) 2:213-218.
K11	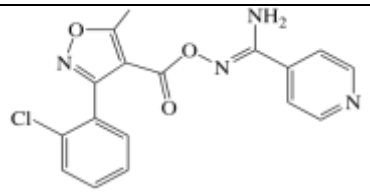 $K_i(A_3)$=5.15μM	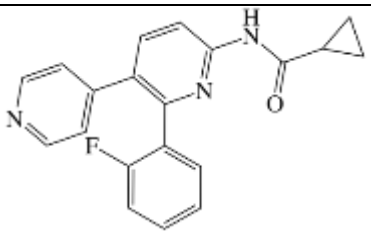 CHEMBL1082028 hA_1R, $hA_{2A}R$, $hA_{2B}R$, hA_3R $K_i(A_3)$=0.82μM $K_i(A_1)$=0.123μM $K_i(A_{2B})$=0.002μM $K_i(A_{2A})$=0.061μM	0.171	Eastwood P et al., Bioorg. Med. Chem. Lett. (2010) 20:1697-1700

K17	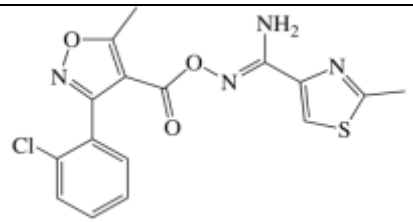 $K_i(A_3)$=4.16μM	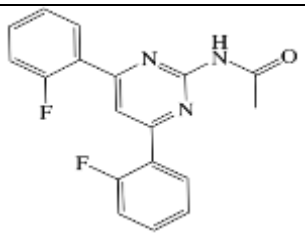 CHEMBL1650163 hA_1R, $hA_{2A}R$, $hA_{2B}R$, hA_3R antag. activity(A_1)=8% antag. activity(A_{2A})=12% antag. activity(A_{2B})=10% antag. activity(A_3)=15%	0.161	Yaziji V et al., J. Med. Chem. (2011) 54:457-471
K18	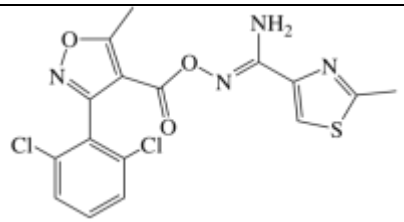 $K_i(A_3)$=0.899μM	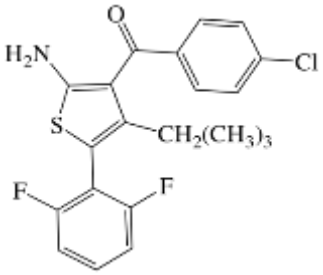 CHEMBL3098291 hA_1R antag. activity (A_1)=18%	0.141	Romagnoli R et al., Bioorg. Med. Chem. (2014) 22:148-166

3.4.4 Evaluation of the ligands as PAINS

In two recent excellent studies, a detailed analysis of PAINS (pan-assay interference compounds) alerts [205] in compound libraries was performed. [206,207] From the analysis, it was concluded that the blind use of PAINS filters to detect compounds with possible PAINS liabilities should be handled with caution, since there is a trend to exclude *a priori* any potentially reactive compound from further consideration. In one of these studies [207] more than 14400 extensively tested compounds containing PAINS substructures were detected, and their hit rates were determined. After examining hundreds of assays, the hit frequency for PAINS was low, with values of two to five hits for PAINS, and many consistently inactive compounds were identified. Future investigations and certain well designed computational tools will be highly encouraged to translate the findings of rigorous large-scale data analysis into practical guidelines with utility for medicinal chemistry. In these studies, 2-aminothiophenes were tested in about 650 assays and never produced a hit for PAINS. [207] Additionally, while in the original study, 2-amino-3-carbonylthiophenes [205] were suspected to be PAINS, extensive SAR studies showed that these compounds are promising allosteric A_1AR modulators. [56,195]

Class A and class B compounds **K1**, **K12-K14, K16, K20-K25, K28, K35** of the present study included a 2-aminothiophene scaffold. Compounds **K3, K5, K9-K11, K15, K17, K18, K26-K36** included the carbonyloxycarboximidamide moiety which is not uncommon structural feature in medicinal chemistry projects. [208] We tested the structure of our compounds in smiles format, and none was identified as PAINS [209]. Additionally, the pharmacological model we used to fit the binding data and determine K_i values of all

our compounds confirms competitive interaction with the receptor and not a PAINS behavior**.** [210] Representative plots from compounds testing are shown in **Figure 3.4**. The results here show clearly specific and A_3-selective binding for a number of compounds. The fact that **K18** and several other compounds have only A_3R binding should serve as a valid proof of specific binding, rather than random nonspecific interaction. Screening against other GPCRs would not provide a better control than the AR subfamily for a possible PAINS behavior of the tested compounds.

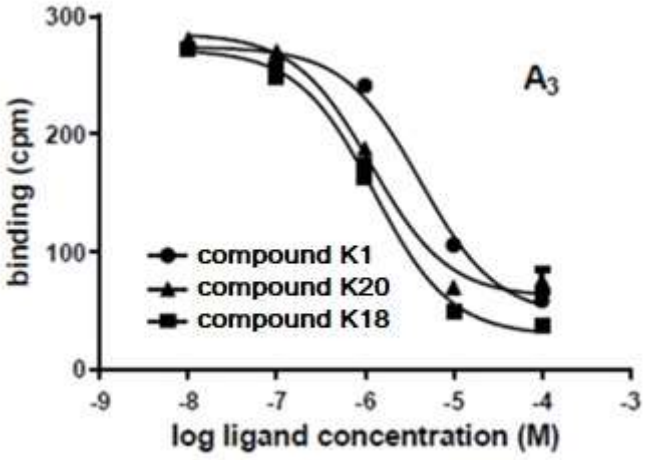

Figure 3.4 Competition binding curves for selected compounds at the A_3 adenosine receptor. The curves show the result of single representative experiments for compounds **K1** (class A), **K20** (class B), and **K18** (class D). The competing radioligand was [^{3}H]HEMADO (1 nM). The K_i values from these individual experiments were 3.1 μM (compound **K1**), 0.92 μM (compound **K20**), and 0.90 μM (compound **K18**). The data were fitted assuming a one-site competition model.

3.5 Investigation of the compounds' affinity to ARs using simulations

3.5.1 Molecular docking calculations

ZM241385 contains an aminotriazolotriazine with a 2-furyl group and a $(CH_2)_2$Ph(OH fragment connected at positions 5- and 2-, i.e., opposite sides of the central heteroaromatic ring. Ligands, for example of classes A, B, D, for example **K1, K20, K5**, respectively, or **K7-K9** of class E include an aromatic ring bearing an exocyclic amino group, as the aminotriazolotriazine in ZM241385, and often two other lipophilic moieties bearing a phenyl group, linked to the aromatic ring. Common structural features in the tested compounds of different classes A-E effect similar contacts with residues of the binding area according to the docking calculations.

The docking calculations showed that ligands **1-39** are anchored inside the same binding cleft for all AR subtypes and can form up to two stabilizing hydrogen bonds with the side chain amide group of the Asn(6.55) [109,130] in TM6. Ligands **K1-K39** can occasionally form tight hydrogen bonds with the carboxylate group of Glu(5.30) in A_1,A_{2A}, A_{2B}Rs.

In complex of ZM241385 with A_{2A}R or in complexes of ligands **K1**, **K7**, **K8**, **K12-K14, K16, K20-K25** with ARs the thiophene ring linked with 2-amino or 2-amido group has aromatic π-π stacking interaction

with the side chain of the conserved Phe(5.29) in the EL2 and additional hydrophobic contacts with Leu(6.51) and Ile(7.39) (**Figures 1.6, 2.4, 3.5**). The same can be argued for K5 and its analogues in class D where Compounds **K12-K14** bind equally well with A_{2A} and A_3Rs while having affinity only to A_3R. In the case of A_3R complexes, residue Glu(5.30) has been replaced by Val which can contribute significantly to van der Waals interactions inside a binding site. One of the two aromatic rings, a furan ring in ZM241385, is positioned deep in the ligand-binding cavity towards TM5 and TM7, forming hydrophobic interactions with His(6.52), Leu(6.51) and Trp(6.48) (**Figures 1.6, 2.4, 3.5**). The furan ring in ZM241385 has an oxygen acceptor atom which forms a hydrogen bond to the amide NH_2 group of Asn(6.55) and has been implicated in both antagonist and agonist binding from mutagenesis experiments.[152153] In the tested ligands one of the two rings can adopt a similar orientation. For example the 5-phenyl ring in compounds of class A and B and a methyl-thiazole or substituted phenyl ring in compounds of class D (**Figures 1.6, 2.4, 3.5**). In ZM241385 the $(CH_2)_2$Ph(OH) moiety, in ligands of classes A and B, the 3-NHCOAr, and of class D the phenyl isoxazole or biphenyl can be oriented either at the solvent-exposed part of the open binding cavity [20] or at the extracellular ends of TM1, TM2 and TM7[52] forming hydrophobic interactions with Leu(7.32) and Met(7.35) and other residues (these residues of TM7 are not shown in **Figures 3.5, 3.6, 3.8-3.17** for clarity reasons).[20,52]. Similar observation can be disccused for ligands of class C or E.

It should be noted that X-ray unveiled the orthosteric binding site only for A_{2A}R since 2008[20] and is assumed to cover a similar region for A_1, A_{2A}, A_{2B}, A_3ARs. This assumption has been proved proved in some cases correct, i.e., it was shown that docking calculations against A_3R binding pocket, using the Abagyan-Katrich model, substantially increased the enrichment of known A_3R ligands among a database of decoys. [4]

In this work the docking poses of all the ligands, active or inactive, include very similar interactions with the binding area for A_1, A_{2A}, A_{2B}Rs and similar with A_3R. Obviously, according to the experimental affinity results each compound has a certain selectivity profile and few analogues are also completely inactive.

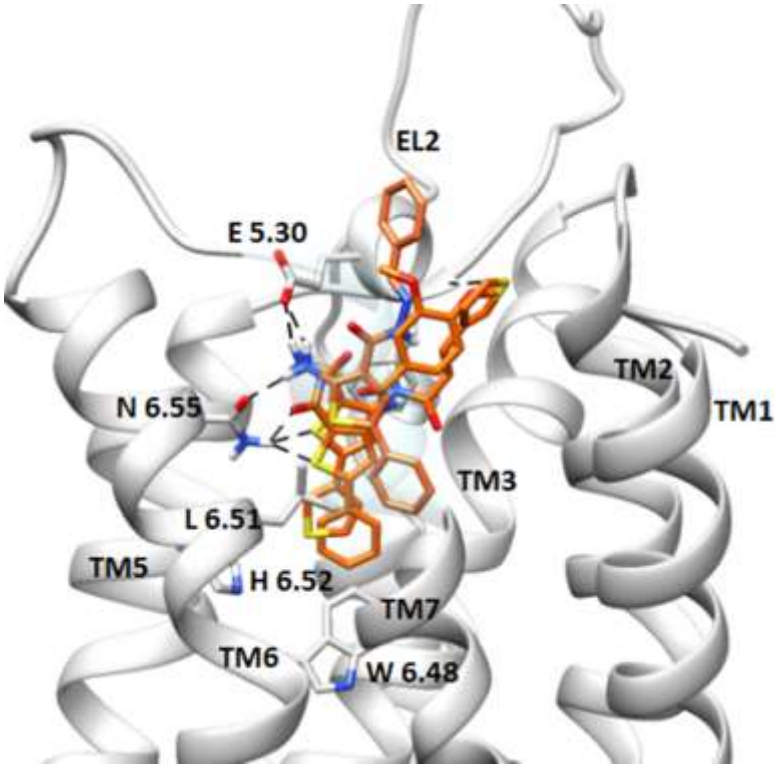

Figure 3.5 Calculated binding orientations for **K22**, **K23**, **K24** in the orthosteric site of the A_{2A}R (PDB ID 3EML) using molecular docking calculations. The part of the A_{2A}R is displayed as a white cartoon, and the

three ligands are shown with orange carbon atoms; the very similar docking poses and interactions are shown.

3.5.2 MD simulations of ARs - ligands complexes

3.5.2.1 Necessity for MD simulations

Since, the complexes between ARs and ligands have considerable therapeutic impact, strategic long MD simulation studies have been performed in order to test the effect of the starting conformation of the ligand, [211], the protein flexibility in improving the reliability of binding conformation, [212] the lipid bilayer, [213] the conformational transition at long simulation times, [214,215] ligand's recognition pathways [216] etc. Further, it has been described how difficult it might be to select a proper binding conformation by taking into account only the docking score or the presence/absence of specific ligand receptor contacts. [211] It has been also reported that it is almost impossible to make a recommendation as to which lipid bilayer would be the best to use in GPCR membrane simulations, particularly when the bilayers contain only a single species of lipid [213] and the convergence of protein dynamics for AR system was not achieved even in 200 ns [214]. The tested molecules **1-39** result in stable docking poses against A_1, A_{2A}, A_{2B} or A_3Rs which can not interptet the bindind affinity results. Thus, we performed MD simulations of docking poses aiming at finding possibly differences in binding mode that can be more helpful in understanding binding preferences.

3.5.2.2 Optimization of system set-up for MD simulations

Molecular docking calculations. It has been demonstrated the importance of MD sampling in considering protein flexibility towards choosing the most reliable binding conformation [212] and it has been shown that binding interactions from structure-based virtual screening against ARs are likely described better through all-atom MD simulations of the protein complexes. [123]. The docking poses used as starting structures for the MD simulations were selected not only to have a highest score but also a plausible profile as regards the hydrophobic and lipophilic contacts. The docking poses of the 39 ligands in complex with A_1, A_{2A}, A_{2B}, and A_3Rs were inserted into hydrated POPE lipid bilayers [213]**.**

Molecular dynamics simulations of ZM241385-A_{2A}R complex in different membrane bilayers - Selection of the lipid bilayer for MD simulations. We performed MD simulations for 70 ns to compare the effect of POPE, POPC and DMPC in the stability of antagonist ZM241385 in complex with the inactive state of hA_{2A}R (PBD ID 3EML**).** [20] The results suggest that POPE and POPC retain more the stability of the complex compared to DMPC (**Figure 3.6**). The RMSD of the ligand position relative to the X-ray conformation after the 70 ns trajectory is approximately 1.4 Å for POPE, 1.8 Å for DMPC and 2.0 Å for POPC (**Figure 3.6**) i.e. is the smallest for POPE. The ligand position was found to be stable for the POPE bilayer even when the trajectory run was extended to 200 ns.

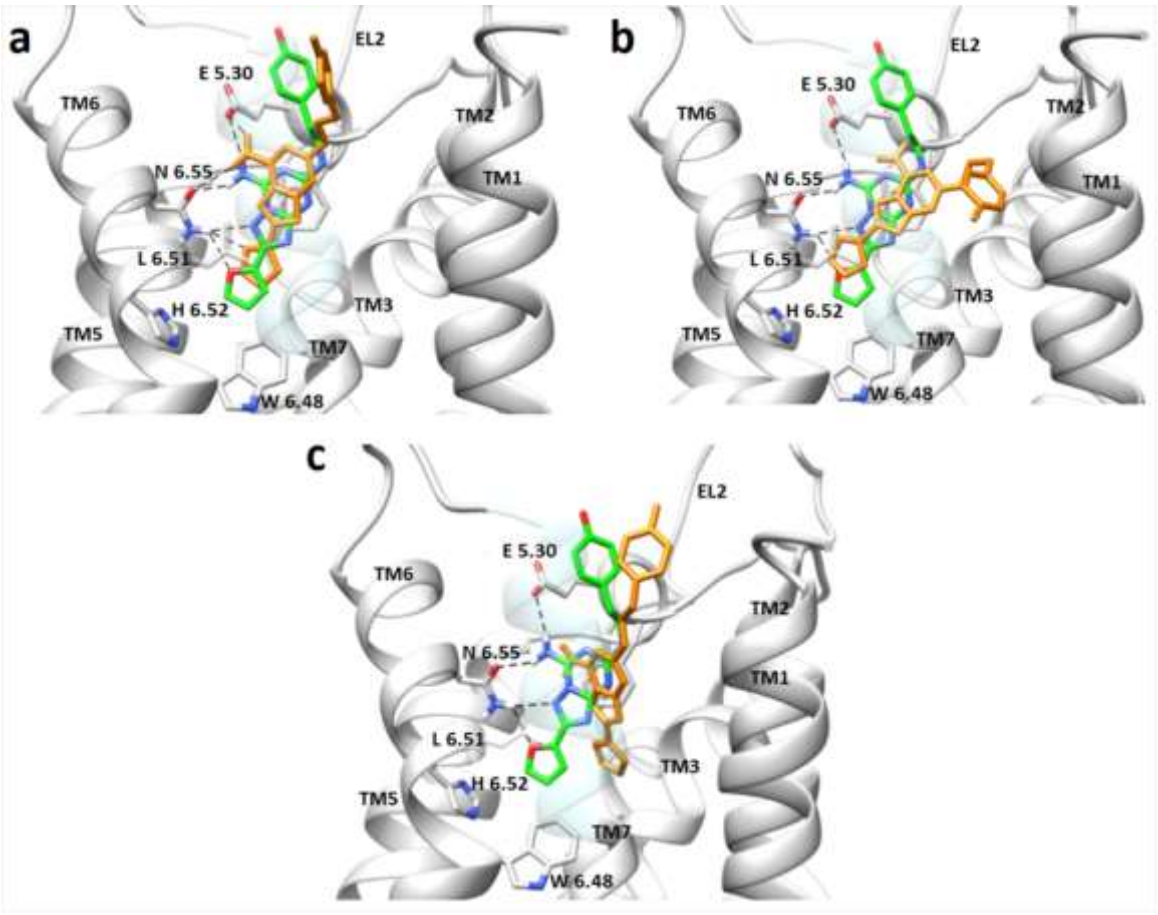
a
EL2
E 5.30
TM6
TM2
N 6.55
TM1
L 6.51
H 6.52
TM3
TM5
TM7
W 6.48
b
EL2
E 5.30
TM6
TM2
N 6.55
TM1
L 6.51
TM3
H 6.52
TM5
TM7
W 6.48
c
EL2
E 5.30
TM6
TM2
N 6.55
TM1
L 6.51
TM3
H 6.52
TM5
TM7
W 6.48

d

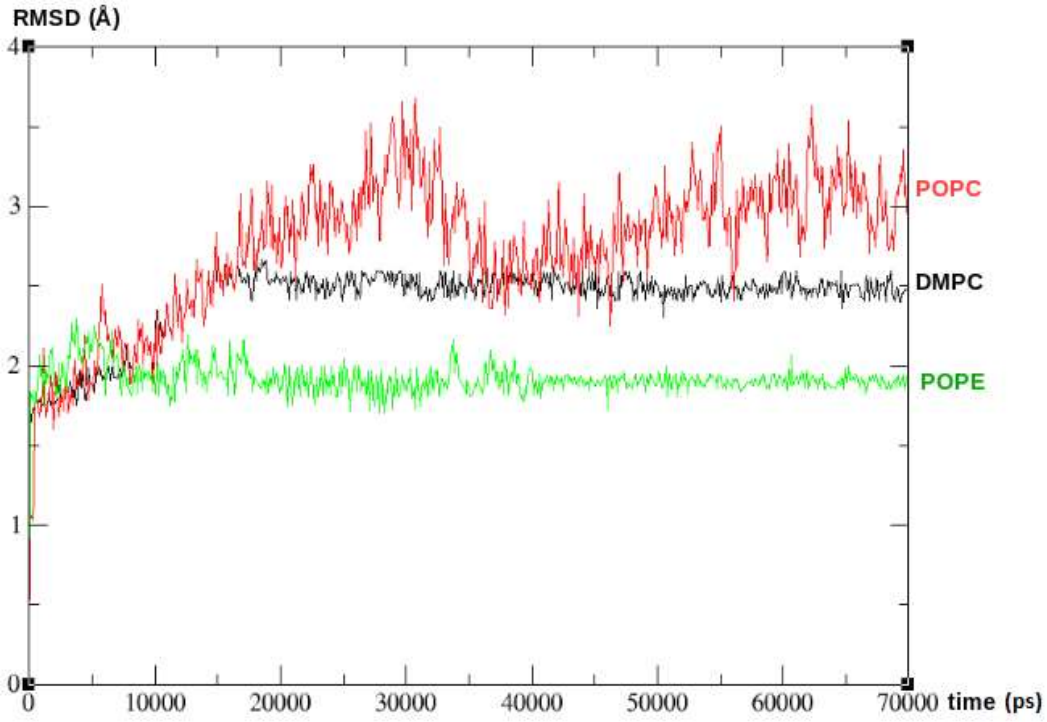

Figure 3.6 (a)-(c) Comparison of the crystallographic coordinates of ZM241385 (ligand in green sticks) with its binding orientation from replicas obtained after an 80 ns MD unrestrained simulation (ligand in orange sticks): (a) in POPE; (b) POPC and (c) DMPC membrane bilayers. MD optimization of the docking pose in POPE showed that ZM-241,385 can adopt a binding orientation in which the amino group of the heterocyclic ring is hydrogen bonded to the carbonyl of amide group of N(6.55) and to E(5.30) carboxylate in EL2. These hydrogen bonding interactions are retained compared to the X-ray crystallographic data. The lipophilic interactions are described in the manuscript in details. The complex is viewed from the membrane side facing helices TM6 and TM7 with the view of TM7 partially omitted. Side chains of amino acids important for binding are displayed as gray sticks. Hydrogen atoms are not displayed except those which are involved in hydrogen bond interactions which are highlighted as black dashed lines. (d) Root mean square deviation ($RMSD_{lig}$ expressed in Å) of ZM241385 in complex with $A_{2A}R$ in different membrane bilayers environment during 70 ns MD simulation compared to its crystallographic position (PDB ID 3EML).

To establish that the comparison was meaningful, the equilibration of the membranes was also tested. To this end, the average area per lipid headgroup [190] was measured [190] in the end of the simulation trajectory of each lipid and compared with experimental results. The calculated values (**Figure 3.7**, **Table 3.3**) approached the experimental ones for pure lipid bilayers.

Table 3.3 Area per lipid obtained from MD simulations of ZM241385-$A_{2A}R$ complex and experimental values (see also **Figure 3.6**).

Lipid type	**Average Area per lipid** (AAL in	**Number of lipids**	**Min AAL** ($Å^2$)	**Max AAL** ($Å^2$)	**Ensemble**	**Experimental value** [217]

	Å^2)					
DMPC	59.881	134	58.222	60.896	NPT	60.6±0.5
POPC	66.964	116	64.588	70.004	NPT	68.3±1.5
POPE	59.894	166	55.331	61.568	NPT	59.75–60.75

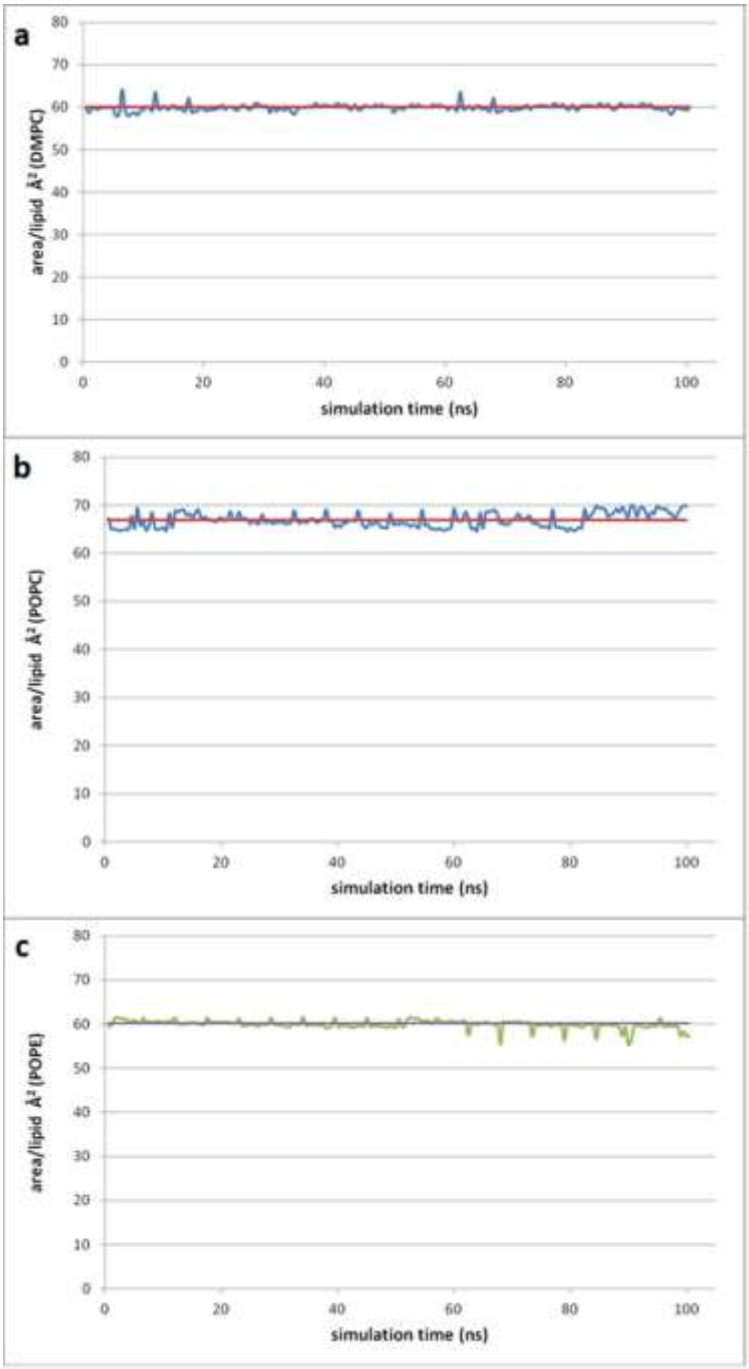

Figure 3.7 Time courses of the average area per lipid for ZM241385-A_{2A}AR complex in (a) DMPC; (b) in POPC; and (c) POPE (see **Figure S4**). Red lines are the experimental values of the area per lipid for a pure bilayer; (A) DMPC (60.6 Å^2); POPC (68.3 Å^2); and POPE bilayers (59.8 Å^2).

Effect of the starting structure. We showed also that the MD simulations for 10 ns in POPE bilayers using the X-ray structure of A_{2A}R-ZM241385 or the corresponding models for this A_{2A}R complex using the homology model of the A_{2A}R apo-protein from Katritch and Abagyan [4] or from Moro [171] led to similar structures as demonstrated by RMSDs ≤ 2 Å for Cα-carbons. Also, MD simulations led to similar structures when the starting structure of A_1R-DU172 complex was the experimental one or the homology model of A_1R apo-protein complex of Katritch and Abagyan [4] or Moro. [171] Similarly, no differences were found in the structures obtained from MD simulations of A_3R-ligand complexes when the A_3R model was an homology model obtained either from A_1 or A_{2A}R experimental structure.
A_1, A_{2A}, A_{2B}Rs contain the E(5.30) residue, except A_3R which have a valine in (5.30) position. This glutamate acid residue in (5.30) position may play an important role in high affinity ligand binding through the formation of a strong hydrogen bond, for example, with an unsubstituted exocyclic amine. Instead, the valine in (5.30) position of A_3R may allow bulky substitutents fitting, for example, bulky substituents on amino group or other lipophilic moieties at this region. Katritch and Abagyan suggested, using the experimental binding results from ligands and docking calculations [4], suggested that the side chain for V(5.30) has a gauche rotamer, compared to trans, which allows the binding of bulkier grous. A_3R binding area is broader than that of A_{2A}R (Section 1.5).

3.5.2.3 MD simulations results

Over two hundreds, 10ns MD simulations, and in some cases longer, were performed using Desmond software [162] with OPLS2005 force field [164,166,177] in order to reveal details on the binding of the ligands to A_1, A_{2A}, A_{2B} or A_3Rs. The numerous 10 ns MD simulations, which are possible only using supercomputers, was inevitable task in order to relax close atom contacts in docking poses and allow the ligand to adopt a reliable binding orientation. In cases where the binding orientation was stable, an extension of the MD simulation to 100 ns with OPLS2005 was applied to test the reliability of the results and in some cases also with AMBER software and amberff14SB force field for the protein complex [168] and lipid14 parameters for the lipid [183].

Compounds of class A. The docking calculations showed that compounds **K1**, **K12-K14, K21, K22** bind inside A_1, A_{2A}, A_3Rs with similar interactions but the 10 ns MD simulations show in several cases that the binding poses of these ligands are not stable.

A_{2A}R: Compounds **K1**, **K21**, **K22** have binding affinities with K_i = 2.67, 3.93 and 4.59 μM, respectively to A_{2A}R while **K12** do not bind to A_{2A}R. The docking calculations show that **K1**, **K12, K21**, **K22** are stabilized inside the binding pocket of A_{2A}R with similar orientation to ZM241385 (**Figures 3.8, Figure 3.11b**). The 10 ns MD and the extension to 100 ns MD simulations suggested a stable binding of **K12, K21**, **K22** inside A_{2A}R. The 2-amino group of thiophene ring forms a hydrogen bonding with the carbonyl of amido group of Asn(6.55) and the carboxylate of Glu(5.30) in EL2 (**Figure 3.8**). The thiophene ring has an aromatic π-π stacking interaction with the conserved phenyl ring of Phe(5.29) in EL2, hydrophobic contacts with Ile(7.39) and sulfur atom forms hydrogen bonding interactions with amido group of Asn(6.55) (**Figure 3.8**). The sizeable lipophilic moiety CONH-N=CH-Ar is oriented at the solvent-exposed part of the open binding cavity in EL2 and EL3 similarly to the $(CH_2)_2$Ph(OH) in the X-ray structure of A_{2A}-ZM241385 (**Figures 2.4, 3.6**) [20] forming hydrophobic interactions with Leu(7.32) and Met(7.35). The 5-phenyl group in **K1, K21**, **K22** is positioned deeply in the ligand-binding cavity towards TM5 and TM7 having hydrophobic interactions with Val(3.32), Leu(3.33), Leu(6.51), His(6.52), and Trp(6.48) (**Figure 3.8b**), similarly to the furyl ring in ZM241385 (**Figures 2.4, 3.6**) [152,153]**.**

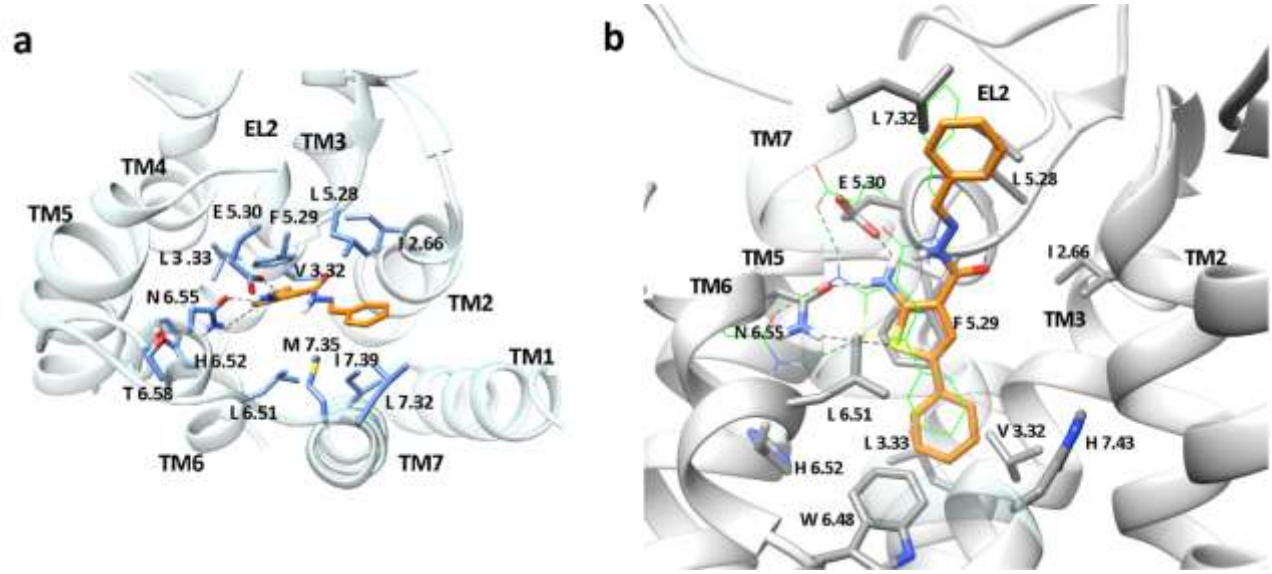

Figure 3.8 Predicted binding mode for ligand **K22 i**n the orthosteric site of the A_{2A}R. (a) Top-view of the orthosteric binding site. Sidechains of amino acids important for binding are shown in blue sticks. (b) Lateral view of the complex, facing helices TM6 and TM7, with the structure of TM7 partially omitted. MD optimization of the docking pose showed that **K22** can adopt a binding orientation in which the amino group of the thiophene ring is hydrogen-bonded to the carbonyl of amide group of N(6.55) and the carboxylate of E(5.30) in EL2. The thiophene ring has an aromatic π-π stacking interaction with the conserved F(5.29) (EL2) and forms important hydrophobic contacts with I(7.39), while the sulfur atom forms H-bonds with the amide group of N(6.55). In panel (a) side chains of amino acids important for binding are displayed in blue sticks. In panel (b) side chains of amino acids important for binding are displayed as gray sticks. Binding orientation of the ligand after the MD simulation is shown in yellow sticks and sidechains of some amino acids involved in ligand binding are displayed as gray sticks while the starting ligand and N(6.55)/E(5.30) side chain positions are shown in green wires. Hydrogen atoms are omitted except for those involved in hydrogen bond interactions, highlighted as black dashed lines. MD simulations of **K22** in complex with the ARs were performed for 100 ns.

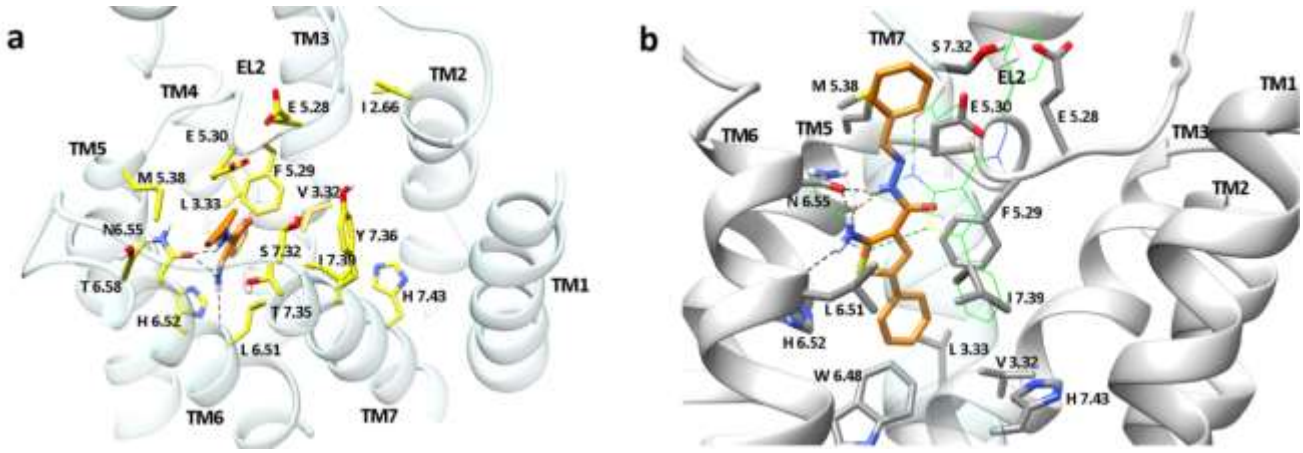

Figure 3.9 Top view and side view of the predicted binding mode for ligand **K22** in the orthosteric site of the A_1R. In panel (a) the sidechains of amino acids important for binding are displayed in yellow sticks. In panel (b) the sidechains of amino acids important for binding are displayed as gray sticks. Binding orientation of the ligand after the MD simulation is shown in yellow sticks and sidechains of some amino acids involved in ligand binding are displayed as gray sticks while the starting ligand and N(6.55)/E(5.30) side chain positions are shown in green wires. Hydrogen atoms are omitted except for those involved in hydrogen bond interactions, highlighted as black dashed lines. MD simulations of **K22** in complex with the ARs were performed for 100 ns.

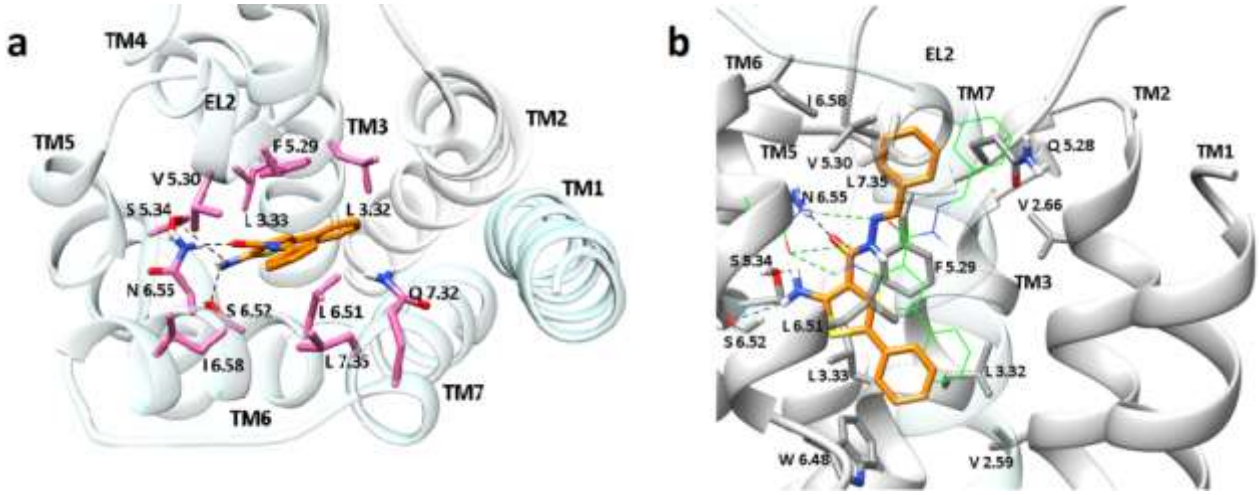

Figure 3.10 Top view and side of the predicted binding mode for ligand **K22** in the orthosteric site of the A_3R. In panel (a) the sidechains of amino acids important for binding are displayed in pink sticks. In panel (b) the sidechains of amino acids important for binding are displayed as gray sticks. Binding orientation of the ligand after the MD simulation is shown in yellow sticks and sidechains of some amino acids involved in ligand binding are displayed as gray sticks while the starting ligand and N(6.55)/E(5.30) side chain positions are shown in green wires. Hydrogen atoms are omitted except for those involved in hydrogen bond interactions, highlighted as black dashed lines. MD simulations of **K22** in complex with the ARs were performed for 100 ns.

A_1R: While the docking calculations showed that compounds **K1**, **K12, K21, K22** bind inside A_1R with similar interactions, the 10 ns MD simulations show that the binding poses of **K1**, **K12, K21** are not stable.
The 10 ns MD simulation and its extension to 100 ns revealed a stable binding orientation for **K22** inside A_1R **(Figure 3.9)**. Indeed, only **K22** has a K_i of 15.2 μM for A_1R, and none of the ligands, **K1**, **K12-K14, K21**, **K22** bind to A_1R.
Due to movements of TM1,TM2,TM3,TM7,EL3 in A_1R, it has been shown that $A_{2A}R$ binding area is elongated and narrower compared to the very wide and open cavity of the A_1R [32]. The $A_{2A}R$ pocket is narrower with Met(7.35) acting as a gatekeeper (**Figures 1.8, 3.8a**) and preventing entry and binding of bulky substituents. There is a common region covered by ZM241385 inside $A_{2A}R$ or DU172 inside A_1R despite their different orientation and height into the cavity and the different shape and extension of the binding area (**Figure 1.8**). Thus, it has been suggested [32] that the binding area in A_1R cover the orthosteric and a secondary allosteric binding pocket, the last not being present in $A_{2A}R$, and when less bulky orthosteric antagonists than DU172, such as DPCPX, are docked into the A_1R, a significant part of the binding site is left un-accommodated. This is shown in **Figures 3.8, 3.9** for compound **K22** adopting the orthosteric

binding area inside A_{2A}, A_1Rs, respectively, with CONH-N=CH-Ar orienting at the solvent-exposed part of the open binding cavity [20].Compared to A_{2A}R complex in the complex of A_1R with **K22** the ligand is positioned closer to TM5 and TM6. This may be the result of the more polar environment at the extracellular opening of the pocket in A_1R compared to A_{2A}R, due to the presence of Thr(7.35) instead of Met and the mutations Leu(5.28)Glu, Leu(7.32)Ser and the slightly shifted conformation of Glu(5.30) (**Figure 3.8**). This more polar environment in A_1R may limit the presence of bulky lipophilic groups at the area between EL2 and TM7 disfavouring also a stable orientation and a hydrogen bonding interaction with Asn(6.55) and Glu(5.30) of the relevant ligands.

Between compounds **K1**, **K21**, and **K22**, only **K22**, having an Ar = Ph without any substitution in CONH-N=CH-Ar binds to A_1R **(Figure 3.9)** compared to one or three methoxy groups attached to the phenyl ring in **K1**, **K21**, respectively (see **Figure 3.11a** for **K1**).

In compound **K12**, 5-phenyl group is missing and the ligand can not form dispersion interactions with residues positioned deep in the orthosteric binding area, i.e., Val(3.32), Leu(3.33), Leu(6.51), and His(6.52) compared to compounds **K1, K21**, **K22**. The docking calculations suggest and the 10 ns MD simulations confirm that compounds **K13, K14** have a condensed cyclopentane or cyclohexane ring, respectively, that cause steric crowding with phenyl group in Phe(5.29) and abolishment of the critical hydrogen bonding interactions with Asn(6.55) and binding affinity for A_1, A_{2A}Rs **(Figures 3.12a,b)**.

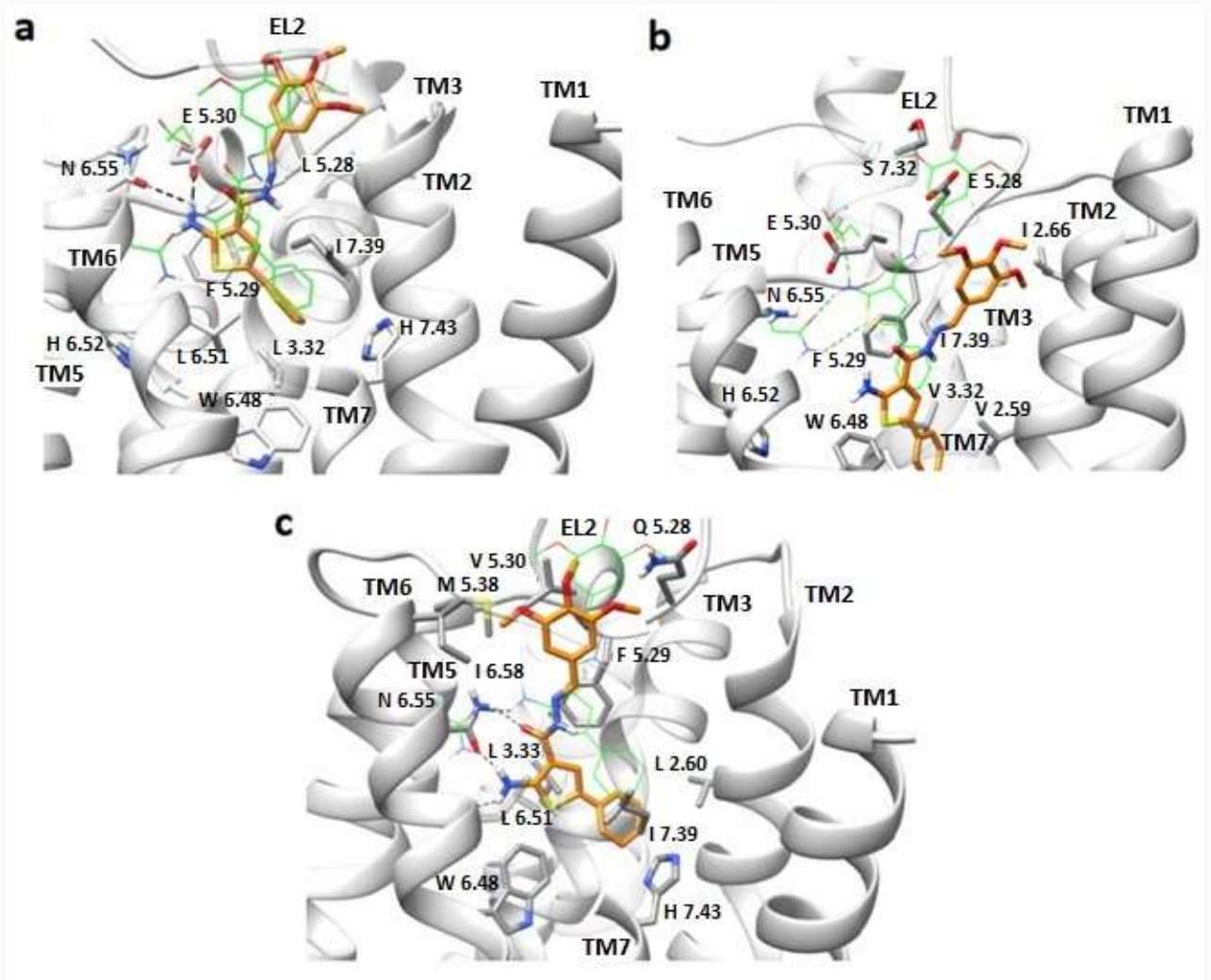

Figure 3.11 The MD simulations of the docking pose of **K1** against A_1R (panel b) showed that the binding orientation is not stable, probably because binding site is narrower in A_1R. In contrast, as it is shown in panels (a,c), the 100 ns MD simulations showed that the binding region of A_3R can accommodate the cyclohexyl ring and ligand **K1** can adopt a binding orientation in which the amino group and sulfur atom of the thiophene ring can form H-bonding interactions with N(6.55). The sidechains of some amino acids involved in ligand binding are displayed as gray sticks. Binding orientation of the ligand after the MD simulation is shown in yellow sticks and sidechains of some amino acids involved in ligand binding are displayed as gray sticks while the starting ligand and N(6.55)/E(5.30) side chain positions are shown in green wires. Hydrogen atoms are omitted except for those involved in hydrogen bond interactions, highlighted as black dashed lines.

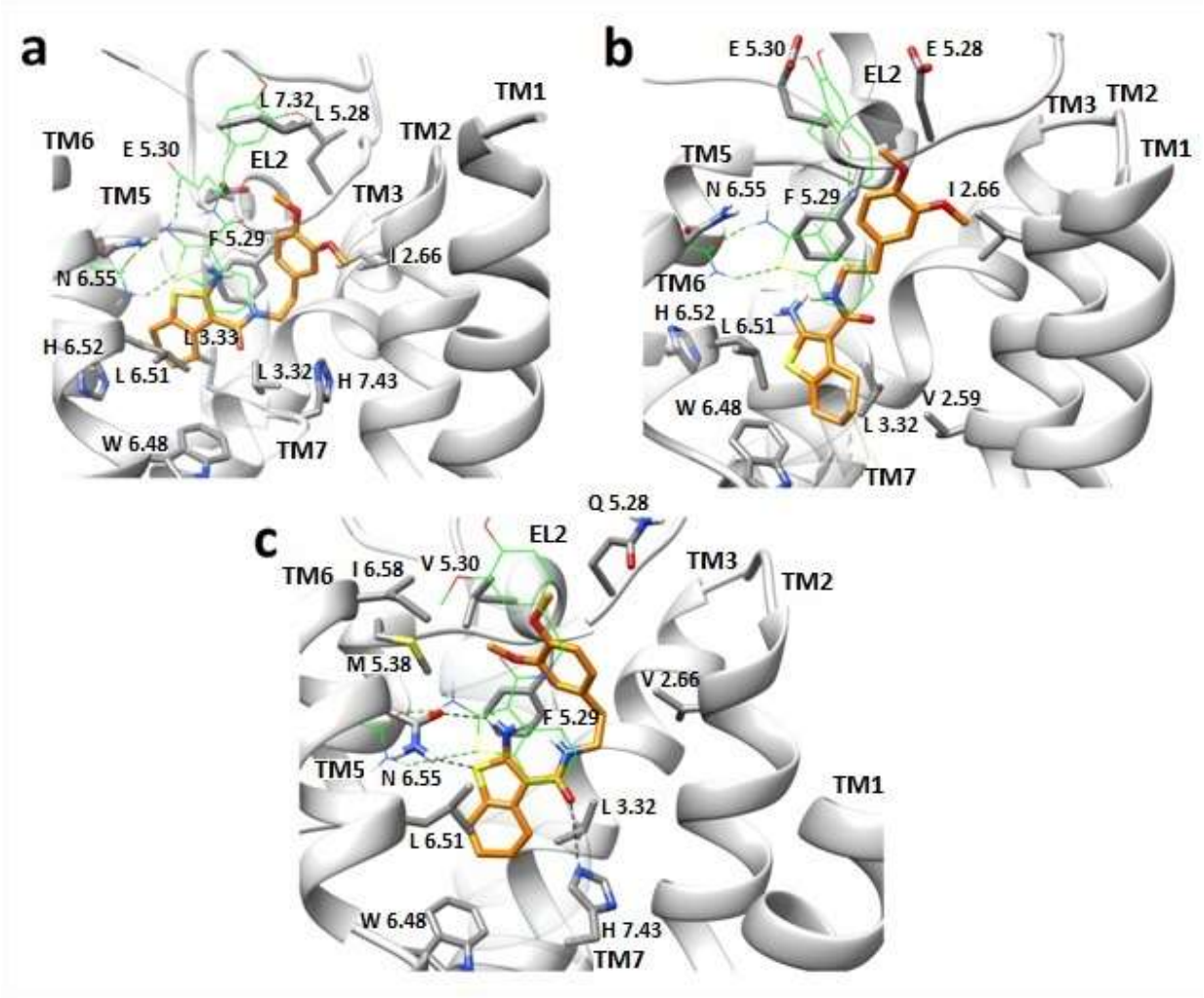

Figure 3.12 The MD simulations of the docking pose of **K14** against A_{2A} (panel a), A_1R (panel b) show that the binding orientation is not stable, probably due to the steric crowding induced by the cyclohexyl ring. (c) In contrast, MD simulations for 100 ns showed that the binding region of A_3R can accommodate the cyclohexyl ring and ligand **K14** can adopt a binding orientation in which the amino group and sulfur atom of the thiophene ring can form H-bonding interactions with N(6.55). The sidechains of some amino acids involved in ligand binding are displayed as gray sticks. Binding orientation of the ligand after the MD simulation is shown in yellow sticks and sidechains of some amino acids involved in ligand binding are displayed as gray sticks while the starting ligand and N(6.55)/E(5.30) side chain positions are shown in green

wires. Hydrogen atoms are omitted except for those involved in hydrogen bond interactions, highlighted as black dashed lines.

A_3R: All molecules **K1**, **K12-K14, K21, K22** have affinity to A_3R with K_i values 37.1, 16.5, 14.8, 5.77, 5.16 and 3.10 μM, respectively. In A_3R Glu(5.30) changes to Val and it might be likely that lipophilic groups included by the ligands may be accommodated more effectively in this region of the binding area compared to the other AR subtypes **(Figure 3.10)**. The changes Thr(6.58)Ile, Met(7.35)Leu compared to A_{2A}R allow similarly the presence of sizeable groups protruding towards the extracellular opening of the pocket (**Figure 3.10**). Katritch and Abagyan suggested [4] that Val(5.30) side chain can adopt a gauche conformer increase substantially the enrichment of known A_3R ligands, with bulky amine substitutions or bulky neighboring fragments, from decoys in docking calculations to hA_3R. We applied this rotamer and calculated reliable binding poses in which CONH$(CH_2)_2$Ar groups in **K12-K14** and CONH-N=CH-Ar groups in **K1**, **K21, K22** orient towards the solvent-exposed part of the open binding cavity **(Figures 3.10, 3.11c, 3.12c)**. The molecules shift slightly towards TM5 and TM6, compared to their binding orientations against A_{2A}, A_1Rs, to fit better the sizeable lipophilic moiety close to Val(5.30). The 100 ns MD simulation shows that **K22** is stabilized through the formation of hydrogen bonds between the 2-amido group of the ligand with carbonyl of the amido side chain of Asn(6.55) and equally with Phe174 (5.43) or Ser239 (6.53) carbonyls of the TM helices. The NHCO moiety of **K22** is interacting with Asn(6.55) **(Figure 3.10).** Hydrogen bonding interactions between amido group in the side chain of Asn(6.55) and sulfur atom of the thiophene ring of the ligand were occasionally observed in the trajectory.
Compounds **K12-K14** are weaker binders compared to **K1**, **K21, K22**. Compound **K12** lacks the 5-phenyl group which allows attractive interactions with residues Leu(6.51) and His(6.52) deeply in the binding area. This 5-aryl group seems to be favorable for binding to A_1 and A_{2A}R according to the results of this study. As discussed previously, in **K13, K14** the condensed cyclopentane and cyclohexane ring reduces the flexibility of the ligand to adopt an optimal orientation for hydrogen bonding interactions with Asn(6.55). Nevertheless, **K13, K14** fit inside the more lipophilic binding area of A_3R, according to the 100 ns MD simulations, in contrast to A_1, A_{2A}Rs (**Figure 3.12**). Between **K1**, **K21, K22**, the most potent binder to A_3R is **K1** in which the substituent at 3-thiophene position is more lipophilic for favorable dispersion interactions in the region around Val(5.30) **(Figures 3.10, 3.11c)**. **K22** binds to A_1, A_{2A} and A_3Rs.

Class B. Compounds **K23** and **K20** have a sizeable lipophilic group at 3-position, i.e., NHCOCH=CH-thiophenyl and NHCO-Ph$(OMe)_2$, respectively, linked at 3-position and a 5-aryl group, i.e., a 5-thiophenyl or 5-phenyl group, respectively, in the 2-amido-thiophene ring. Compared to compounds of class A which have a 3-CONHR group, most of them, in a 2-amino-5-aryl-thiophene ring, compounds of class B have a 3-NHCOR group in a 2-amido-5-aryl-thiophene ring. As discussed previously for **K22**, our docking calculations and MD simulations with A_{2A}, A_1Rs show that the sizeable lipophilic group in **K20** and **K23** is oriented in the area of EL2 **(Figure 3.13)**. The affinity of **K20**, **K23** measured against A_{2A}R is K_i = 1.09, 1.18, μM and against A_1R is 7.29 and 4.69 μM, respectively. Similarly to 2-amino group binding to Asn(6.55) in class A molecules, the 100 ns MD simulations show that the 2-amido group of thiophene is hydrogen bonded to the amido group of Asn(6.55) in A_{2A} and A_1R and occasionally with carboxylate group in A_{2A}R, while sulfur of the thiophene ring may also form a H-bond with amido group of Asn(6.55). The 100 ns MD simulations show that the van der Waals interactions for **K20** and **K23** inside the binding cavity of A_{2A}R are similar to those described above for the A_{2A}-**K22** complex. What we observed from the 100 ns MD simulations for A_1R complexes with compound **K20** is that, compared to A_{2A}R complexes, **K20** moves slightly higher in the orthosteric binding site and the 5-aryl-thiophene ring is inclined so the 3-NHCOR substituent is directed between TM7 and TM2. The carbonyl of 2-thiophene amido group of the ligand can

be hydrogen bonded to the amido group of Asn(6.55). This movement can be realized due to the broader cavity between TM1, TM2 and TM5, TM6 as showed recently in the X-ray structure of A_1AR complex (PDB ID 5UEN) [32]. The ligand is embraced by Tyr(7.36), His(7.43), Leu(7.32), Leu(6.51), Phe(5.29), Leu(5.28), Ile(2.66) and the thiophene ring has an aromatic π-π stacking interaction with Phe(5.29) **(Figure 3.13)**. This orientation cannot be adopted by **K20** possibly because of its longer 3-NHCOR group. The 100 ns MD simulations showed that in this case the entire molecule shifts slightly towards TM2. The carbonyl of 2-thiophene amido group of the ligand can be hydrogen bonded to the amido group of Asn(6.55) and the amino part of the 2-amido group to the carboxylate of Glu(5.30) while NH of the 3-NHCOR can be hydrogen bonded also with Glu(5.30). The replacement of Glu(5.30) with Val in A_3R orthosteric cavity retained the binding of compounds **K20** and **K23** as showed by K_i values of 0.918 and 1.65 μM, respectively, with the latter value corresponding to one of the lowest affinities against A_3R. The 100 ns MD simulations show that the molecules shift slightly towards TM5 and TM6, compared to their binding orientations against A_{2A} and A_1Rs, to fit better their sizeable lipophilic groups close to Val(5.30) **(Figure 3.13)**. The ligands are stabilized through the formation of a bidentate hydrogen bond between the 2-amido group of the ligand and the amide side chain of Asn(6.55).

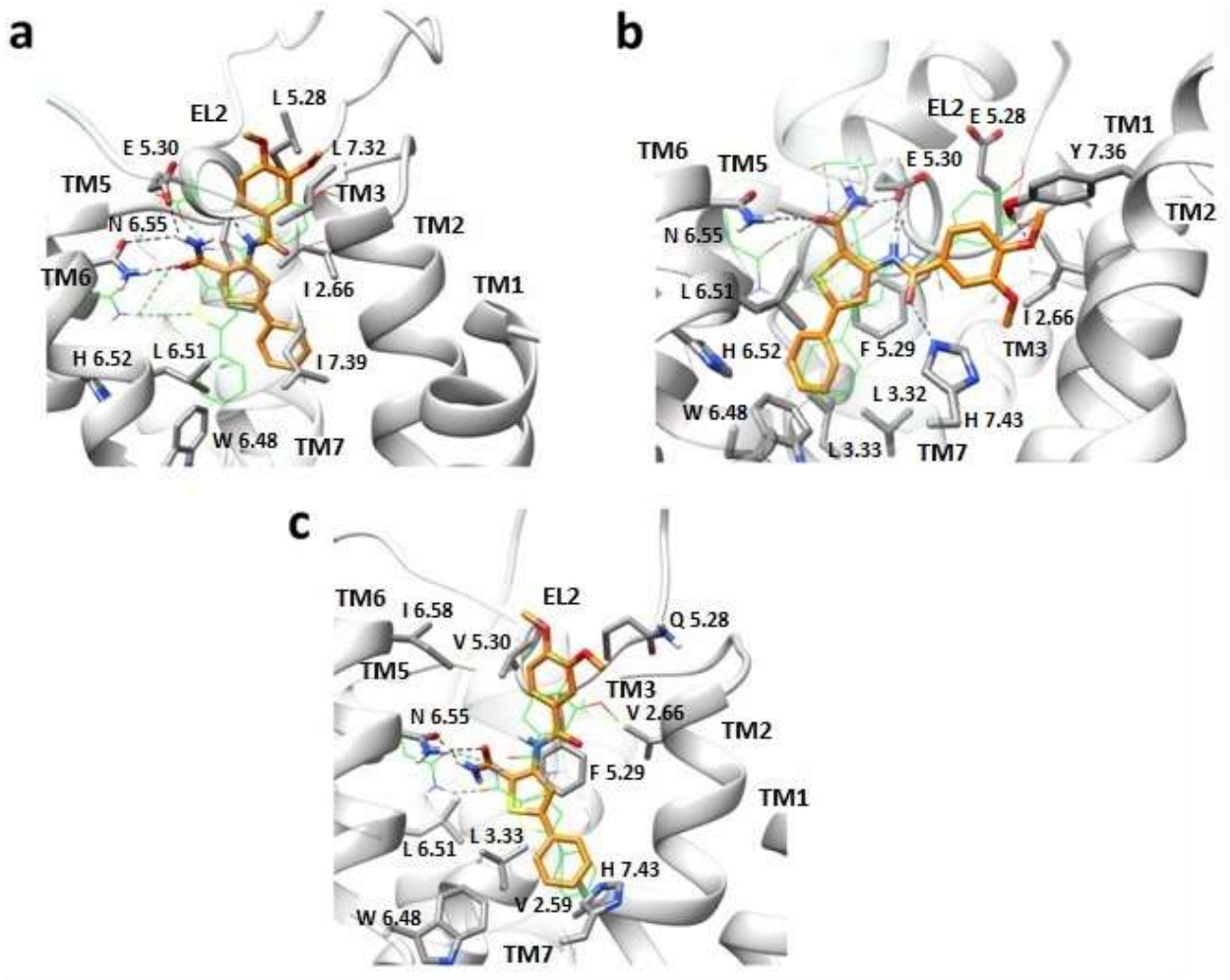

Figure 3.13 Predicted binding modes before and after 100 ns MD simulations for ligand **K20** in the orthosteric binding site of (a) A_1, (b) A_{2A} and (c) A_3AR, resulting in stable complexes. Compound **K20** can adopt a binding orientation inside A_{2A}AR in which the amido group of thiophene ring is hydrogen-bonded to N(6.55) and E(5.30), and van der Waals interactions stabilize the ligand inside the binding cavity. The

replacement of E(5.30) with V in A_3R orthosteric cavity (panel c) retained the binding of compound **K20**, as a result of hydrogen-bonding to N(6.55) and additional favourable van der Waals interactions of its bulky lipophilic group in the vicinity of V(5.30). In A_1R, which has a broader binding cavity, the 5-aryl-thiophene ring is inclined and the 3-NHCOR substituent is directed towards TM2. Binding orientation of the ligand after the MD simulation is shown in yellow sticks and sidechains of some amino acids involved in ligand binding are displayed as gray sticks while the starting ligand and N(6.55)/E(5.30) side chain positions are shown in green wires. Hydrogen atoms are omitted except for those involved in hydrogen bond interactions, highlighted as black dashed lines.

In compound **K25**, the group at 3-position of the thiophene ring is $NHCOCH_2SPh(CF_3)_2$. The MD simulations predicted that **K25** cannot be stabilized inside the orthosteric binding area of A_{2A} and A_1Rs. The orientation of NHCOR group towards the solvent exposed area **K25** is not favorable, because it has two polar CF_3 groups in the area close to Glu(5.30). Similarly, if the sizeable NHCOR group orients towards TM2 the molecule can not anchor the p-Cl-phenyl deep in the receptor and loses dispersion interactions. In contrast an orientation of $NHCOCH_2SPh(CF_3)_2$ pointing to the solvent exposed area is favored by the replacement of Glu(5.30) with Val according to the 100 ns MD simulation. The results are in agreement, with the fact that compound **18** is the only ligand of class B which is specific for A_3R (K_i = 1.55 μM). Compared to **K16, K20, K23, K25, K28**, **K35** lacks of the 5-phenyl substituent and this led to affinity only against A_1 and A_3R (K_i = 7.48 and 5.39 μM). The results showed that a substituent buried deeply between TM3, TM5, TM6 and TM7 and being in contact with Val(3.32), Leu(3.33), Leu(6.51), and His(6.52) is important for affinity against A_{2A}R, similarly to the 2-furyl substituent in ZM241385 as has been demonstrated from antagonist and agonist binding and mutagenesis experiments. [152,153] Compound **K16** lacks the sizeable acylamino substituent at 3-thiophene ring position compared to **K20** and **K23**; it has a moderate affinity against A_{2A} and A_3Rs and no affinity against A_1R.

Class C. This class includes methanimidothioate derivatives **K2** and **K19**. Compound **K19** lacks any affinity compared to derivative **K2** which exhibited moderate A_3AR affinity and a very weak A_{2A}AR affinity (K_i values were 16.6 and 61.3 μM respectively). It seems that the substitution pattern is important for the affinity profile and this may trigger additional SAR studies in the future.

Class D. Members of this class are compounds **K3-K5**, **K9, K10, K11, K15, K17, K18, K26, K27, K29-K39** which have a carbonyloxycarboximidamide moiety. **K4** has an ureacarboximidamide moiety. In most compounds of Class D the carbonyl group of carbonyloxycarboximidamide moiety is connected with a biaryl group: (a) at 4-position of 3-phenyl-5-methyl-isoxazole, (b) at o-, or p-position of a biphenyl, while the carboximidamide carbon is connected to an aromatic moiety, like a substituted phenyl, pyridinyl or 4-thiazolyl group. The carbonyloxycarboximidamide derivatives **K10**, **K15**, **K17, K18, K26**, **K27**, **K31**, **K32** bind selectively to A_3R, with moderate to low micromolar K_i values 4.49, 30.9, 4.16, 0.899, 5.07, 11.9, 44.3, 4.49 μM. Compared to **K15** the presence of the bulky iodine in the phenyl group in **K9** led to increase in A_1, A_3R affinity with K_i values 6.90, 4.13 μM, respectively compared to > μM, 30.0 μM respectively, in **K15**. Considering the structures of **K5**, **K17**, and **K18** with a 2-methyl-1,3-thiazole linked to the carboximidamide carbon, the presence of a chloro substituent in the phenyl ring of 3-phenyl-isoxazole favors A_3R selectivity. The measured K_i values for **K5** are 21.8, 9.45 μM for A_{2A}, A_3R while **K1** , **K18** have A_3R selectivity with K_i values 4.16, 0.899 μM respectively. The binding profile of compound **K5** is shown in **Figure 3.14**. The change of the pyridinyl nitrogen position from 2-, to 3-, to 4-positions in **K32**, **K10, K11** results in a small decrease for A_3R affinity, with a change of K_i value from 2.40, 4.49, 5.15 μM, and the appearance of a weak A_{2A}R affinity (K_i =30 μM). In the inactive derivative **3**, the monoaryl and biaryl groups are connected to the

carbonyloxycarboximidamide fragment in a transposed way. In the inactive aminomethylidenehydrazine-1-carboxamide analogue **K4** the carboxy group has been replaced by an urea fragment.

In addition, following MD simulations of compounds **K26, K27, K29-K34** and **K36-K39**, we observed that **K26** with o-diphenylcarbonyl instead of the phenyl-iosxazole-carbonyl bind also to A_3R with a K_i =5.07 μM and displayed a similar binding pose to that of **K5**. We also observed, compared to **K26, K27**, the p-substitution in compounds **K29** and **K36-38** was not favourable for binding. Addinitonal MD simulations results for this class of interesteting compounds will be presented in Chapters 4 and 5.

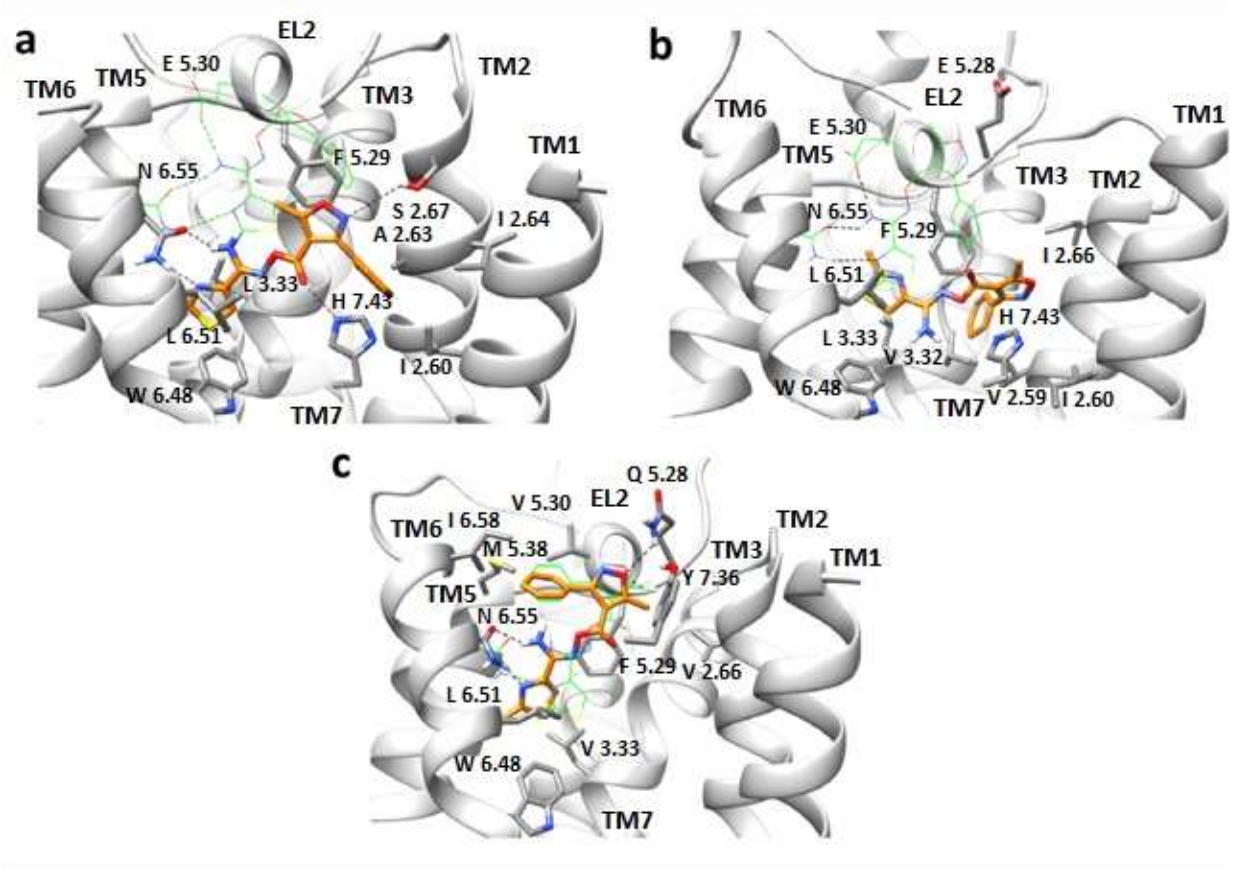

d

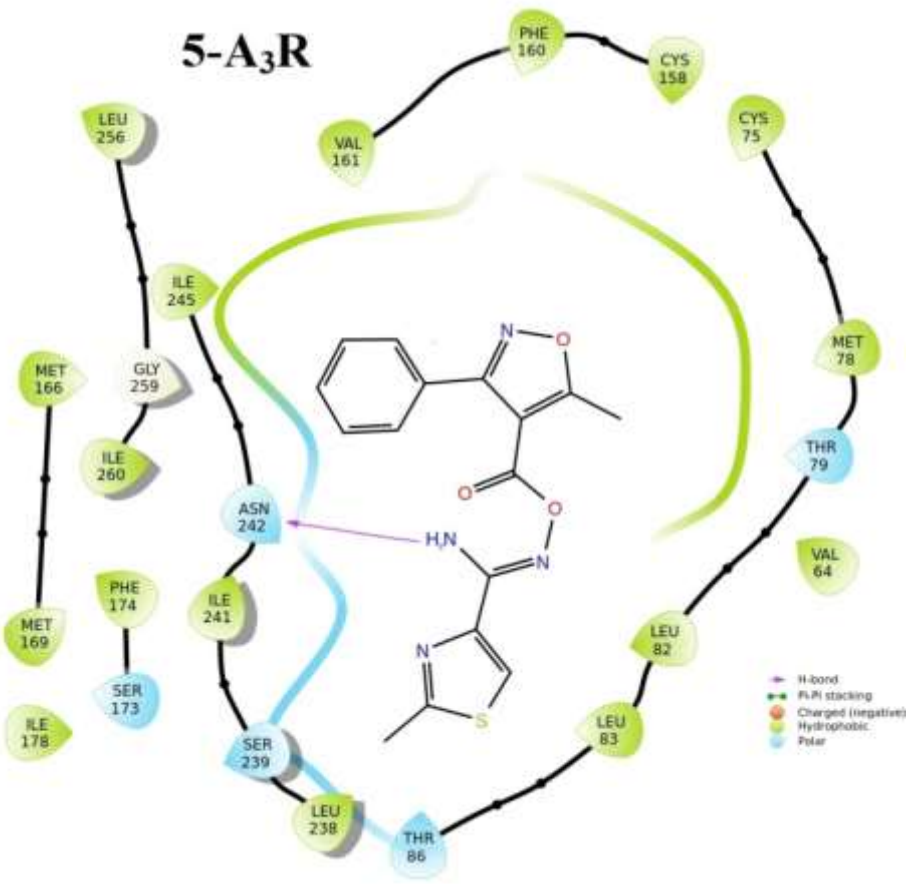

Figure 3.14 (a) Predicted binding of **K5** in the orthosteric binding area of the A_3R using docking calculations and MD simulations, with the docking pose being used as a starting structure. The ligand was stabilized inside the $A_{2A}AR$ binding area between TM5, TM6 and TM2, with its monoaryl group close to TM5 and the phenyl-isoxazolyl substituent close to TM2. (b) This area is wider and the ligand cannot bind tightly inside A_1R. (c) Binding of **K5** inside A_3R is highly favoured and the ligand engaged in many stabilizing interactions. In the depicted binding orientation the phenyl group of the 3-phenyl-isoxazole interacts through attractive van der Waals forces with the iPr side chain of V(5.30) and the isoxazole forms an aromatic π-π stacking interaction with the phenyl group of F(5.29). The amino group of the carbonyloxycarboximidamide fragment is H-bonded to the amide side chain of N(6.55). Nitrogen and oxygen atoms of the isoxazole ring can be hydrogen-bonded to the NH groups of F(5.29) or V(5.30). The thiazolyl group can be hydrogen-bonded to N(6.55) (see also panel d). Binding orientation of the ligand after the MD simulation is shown in yellow sticks and sidechains of some amino acids involved in ligand binding are displayed as gray sticks while the starting ligand and N(6.55)/E(5.30) side chain positions are shown in green wires. Hydrogen atoms are omitted except for those involved in hydrogen bond interactions, highlighted as black dashed lines.

Class E. Compound **K6** includes an urea group linked to 1,2-pyrazole and the docking poses shows that this molecule may bind to the $A_{2A}R$ or A_1R binding pocket with strong hydrogen bonding interactions. The urea group can form two hydrogen bonds with the E(5.30) carboxylate group and 1,2-pyrazole can form two hydrogen bonds with the N(6.55) amide side chain. The 1,2-pyrazole ring can be stabilized through π-π stacking interactions with F(5.29). The Ph(OCF_3) group is oriented towards TM2 and the thiophene ring is

oriented deep in the receptor favoring interactions with L(6.51). Similar interactions are suggested from docking poses against A_3R. However, the MD simulations show that the electronegative OCF_3 group can not be in vicinity with E(5.30) and the molecule can not rearrange its structure in order to allow favorable interactions, due to restricted motion of the urea fragment substituent, leading to unstable binding to A_{2A} and A_1R. This orientation is more favorable in A_3R with Ph(OCF_3) interacting with V(5.30) leading to the mediocre affinity with K_i = 30.6 μM. The docking calculations inside A_1 and A_{2A}R show hydrogen bonding interaction between the amino group of compound **K7** and the E(5.30) carboxylate and between the 4-carbonyl group of the ligand and the amino group of N(6.55) amide side chain. Similar hydrogen bonding interactions are also predicted between **K7** and N(6.55) inside A_3R. The sizeable $CO(CH_2)_2SPh(OMe)$ is oriented towards the solvent exposed area and this position is favored by the presence of V(5.30), which is in agreement with K_i = 18.3 μM, while it is unstable inside the A_1 and A_{2A}Rs due to the size of this group in accordance to the MD simulations. Compound **K8** includes an exocyclic amino group and a carbonyl of an ester group linked at 3,4-positions of 1,2-pyrazole. In compound **K8**, the pyrimidin-4-amine may form hydrogen bonds with E(5.30) and N(6.55), but the electronegative SO_2 makes the binding orientation unstable according to the MD simulations, possibly due to repulsive interactions (**Figure 3.15**).

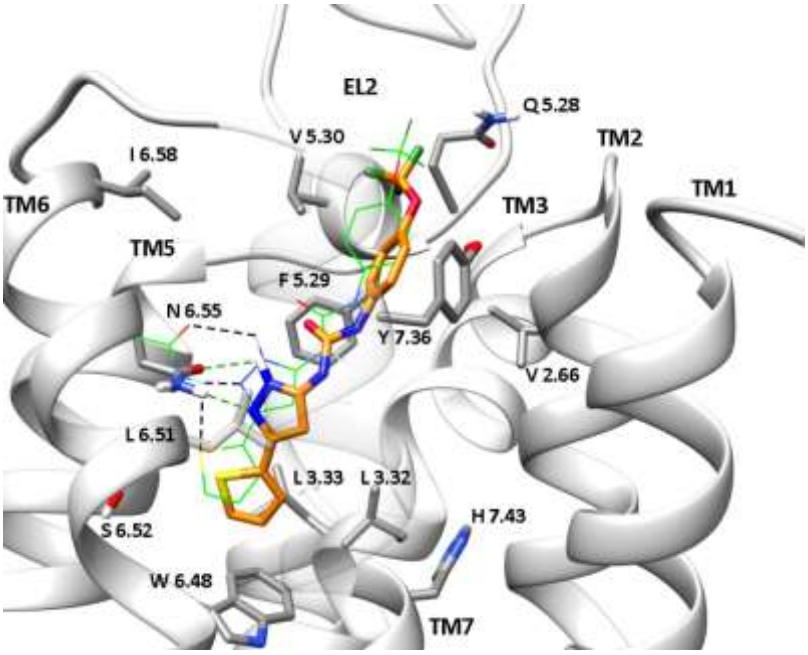

Figure 3.15 Predicted binding modes for ligand **K6** in the orthosteric site of the A_3R.

3.5.2.4 Measure of the AR-ligand complexes stability by MD simulations

Changes in vdW interactions due to variations of the structure of the ligand structure and of the orthosteric binding site (see **Figure 3.6**) may result in significant changes of hydrogen bonding and the overall strength of the binding interactions. Firstly, the MD simulations of the complexes showed whether the ligand remained or escaped from the orthosteric binding area. To quantify this, the RMSD of the ligand ($RMSD_{lig}$) was measured in respect to its docking pose coordinates (**Table 3.4**). For complexes where the ligand escapes from the orthosteric binding area, abolishing the combination of stabilizing H-bonding and van der

Waals interactions, the $RMSD_{lig.}$ values were in most of the cases ≥ 4 Å. In those cases where the ligand retained a binding orientation similar to the starting docking pose the $RMSD_{lig.}$ values were < 3 Å. It was observed that the former complexes correspond to the inactive compounds (K_i > 50 μM; see **Table 3.1**) and the latter complexes to compounds with a statistically significant experimental binding affinity ($K_i \leq 30$ μM; see **Table 3.1**).

Table 3.4 RMSD values of ligand ($RMSD_{ligand}$ for heavy atoms) and protein ($RMSD_{protein}$ for Ca carbons) from MD simulations for selected complexes of ligands **K1-K39**, **coll6, ZM241385, bara_4p, ZINC23192718, ZINC61843566, ZINC18155583,** with A_1, A_{2A}, and A_3Rs embedded in hydrated POPE bilayers using Desmond/OPLS2005 (20 ns).

Ligand	**A_1R**		**A_{2A}R**		**A_3R**	
	$RMSD_{protein}$	**$RMSD_{ligand}$**	**$RMSD_{protein}$**	**$RMSD_{ligand}$**	**$RMSD_{protein}$**	**$RMSD_{ligand}$**
K1 [1,2]	1.23	4.62	1.40	2.18	1.97	2.22
K2 [1]	1.77	9.21	1.49	3.97	1.11	2.18
K3	1.63	4.50	3.74	5.43	3.10	5.37
K4	2.20	4.42	4.29	5.35	2.50	8.60
K5 [1,2,3]	1.20	4.19	1.15	3.92	1.15	2.27
K6 [1]	1.60	4.27	3.25	5.48	1.10	2.81
K7 [1]	2.77	4.14	3.56	4.25	1.13	3.05
K8	4.20	5.68	3.70	5.81	3.73	4.09
K12 [1]	1.81	4.29	3.22	4.57	1.25	2.38
K13 [1]	2.57	5.44	2.69	4.21	1.86	2.90
K14 [1,2]	3.28	6.58	2.81	4.82	1.08	2.78
K21 [1]	1.61	4.93	1.90	1.18	1.51	2.17
K22 [1,2,3]	1.28	2.21	1.35	3.11	1.65	2.41
K16 [1]	3.30	4.20	1.53	2.42	1.25	2.62
K24 [1]	1.53	2.83	1.35	5.40	1.32	2.75
K23 [1]	1.41	1.70	1.31	2.07	1.80	2.53
K20 [1,2,3]	1.32	2.70	1.27	2.28	2.23	2.75
K25 [1]	1.27	4.53	1.22	5.47	1.25	2.30
K19	3.03	4.71	3.59	4.22	2.13	4.58
K15 [1]	3.25	4.66	2.87	4.48	1.47	2.70
K9 [1]	1.17	2.05	3.10	4.97	1.32	2.36
K10 [1]	2.62	3.77	2.92	3.55	1.21	2.51
K11 [1]	2.18	3.92	2.68	2.63	1.35	2.43
K17 [1]	2.33	4.09	2.11	3.76	0.82	2.24
K18 [1]	2.47	5.57	2.23	4.67	0.95	2.32
K35 [1]	1.80	2.80	1.30	4.10	1.40	2.24
K28 [1]	2.50	2.20	1.40	5.20	1.95	4.10
coll6 [1]	1.23	4.02	1.90	4.28	1.15	1.52
ZM241385 [1]	1.77	3.55	1.35	1.85	1.10	5.53
jaco_psb11 [1]	1.63	0.62	1.53	3.85	1.13	3.95
ZINC23192718 [1]	2.20	-[4]	1.35	4.23	3.73	-[4]
ZINC61843566 [1]	1.20	-[4]	1.31	3.88	1.25	-[4]

ZINC18155583 [1]	1.53	-[4]	2.81	4.13	1.86	-[4]
bara_4p [1]	1.41	1.19	1.90	1.47	1.08	0.82

[1] 10 ns or 100 ns. [2] MD simulations for ligands **K1-K39, coll6, ZM241385, jaco_psb11, bara_4p** with A_1 or A_{2A} or A_3R and **ZINC23192718, ZINC61843566, ZINC18155583** with A_{2A}R embedded in hydrated POPE bilayers using Desmond/OPLS2005 (for the chemical structure of **coll6, jaco_psb11, bara_4p**, **ZINC23192718, ZINC61843566, ZINC18155583**, see **Katritch, Kufareva, and Abagyan 2011b**). 100 ns MD simulations for potent ligands complexes **K1**-A_{2A}, **K1**-A_3, **K5**-A_{2A}, **K5**-A_3, **K22**-A_{2A}, **K13**-A_3, **K20**-A_{2A}, **K20**-A_1, **K20**-A_3 complexes embedded in hydrated POPE bilayers using Amber/ff14SB. [3] Complexes of ligands **K5**, **K22**, **K20** using Moro or Katritch-Abagyan homology models converge to the same structure. [4]MD simulations of ligands **ZINC23192718, ZINC61843566, ZINC18155583** in complex with A_1 and A_3R were not tested.

We also selected a set of three ligands each being selective against A_1R (coll6), A_{2A}R (ZM241385) and A_3R (jaco_psb11) found in ref. [4]. After docking using Gold against these AR subtypes, it was found that these compounds also docked well inside the binding area of every AR. The MD simulations resulted in a binding orientation similar to the docking pose, only for the AR to which the ligand is selective ($RMSD_{lig}$ < 1.5 Å) while in any other case the ligand escaped from the binding area ($RMSD_{lig}$ ≥ 4 Å) (**Table 3.4** and **Figures 3.16-3.19**). Similarly, compounds ZINC23192718, ZINC61843566, and ZINC18155583, which are decoys for A_{2A}R, produced plausible docking poses but during the short MD simulation the ligands escaped from the A_{2A}R binding area. However, when bara_4p or veld_7 in ref. [4] were tested for their binding to A_1, A_{2A} and A_3 it was found that they docked well inside the binding area of the different ARs and that binding orientation of the starting docking pose was retained during the MD simulations for all the complexes despite the fact that bara_4p was A_3R selective and veld_7 was A_1R selective (**Table 3.4**).

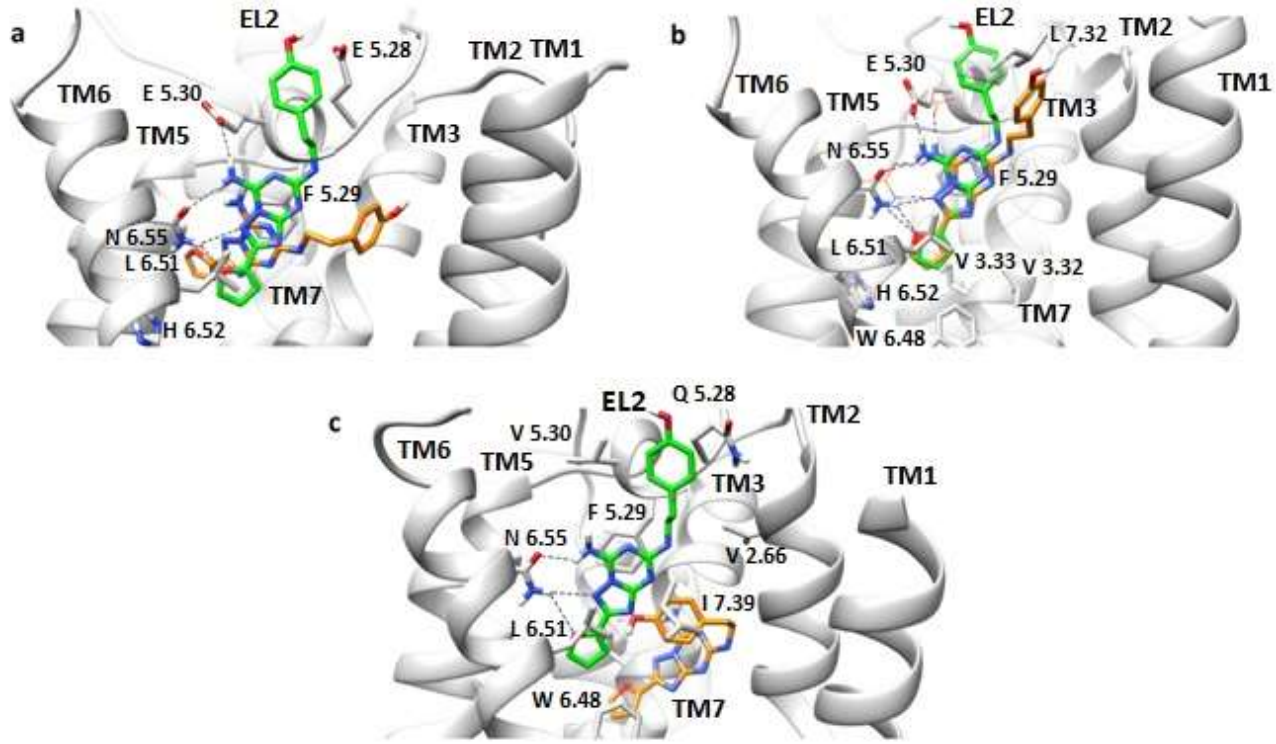

Figure 3.16 (a)-(c) MD simulation (ligand in orange sticks) of the docking pose (ligand in green sticks) of selective A_{2A}R ZM241385 against A_1, A_{2A} and A_3Rs respectively after 10 ns. Side chains of some amino acids involved in ligand binding are displayed as gray sticks. Hydrogen atoms are not displayed except those which are involved in hydrogen bond interactions and are highlighted as black dashed lines.

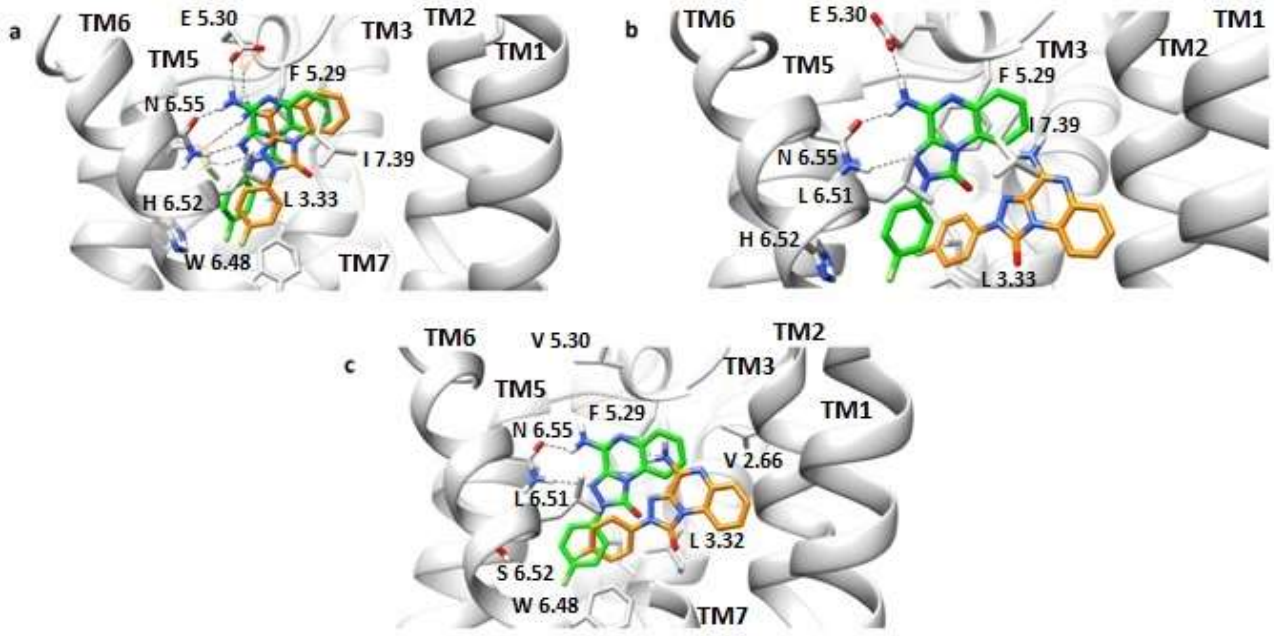

Figure 3.17 (a)-(c) MD simulation (ligand in orange sticks) of the docking pose (ligand in green sticks) of selective A_1R coll6 against A_1, A_{2A} and A_3Rs respectively after 10 ns. Side chains of some amino acids involved in ligand binding are displayed as gray sticks. Hydrogen atoms are not displayed except those which are involved in hydrogen bond interactions and are highlighted as black dashed lines.

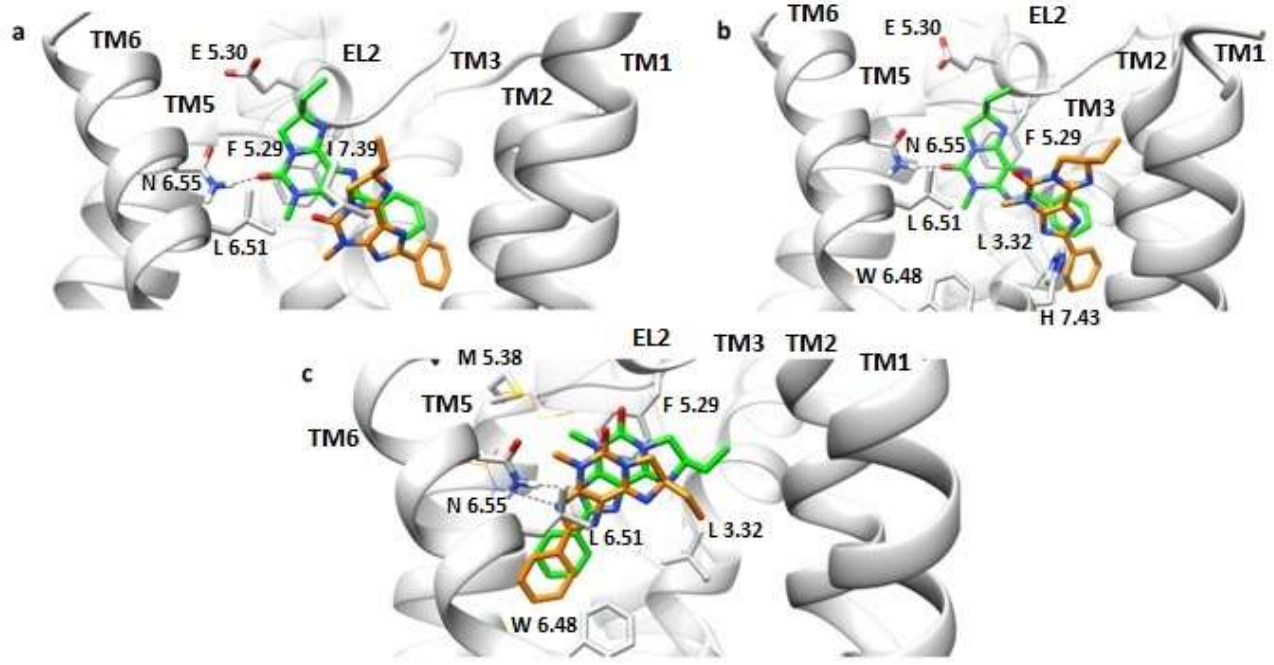

Figure 3.18 (a)-(c) MD simulation (ligand in orange sticks) of the docking pose (ligand in green sticks) of selective A_3R jaco_psb11 against A_1, A_{2A} and A_3Rs respectively after 10 ns. Side chains of some amino acids involved in ligand binding are displayed as gray sticks. Hydrogen atoms are not displayed except those which are involved in hydrogen bond interactions and are highlighted as black dashed lines.

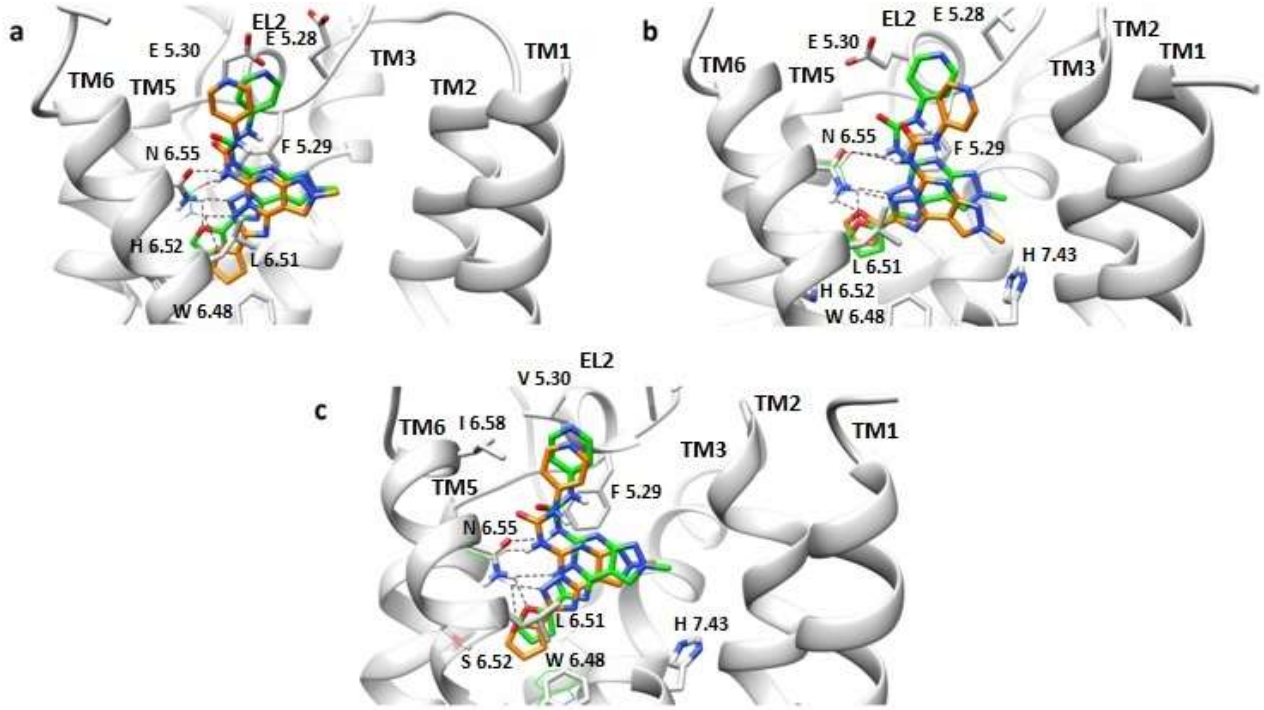

Figure 3.19 (a)-(c) MD simulation (ligand in orange sticks) of the docking pose (ligand in green sticks) of selective A_3R bara_4p (see ref [4]) against A_1, A_{2A} and A_3Rs respectively after 10 ns. Side chains of some amino acids involved in ligand binding are displayed as gray sticks. Hydrogen atoms are not displayed except those which are involved in hydrogen bond interactions and are highlighted as black dashed lines.

As is shown above, if a ligand is observed to stay bound inside the binding site through MD simulations, it still may not be potent because its interactions still are not sufficiently favorable. A ligand which escapes from the binding area devoids of biological potency. A potent ligand always adopts a stable binding orientation. This exact behavior was observed during the MD simulations of the particular set of ligands used in this work. The results of the procedure followed in this work which is based on $RMSD_{lig}$ were consistent with binding behavior of the compounds **K1-K39**. This procedure is not suggested as generally applicable to predict or explain potency to other systems. The in silico quantitative assessment of the experimental binding affinities needs the application of computational binding free energy methods.

3.6 Conclusions

Pharmaceutical companies and academic research laboratories are involved in intense efforts to identify antagonists with selectivity for each adenosine receptor (AR) subtype as potential clinical candidates for "soft" treatment of different diseases. A_{2A}R antagonists can be useful for treating cancer, central nervous system (CNS) disorders; A_1R antagonists can provide kidney-protective agents, anti-asthmatic and CNS

agents; A_3R antagonists are promising for therapeutic applications in asthma, glaucoma and A_{2B}R antagonists for diabetes, asthma and chronic obstructive pulmonary disease.

The reported crystal structures of A_{2A}R in complex with agonists or antagonists [20,30,34,52,155,156] and of A_1R with an antagonist, [32,35] along with other advances attributed to the progress of GPCR crystallography [154] have made structure-based approaches an attractive strategy for drug design against adenosine receptors which are pharmaceutically important targets. The A_{2A}R is one of the best studied receptors of all class A GPCRs. Additionally, among the 688 known GPCRs, class A is the 7th more intensely investigated. The application of virtual screening and medicinal chemistry studies for a few decades now has resulted in a high number of bioactive compounds (~ 11000) against A_{2A}R as was retrieved from ChEMBL20.

In the present study, we performed virtual screening of a small Maybridge library of 14400 compounds against A_{2A}R, using its crystallographic structure in complex with the antagonist ZM241385, through a combination of structure-based and ligand-based procedures. After docking, the ligand poses were re-scored by applying CHARMM energy minimization and consideration of desolvation energy electrostatics using the Poisson-Boltzmann equation. Out of the eight selected and tested compounds, three showed micromolar affinity for the A_{2A} and A_3Rs and two were low micromolar binders only to the A_3R receptor. Thus, although initially targeting the A_{2A}R, the project resulted in the following percent of successful binder hits: 25% for A_{2A} and 63% for A_3R.

In a second step, based on the structure of mainly two promising active hits, possessing a 2-amino-thiophene-3-carboxamide and a carbonyloxycarboximidamide chemotype respectively, 19 more compounds were selected by similarity for testing. For this second series of 19 compounds, 17 were found to bind to the ARs family. Thus, of particular interest are 2-amino-thiophene-3-carboxamides, the 3-acylamino-5-aryl-thiophene-2-carboxamides, and carbonyloxycarboximidamide derivatives which were selective and possess a micromolar to low micromolar affinity for the A_3R. Eight of those revealed A_3-selective affinity with K_i values in the micromolar to low micromolar regime. We then focused more on the carbonyloxycarboximidamide chemotype and in particular on **K18** (O4-{[3-(2,6-dichlorophenyl)-5-methylisoxazol-4-yl]carbonyl}-2-methyl-1,3-thiazole-4-carbohydroximamide) with low micromolar binding affinity to A_3R and we purchased and tested additional 12 analogs including mainly compounds that bear a biphenyl instead of 3-phenyl-isoxazole.

The 39 tested molecules resulted in similar docking poses against A_1, A_{2A}, A_{2B} or A_3Rs. Using the docking poses of the ligands as starting structures, the performance of hundreds of 20ns-molecular dynamics (MD) simulations, using Desmond/OPLS2005, allow the differentiation of stable and unstable docking poses based on the RMSD values of the displacement of the ligand from its starting docking pose inside the orthosteric binding area. Generally, stable or unstable docking poses agree with the experimental results of radiolabelled values of binding affinity. The stability of the stable complexes were further tested using 100ns-MD simulations with Desmond/OLPS2005 and Amber/ff14sb provided the basic features of the binding interactions with A_1, A_{2A}, and A_3Rs for compounds exhibiting affinity.

The MD simulations show the basic features of the binding interactions with A_1, A_{2A}, and A_3Rs for compounds exhibiting affinity. The complexes with A_{2A} and A_1Rs were stabilized through hydrogen bonding interactions between an amino or amido group of the ligand and N(6.55) of the AR. E(5.30) can be involved also in hydrogen bonding interactions with the bound ligand. A_{2A}R ligands include a lipophilic bulky substituent which was oriented towards the extracellular area, close to EL2 and TM7, and a smaller lipophilic group which was fitted deep in the binding region, close to L(6.51) and H(6.52). Similar interactions have been described in the X-ray structures between antagonists and A_{2A}R. [20,30,52] Interestingly, for the A_1R ligands the ligand covers a larger space between TM5/TM6 and TM1/TM2, as shown in the recent X-ray structure between an antagonist and A_1R. [32] Many of the ligands studied in this report, i.e. **K1, K2 K5-K7, K9-K14, K16, K18, K20-K27, K31, K32, K35**, bind to A_3R. We suggest that selectivity against

A_3R is boosted by increasing the size and lipophilicity of a suitable substituent reflecting a better fit with V(5.30). Compounds **K6**, **K7, K10, K12-K15, K17, K18, K25, K27, K31, K32** are selective binders to A_3R. These findings are in line with the previously published results on highly selective A_3R agonists and antagonists with a bulky group in a compatible position, e.g. the introduction of a 3-iodo-benzyl group in N^6 position in 2-Chloro-N^6-(3-iodobenzyl)-adenosine-5′-N-methyluronamide (Cl-IB-MECA) increases the affinity of this adenosine derivative for A_3R.

Relatively novel chemotypes of ARs ligands were identified with low T_c values (< 0.17) compared to the known ARs ligands: (a) The 2-amino thiophene-3-carboxamide (2-NH_2 and 3-CONHR; class A) thiophenes with low micromolar affibity to $A_{2A}R$ and A_3R. (b) The 3-acylamino-5-aryl-thiophene-2-carboxamides (class B) including the new substitution pattern (2-$CONH_2$ and 3-NHCOR) of the thiophene ring, which -compared to 2-NH_2 and 3-CONHR' substitution pattern- enhances the affinity for A_1R and A_3R. (c) The carbonyloxycarboximidamide derivatives (class D), many having selective A_3R affinity.

We consider these findings to be an important contribution to the field of structure-based drug design against ARs. This reserach provides also a valuable example, showing that the *in silico* screening of a small library against a receptor family can lead to novel hits, when a careful methodology for the ranking of the ligands' as regards receptor's affinity is applied (**Figures 2.5, 3.3**).

Chapter 4

Pharmacological Characterization of Novel Adenosine Receptor A_3R Antagonists

4.1 Theoretical Background

4.1.1 Fluorescence Resonance Energy Transfer

Förster Resonance Energy Transfer or Fluorescence Resonance Energy Transfer (FRET) is a mechanism that describes the energy transfer between two light-sensitive molecules or molecules-chromophores [218]. A donor chromophore, initially in its electronic excited state, transfers energy to an acceptor chromophore group via the non-radiative dipole-dipole coupling [219]. The FRET mechanism is extremely sensitive to the small distance changes, due to the fact that the efficiency of this energy transfer is inversely proportional to the 6^{th} power of the donor-acceptor distance [220]. The FRET measurement efficiency can be used to determine if two fluorophores are within a certain distance of each other or not [221]. A typical example of FRET is presented in the **Figure 4.1**. **BRET** (Bioluminescence Resonance Energy Transfer) is based on FRET methodology but it uses a bioluminescent enzyme (usually luciferase) in order to produce the photon emission signal.
An example of a fluorescent molecules is CA200645, a high affinity AR xanthine amine congener (XAC) derivative containing an oligoamide linker connected to the BY630 fluorophore, which acts as a fluorescent antagonist at both A_1R and A_3R with a slow off-rate (Koff) [222].

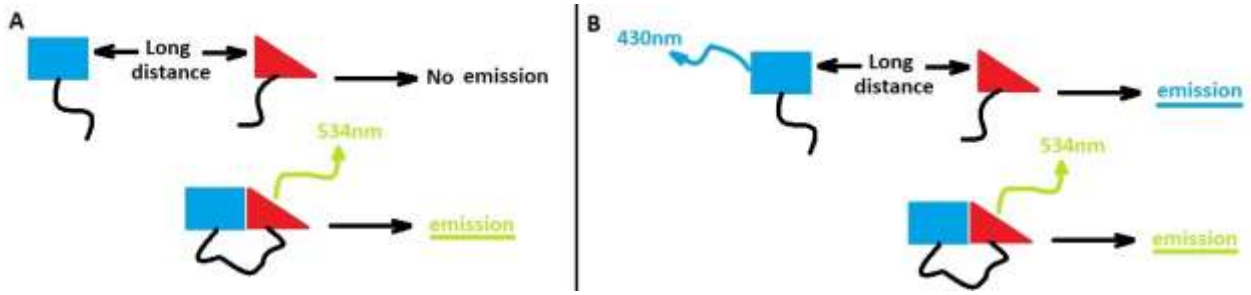

Figure 4.1 Figures (A) and (B) represent two typical FRET cases. The first one, when the two chromophores are separated with a long distance, no emission is observed. After coming closer, green light is observed. At the second case (B), the one of the chromophore's wavelength, here 430 nm shown as blue light, change after the binding to the other, into green, i.e. the wavelength shifts towards the 534 nm. In case (A) the donor chromophore is shown with a blue rectangle and the aceptor chromophore is shown with a red triangle; (B) the inverse stands for case (B).

4.1.2 cAMP accumulation assay

The cAMP detection is based on the competition between cAMP, which is generated within the cells, and a synthetic cAMP bound to a biotin-group. The latter works as a probe that is recognized by streptavidin molecules (donors) and the anti-cAMP antibody (acceptor) that is placed on beads of streptavidin. The beads are brought into proximity and the biotin-streptavidin complex formation produces a signal. Increased intracellular concentrations of cAMP following G_s-coupled GPCR activation by an agonist results in the displacement of the biotinylated cAMP probe and leads to a proportional signal decrease **(Figure 4.2)**. The effect of antagonists and reverse agonists can similarly be detected. G_i-coupled receptor activation can be detected after pre-stimulating cells with forskolin which active adenylyl cyclase. The cAMP signal concentration generally can be measured with fluorescence, luminescence, or radioactive-based assays.

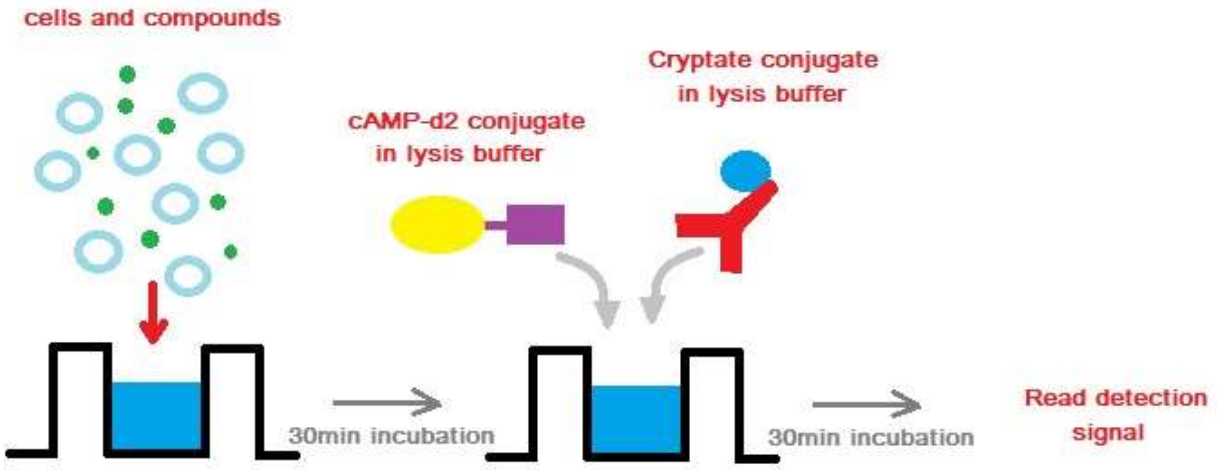

Figure 4.2 Figure that descibes schematically cAMP accumulation assay. The assay is based on the detection and the conjugation of the streptavidin (d-donor) by the biotin bound ob the antibody. The antibody when is bound to the cAMP-streptavidin brings the biotin and streptavidin together and this complex formation creates the detection signal.

The LANCE kit, developed by Perkin Elmer, was used for the cAMP accumulation measurements in this thesis. The applied procedure, is based on the disruption of the FRET complex, formed between a fluorescent Europium (Eu) chelator linked to the biotinylated-cAMP molecule, though a streptavidin–biotin interaction. Alternatively, in the case of the LANCE® ultra version of standard kit, it can be applied a direct covalent linking of the Eu chelator with cAMP and a fluorescently labeled anti-cAMP antibody [223]. In the absence of unlabeled cAMP, the FRET complex readily forms and maximal FRET is achieved. In the presence of cAMP, the FRET complex is disrupted by unlabeled cAMP competition with biotinylated-cAMP at the anti-cAMP antibody binding site, and FRET is significantly reduced. Therefore, the concentration of cAMP produced by adenylyl cyclase is proportional to FRET output along a sigmoidal cAMP competition curve [223].

4.1.3 Phospho-ERK assay

The Phospho-ERK assay is based on HTRF® (Homogeneous Time Resolved Fluorescence) which is the most frequently used generic assay technology to measure analytes in a homogenous format. This technology combines FRET with time-resolved measurement (TR) [224]. In TR-FRET assays, a signal is generated through fluorescent resonance energy transfer between a donor and an acceptor molecule when they come adjacent to each other. The final signal is proportional to the extent of product formation [224]. Generally, HTRF

techniques are characterized by noteworthy sensitivity and robustness for the molecular interactions detection.
The extracellular signal-regulated kinases (ERKs) are key components of multiple important cell signaling pathways regulating diverse biological responses. This signaling is characterized by phosphorylation cascades leading to ERK1/2 activation and promoted by various cell surface receptors including GPCRs and receptor tyrosine kinases (RTKs) [225]. Principle of HTRF®-based phospho-ERK assay consists of three experimental steps: activation, cell lysis, and HTRF detection to quantify the total ERK1/2 as well as the phosphorylation of ERK1/2 mediated by the major cell surface receptors (**Figure 4.3**).

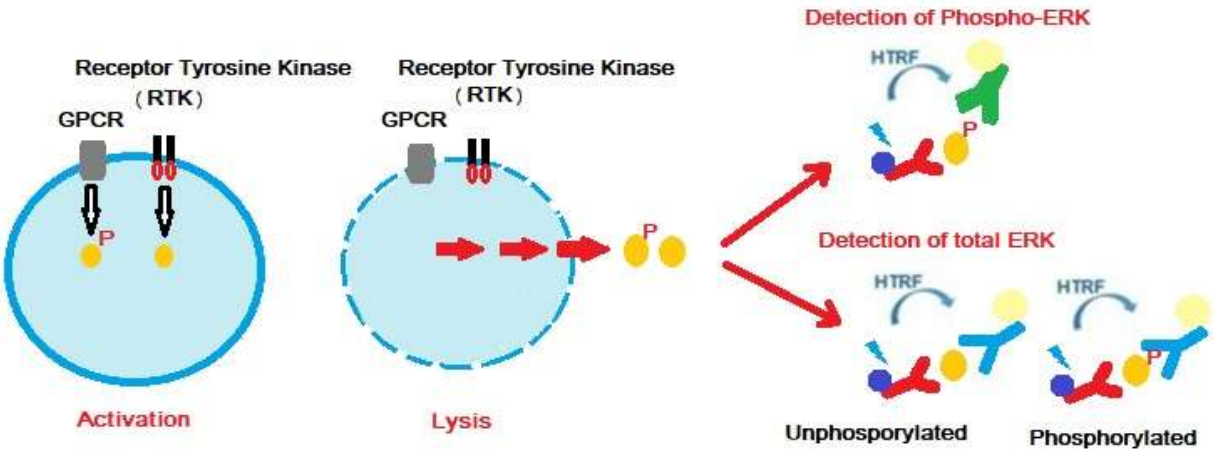

Figure 4.3. The principle of the Phospho-ERK technique. The phospho-groups (shown in image with "P") produced by the Kinases (here the Receptor Tyrosine Kinase) are strongly bound to the antibodies. The two antibodies' simultaneous interaction leads to a FRET between the Europium group (Europium cryptate) carried on the first antibody and the sensitized, d2, covalently bound on the second antibody. The emission at 665nm follows as the assay's signal.

4.2 Purpose of the work

The A_3R is involved in a range of pathologies including cardiovascular, neurological and tumour-related diseases. Unsurprisingly therefore, A_3R is a pharmaceutical target. Interestingly, the A_3R has been described as enigmatic, whereby many of the effects attributed to A_3Rs are contradictory [62]. Despite this, A_3R antagonists having been described as potential treatments of asthma, chronic obstructive pulmonary disease (COPD) and glaucoma, [226,227] continuous research into both agonists and antagonists at the A_3R are warranted. While a number of novel potent and selective A_3R antagonists have been previously described [199,228,229], one of the challenges associated with the druggability of the AR family has been the targeting of individual subtypes with sufficient specificity to limit off-target side effects [73].
Although all AR members are activated by the endogenous agonist adenosine the $A_{2A}R$ and $A_{2B}R$ are predominantly G_s-coupled whereas A_1R and A_3R generally couple to $G_{i/o}$. This classical pathway following A_3R activation and $G_{i/o}$ coupling is the inhibition of adenylyl cyclase (AC) results in a decrease in cAMP levels, although extracellular signal-regulated kinase 1/2 (ERK1/2) activation has also been described [45].
The A_1R and $A_{2A}R$ are two of the best structurally characterised G protein-coupled receptors (GPCRs), with multiple structures available for both [15,32,35,47,54], although the A_3R structure is yet to be resolved. The limited

availability of diverse high-resolution structures of the A_3R bound to pharmacologically distinct ligands has meant there is a discrepancy between the capability to predict compound binding versus pharmacological behaviour [230]. With this in mind, the potential antagonists (**K1-K25, K28** and **K35**) [61] and some newly identified potential antagonists (**K26, K27, K29-K34** and **K36-K39**) were pharmacologically characterised using A_3R-mediated inhibition of cAMP accumulation. We identified a potent and selective A_3R antagonist, **K18** (O4-{[3-(2,6-dichlorophenyl)-5-methylisoxazol-4-yl]carbonyl}-2-methyl-1,3-thiazole-4-carbohydroximamide) and, using MD simulations combined with site-directed mutagenesis, elude its potential binding site. Kinetic binding experiments of **K5, K17** and **K18** using a bioluminescence resonance energy transfer (BRET) method combined with functional assays led to the identification of important structural features of **K18** for binding and activity. Further evaluation of this compound (and structurally related analogues) may afford a novel therapeutic benefit in pathologies such as inflammation and asthma.

4.3 Methods

4.3.1 Cell culture and Transfection

Cell lines were maintained using standard subculturing routines as guided by the European Collection of Cell Culture (ECCC) and checked annually for mycoplasma infection using an EZ-PCR mycoplasma test kit from Biological Industries (Kibbutz Beit-Haemek, Israel). All procedures were performed in a sterile tissue culture hood using aseptic technique and solutions used in the propagation of each cell line were sterile and pre-warmed to 37 ºC. All cells were maintained at 37 °C with 5% CO_2, in a humidified atmosphere. CHO-**K1**-A_1R or CHO-**K1**-A_3R cells were routinely cultured in Hams F-12 nutrient mix (21765029, Thermo Fisher Scientific) supplemented with 10% Foetal bovine serum (FBS) (F9665, Sigma-Aldrich). Flp-In-CHO cells purchased from Thermo Fisher Scientific (R75807) were maintained in Hams F-12 nutrient mix supplemented with 10% FBS containing 100 µg/mL Zeocin™ Selection Antibiotic (Thermo Fisher Scientific).

Stable Flp-In-CHO cell lines were generated through co-transfection of the pcDNA5/FRT expression vector (Thermo Fisher Scientific) containing the gene of interest and the Flp recombinase expressing plasmid, pOG44 (Thermo Fisher Scientific). Transfection of cells seeded in a T25 flask at a confluency of ≥80% was performed using TransIT®-CHO Transfection Kit (MIR 2174, Mirus Bio), in accordance with the manufacturer's instructions. Here, a total of 6 µg of DNA (receptor to pOG44 ratio of 1:9) was transfected per flask at a DNA:Mirus reagent ratio of 1:3 (w/v). Post-transfection, selection using 600 µg/mL hygromycin B (Thermo Fisher Scientific), concentration determined through preforming a kill curve, was performed for two days prior to transferring the cells into a fresh T25 flask. Stable Flp-In-CHO cell lines expressing the receptor of interest were selected using 600 µg/mL hygromycin B whereby the media was changed every two days. Successful mutant cell line generation for non-signalling mutants was confirmed by Zeocin™ sensitivity (100 µg/mL).

4.3.2 Constructs

The human A_3R originally in pcDNA3.1+ (ADRA3000000, cdna.org) was cloned into the pcDNA5/FRT expression vector and co-transfected with pOG44 to generate a stable Flp-InCHO cell line. Mutations within the A_3R were made using the QuikChange Lightening SiteDirected Mutagenesis Kit (Agilent Technologies)

in accordance with the manufacturer's instructions. All oligo-nucleotides used for mutagenesis were designed using the online Agilent Genomics 'QuikChange Primer Design' tool and purchased from Merck. All constructs were confirmed by in-house Sanger sequencing.

4.3.3 Compounds

Adenosine, NECA, IB-MECA, and MRS 1220 (N-[9-chloro-2-(furan-2-yl)-[1,2,4]triazolo[1,5-c]quinazolin-5-yl]-2-phenylacetamide) were purchased from Sigma-Aldrich and dissolved in dimethyl-sulphoxide (DMSO). Compounds under investigation were purchased from emolecules and dissolved in DMSO.

4.3.4 cAMP accumulation assay

For cAMP accumulation ($A_{2A}R$ and $A_{2B}R$) or cAMP formation inhibition (A_1R or A_3R) experiments, cells were harvested and re-suspended in stimulation buffer (PBS containing 0.1% BSA and 25 μM rolipram) and seeded at a density of 2,000 cells per well in a white 384-well Optiplate and stimulated for 30 min with a range of agonist concentrations. In order to allow the A_1R/A_3R mediated Gi/o response to be determined, co-stimulation with forskolin, an activator of adenylyl cyclase [231], at the indicated concentration (depending on cell line) was performed. For testing the potential antagonists, cells received a co-stimulation stimulated with forskolin, agonist and compound/DMSO control. cAMP levels were then determined using a LANCE® cAMP kit as described previously [232]. In order to reduce evaporation of small volumes, the plate was sealed with a ThermalSeal® film (EXCEL Scientific) at all stages.

4.3.5 Phospho-ERK assay

ERK1/2 phosphorylation was measured using the homogeneous time resolved fluorescence (HTRF)® Phospho-ERK (T202/Y204) Cellular Assay Kit (Cisbio Bioassays, Codolet, France) two-plate format in accordance with the manufacturer's instructions. A_3R expressing Flp-InCHO were seeded at a density of 2,000 cells per well in a white 384-well Optiplate and stimulated with agonist and test compounds for 5 min at 37°C. Plate reading was conducted using a Mithras LB 940 (Berthold technology). All results were normalised to 5 min.stimulation with 1 μM PMA, a direct protein kinase C (PKC) activator. To determine if the measured pERK1/2 level was Gi-mediated, we treated cells with Pertussis toxin (PTX) (Tocris Biosciences) for 16 h at 100 ng/mL prior to pERK assay.

4.3.6 Radioligand Binding

The radioligand binding measurements were performed with the procedures described in paragraphs 2.3.1.6 and 2.3.1.7.

4.3.7 Determination of the association rate and dissociation rate constants for A_3R antagonists

Through the use of NanoBRET, real-time quantitative pharmacology of ligand-receptor interactions can be investigated in living cells. CA200645, a high affinity AR xanthine amine congener (XAC) derivative containing a polyamide linker connected to the BY630 fluorophore, acts as a fluorescent antagonist at both A_1R and A_3R with a slow off-rate [222]. Using a N-terminally NanoLuc (Nluc)-tagged A_3R expressing cell line, competition binding assays were performed. The kinetic data were fitted with the 'kinetic of competitive binding' model [233] to determine affinity (pK_i) values and the association rate constant (k_{on}) and dissociation rates (k_{off}) for unlabelled A_3R antagonists. This model resulted in several cases in an ambiguous fit [234]. We developed a new model which expands on the 'kinetic of competitive binding' model to accommodate very rapid competitor dissociation, assuming the unlabelled ligand rapidly equilibrates with the free receptor. This method allows determination of compound affinity (pK_i) from the kinetic data.
Filtered light emission at 450 nm and > 610 nm (640-685 nm band pass filter) was measured using a Mithras LB 940 and the raw BRET ratio calculated by dividing the 610 nm emission with the 450 nm emission. Here, Nluc on the N-terminus of A_3R acted as the BRET donor (luciferase oxidizing its substrate) and CA200645 acted as the fluorescent acceptor. CA200645 was used at 25 nM, as previously reported [235]. BRET was measured following the addition of the Nluc substrate, furimazine (0.1 µM).

4.3.8 Receptor binding kinetics data analysis

Specific binding of tracer vs time data was analyzed using the Motulsky and Mahan method [233] to determine the test compound association rate constant and dissociation rate constant. Data were fit to the "Kinetics of competitive binding" equation (1) in Prism 8.0 [150]

$$[RL]_t = \frac{N[L]k_1}{K_F - K_S}\left[\frac{k_4(K_F - K_S)}{K_F K_S} - \frac{k_4 - K_S}{K_S}e^{-K_S t} + \frac{k_4 - K_F}{K_F}e^{-K_F t}\right] \quad (1)$$

where

$$K_F = 0.5\left\{K_A + K_B + \sqrt{(K_A - K_B)^2 + 4[L][l]k_1k_3}\right\} \quad (2)$$

$$K_S = 0.5\left\{K_A + K_B - \sqrt{(K_A - K_B)^2 + 4[L][l]k_1k_3}\right\} \quad (3)$$

$$K_A = [L]k_1 + k_2 \quad (4)$$

$$K_B = [l]k_3 + k_4 \quad (5)$$

In equations (1)-(5), [RL]$_t$ is specific binding at time t, N is the B_{max}, $[L]$ is the tracer concentration, $[l]$ is the unlabelled competitor compound concentration, k_1 is the tracer association rate constant, k_2 is the the tracer

dissociation rate constant, k_3 is the compound association rate constant and k_4 is the compound dissociation rate constant. Equation (1) assumes rapid equilibration between compound and receptor and consequently provides an estimate of the equilibrium binding affinity of the compound (K_i), but not the binding kinetics of the compound. To estimate the binding kinetics we applied equation (6)

$$[RL]_t = \frac{N[L]k_1(1-\rho_l)}{k_{obs,+l}} 1 - e^{-k_{obs,+l}t} \quad (6)$$

where ρ_l is frantional occupancy of receptors not bound by L as defined in equation (7)

$$\rho_l = \frac{[l]}{K_l + [l]} \quad (7)$$

and $k_{obs,+l}$ is the observed association rate of trancer in the presence of competitor, defined according to equation (8)

$$k_{obs,+l} = [L]k_1(1-\rho_l) + k_2 \quad (8)$$

The fits to the two equations were compared statistically using a partial F-test in Prism 8 [236].

4.3.9 Data and Statistical analysis of biological experiments

All in vitro assay data was analyzed using Prism 8.0 [150], with all dose-inhibition or response curves being fitted using a three-parameter logistic equation to calculate response range E_{max} and IC_{50}/EC_{50}. Dose-inhibition/dose-response curves were normalised to forskolin response or forskolin inhibition (A_1R or A_3R), relative to NECA or IB-MECA, respectively. In the case of pERK1/2 response, normalization was performed to PMA.

Schild analysis was performed to obtain pA_2 values (the negative logarithm to base 10 of the molar concentration of an antagonist that makes it necessary to double the concentration of the agonist to elicit the original sub-maximal response obtained by agonist alone **(Schild, 1947)** for the potential antagonists. In cases where the Schild slope did not differ significantly from unity, the slope was constrained to unity giving an estimate of antagonist affinity (pK_B). pA_2 and pK_B coincide when the slope is exactly unity. The pA_2 values obtained through conducting Schild analysis of **K18** against WT and mutant A_3Rs were compared in order to indicate important residues involved in **K18** binding.The data and statistical analysis comply with the recommendations on experimental design and analysis in pharmacology [238]. Statistical significance (*, p< 0.05; **, p<0.01; ***, p<0.001; ****, p<0.0001) was calculated using a one-way ANOVA with a Dunnett's post-test for multiple comparisons or Students't-test, as appropriate. Compounds taken forwards for further experiments after initial screening were identified as having the highest statistical significance (P value of 0.001 (***) or <0.0001 (****)). All statistical analysis was performed using Prism 8.0 on data which were acquired from experiments performed a minimum of five times, conducted in duplicate.

.

4.3.10 MM-PBSA calculations

Essentials for the background for MM-MBSA or MM-GBSA methods are decribed in 5.1.1. Binding free energies of the complexes between **K5, K17** and **K18** and A_3R were calculated by the 1-trajectory MM-PBSA approach [239]. Effective binding energies (ΔG_{eff}) were computed considering the gas phase energy and solvation free energy contributions to binding. For this, structural ensembles were extracted in intervals of 50 ps from the last 50 ns of the production simulations for each complex. Prior to the calculations all water molecules, ions, and lipids were removed, and the structures were positioned such that the geometric center of each complex was located at the coordinate origin. The polar part of the solvation free energy was determined by calculations using Poisson-Boltzmann (PB) calculations [240]. In these calculations, a dielectric constant of $\varepsilon_{solute} = 1$ was assigned to the binding area and $\varepsilon_{solute} = 80$ for water.

4.4 Results

4.4.1 Identification of A_3R selective antagonists

We initially conducted a blinded screen of 39 compounds (**K1-K39**) to identify selective A_3R antagonists some of which have previously been identified to bind A_1R, A_3R or $A_{2A}R$ [61]**.** Our screen was carried out using A_3R expressing Flp-In™-Chinese hamster ovary (CHO) cells where cAMP accumulation was detected following a combined stimulation of 10 μM forskolin (to allow A_3R mediated $G_{i/o}$ response to be observed), 1 μM tested compound and the predetermined IC_{80} concentration of NECA (3.16 nM). Compound **K1-K39** were identified by unblinding (**Table 4.1**). For the purpose of structure-activity relationships studies, the previously uncharacterised compounds (**K26, K27, K29-K34** and **K36-K39**), were assayed both functionally and through radioligand binding (**Table 4.1**).

Co-stimulation with 10 μM of both forskolin and NECA reduced the cAMP accumulation when compared to 10 μM forskolin alone and this was completely reversed with the known A_3R antagonist MRS 1220 or partial reversed by compounds **K1, K10, K11, K17, K18, K20, K23, K25** and **K32** (**Table 4.1, Figure 4.4**). Of these nine potential A_3R antagonists, eight (excluding **K11**) appeared to be antagonists at the tested concentration of 1 μM (**Figure 4.5** and **Table 4.2**).

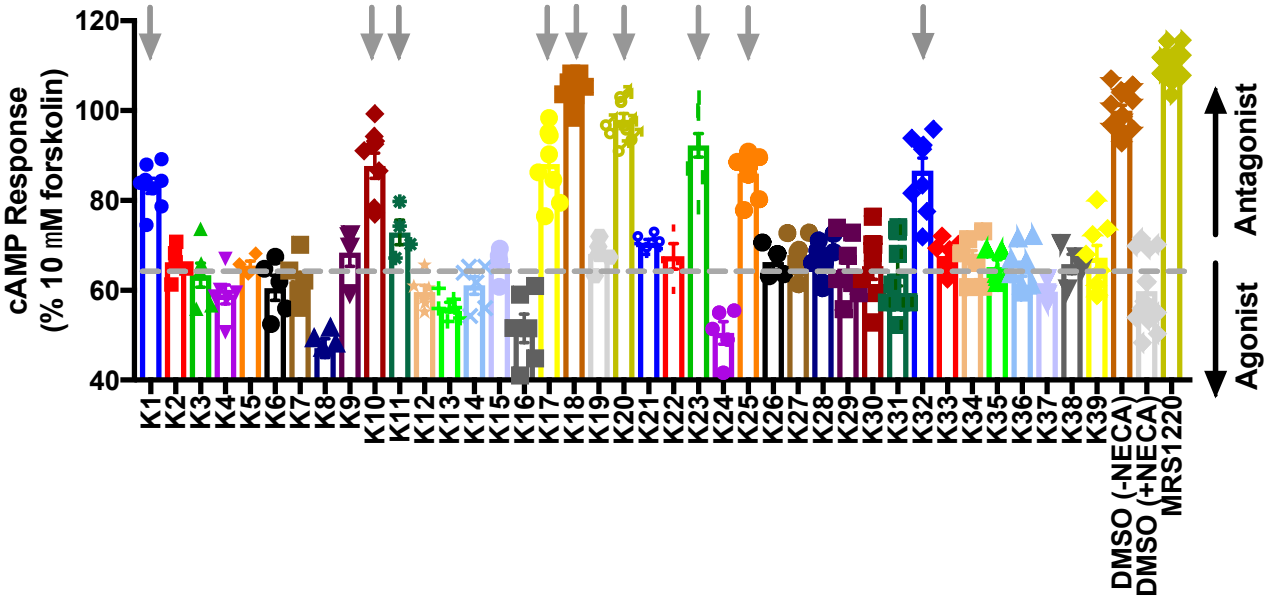

Figure 4.4. Screening for potential antagonists at the A_3R: cAMP accumulation was determined in Flp-In CHO cells stably expressing A_3R (2000 cells/well) co-stimulated for 30 minutes with 10 μM forskolin, NECA at the pre-determined IC_{80} concentration (3.16 nM) and 1 μM of compound/DMSO control. An elevation in cAMP accumulation above that of 10 μM forskolin and NECA, as indicated by the grey dotted line, suggesting the compound is acting as an antagonist (black upwards arrow). Included is MRS 1220 (1 μM) as a positive control for competitive antagonist of A_3R. A reduction of cAMP accumulation (black downwards arrow) could indicate a compound is acting as an agonist. All values are mean ± SEM expressed as % 10 μM forskolin response ('DMSO') where *n* = 3 independent experimental repeats, conducted in duplicate. Grey downward arrow indicates potential antagonists with a cAMP level >71%.

All compounds that have an antagonistic avtivity against an AR-subtype were found to bind this particular AR-subtype in radiolabeled assays (**Figure 4.4**). However, a number of compounds previously documented (**K5, K9, K21, K22** and **K24**; [61]**)** or determined in this study (**K26, K27** and **K34**) to have sub-micromolar binding affinities for A_3R showed no activity in our cAMP-based screen (**Table 4.1**). To ensure robustness of our functional screen, full inhibition curves of NECA in the presence or absence of tested compounds (1 μM or 10 μM) were constructed in A_3R Flp-In CHO cells. In this preliminary data all nine compounds (**K5, K9, K11, K21, K22, K24, K26, K27** and **K34**) appeared to reduce the NECA potency at the highest tested concentration (10 μM) but showed no effect at 1 μM and thus appear to be low potency antagonists at the A_3R (**Figure 4.5**).

4.4.2 AR subtype selectivity and specificity

The similarity of the different ARs has meant many compounds display reduced selectivity. Using the A_3R Flp-In CHO or CHO-K1 cells expressing A_1R, $A_{2A}R$ or $A_{2B}R$ incubated with a single high concentration of antagonist (10 μM) and increasing concentrations of NECA identified **K10, K17, K18** and **K25** as A_3R selective antagonists (**Figure 4.5**). K20 and K23 were antagonists at both the A_1R and A_3R (**Figure 4.5** and **Table 4.2**). **K1, K20** and **K23** showed weak antagonism at the $A_{2A}R$ and none of the tested antagonist which

showed any antagonism of the NECA stimulated response at the A_{2B}R. These selectivity findings agree with our previously published radioligand binding data [61].

4.4.3 Characterisation of competitive antagonists at the A_3R

All eight A_3R antagonists were confirmed to antagonise IB-MECA (**Figure 4.6** and **Table 4.3**) and preliminary data suggests this extends to NECA antagonism in a concentration-dependent manner. Schild analysis characterised **K10, K17, K18, K20, K23, K25** and **K32** as competitive antagonists at the A_3R (Schild slope not significantly different from unity, **Figure 4.5**). Interestingly, the Schild slope deviated from unity for **K1** and **K25** (in competition experiments with NECA, but not IB-MECA) suggesting a more complicated mechanism of antagonism at the A_3R. K20 and K23 were also characterised as competitive antagonists at the A_1R.

When comparing the activity of A_3R selective antagonists (**K10, K17, K18** and **K25**), **K18** was the most potent, showed A_3R specificity and greater A_3R binding affinity (**Table 4.2**) irrespective of agonist used and we propose it as our lead compound. Furthermore, all eight characterised A_3R antagonists showed a concentration-dependent inverse agonism of the A_3R when compared to DMSO control (**Figure 4.6**). This was also found to be the case for DPCPX, **K20** and **K23** at the A_1R.

In addition, we wanted to determine if **K18** could also antagonise the activity of the A_3R when an alternative downstream signalling component was measured; ERK1/2 phosphorylation (**Figure 4.7**). In line with previously reported findings [45], agonists at the A_3R increased ERK1/2 phosphorylation after 5 minutes, with IB-MECA 10-fold more potent than NECA and preliminary data suggests this was entirely $G_{i/o}$-mediated (pERK1/2 levels were abolished upon addition of pertussis toxin (PTX). **K18** was able to antagonise A_3R-mediated phosphorylation of ERK1/2 with the antagonist affinity not significantly different compared to the cAMP-inhibition assay (**Figure 4.7C**).

Table 4.1 Mean cAMP accumulation as measured in Flp-In CHO cells stably expressing A_3R following stimulation with 10 μM forskolin only (DMSO) or10 μM forskolin, NECA at the predetermined IC_{80} concentration and 1 μM test compound/MRS 1220/DMSO control. Binding affinities were obtained through radioligand binding assays against the A_1R, $A_{2A}R$ and A_3R.

Compound	**Compound name**	**Chemical structure**	**cAMP accumulation**		**Radioligand binding(Ki (μM))[c]**		
			Mean[a]	**Mean difference[b]**	**A_3R**	**A_1R**	**$A_{2A}R$**
	NECA	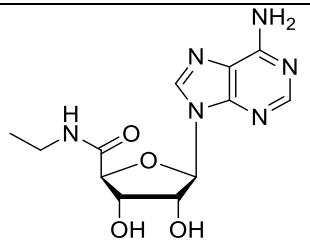	59.81 ±1.96		ND	ND	ND
	DMSO	CH_3-SO-CH_3	100.00 ±1.15 ****	-35.73	ND	ND	ND
	MRS 1220	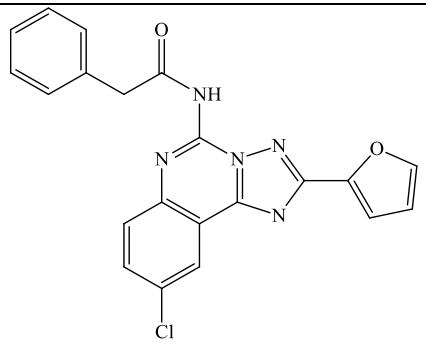	111.10 ±1.13 ****	-49.44	ND	ND	ND

K1	HTS12884SC[1]	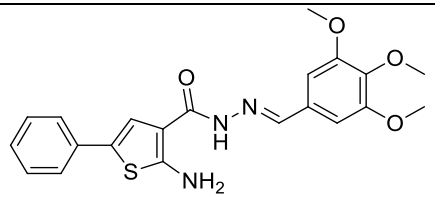	83.26 ±1.68****	-23.45	**3.10**	>100	**2.67**
K8	KM03338[1]	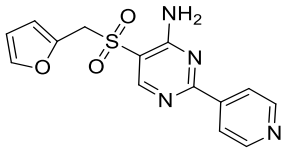	47.13 ±2.09**	12.69	>100	>100	>100
K22	STK300529[1]	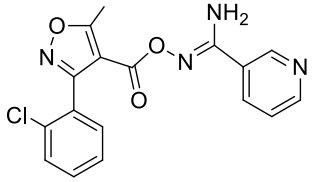	87.73 ±2.78****	-27.91	**4.49**	>60	>60
K23	SKT323144[1]	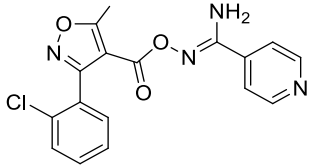	72.88 ±3.24**	-13.07	**5.15**	>60	30
K24	SPB02734[1]	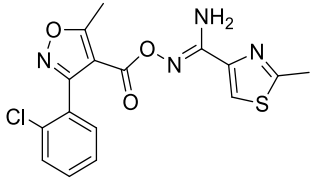	88.11 ±2.75****	-28.30	**4.16**	>30	>60
K25	SPB02735[1]	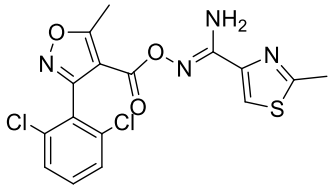	103.8 ±1.24****	-43.94	**0.89**	>100	>100

K17	GK03725[1]	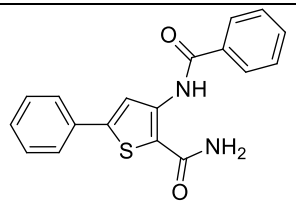	97.95 ±1.39****	-38.13	**0.91**	**1.09**	**7.29**
K16	GK01176[1]	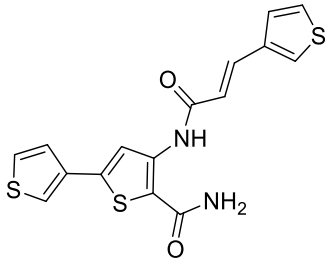	92.27 ±2.62****	-32.46	**1.65**	**1.18**	**4.69**
K18	GK01513[1]	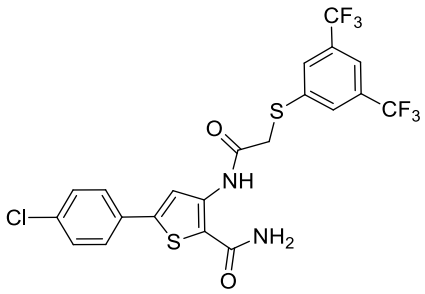	85.99 ±1.61****	-26.17	**1.55**	>100	>100
K32	STK323544	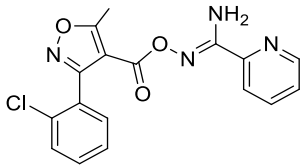	86.66 ±2.78****	-26.85	**2.40**	>100	>100

K2	S05993[1]	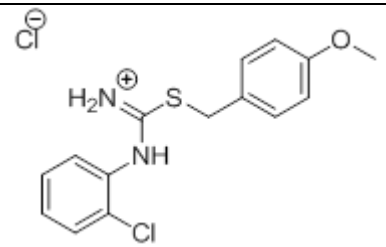	66.28 ±1.61	-6.47	16.6	>100	61.3
K3	SEW01061[1]	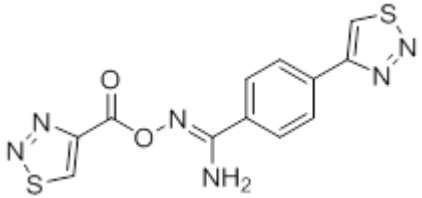	63.37 ±2.68	-3.55	>100	>100	>100
K4	SPB06895[1]	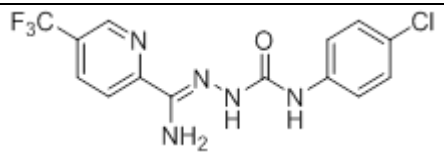	59.06 ±2.12	0.75	>100	>100	>100
K5	SPB02733[1]	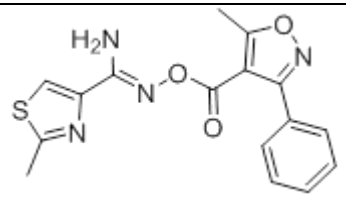	65.54 ±1.98	-5.73	**9.45**	>100	21.8
K6	KM08495[1]	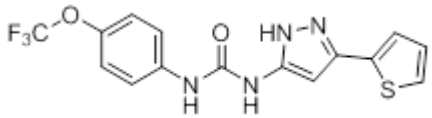	60.52 ±2.78	-0.71	30.6	>100	>100
K7	HTS06244[1]	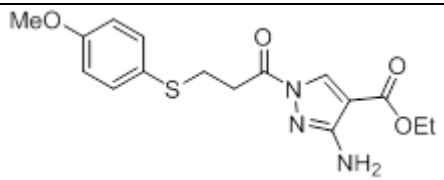	61.96 ±1.99	-2.15	18.3	>100	>100

K9	STK323059[1]	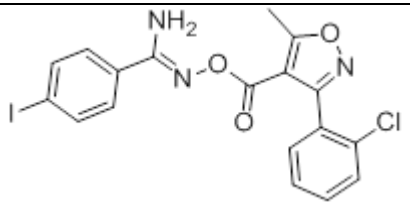	68.41 ±3.08	-8.60	**4.13**	**6.91**	>100
K12	STK441862[1]	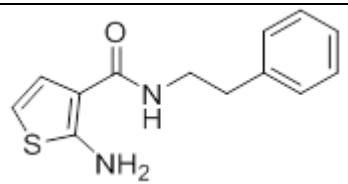	59.66 ±1.48	0.16	37.1	>100	>60
K13	STK448949[1]	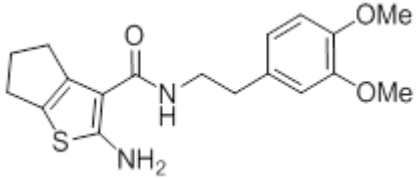	56.25 ±1.11	3.57	16.5	>30	>60
K14	STK450213[1]	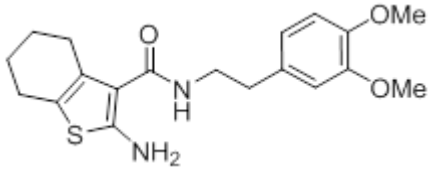	61.09 ±1.96	-1.27	14.8	>30	>60
K15	STK106598[1]	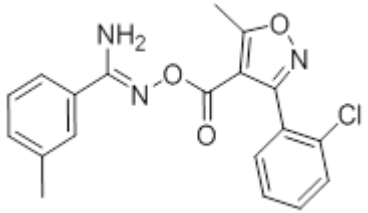	66.14 ±1.86	-6.32	30.9	>100	>100

K16	Z56987720[1]	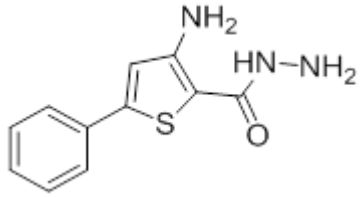	51.51 ±3.16	8.31	19.7	>30	31.7
K19	RDR01677[1]	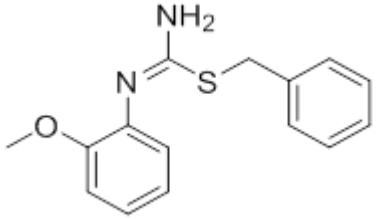	68.12 ±1.44	-8.31	>100	>100	>100
K21	HTS13009[1]	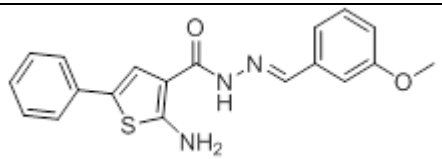	70.57 ±1.47	-10.76	**5.77**	>100	**3.93**
K22	HTS12882[1]	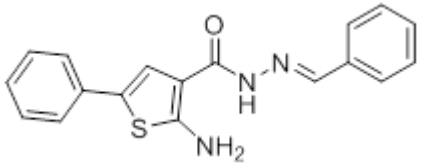	67.56 ±2.85	-7.75	**5.16**	15.2	**4.59**
K24	GK01514[1]	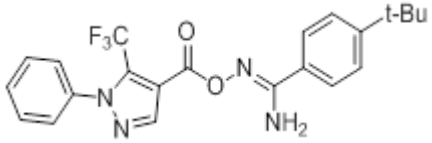	50.51 ±2.23	9.31	**5.39**	**7.48**	>100
K26	7709975	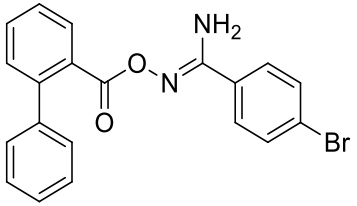	66.34 ±1.81	-6.52	**5.07**	>30	25.1

K27	7709775	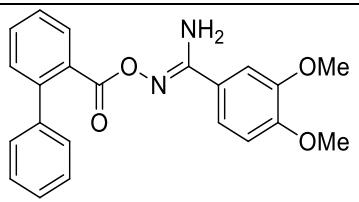	67.84 ±1.39	-8.02	11.9	>30	30.0
K28	GK00478[1]	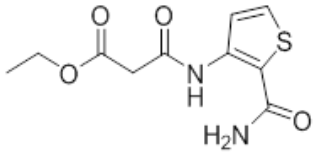	66.33 ±1.45	-6.52	>100	18.0	30.0
K29	5687250	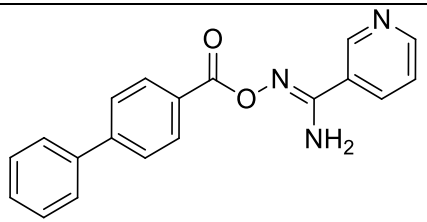	64.83 ±2.59	-5.02	>100	>100	>100
K30	6169223	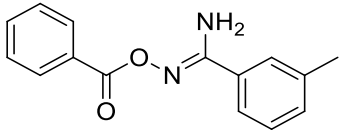	65.40 ±2.97	-5.59	>30	>100	>100
K31	7721356	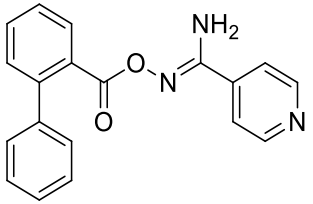	63.81 ±2.72	-4.00	44.3	>100	>30

K33	STK300607	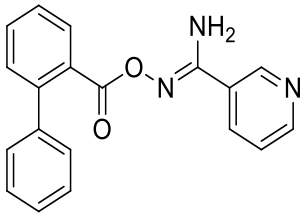	67.64 ±1.31	-7.83	>30	>100	>100
K34	7713195	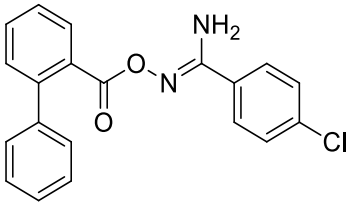	66.73 ±2.14	-6.91	**7.53**	>100	>100
K35	Z1848163164[1]	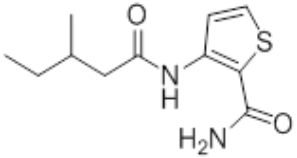	65.21 ±1.55	-5.40	27.4	**7.33**	>30
K36	STK710194	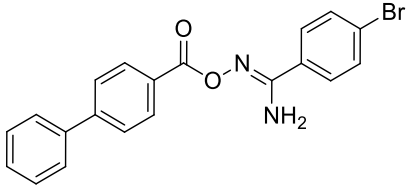	64.69 ±1.60	-4.88	>100	>100	>100
K37	5685368	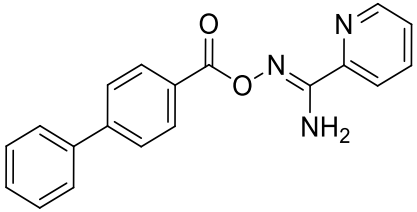	59.68 ±1.14	0.13	>100	>100	>100

K38	7968745	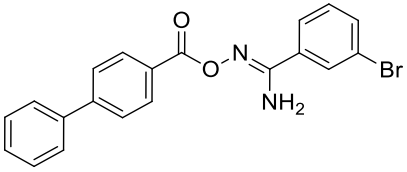	65.88 ±2.14	-6.063	>100	>100	>100
K39	7712234	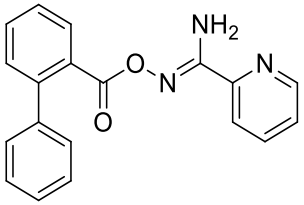	67.29 ±2.72	-7.48	22.9	>100	>30

[1]Indicates previously published in Lagarias *et al.,* 2018 and is shown in grey

[a]cAMP accumulation mean ± SEM expressed as %10 μM forskolin response where $n \geq 3$ independent experimental repeats, conducted in duplicate. Potential antagonists were selected for further investigation based on a high mean cAMP accumulation (>71%).

[b]Difference between the mean cAMP accumulation between 'NECA' and each compound expressed as %10 μM forskolin response

[c]Binding affinity measured in three independent experiments. Bold denotes binding affinity < 10 μM. All compounds did not exhibit binding evidence to $A_{2B}R$.

	A_3R	A_1R	$A_{2A}R$	$A_{2B}R$
K1	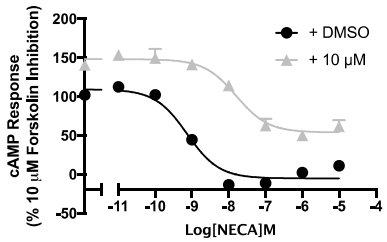	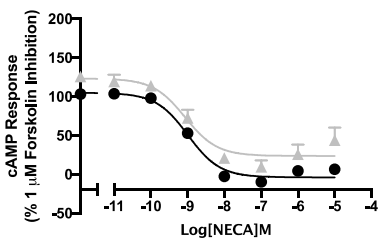	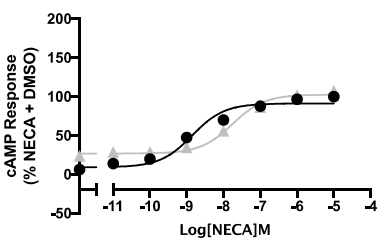	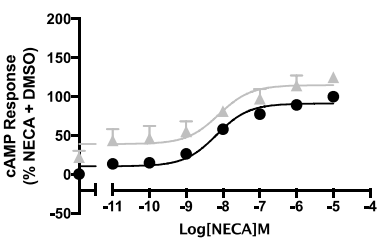
K10	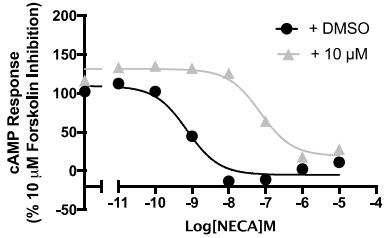	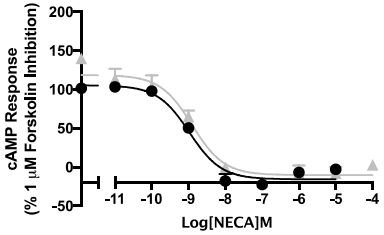	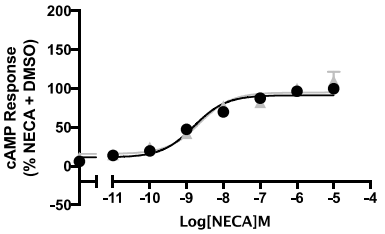	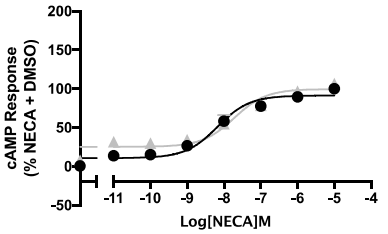
K17	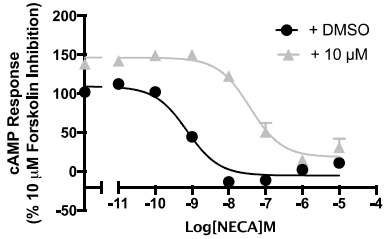	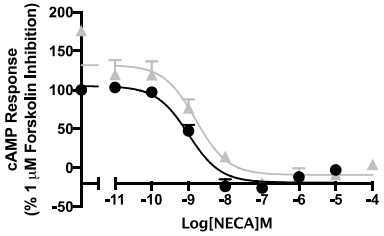	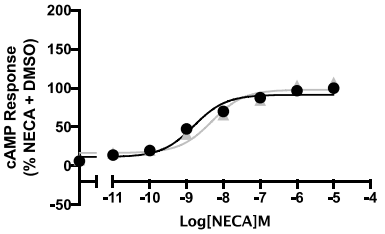	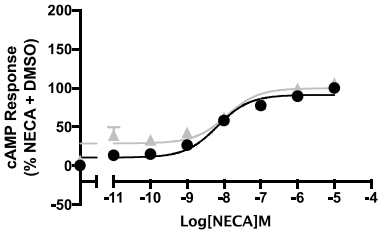

K18	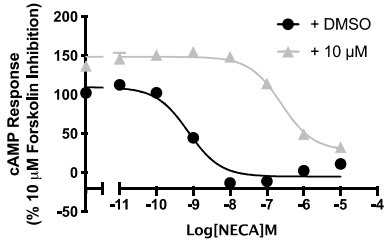	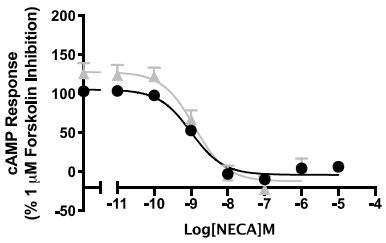	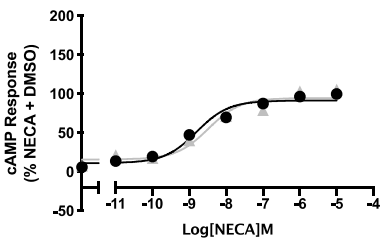	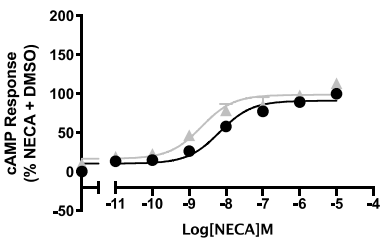
K20	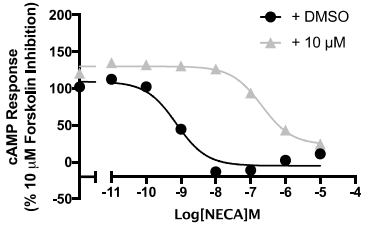	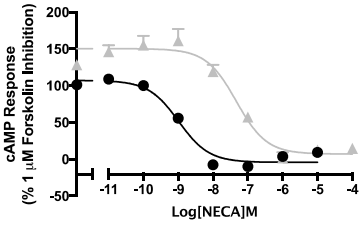	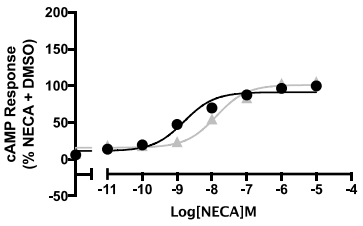	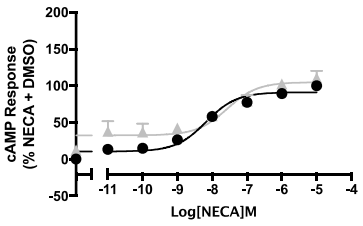
K32	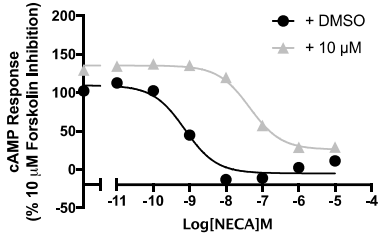	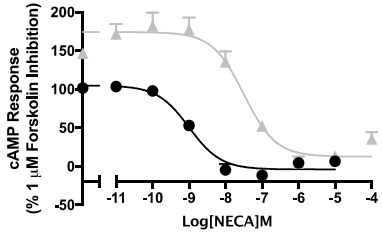	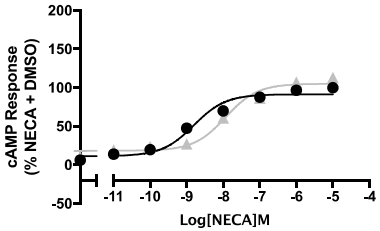	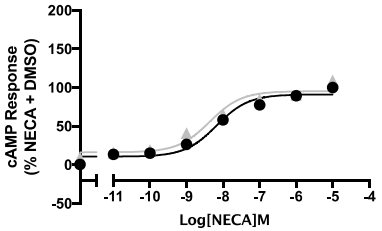
K25	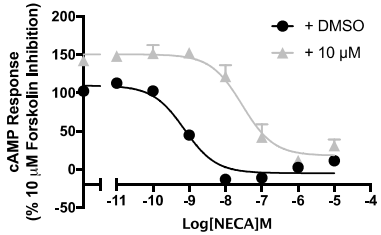	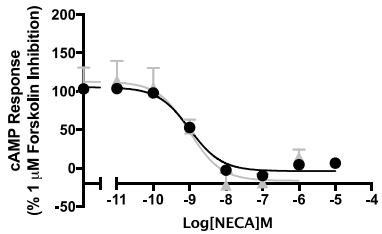	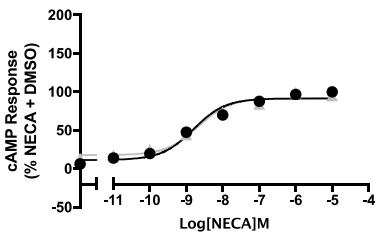	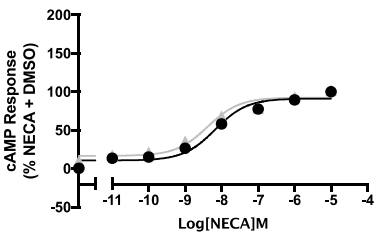

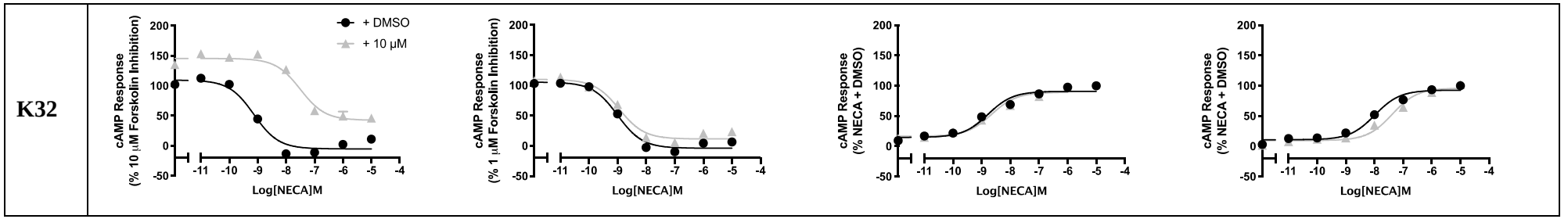

Figure 4.5 Characterisation of A_3R antagonist at all AR subtypes. A_3R Flp-In CHO cells or CHO-K1 cells (2000 cells/well) stably expressing one of the remaining AR subtypes were exposed to forskolin in the case of G_i-coupled A_1R and A_3R (1 μM or 10 μM, respectively) or DMSO control in the case of G_s-coupled A_{2A}R and A_{2B}R, NECA and test compound (10 μM) for 30 min and cAMP accumulation detected. All values are mean ± SEM expressed as percentage forskolin inhibition (A_1R and A_3R) or stimulation (A_{2A}R and A_{2B}R), relative to NECA. $n \geq 3$ independent experimental repeats, conducted in duplicate.

Table 4.2 Potency of NECA stimulated cAMP inhibition or accumulation as determined in Flp-In CHO or CHO-K1 cells expressing one of four ARs subtype (A_3R, A_1R, A_{2A}R or A_{2B}R) and corresponding binding affinity of potential antagonists. Cells stably expressing A_3R, A_1R, A_{2A}R or A_{2B}R were stimulated with forskolin, 10 μM tested compound/DMSO and increasing concentrations of NECA. Binding affinities were obtained through radioligand binding assays as detailed in [61].

	pIC_{50}/pEC_{50}[a]				**K_i (μM)[b]**			
	A_3R	**A_1R**	**A_{2A}R**	**A_{2B}R**	**A_3R**	**A_1R**	**A_{2A}R**	**A_{2B}R**
NECA only	8.94 ±0.1	9.00 ±0.1	8.80 ±0.1	8.18 ±0.1	ND	ND	ND	ND
K1	7.80 ±0.1	9.07 ±0.2	7.75 ±0.1	8.36 ±0.2	3.10	>100	2.67	ND
K10	7.15 ±0.1	8.90 ±0.1	8.64 ±0.1	8.45 ±0.2	4.49	>60	>60	ND
K17	7.43 ±0.1	8.80 ±0.2	8.48 ±0.1	8.40 ±0.2	4.16	>30	>60	ND
K18	6.61 ±0.1	8.81 ±0.2	8.37 ±0.2	8.67 ±0.2	0.89	>100	>100	ND
K20	6.68 ±0.1	7.38 ±0.1	7.88 ±0.1	8.14 ±0.2	0.91	1.09	7.29	ND
K23	7.35 ±0.1	7.49 ±0.1	7.94 ±0.1	8.36 ±0.2	1.65	1.18	4.69	ND
K25	7.54 ±0.2	9.01 ±0.2	8.68 ±0.1	8.38 ±0.1	1.55	>100	>100	ND
K32	7.54 ±0.2	8.86 ±0.1	8.65 ±0.1	7.38 ±0.1	2.4	>100	>100	ND

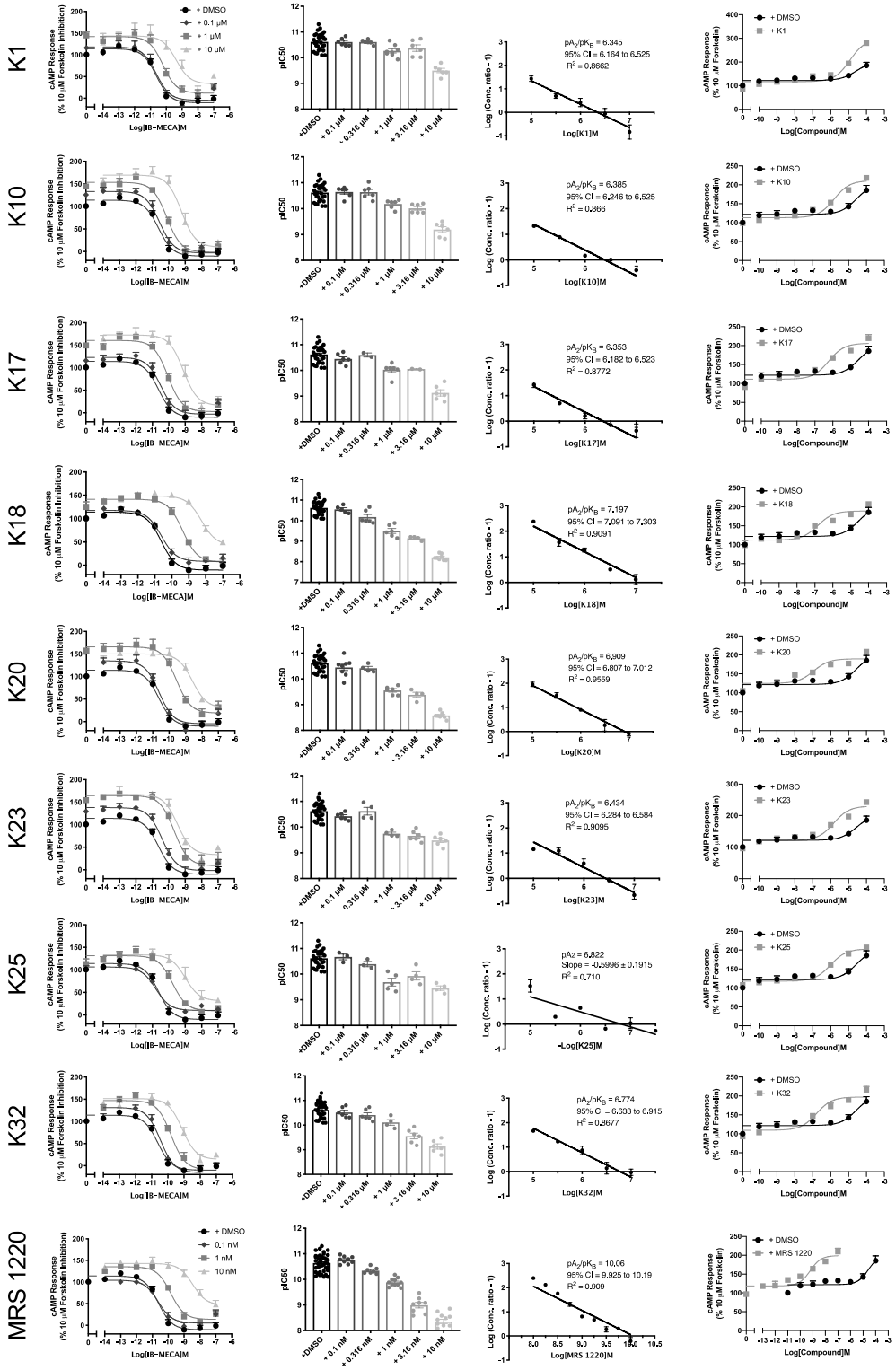

Figure 4.6 IB-MECA stimulated cAMP inhibition at WT A_3R: activity of MRS 1220 and potential antagonists. Flp-In-CHO cells (2000 cells/well) stably expressing WT A_3R were exposed to forskolin 10

μM, IB-MECA and test compound/MRS 1220/DMSO control for 30 min and cAMP accumulation detected. **A**) Representative dose response curves are shown as mean ± SEM expressed as percentage forskolin inhibition (10 μM) relative to IB-MECA. Key indicated in K1 is identical for all 'K' test compounds shown. **B**) pIC_{50} values for individual repeats including half-log concentration are shown as mean ± SEM **C**) Schild analysis of data represented in **A/B**. A slope of 1 indicates a competitive antagonist**.** The x-axis is expressed as -log (molar concentration of antagonist) giving a negative Schild slope. **D**) Inverse agonism at the A_3R. cAMP accumulation following a 30-minute stimulation with forskolin (10 μM) and increasing concentrations of antagonist/DMSO control was determined in WT A_3R expressing Flp-In-CHO cells. Representative dose response curves are shown as mean ± SEM expressed as percentage forskolin (10 μM), relative to IB-MECA.

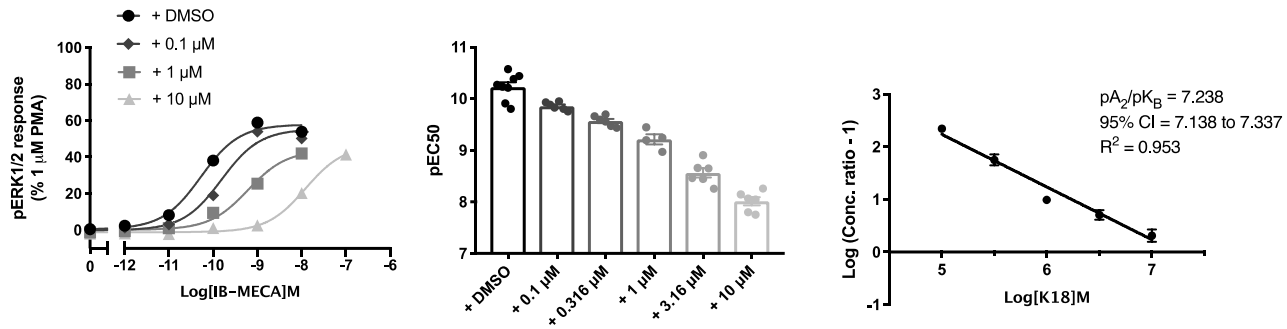

Figure 4.7. K18 also reduced levels of agonist stimulated ERK1/2 phosphorylation. pERK1/2 was detected in Flp-In-CHO cells stably expressing A_3R (2000 cells/well) stimulated for 5 min with IB-MECA, with or without **K18**. (A) Representative dose-response curves for IB-MECA with **K18** at the indicated concentration or DMSO control shown as mean ± SEM expressed as % 1μM PMA response. (B) pEC_{50} values for individual repeats are shown as mean ± SEM. C) Schild analysis of data represented in A/B.

4.4.4 MD simulation of the binding mode of K18 at A_3R

We next intended to investigate the potential binding pose of **K18** within the A_3R orthosteric site. Building upon our previous studies where we have generated a homology model of the A_3R, **K18** was docked into the orthosteric site of the A_3R using the GoldScore scoring function and the highest scoring pose was inserted in a hydrated POPE bilayer. The complex was subjected to MD simulations in the orthosteric binding site of A_3R with Amber14ff for 100 ns and the trajectory analyzed for protein-ligand interactions.

We identified a potential binding pose of **K18** within the established orthosteric A_3R binding pocket (**Figure 4.8)**. A number of residues were identified as potentially important in binding of **K18** within the orthosteric binding site and included $L90^{3.32}$, $F168^{5.29}$, $V169^{5.30}$, $M177^{5.40}$, $L246^{6.51}$, $I249^{6.54}$, $N250^{6.55}$ and $L264^{7.34}$**(Figure 4.8A)** (numbers in superscripts refer to the Ballesteros–Weinstein numbering [129]. The MD simulations showed that **K18** forms hydrogen bonds, van der Waals and π-π interactions inside the orthosteric binding site of A_3R **(Figure 4.8A)**. More specifically, MD simulations showed that the 3-(dichlorophenyl) group can be positioned close to $V169^{5.30}$, $M177^{5.40}$, $I249^{6.54}$ and $L264^{7.34}$ of the A_3R orthosteric binding site forming attractive vdW interactions. The isoxazole ring is engaged in an aromatic π-π stacking interaction with the phenyl group of $F168^{5.29}$ (**Figure 4.7A**). The thiazole ring is oriented deeper into the receptor favoring interactions with $L246^{6.51}$, $L90^{3.32}$ and $I268^{7.39}$. Hydrogen bonding interactions can be formed between: (a) the amino group of the carbonyloxycarboximidamide molecular segment and the amide

side chain of N250$^{6.55}$; (b) the nitrogen or the sulfur atom of the thiazole ring and N250$^{6.55}$ side chain **(Figure 4.8A)**. For structural comparison and insight, we also modeled **K5** and **K17** binding at the A_3R given the structural similarity: **K5** when compared to **K17** and **K18** possess one and two chlorine atoms attached to the phenyl ring, respectively **(Fig. 4.8B** and **C)**. It should be noted that although **K17**, **K18** are antagonists, **K5** do not show an antaginistic activity. Interpratation of these activity results for **K5**, **K17** and **K18** and furher investigation of the binding profile of K18 will be inestigated in detail in Chapter 5.

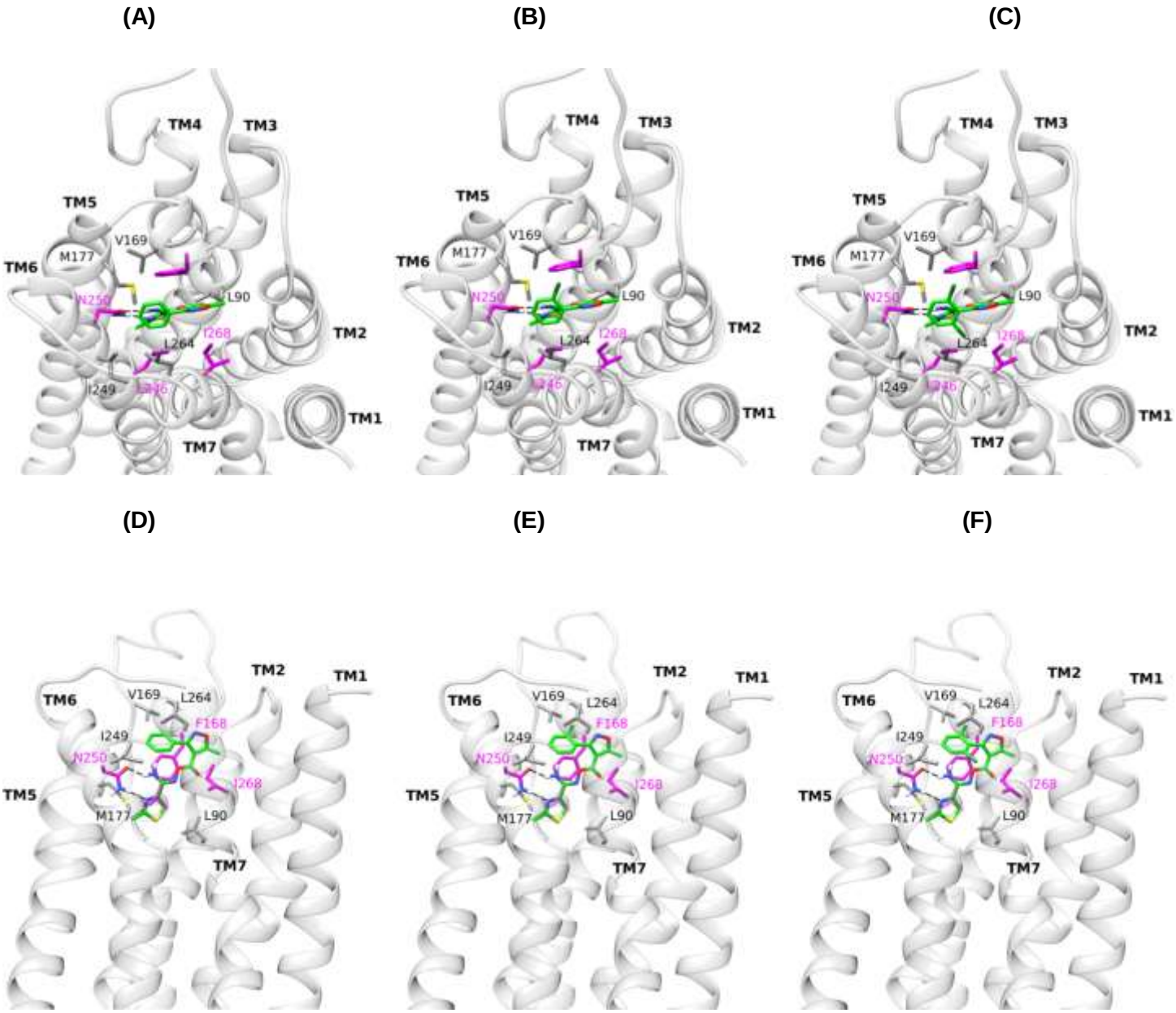

Figure 4.8 Orthosteric binding area average structure of WT A_3R in complex with **K5, K17** and **K18** from MD simulations with Amber14ff. Side (A),top (D) view of K5 complex; side (B), top (E) view of K17 complex; side (C), top (F) view of **K18** complex. Side chains of critical residues for binding indicated from the MD simulations are shown in sticks. Residues L90$^{3.32}$, V169$^{5.30}$, M177$^{5.40}$, I249$^{6.54}$ and L264$^{7.34}$, in which carbon atoms are shown in grey, were confirmed experimentally; in residues F168$^{5.29}$, L246$^{6.51}$, I268$^{7.39}$ and

$N250^{6.55}$ carbon atoms are shown in magenta; nitrogen, oxygen and sulfur atoms are shown in blue, red and yellow respectively.

4.4.5 Experimental evaluation of the binding mode of K18 at A_3R

The potential binding site of lead A_3R selective antagonist, **K18**, was investigated through the use of point mutations as an experimental approach to give insight into structure-function relationships. The determination of critical residues for antagonist binding becomes particularly difficult in the case of competitive antagonists whereby important amino acids are likely overlapping with those for agonist binding. Through performing Schild analysis, whereby the pA2 is independent of agonist, we were able to experimentally determine the effect of receptor mutation on antagonist binding. Whereas an increase in the pA2 for a particular mutant when compared to WT suggested the antagonist was more potent, a decrease indicated a reduced potency. Of the identified residues predicted to mediate an interaction between **25** and the A_3R, the ones which showed (according to the MD simulations) the most frequent and the most important contacts were chosen for investigation and included amino acids $L90^{3.32}$, $F168^{5.29}$, $V169^{5.30}$, $M177^{5.40}$, $L246^{6.51}$, $I249^{6.54,}$ $N250^{6.55}$, $L264^{7.34}$ and $I268^{7.39}$ **(Figure 4.8)**. Site-directed mutagenesis was performed replacing each residue with an alanine and expressed then in the Flp-In-CHO™ cells lines. Each mutant was then screened for their ability to suppress forskolin-induced cAMP accumulation in response to NECA/IB MECA stimulation in the presence and absence of **K18**.
Mutation of residues $F168^{5.29}$, $L246^{6.51}$, $N250^{6.55}$ and $I268^{7.39}$ abolished agonist induced suppression of forskolin-induced cAMP accumulation and were discontinued in this study [241]. Both $L90A^{3.32}$ and $M177A^{5.40}$ showed a significantly decreased NECA and IB-MECA potency. $L264A^{7.34}$ showed a slight decrease in IB-MECA potency whereas the potency of NECA was similar to WT. Whereas the NECA stimulated cAMP inhibition in $V169A^{5.30}$ or $I249A^{6.54}$ expressing Flp-In CHOs was comparable to WT, the IB-MECA stimulated cAMP inhibition was enhanced in potency **(Table 5)**. Mutation of $V169^{5.30}$ to glutamate, the amino acid present in the remaining three AR subtypes, enhanced both NECA and IB-MECA potency.

4.4.6 Schild analysis of K18 at WT and mutant A_3R

The pA2 values obtained through conducting Schild analysis of **K18** at WT and mutant A_3R were compared in order to determine the potential antagonist binding site (**Figure 4.9, Table 4.3**). The pA2 value for $I249A^{6.54}$ A_3R was similar to WT, whereas $M177A^{5.40}$ and $V169A^{5.30}$ were significantly smaller. Interestingly we found an increase in the pA2 for $L90A^{3.32}$ and $L264A^{7.34}$ when compared to WT, suggesting an enhanced ability of **K18** to act as an antagonist. Our confidence in the obtained pA2 values for **K18** was enhanced by testing with NECA and IB-MECA at an A_3R mutant that caused enhanced activity ($L90A^{3.32}$). As would be expected, the pA2 values for this mutant were not significantly different between agonists, confirming agonist independence. These experimental findings are reflected in our final binding pose of **K18** at the WT A_3R (**Figure 4.8**).

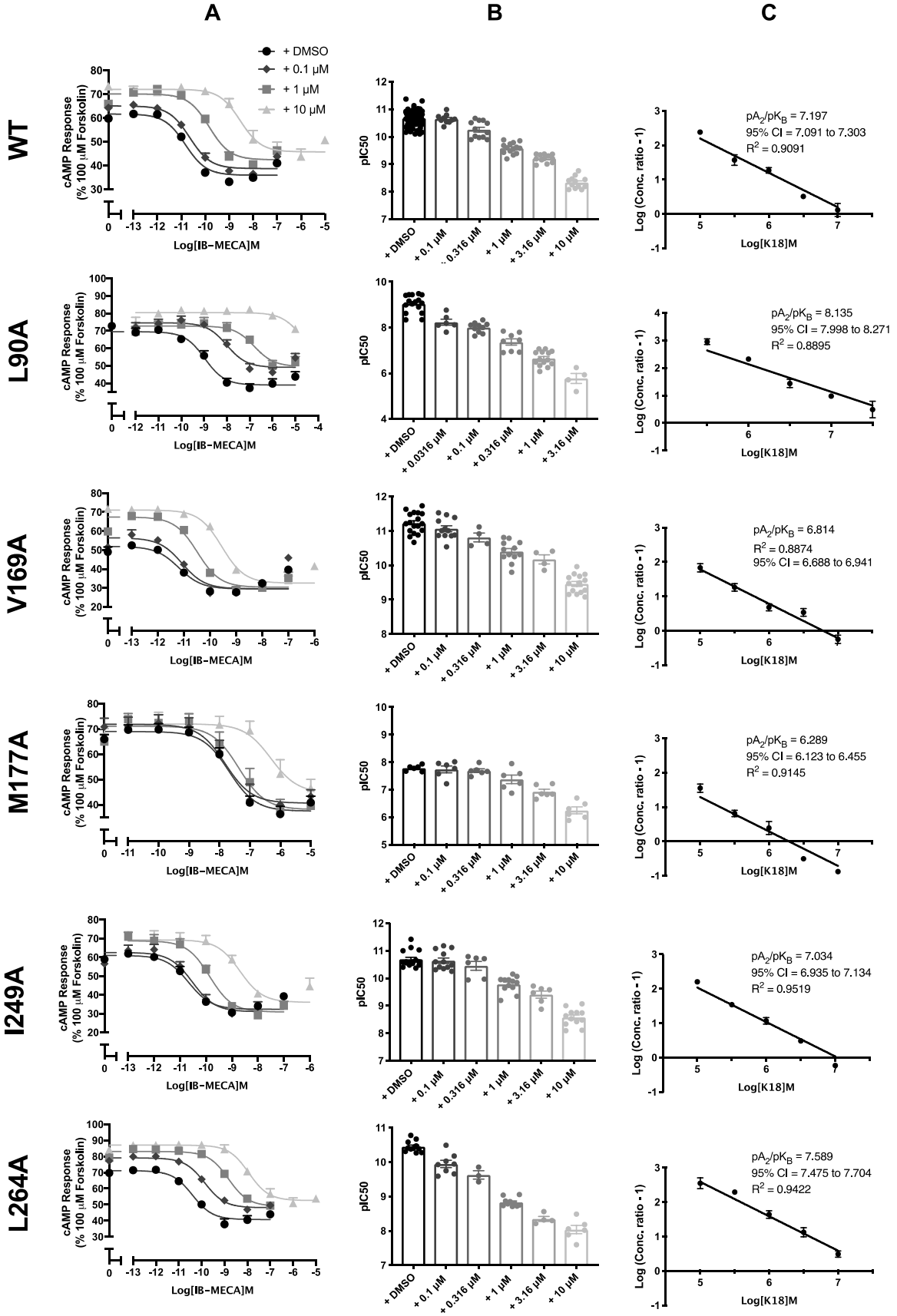
A
B
C
WT
L90A
V169A
M177A
I249A
L264A
+ DMSO
+ 0.1 μM
+ 1 μM
+ 10 μM
cAMP Response (% 100 μM Forskolin)
Log[IB-MECA]M
pIC50
Log (Conc. ratio - 1)
Log[K18]M
pA2/pKB = 7.197
95% CI = 7.091 to 7.303
R2 = 0.9091
pA2/pKB = 8.135
95% CI = 7.998 to 8.271
R2 = 0.8895
pA2/pKB = 6.814
R2 = 0.8874
95% CI = 6.688 to 6.941
pA2/pKB = 6.289
95% CI = 6.123 to 6.455
R2 = 0.9145
pA2/pKB = 7.034
95% CI = 6.935 to 7.134
R2 = 0.9519
pA2/pKB = 7.589
95% CI = 7.475 to 7.704
R2 = 0.9422

Figure 4.9 IB-MECA stimulated cAMP inhibition at WT or mutant A_3R with increasing concentrations of **K18**. Flp-In-CHO cells (2000 cells/well) stably expressing WT or mutant A_3R were exposed to forskolin 10 μM, IB-MECA and **K18** at varying concentrations for 30 min and cAMP accumulation detected. A) Representative dose response curves are shown as mean ± SEM expressed as percentage maximum forskolin response (100 μM). B) pIC_{50} values for individual repeats including half-log concentration are shown as mean ± SEM C) Schild analysis of data represented in A/B.

Table 4.3 Antagonistic potency of **K18** at A_3R mutants. cAMP accumulation as measured in Flp-In-CHO cells stably expressing WT or mutant A_3R following stimulation with 10 μM forskolin, varying concentrations of IB-MECA and +/- **K18** at the indicated concentration.

			+ DMSO		
	pIC_{50} [a]	**E_{min} [b]**	**Basal [c]**	**True Basal [d]**	**Span [e]**
WT	10.64 ±0.1	33.5± 2.0	64.7 ±1.8	58.7 ±0.5	31.2 ±2.6
L90A	8.67 ±0.1	36.8 ±1.8	69.5 ±1.7	67.8 ±1.5	32.8 ±2.4
V169A	11.23 ±0.1	29.5 ±1.6	57.0 ±1.4	53.8 ±1.5	27.5 ±2.0
M177A	7.64 ±0.1	38.0 ±2.2	70.1 ±1.5	66.7 ±1.3	32.1 ±2.6
I249A	10.67 ±0.1	32.9 ±1.9	61.0 ±1.6	61.2 ±1.0	32.4 ±1.6
L264A	10.29 ±0.1	38.4 ±1.7	64.8 ±1.6	68.8 ±1.3	26.5 ±2.2
V169E	11.48 ±0.1	38.1 ± 1.5	66.1 ±2.1	67.4 ±1.6	28.1 ±2.4
			+ 0.1 μM K18		
WT	10.65 ±0.1	38.7 ±0.9	65.1 ±0.9	64.2 ±0.9	26.4 ±1.2
L90A	8.00 ±0.2	49.1 ±1.6	74.6 ±1.4	72.0 ±2.6	25.5 ±2.1
V169A	11.07 ±0.1	29.6 ±1.3	56.4 ±1.2	54.1 ±2.3	26.8 ±1.7
M177A	7.81 ±0.2	40.6 ±2.7	71.9 ±1.9	70.9 ±3.4	31.2 ±3.3
I249A	10.52 ±0.1	31.1 ±1.8	62.6 ±1.3	65.5 ±1.4	31.5 ±2.1
L264A	9.87 ±0.1	48.2 ±1.2	79.1 ±0.9	77.3 ±2.2	31.0 ±1.5
V169E	11.21 ±0.1	39.7 ± 1.0	74.7 ±1.3	73.7 ±1.6	35.0 ±1.6
			+ 1 μM K18		
WT	9.50 ±0.1	42.4 ±1.1	70.1 ±0.9	64.4 ±1.5	27.7 ±1.4
L90A	6.80 ±0.2	49.6 ±2.6	72.7 ±1.4	69.5 ±3.0	23.2 ±2.8
V169A	10.49 ±0.1	30.4 ±1.1	67.4 ±1.0	65.4 ±1.3	37.1 ±1.3
M177A	7.36 ±0.2	38.1 ±3.0	71.1 ±1.9	65.1 ±2.9	33.0 ±3.4
I249A	9.86 ±0.1	30.9 ±1.7	68.8 ±1.4	71.9 ±2.4	37.9 ±2.1
L264A	8.83 ±0.1	49.1 ±1.7	83.1 ±0.9	79.3 ±2.0	34.0 ±1.9
V169E	10.49 ±0.1	43.4 ± 1.0	81.1 ±0.9	78.8 ±1.2	37.7 ±1.4
			+ 10 μM K18		
WT	8.33 ±0.2	45.8 ±1.6	72.1 ±1.1	68.8 ±1.5	26.3 ±1.8
L90A	5.58 ±0.4	55.4 ±6.8	80.4 ±1.3	73.6 ±2.1	25.0 ±6.7
V169A	9.55 ±0.1	32.6 ±1.0	71.1 ±0.7	68.6 ±0.7	38.6 ±1.1
M177A	6.31 ±0.3	44.7 ±4.0	72.0 ±1.5	67.7 ±2.5	27.4 ±4.1
I249A	8.69 ±0.2	36.1 ±2.3	69.3 ±2.5	72.9 ±1.2	33.2 ±2.5
L264A	7.94 ±0.1	52.6 ±1.7	87.1 ±1.1	81.5 ±2.6	34.5 ±1.9
V169E	9.23 ±0.1	43.9 ± 1.1	83.1 ±0.8	80.4 ±1.6	39.2 ±1.3

[a]Negative logarithm of IB-MECA concentration required to produce a half-maximal response

[b] Minimum cAMP accumulation of IB-MECA as %100 μM forskolin. The lower plateau of the fitted sigmoidal dose response curve

[c] The upper plateau of the fitted sigmoidal dose response curve corresponding %100 μM forskolin

[d] The cAMP accumulation when stimulated with 10 μM forskolin only + DMSO/**K18** at the indicated concentration

[e] The difference between E_{min} and basal signalling

Statistical significance compared to WT IB-MECA stimulation +/- **K18** at each indicated concentration was determined by one-way ANOVA with Dunnett's post-test.

4.4.7 Kinetics of A_3R antagonists determined through BRET

BRET techniques have been successfully used to determine the real time kinetics of ligand binding to GPCRs [242]. In BRET ligand-binding experiments, we investigated the ability of the selective A_3R antagonist **K5, K17** or **K18** to inhibit specific binding of the fluorescent A_3R antagonist CA200645 to Nluc-A_3R. The kinetic parameters for CA200645 at Nluc-A_3R were initially determined as k_{on} (k_1) = 2.86 ± 0.89 x 107 M^{-1}, k_{off} (k_2) = 0.4397 ± 0.014 min-1 with a K_D of 17.92 ± 4.45 nM [243]. It was noticed in the analysis for **K5, K17** or **K18** that the fit in some cases was ambiguous [234] and/or the fitted value of the compound dissociation rate constant was high (k_4> 1 min-1, corresponding to a dissociation $t_{1/2}$ of < 42 sec). This model allowed estimate of the equilibrium binding affinity of the compound (K_i) but not the binding kinetics of **K5, K17** or **K18 (Table 4)**. These pK_i values were found to be similar to those calculated through fitting the Cheng-Prusoff equation [244] and notably, the order of affinity for **K5, K17** or **K18** reflected that determined through Schild analysis and previously published radioligand binding **(Table 4.2)**.

4.5 Results and Discussion

In silico SBDD efforts in ligand discovery have proven to be highly successful [245]. However, given the broad and similar orthosteric binding site of ARs, the search for an AR subtype specific compound often leads to compounds active at more than one of the AR subtypes [125]. Given that AR subtypes play distinct roles throughout the body, obtaining highly specific receptor antagonists and agonists is crucial. Here, we presented the pharmacological characterisation of eight A_3R antagonists identified though virtual screening. Of these eight compounds, **K10, K17, K18, K20, K23, K25** and **K32** were determined to be competitive. Whereas **K20** and **K23** were antagonists at both the A_1R and A_3R, **K10**, **K17, K18, K25** and **K32** were A_3R selective antagonists. Indeed, we found no functional activity, or indeed binding affinity (< 30 μM), at the other AR subtypes.

K1, K20 and **K23** showed weak antagonism of the A_{2A}R with no activity at the A_{2B}R **(Figure 1, Table 2)**. These selectivity findings were in agreement with our radioligand binding data for **K1-25**, **K28** and **K35** [61]. However, a number of compounds previously determined to have micromolar binding affinity for A_3R (**K5, K9, K21, K22, K24, K26, K27** and **K34**), showed no antagonistic potency in our initial functional screen. Further testing confirmed that these compounds were low potency antagonists and, although supporting the previously published radioligand binding data, confirmed the need for functional testing: not all compounds with binding affinity showed high functional potency.

We showed the A_3R, when expressed in Flp-In™-CHO cells, displays constitutive activity. Compounds which preferably bind to the inactive (R) state, decreasing the level of constitutive activity [246] and in the case of a $G_{i/o}$-coupled GPCR leading to an elevated cAMP, are referred to as inverse agonists. All eight characterised A_3R antagonists and both characterised A_1R antagonists (**K20** and **K23**) were found to act as inverse agonists. We also reported an elevation in cAMP accumulation when cells were stimulated with DMSO, which was concentration-dependent. Given that even low concentrations of DMSO has been reported to interfere with important cellular processes [247], the interpretation of these data should be made with caution. The virtual screening described in reference [61] used a combination of a ligand-based and structure-based strategies based upon the experimental structure of $A_{2A}R$ in complex with the selective antagonist/inverse agonist ZM241385 [14,20]. Our high hit rate for A_3R selective antagonist appears counter-intuitive since the ligand-based virtual screening tool Rapid Overlay of Chemical Structures (ROCS) was used to predict structures similar to ZM241385 [61]. Indeed, ZM241385 has little affinity for A_3R and 500- to 1000-fold selectivity for $A_{2A}R$ over A_1R. However, as reported previously, the search for an AR subtype specific compound often leads to compounds active at multiple AR subtypes [125].

We hypothesized that the presence of a chloro substituent in the phenyl ring of 3-phenyl-isoxazole favoured A_3R affinity, as following 0Cl < 1Cl < 2Cl i.e. **K5** < **K17** < **K18**. This theory is supported by both radioligand binding, NanoBRET ligand-binding and functional data. Moreover, MD simulations showed that these compounds adopted a similar binding mode at the A_3R orthosteric binding site, but the free-energy MM-PBSA calculations showed that **K18**, having two chlorine atoms and an increased lipophilicity, leaves the solution state more efficiently and enters the highly lipophilic binding area. Importantly, substitution of the 1,3-thiazole ring in **K17** with either a 2-pyridinyl ring (**K32**) or a 3-pyridinyl ring (**K10**) but not a 4-pyridinyl ring (**K11**) maintained A_3R antagonistic potency. Although we have not directly determined the effects of similar pyridinyl ring substitutions on the higher affinity antagonist **K18**, we suspect there would be no significant increase in the potency of K18 given the small changes we observed for **K17**.

For the first time, we demonstrated the utilisation of a new model which expands on the 'Kinetic of competitive binding' model [233], built into Prism, for fitting fast kinetics data obtained from NanoBRET experiments and assumes the unlabelled ligand rapidly equilibrates with the free receptor. Very rapid competitor dissociation can lead to failure of the fit, eliciting either an ambiguous fit [234] or unrealistically large k_3 and k_4 values. Whereas we were able to successfully fit the MRS 1220 kinetic data with the Motulsky and Mahan model due to its slow dissociation, fitting of **K5, K17** and **K18** kinetic data with this model often resulted in an ambiguous fit. Our new model, assuming fast compound dissociation, successfully fitted the data and allowed the determination of binding affinity. In the cases where the data was able to fit the Motulsky and Mahan model, the dissociation constant was higher (of the order of 1 min^{-1}), indicating rapid dissociation. Although we found nearly a 10-fold differences in determined binding affinity for MRS 1220, **K5, K17** and **K18** between BRET ligand binding and radioligand binding assays, we demonstrated the order of affinity remains consistent. Indeed, this was seen across all three experimental approaches: Schild analysis, NanoBRET ligand-binding assay and radioligand binding.

Combining MD simulations with mutagenesis data, we presented a final binding pose of K18 appears to be within the orthosteric binding site, involving residues previously described to be involved in binding of A_3R compounds[248]. We reported no detectable $G_{i/o}$ response following co-stimulation with forskolin and NECA or IB-MECA for A_3R mutants F168A$^{5.29}$, L246A$^{6.51}$, N250A$^{6.55}$ and I268A$^{7.39}$ (Stamatis et al. 2019) and our findings are in line with previous mutagenesis studies investigating residues important for agonist and antagonist binding at the human A_3R [249,250]. Our MD simulations published elsewhere (**Lagarias *et al.*, 2019**) have investigated the selectivity profile of **K18** and have demonstrated that K18 failed to bind A_1R and $A_{2A}R$ due to a more polar area close to TM5, TM6 when compared to A_3R.

We reported no detectable Gi/o response following co-stimulation with forskolin and NECA or IBMECA for A_3R mutants F168A$^{5.29}$, L246A$^{6.51}$, N250A$^{6.55}$ and I268A$^{7.39}$ [241]. These findings are in line with previous mutagenesis studies investigating residues important for agonist and antagonist binding at the human A_3R [128,250] L90A$^{3.32}$, V169A$^{5.30}$, M177A$^{5.40}$, I249A$^{6.54}$ and L264A$^{7.34}$ A_3R all showed a detectable Gi/o response when stimulated with agonists [241].
Through performing Schild analysis (results of which were used to inform modelling in Lagarias *et al.*, 2019) we experimentally determined the effect of receptor mutation on antagonist affinity for L90A$^{3.32}$, V169A/E$^{5.30}$, M177A$^{5.40}$, I249A$^{6.54}$ and L264A$^{7.34}$ A_3R. The pA_2 value for I249A$^{6.54}$ A_3R was similar to WT, whereas M177A$^{5.40}$ and V169A$^{5.30}$ were significantly smaller suggesting these residues appear to be involved in **K18** binding. Interestingly we found an increase in **K18** affinity at L90A$^{3.32}$ and L264A$^{7.34}$ when compared to WT.

In conclusion, we present findings of a unique scaffold (**K18**) which can be used as a starting point for detailed structure-activity relationships and represents a useful tool that warrants further assessment. Furthermore, we introduce **K25** as a potential rat A_3R antagonist which also warrants further investigation.

4.6 Conclusion

The adenosine A_3 receptor (A_3R) belongs to a family of four adenosine receptor (AR) subtypes which all play distinct roles throughout the body. A_3R antagonists have been described as potential treatments for numerous diseases including asthma. Given the similarity between ARs orthosteric binding sites, obtaining highly selective receptor antagonists is a challenging but critical task.
39 potential A_3R, antagonists were screened using agonist-induced inhibition of cAMP. Positive hits were assessed for AR subtype selectivity through cAMP accumulation assays. The antagonist affinity was determined using Schild analysis (pA2 values) and fluorescent ligand binding. Further, a likely binding pose of the most potent antagonist **K18** was determined through MD simulations using a homology model of A_3R, combined with mutagenesis studies.
Eventually it was suggested that **K18**, which contains a 3-(dichlorophenyl)-isoxazole group connected through carbonyloxycarboximidamide fragment with a 1,3-thiazole ring, is a specific A_3R (<1 µM) competitive antagonist. Structure-activity relationship investigations revealed that loss of the 3-(dichlorophenyl)-isoxazole group significantly attenuated **K18** antagonistic potency. Mutagenic studies supported by MD simulations identified the residues important for binding in the A_3R orthosteric site.
Finally, we introduce a model that enables estimates of the equilibrium binding affinity for rapidly dissociating compounds from real-time fluorescent ligand-binding studies. These results demonstrate the pharmacological characterization of a selective competitive A_3R antagonist and the description of its orthosteric binding mode.

Chapter 5

Insights to the Binding of the Selective Adenosine A_3R Antagonist K18

5.1 Theoretical background

5.1.1 Molecular Mechanics - Poisson Boltzmann Surface Area Method

Calculating binding energies in ligand-receptor complexes is of fundamental importance in finding a candidate drug molecule in this approach [251]. The huge number of interactions between the solvent molecules and the system consisting a ligand A which binds to a receptor R to form a complex R-A hampers the accuracy and increases the accuracy of the calculation of an accurate value for ΔG_{bind}.
The calculation compels a different procedure and Molecular Mechanics - Poisson Boltzmann (MM-PBSA) or Molecular Mechanics - Generalized Born Surface Area (MM-GBSA) methods use the thermodynamic cycle shown in **Scheme 5.1**

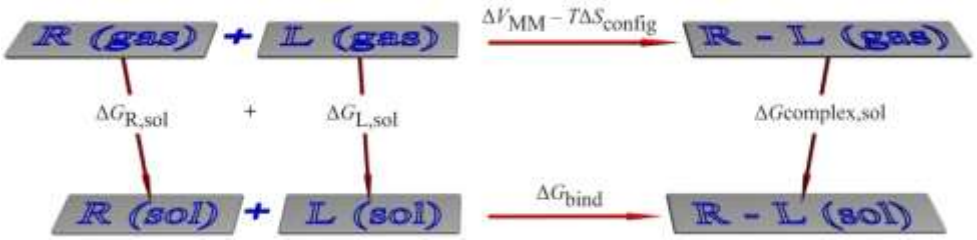

Scheme 5.1. The free energy for the formation of ligand A-receptor R complex can be calculated using the end-points of this thermodynamic cycle including the bound and unbound states of the ligand according to **equation 5.1**[252].

According to thermodynamic cycle the ΔG_{bind} is calculated using equation (5.1)

$$\Delta G_{bind} = \Delta V_{MM} + \left(\Delta G_{sol}^{PL} - \Delta G_{sol}^{P} \quad \Delta G_{sol}^{L}\right) - T\Delta S_{config} \qquad (5.1)$$

If entropy change is taken to be approximately zero or if we compare complexes with similar entropy changes then **equation 5.1** can be transformed to **equation (5.2)** for the calculation of effective binding free energies (ΔG_{eff})

$$\Delta G_{eff} = \Delta V_{MM} + \Delta\Delta G_{sol} \quad (5.2)$$

$$\Delta\Delta G_{sol} = \Delta G_{sol}^{PL} - \left(\Delta G_{sol}^{P} + \Delta G_{sol}^{L}\right) \quad (5.3)$$

ΔV_{MM} defines the interaction energy between the protein and the ligand, as calculated by molecular mechanics in the gas phase, see equations (3.9) or (3.10). ΔG_{sol} is the desolvation free energy for transferring the ligand (L) or the protein (P) or the complex (PL) from water to the binding area calculated using the PBSA or GBSA model. Using an implicit solvent representation for the calculation of the effective binding

energy is an approximation to reduce the computational cost of the calculations. The terms for each complex ΔE_{MM} and ΔG_{sol} are calculated for a molecule of N atoms using **equations (5.4)** and **(5.5)**

$$\Delta V_{MM} = \Delta V_{elec} + \Delta V_{vdW} \quad (5.4)$$

$$\Delta G_{sol} = \Delta G_{P} + \Delta G_{NP} \quad (5.5)$$

In **equation (5.4**) ΔV_{elec} and ΔV_{vdW} are the electrostatic and the van der Waals interaction energies included by ΔV_{MM}, respectively, since bonding terms are neglected.

In **equation (5.5)** ΔG_P is the electrostatic or polar contribution to the free energy of solvation and the term ΔG_{NP} is the non-polar or hydrophobic contribution to the solvation free energy. The polar part of the solvation binding free energy in medium is given by the **equation (5.6)**

$$G_P = -\frac{1}{2}\sum_i q(\mathbf{r}_i)\varphi_i(\mathbf{r}_i) \quad (5.6)$$

The difference in electrostatic energy between water (ε_{solute}=80) and protein (ε_{solute}=1) ΔG_P, for L, P and PL (**see equation (5.3**)), is given by the **equation (5.7)**

$$\Delta G_P = -\frac{1}{2}\sum_i q_i(\varphi_i^{80} - \varphi_i^{1}) \quad (5.7)$$

The calculation of electrostatic potential φ_i needed to compute ΔG_P can be calculated using the Poisson Boltzmann (PB) or Generalized Born (GB) equations. [253]

Thus, for the calculation of electrostatic potential of the solute as function of solute charges, the Poisson – Boltzmann equation (PBE) [254] whicjh is mathematically a three-dimensional second-order nonlinear elliptic partial differential equation. The PBE can be approximated when the ionic strngth and electric field are week to its the linear form given by **equation (5.8)**

$$\nabla\left(\varepsilon(\mathbf{r})\nabla\varphi(\mathbf{r})\right) - \kappa^2\varphi_{RF}(\mathbf{r}) = -4\pi\rho(\mathbf{r}) \quad (5.8)$$

and

$$\kappa^2 = \frac{8\pi q^2 I}{k_B T} \quad (5.9)$$

where q correspond to the partial charges and κ is the Debye-Hückel length. The salt term in the PBE can be linearized when the exponent of the Boltzmann factor is close to zero. However, the approximation apparently does not hold in highly charged biomolecular systems**.** [255,256] Thus, it is recommended that a full nonlinear PBE solver should be used for such systems.

Obtaining analytical solutions of the linearized and nonlinear PBEs is extremely complicated, even in the few simple cases for which they exist. In the past decades, however, several computational methods have been developed to solve the PBE. [257]

In pbsa (a module in the AMBER package, one of the most popular computer tools to solve PBE) [258] four common linear FD PBE and six nonlinear finite difference (FD) solvers are implemented. [259]. Other solver is

ZAP algorithm [260] which was incorporated into the CHARMM package, providing a fast, stable, smooth permittivity model for implicit solvation energy calculations.[145]. Other is the DelPh algorithm. [261] and APBS. [254] The progress made in developing more accurate and efficient solutions to model the electrostatics in biomolecular systems, such as the finite element and boundary element methods, was recently reviewed. [257] In the AMBER 2018 release, [259] two new solvers were added to use NVIDIA GPUs to accelerate the FDPB calculations. [262] The GPU version of pbsa is called pbsa.cuda.

In MD applications, the associated computational costs are often very high, as the PBE needs to be solved every time the conformation of a molecule changes. To solve the problem, the GB model, a faster and more efficient approximation of PBE, has been developed.To reduce the computational cost, the Generalized Born (GB) model can be applied as an approximation of the PB equation [263]. Here, ΔG_P is the contribution of the Coulomb and Born energy in the two dielectric environments according to **equation (5.10)**

$$\Delta G_{el} = -(1-\frac{1}{\varepsilon}) \sum_{i=1}^{N}\sum_{j\neq\neq}^{N}\frac{q_i q_j}{r_{ij}} - \frac{1}{2}(1-\frac{1}{\varepsilon}) \sum_{i=1}^{N}\frac{q_i^2}{R_i} \qquad (5.10)$$

where q_i and R_i are the charges and atomic radii for each atom i from the N atoms. In equation (5.10) the two terms, i.e., Coulomb interaction and Born expression can be merged using the term $\gamma_{kk'}$, which has length dimensions. The $\gamma_{kk'}$ term is a function of diatomic distance and Born radii and the resulting is **equation (5.11)**

$$\Delta G_{el} = -\frac{1}{2}(1-\frac{1}{\varepsilon}) \sum_{k,k'}^{atoms} q_k q_{k'} \gamma_{kk'} \qquad (5.11)$$

where summation refers to atoms k, k' each having a partial charge q. The selection of a succesfull form for $\gamma_{kk'}$ is critical in order equation (5.11) to be a good approximation PB equation. Still proposed functional form given by **equation (5.12)**

$$\gamma_{kk'} = \left(r_{kk'}^2 + R_k R_{k'} e^{\,r_{kk'}^2/d_{kk'}R_k R_{k'}}\right)^{-1/2} \qquad (5.12)$$

where $r_{kk'}$ is the diatomic distance, R_k is the active Born radius of atom k, and $d_{kk'}$ is a parameter, that while can be varied for different pair of atoms, a value of 4 is typically used expression [264–266]. In the simple case of a spherical atom with a centered charge, active Born radius is simply the same as the van der Waals radius of the atom. Generally, the Born radius of atom k depends on the distances between all other atoms in the molecule, and their respective volumes. One way to think about the active Born radius is that it is an average distance to the atom-solvent boundary with the shape having the atom in the molecule. Born radii are complicated to compute, and a number of different numerical and analytical approaches to facilitate these computations have been presented. [265,266]

From **equation (5.12)** the alculation is strongly dependent on the efficient Born radii. The first GB model implemented in the AMBER software package, which is called the GB_{HCT} model (igb = 1), was developed by Hawkins, Cramer, and Truhlar with theparameters described by Case [266 267]. Another widely used GB model, GB_{OBC}, was developed by Onufriev, Bashford, and Case (igb = 2 or 5 in AMBER). [268] In this model, the effective Born radii are readjusted to account for the interstitial spaces between atom spheres missed by the GB_{HCT} approximation. As such, GB_{OBC} has a closer approximation to true molecular volume than GB_{HCT}, albeit in an average sense. The GBn models (igb = 7 or 8 in AMBER) yield results in considerably better

agreement with PB and explicit solvent than the GB_{OBC} models on molecular surfaces of MD snapshots under numerous circumstances.[269] The GBn model, parametrized for peptides and proteins, is not recommended for nucleic acids. The GBn models have also been implemented in CHARMM [145] referring to the works reported by **Brooks et al.**[270]

In fact, the choice of the solute dielectric constant is strictly system-dependent and requires precise study of the binding sites to obtain the most suitable ε_{in}. Although εin is dependent on the characteristics of the binding site (a higher εin for a highly charged binding site and a lower εin for a hydrophobic site), frequently the calculations are best with ε_{in} = 2−4, especially in larger data sets of diverse proteins. [271] For the neuraminidase and α-thrombin systems, which are characterized by highly charged binding sites and the ability to form ion−ion interactions with negatively charged ligands, using ε_{in} = 4 is necessary to achieve good correlation [272] and for more hydrophobic contacts ε_{in} = 2 it is preferred.
Since the atomic charges used to calculate the polar solvation energy have fixed values, they cannot be adapted to respond to the dielectric changes when a solute is solvated in the solvent. Therefore, a charge model that takes the solvent effect into account is critical for the accurate calculation of solvation free energies. Applying a single dielectric constant ε_{in} to describe the heterogeneous dielectric environment of a solute can cause errors.
The application of variable dielectric constants can help to improve the accuracy of binding free energy predictions. The solvation free energy prediction method based on variable dielectric constant (**Scheme 5.2**) was first tested on six pharmaceutically relevant targets, namely, CDK2, fXa, p38_u, PDE10A, human carbonic anhydrase, and p38_pp, in complex with several ligands. They assigned five different εin values (1, 2, 4, 8, and 20) for each type of polar or ionizable residue (Ser, Thr, Asn, Gln, His, Lys, Arg, Asp, or Glu) and assigned the same dielectric constant for the other types of residues. Especially for the systems whose binding sites composed of nonpolar residues and the ligand−receptor electrostatic interactions are negligible (PDE10A and p38_pp), the predictions are not significantly improved. For two distinct data sets using VSGB-1.0, [273] and VSGB-2.0 [274], which use variable dielectric model and a novel energy function, the VSGB-2.0 model may approach the accuracy needed for determining the absolute free energy via linear regression without any conformational sampling.

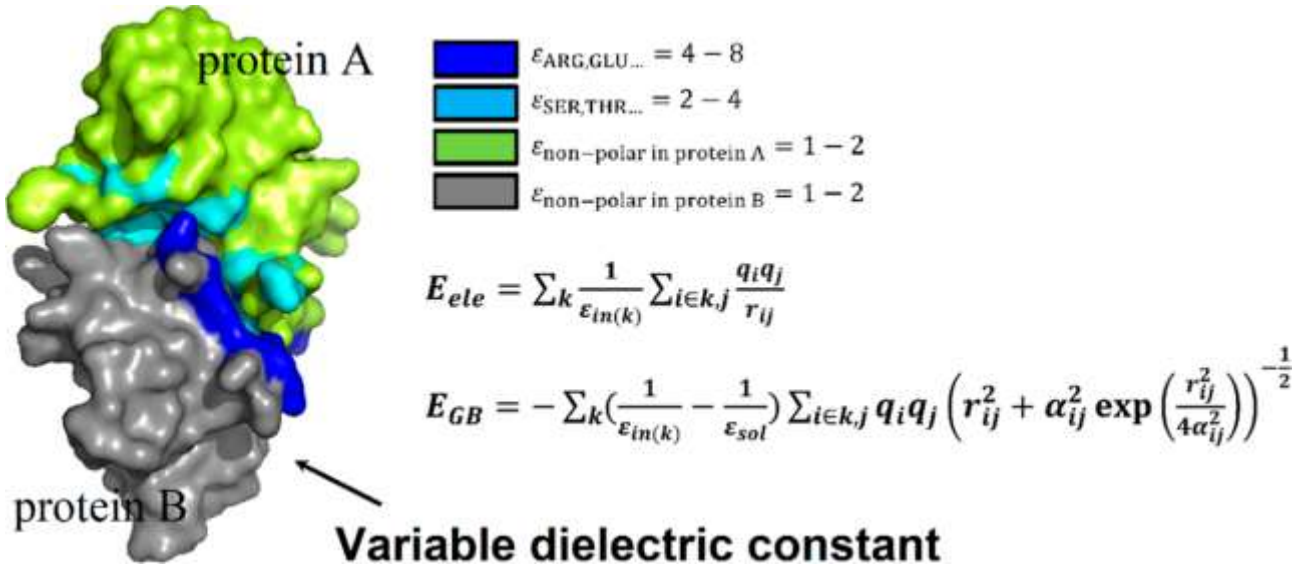

Scheme 5.2 Graphical representation of the variable dielectric constant MM-GBSA method.

The non-polar component of solvation free energy is calculated according to **equation (5.13)** used also by AMBER software

$$\Delta G_{\mathrm{NP}} = \Delta G_{\mathrm{cav}} + \Delta G_{\mathrm{vdW}} = \gamma SASA + \beta \quad (5.13)$$

where SASA (solvent accessible surface area) is the total area that thesolvent can access around solute, γ is surface tension and β is a added as a correction factor. Typical values for γ and β are 0.005420 kcal mol^{-1}Å^{-2} and -1.008000 kcal mol^{-1}, respectively (the non polar energy can be considered to include an energy cost for creating a cavity for the solute inside the solvent and van der Waals interactions between solute and solvent molecules). The limitations of this simplified SASA model have been demonstrated previously. A more modern method in which the nonpolar solvation energy is divided into cavity and dispersion (CD) terms was reported**.** [275] A cavity capable of accommodating the solute in the solvent is created, and then the nonpolar solute is introduced into the cavity. The energy for cavity formation is often estimated using a linear relation to the molecular surface (SASA), similar to the SASA model. Hence, the nonpolar solvation energy should be described as

$$\Delta G_{\mathrm{NP}}^{\mathrm{CD}} = \gamma SASA + \beta + \Delta G_{\mathrm{disp}} \quad (5.13)$$

A solvent-accessible volume (or surface) integration can be utilized to calculate the dispersion term (ΔG_{disp}). The scaling factors are typically set to γ = 0.0378 kcal·mol^{-1}·Å^{-2} and b = −0.569 kcal mol^{-1} in the AMBER package.

Since the continuum models ignore all information about water molecules in water-exposed binding sites including the number and entropy changes) before and after ligand binding sometimes the treatment of the water molecules as a part of the receptor, provided improved results in some cases [276–279] or this approach yielded worse predictions. [280]

Although several attempts have been made, none of the above-mentioned methods (namely, the SASA, CD and PCM methods) can yield accurate predictions for systems with more water-exposed binding sites because the continuum models ignore all information about water molecules (including the number and entropy changes) before and after ligand binding. One approach to solve this problem is to treat the water molecules as a part of the receptor, and improved results have been obtained for some cases; however, the performance is strongly impacted by the number of explicit water molecules, and sometimes this approach yields worse predictions. Another way is to replace the desolvation in MM/GBSA by the free energy combined with displacement of binding-site water molecules upon ligand binding estimated by the WaterMap approach, which yields varying results**.** [281]

Usually the binding free energy methods like MM-PBSA or MM-GBSA are applied in a set of congeneric series of compounds and can provide good accuracy regarding the correlation between calculated ΔG_{bind} and experimental pK_{i} values for K_{i}'s covering a range of 10^3 corresponding to a $\Delta\Delta G_{\mathrm{bind}}$ scale equal to 4-5 kcal mol^{-1}. [108,240,282]. [31]

For two compounds having a K_{i} of 50 μM corresponds and another with K_{i} = 5 μM ΔG_{bind} is 1.5 kcal mol^{-1}, which is well below the accuracy of the MM-PBSA method. In order to calculate accurately smaller differences in affinity more accurate but computationally demanded free energy methods are needed, like FEP/MD, TI/MD etc [283] Our group has previously applied such methods for this narrow range of binding free energies with success [284 285] but this approach cannot be applied for virtual screening purposes.

The computational duration is 50 times longer with the PB model. [286]. The accuracy of the calculated energy using the GB approach is compromised at the expense of computational speed. The correlation and the computational demands make the GB approach attractive, especially for qualitative analysis, though the GB method in principle is not as accurate as PB. [239] However, some studies have shown that optimal prediction of MM-GBSA with a solute dielectric constant of 2.0 is better than using MM-PBSA for 98 ligand complexes. [287]

Besides the applications in virtual screening, the end-point approaches have been also used in the lead optimization stage of drug design campaigns for fast and accurate prediction of the binding affinities of the newly modified compounds. Recently the capability of MM-PB(GB)SA rescoring in lead optimization has been investigated, and more and more advanced molecular simulations and free energy calculations with MM-PB(GB)SA have been successfully applied to the optimization of lead compounds. [108,109]

5.2 Purpose of the work

The experimental $A_{2A}R$ and A_1R structures provide excellent templates for structure-based drug design. [27,288] In contrast, the experimental structure for A_3R has, to date, not been resolved. It has been observed that differences in the residues of the upper region of the orthosteric binding area define the selectivity of ligands against AR subtypes. The lipophilic area in-between extracellular loop (EL)2, TM5,TM6 is unique for A_3R and has a characteristic residue $V169^{5.30}$, while A_1R and $A_{2A}R$ and $A_{2B}R$ have a glutamate acid residue in the same position. [215] The A_3R accommodates ligands having groups of increased lipophilicity fitted in the area close to $V169^{5.30}$. As a first approach, we have used a homology model of A_3R, built based on $A_{2A}R$ in order to study the orthosteric binding area related to the function of this receptor. In another study we performed mutagenesis and intensive computational work to investigate the binding profile of the selective agonist 1-deoxy-1-[6-[[(3-iodophenyl)methyl]amino]-9*H*-purin-9-yl]-*N*-methyl-β-D-ribofuranuronamide (IB-MECA) and the non-selective NECA to A_3R. [241] A fair description was accomplished using homology models for the mutant A_3Rs, MD simulations with the amber99sb force field and MM-GBSA binding free energy calculations. [241]

In Chapter 2, we desribed the results from *in silico* screening of 14400 compounds of Maybridge HitFinder library against the crystal structure of $A_{2A}R$ complex bound with the selective antagonist ZM241385 using a combination of ligand- and structure-based approaches. We identified carbohydroximamide derivatives, like **K5, K8, K10, K11, K17, K32**, as novel and interesting chemical class of AR binders. [61] Among these molecules **K18** is a selective low micromolar binder at A_3R. [61] In a subsequent study, we certified that **K10, K17, K18 and K32**, are potent and selective competitive A_3R antagonists with particular interest for further development, although **K10, K17, K32** are less potent than **K18.** [243] In **Scheme 5.2** are shown the chemical structure of **K18** and analogues, their dissociation constants (Ki) from radiolabelled binding experiments, [61] and antagonistic potencies (pA_2; see **Table 5.1** for definition) determined using a biological assay. [243] In addition, in this current study we have experimentally characterized the effects of the following A_3R mutations: $L90^{3.32}$, $V169^{5.30}$, $M174^{5.35}$, $M177^{5.38}$, $I249^{6.54}$, $I253^{6.58}$, $L264^{7.35}$, $W185^{5.46}/V169^{5.30}$ to alanine and $I253^{6.58}$, $V169^{5.30}$ to glutamate acid within the orthosteric binding area of A_3R to the antagonistic potency of **K18** using functional assays [243].

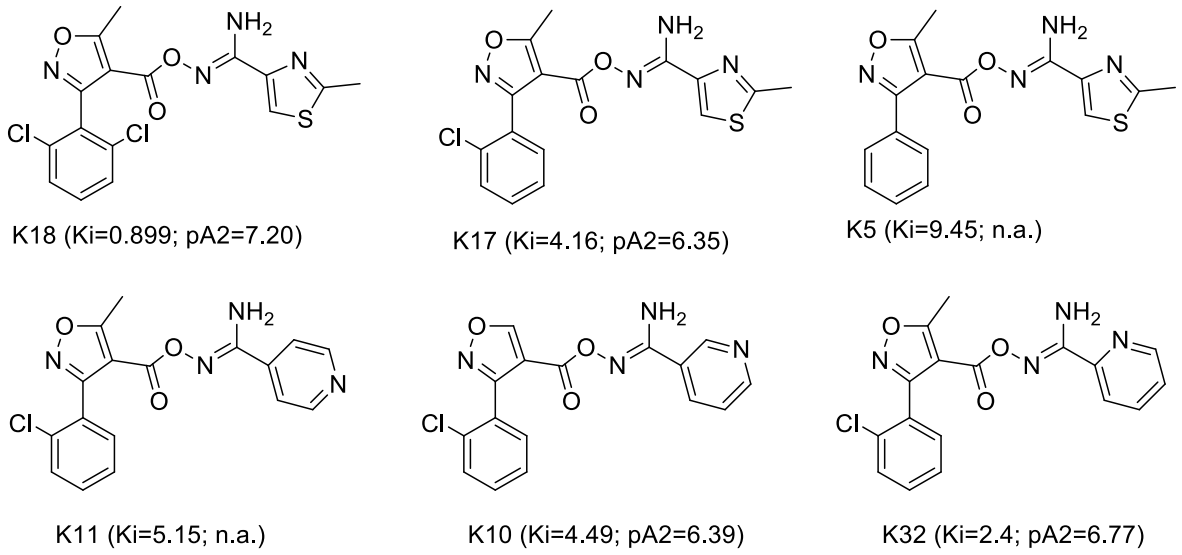

Scheme 5.2 Chemical structures, binding dissociation constants, and antagonist potencies in micromolar concentrations for **K18** and **K11, K10, K32** (n.a. means an inactive compound).

As a continuation of these studies, here we have investigated the binding profile of **K18** at WT A_3R. We have applied MD simulations, MM-PBSA and MM-GBSA calculations to study the binding conformation of **K18** using experimental evidence from mutagenesis results in ref. [243]. Due to the lack of pyridine analogues to **K18** commercially available, we have explored the binding of the pyridine analogues of **K17**, i.e. molecules **K32, K10, K11**, aiming at improving potency of **K18** and getting information for its binding by investigating structure-activity relationships of various parts of the molecule. In the previous study the comparison of antagonistic potency by reducing the number of chloro substituents was explored in the **K18** series**; K5, K17**, **K18**. In an effort to understand the effect of critical residues for binding and interactions of K18 with the orthosteric binding area, we have studied the binding interactions of **K18** with 14 A_3R mutated receptors using MD simulations and MM-GBSA calculations and experimental site-directed mutagenesis results. [243]

5.3 Methods

5.3.1 Preparation of Receptor Structures

The crystal structure of the complex of an inactive form of the WT $A_{2A}R$ (PDB ID 3EML) [20] with ZM241385 was superimposed to a model of an inactive WT A_3R ($N12^{1.32}$ - $H304^{7.75}$) derived from Adenosiland web-service [171] that was built using the crystal structure of $A_{2A}R$ (PDB ID 3EML). The inactive protein conformation of $A_{2A}R$ was removed resulting in a ZM241385-inactive WT A_3R model. In the A_3R WT model, the side chain of $V169^{5.30}$ was rotated as suggested [4] to increase the free space for the accommodation of agonists with bulky substitutions. [4] The ZM241385-inactive $A_{2A}R$ protein complex (PDB ID 3EML) was superimposed to NECA intermediate active $A_{2A}R$ protein complex with PDB ID 2YDV. [156] Then the NECA and inactive protein conformation were removed resulting in a complex of ZM241385 with the intermediate active $A_{2A}R$ form. As a next step, the ARs were optimized using the Protein Preparation Wizard implementation in Schrodinger suite. [289] In this process, the bond orders and disulfide bonds were assigned,

and missing hydrogen atoms are added. Additionally, N- and C-termini of the protein model are capped by acetyl and N-methyl-amino groups, respectively. The systems were subjected in an all-atom minimization using the OPLS2005 force field [290] with heavy atom RMSD values constrained to 0.30 Å.

For the simulations of **K5, K17, K18, K40-K44** with an inactive form of A_3R the complexes were prepared from docking of **K5, K17, K18, K40-K44** to A_3R using as a template correspondingly the structure of WT A_3R in complex with ZM241385 (PDB ID 3EML). The complexes of the ligands with WT A_3R were subjected in minimization using the previously described protocol. [241]

For the simulations of **K18** with an inactive form of $A_{2A}R$ and A_1R the complexes were prepared from docking of **K18** to these receptors using as a template correspondingly the crystal structure of WT $A_{2A}R$ in complex with ZM241385 (PDB ID 3EML) and the crystal structure of WT A_1R in complex with 1-butyl-3-(3-hydroxypropyl)-8-(3-noradamantyl)xanthine (PSB36). [35] The complexes with **K18** were subjected in minimization using the previously described protocol. [241]

After MD simulation of the **K18**-A_3R complex, prepared from docking calculations as is described below, the equilibrated structure was used for the preparation of the mutant receptor models of WT A_3R complex by changing the studied residues to alanine, through the "Build" tool of Maestro. [291] Thus, complexes of K18 with $L90^{3.32}A$, $V169^{5.30}A$, $M174^{5.35}A$, $M177^{5.38}A$, $I249^{6.54}A$, $I253^{6.58}A$, $I264^{7.35}A$, $W185^{5.46}A/V169^{5.30}A$ A_3Rs and with $I253^{6.58}E$, $V169^{5.30}E$ A_3Rs were prepared. All 14 of A_3Rs mutants in complex with **K18** were subjected in minimization using the previous protocol. [241]

5.3.2 Molecular docking calculations

K5, K17 K18 was prepared for docking calculations using Maestro. [135] The ZM241385-WT A_3R model prepared as previously descibed or in subsection 3.3.1 was used as a template for docking of **K18** in the *apo* A_3R. For this purpose, ZM241385, utilized as a reference ligand, and *apo* protein WT A_3R were saved separately. Ligand binding site was defined within 10 Å of ZM241385 coordinates. Molecular docking calculations of the energy minimized form of **K5, K17 K18** were performed using GoldScore [136] and ChemScore [138] scoring functions in GOLD 5.2 software [136,292,293] and 30 genetic algorithm runs. The "allow early termination" option, which terminates ligand searching if the top three solutions have an RMSD difference less than 1.5 Å was inactivated, and the "Generate Diverse Solutions" option, which sets smallest inter-cluster RMSD to 1.5 Å, was activated. All other parameters were set to their default values. The resulting highest-scoring pose had the dichlorophenyl group with an orientation towards TM5, TM6 and the second one had the dichlorophenyl group with an orientation towards TM1, TM2. From now on we will refer to these docking poses as "up TM5,TM6" and "up TM1,TM2". For the investigation of the most likely conformation of **K18** inside the WT A_3R we kept the 6^{th} scored docking pose with the isoxazole-dichlorophenyl instead of the thiazole ring oriented deep in the A_3R. This will be referred as "down" docking pose. The 14 mutant A_3Rs in complex with the best docking pose of **K18** in the WT A_3R were used for molecular docking calculations using the same procedure described above.

5.3.3 Structure-activity relationships for compounds similar to K18

A set of 75 structures were selected from PubMed based on their best similarity with **K18** using TanimotoCombo metric, which is the sum of the ShapeTanimoto (metric of shape) and ColorTanimoto (metric of functional group) scores, [140] and were prepared for docking calculations using Maestro. [135] The energy minimized form of these 75 structures was docked in the inactive form of WT A_3R using Glide XP;

the docking poses produced were subjected to Induced Fit Docking (IFD). [294] The complexes of the twenty highest score ligands with A_3R were subjected to MD simulations and MM-PBSA calculations. The commercially available compounds **K40-K43** (Scheme 1) which contain both 3-(dichlorophenyl)-5-methylisoxazole and thiazole were selected, purchased and biologically tested.

5.3.4 MD simulations between ligands and A_3Rs

5.3.4.1 MD simulations of K5, K17, K18, K40-K44 with WT A_3R

MD simulations with DESMOND. Complexes between the docking poses of **K18**, i.e. "up TM5,TM6", "up TM1,TM2" and "down", and the docking poses "up TM5,TM6" of molecules **K5, K17**, **K40-K44** with the WT A_3R model were inserted in a pre-equilibrated hydrated POPE membrane bilayer. The MD simulations were performed using Desmond v11.1 software [162,295] and the amber99sb force field. The orthorhombic periodic box boundaries were set 15 Å away from the protein atoms. The system contained 150 lipids, 15,000 water molecules corresponding to the TIP3P water model and salt concentration 0.15M NaCl and was built using the System Builder utility of Desmond. [162,176,296] The total number of atoms of each complex was approximately ~70,000. Desmond Viparr tool was used to assign amber99sb force field parameters [297,298] to protein and lipid, and GAFF [184] force field parameters for the ligand. MD simulations were performed at 310 K in order to ensure that the membrane state is above the main phase transition temperature of 298 K for POPE bilayers. [182]

Particle Mesh Ewald (PME) was employed to calculate long-range electrostatic interactions [178,179] with a grid spacing of 0.8 Å. The SHAKE algorithm was used to constrain heavy atom-hydrogen bonds at ideal lengths and angles [189]. Van der Waals and short-range electrostatic interactions were smoothly truncated at 9.0 Å. The Nosé-Hoover thermostat [299] was utilized to maintain a constant temperature , and the Martyna-Tobias-Klein barostat [180] was used to control the pressure. The equations of motion were integrated using the multistep RESPA integrator [181] with an inner time step of 2 fs for bonded interactions and non-bonded interactions within a cutoff of 9 Å. An outer time step of 6.0 fs was used for non-bonded interactions beyond the cut-off. MD simulations were performed using a modification of the default protocol provided by Schrodinger Desmond Maestro v11.1 The protocol consists of a series of restrained minimizations and MD simulations designed to relax the system, while not deviating substantially from the initial coordinates. First, two rounds of steepest descent minimization were performed using a maximum of 2,000 steps and harmonic restraints of 50 kcal mol^{-1} $Å^{-2}$ applied on all solute atoms, followed by 10,000 steps of minimization without restraints. The first simulation was run for 200 ps at a temperature of 10 K in the NVT ensemble with solute-heavy atoms restrained by a force constant of 50 kcal mol^{-1} $Å^{-2}$. The temperature was then raised during a 200 ps MD simulation to 310 K in the NVT ensemble with the force constant retained. The heating was then followed by equilibration simulations. First, two 1 ns stages of NPT equilibration were performed. In the first 1 ns stage, the heavy atoms of the system were restrained by applying a force constant of 10 kcal mol^{-1} $Å^{-2}$ for the harmonic constraints, and in the second 1 ns stage, the heavy atoms of the protein-ligand complex were restrained by applying a force constant of 2 kcal mol^{-1} $Å^{-2}$ to equilibrate solvent and lipids. The replicas of the system were saved every 10 ps. In the production phase, the relaxed systems were simulated in the NPT ensemble conditions for 100 ns. Within this simulation time, the total energy and RMSD of the protein backbone Cα atoms reached a plateau, and the systems were considered equilibrated and suitable for statistical analysis.

MD simulations with AMBER14. The MD simulations were also performed at 310 K using a buffered orthorhombic system in 10 Å distance from the solute atoms with periodic boundary conditions for all the complexes using AMBER14 software. Each complex-bilayer system was processed by the LEaP module in AmberTools14 under the AMBER14 software package. [167] Amberff14SB force field parameters [168] were applied to the protein, lipid14 to the lipids, [183] Generalized Amber Force Field (GAFF) to the ligands [184] and TIP3P [176] to the water molecules for the calculation of bonded, van der Waals and electrostatic interactions. Atomic charges were computed according to the RESP procedure [300] using Gaussian09 [301] and antechamber module of AmberTools14**.** [167] The MD simulations protocols are described in the Supporting Information. In the production phase, the relaxed systems were simulated in the NPT ensemble conditions for 100 ns. Within this simulation time, the total energy and the RMSD of the protein's backbone Cα atoms reached a plateau **(Figure S7)**, therefore the systems were considered equilibrated and suitable for statistical analysis.

MD simulations in explicit solvent were performed using the SANDER module and the new implementation PMEMD. SANDER is the basic MD engine of Amber and was used to do minimization, while PMEMD is the high performance implementation of the MD engine that contains a subset of features of sander and was used for the next steps of MD simulations. [167] MD simulation protocol consists of five stages: a) Minimization, b) Heating, c) Adjustment of density, d) Equilibration and e) Production. The systems were minimized in SANDER by 2500 steps of steepest descent to remove bad contacts and 7500 steps of conjugated gradient minimization in the presence of a harmonic restraint with a force constant of 5 kcal mol^{-1} $Å^{-2}$ on all atoms of protein and ligand and non-bonded cutoff of 8.0 Å. The next stage in MD simulation protocol is to allow the system to heat up from 0 K to 310 K. Langevin thermostat [187] as implemented in Amber14 [167] was used for temperature control employing a Langevin collision frequency of 2.0 ps^{-1}. The system in two consecutive steps to 310 K in the presence of a harmonic restraint with a force constant of 10 kcal mol^{-1} $Å^{-2}$ on all membrane, protein, and ligand atoms. In the first step, systems were heated to 100 K in a NVT of 50 ps length where the adjustment of the density was realized using the Berendsen barostat [188] with a 2 ps coupling time. In the second step, the temperature was raised to 310 K in a NPTγ (with γ = 10 dyn cm^{-1}) simulation of 500 ps length. Subsequently, the systems were equilibrated without restraints in a NPTγ simulation of 1 ns length with T = 310 K and γ = 10 dyn cm^{-1}. The equilibration phase was followed by production simulation for 100 ns with system-specific lengths using the same protocol as in the final equilibration step. The simulation temperature of 310 K was well above the gel to liquid crystalline phase transition temperature of POPE lipids of 298 K. [182] In the NPTγ simulations semiisotropic pressure scaling to p = 1 bar was applied using a pressure relaxation time of 1.0 ps. For the treatment of long-range electrostatic interactions the Particle-mesh Ewald summation method [178,179] was used, and short-range non-bonding interactions were truncated with an 8 Å cutoff. Bonds involving hydrogen atoms were constrained by the SHAKE algorithm,[189] and a time step of 2 fs was used for the integration of the equations of motion. Snapshots recorded every 20 ps during the production MD simulations were considered for analysis. Properties and dynamics of the protein and ligand systems as well as of the membrane were analyzed with the *ptraj* and *cpptraj* modules of AmberTools12.[167] In the production phase, the relaxed systems were simulated in the NPT ensemble conditions for 100 ns. Within this simulation time, the total energy and the RMSD of the protein's backbone Cα atoms reached a plateau, therefore the systems were considered equilibrated and suitable for statistical analysis.

5.3.4.2. MD simulations of K18 with mutant A_3Rs

The stability of the complexes between **K18** and the 14 mutant A_3Rs was investigated using MD simulations for 100 ns with Desmond v11.1 and the amber99sb force field using the MD simulation protocol described above. Within this simulation time, the total energy and RMSD of the of the protein backbone Cα atoms reached a plateau, and the systems were considered equilibrated and suitable for statistical analysis.

5.3.4.3 Analysis of MD simulations trajectories

The visualization of produced trajectories was performed using the GUI of Maestro [295] and the protein-ligand interaction analysis was done with the Simulation Interaction Diagram (SID) tool, available with Schrodinger Desmond v. 11.1. [295,162] For hydrogen bond interactions, a distance of 2.5 Å between donor and acceptor heavy atoms, and an angle ≥120° between donor-hydrogen-acceptor atoms and ≥ 90° between hydrogen-acceptor-bonded atom were considered. Non-specific hydrophobic contacts were identified when the side chain of a hydrophobic residue fell within 3.6 Å from a ligand's aromatic or aliphatic carbon, while π-π interactions were characterized by stacking of two aromatic groups face-to-face or face-to-edge. Water-mediated interactions were characterized by a distance of 2.7 Å between donor and acceptor atoms, as well as an angle ≥ 110° between donor-hydrogen-acceptor atoms and ≥ 80° between hydrogen-acceptor-bonded atom. The visualization of produced trajectories and structures was performed using the programs Chimera [174] and VMD. [302] All the MD simulations were run on GTX 1060 GPUs in lab workstations or on the ARIS Supercomputer.

5.3.5 MM-PBSA and MM-GBSA calculations

The effective binding free energies (ΔG_{eff}) of the complexes between **K5, K17,** the three docking poses of **K18**, the docking poses of **K40-K43** and WR A_3R were computed considering the gas phase energy and solvation free energy contributions to binding [303] using the 1-trajectory MM-PBSA and MM-GBSA approach. [108,239,240,253] Prior to the calculations all water molecules, ions, and lipids were removed, and the structures were positioned such that the geometric center of each complex was located at the coordinate origin. In these calculations, a dielectric constant of $\varepsilon_{solute} = 1$ was assigned to the binding area and $\varepsilon_{solute} = 80$ for water.

For MM-PBSA calculations, molecular mechanics energies and the non-polar contribution to the solvation free energy were computed with the *mmpbsa.pl* module [286] of Amber14 [167]Structural ensembles for each complex were extracted every 50 ps from the last 50 ns (and thus the snapshots are not correlated) of the production simulation, where RMSD values of the heavy atoms of the binding site included the ligand reached a plateau.

For MM-GBSA calculations the relevant module in Schrodinger Suite was used, i.e. the thermal_mmgbsa.pyscript that takes individual trajectory snapshots and calculates ΔG_{eff} and its energetic contributions. The script thermal_mmgbsa.py takes individual trajectory snapshots and calculates ΔG_{eff} and its energetic contributions. Prime's thermal_mmgbsa.py uses the OPLS2.1/3/3e force field and the refined VSGB 2.1 solvation model. **(J. Li et al. 2011)** Snapshots from the equilibrated region of MD simulation trajectory for each A_3R-ligand complex are extracted every 40 ps, of the of the production part.

5.3.6 Biological methods

5.3.6.1 Cell lines and cAMP assays

Stable mutant A_3R Flp-In-CHO cell lines were generated and maintained as previously described. [243, 241] cAMP inhibition experiments were conducted using a LANCE® cAMP kit as described previously. [232] Briefly, Flp-In-CHO cells stably expressing mutant A_3R were seeded at a density of 2000 cells per well of a white 384-well optiplate and stimulated for 30 min with a range of IB-MECA concentrations, with or without K18, in the presence of 0.1% bovine serum albumin, 25 μM rolipram and 10 μM forskolin (to enable detection of the A_3R-mediated inhibition of cAMP production). The concentration of DMSO was maintained at 2% for all cAMP assays.

5.3.6.2 Compounds

IB-MECA was purchased from Sigma-Aldrich and dissolved in dimethyl-sulphoxide (DMSO). K18 and K40-43 (Scheme S1) were purchased from e-molecules and dissolved in DMSO.

5.3.6.3 Data analysis of biological experiments

All in vitro assay data were analyzed using Prism 8.0 (GraphPad software, San Diego, CA), with all dose-inhibition curves fitted using a 3-parameter logistic equation to calculate response range and pIC_{50}. Dose-inhibition response curves were normalized to forskolin inhibition relative to IB-MECA. The data and statistical analysis comply with the recommendations on experimental design and analysis in pharmacology. [243] Schild analysis was performed to obtain pA_2 values (the negative logarithm to base 10 of the molar concentration of an antagonist that makes it necessary to double the concentration of the agonist to elicit the original submaximal response obtained by agonist alone) [237] for antagonists at mutant A_3R. The slope was constrained to unity giving an estimate of antagonist affinity (pK_B) in cases where the Schild slope did not differ significantly from unity.

5.4 Results & Discussion

5.4.1 Validation of the force field for the MD simulations

Since there is no experimental structure for A_3R, in a previous study [241] we tested how different force fields describe the interactions between agonist NECA and the orthosteric binding area of $A_{2A}R$ and compared with experimental structure of the complex between NECA and A_{2A} active-like form. [156] We found that amber99sb can accurately describe the interactions as well as the conformation of helical TM regions. [241] Here, we have explored the conformational changes of active-like state of $A_{2A}R$ upon ZM241385 binding towards an inactive state of $A_{2A}R$, [7,8,10] using 500 ns MD simulations of ZM213485 in complex with the active-like conformation of $A_{2A}R$ (PDB ID 2YDV) [156] in hydrated POPE bilayers.

After 300 ns of simulation of the active-like $A_{2A}R$ form [156] in complex with ZM241385 the receptor adopted an inactive-like conformation of $A_{2A}R$ with an RMSD of c.a. 2 Å compared to the PDB ID 3EML (**Figure 5.1**). The observed conformational changes are: (a) Decrease in the distance between TM3-TM6 **Figure**

5.1A,B); the distance between R102$^{3.50}$ and A232$^{6.34}$ Cα carbons changes from 11 to 7.5 Å (**Figure 5.1C**). (b) Decrease in the distance between TM3-TM5; the distance between I104$^{3.52}$ and I200$^{5.61}$ Cα carbons decreases from 11 to 9.8 Å. (c) Significant change in χ_1, χ_2 dihedrals values of residue W243$^{6.48}$ from -80º, -120º to -70º, +90º respectively; this change in the dihedrals causes W243$^{6.48}$ indole ring placement almost horizontal to TM3. (d) Formation of the ionic lock between R102$^{3.50}$ and E228$^{6.30}$ (**Figure 5.1B**). These observations reveal that amber99sb force field is sensitive in describing the active-like $A_{2A}R$ receptor conformational changes when is bound to an antagonist and is suitable for the simulations between **K18** and analogues in complex with WT and mutant A_3Rs.

Such studies have been previously performed. For example, a study on the complexes between agonists and the active form of β_2 adrenergic receptor receptor aiming at observing several forms in the conformational space (active-inactive state of the receptor) using both convenient and accerelated MD simulations and as starting structures the complex between an agonist and the active from or the empty active form of the receptor [304] using, like accerelated MD or metadynamics. [305] Towards this aim μs MD simulations were also [306–309]

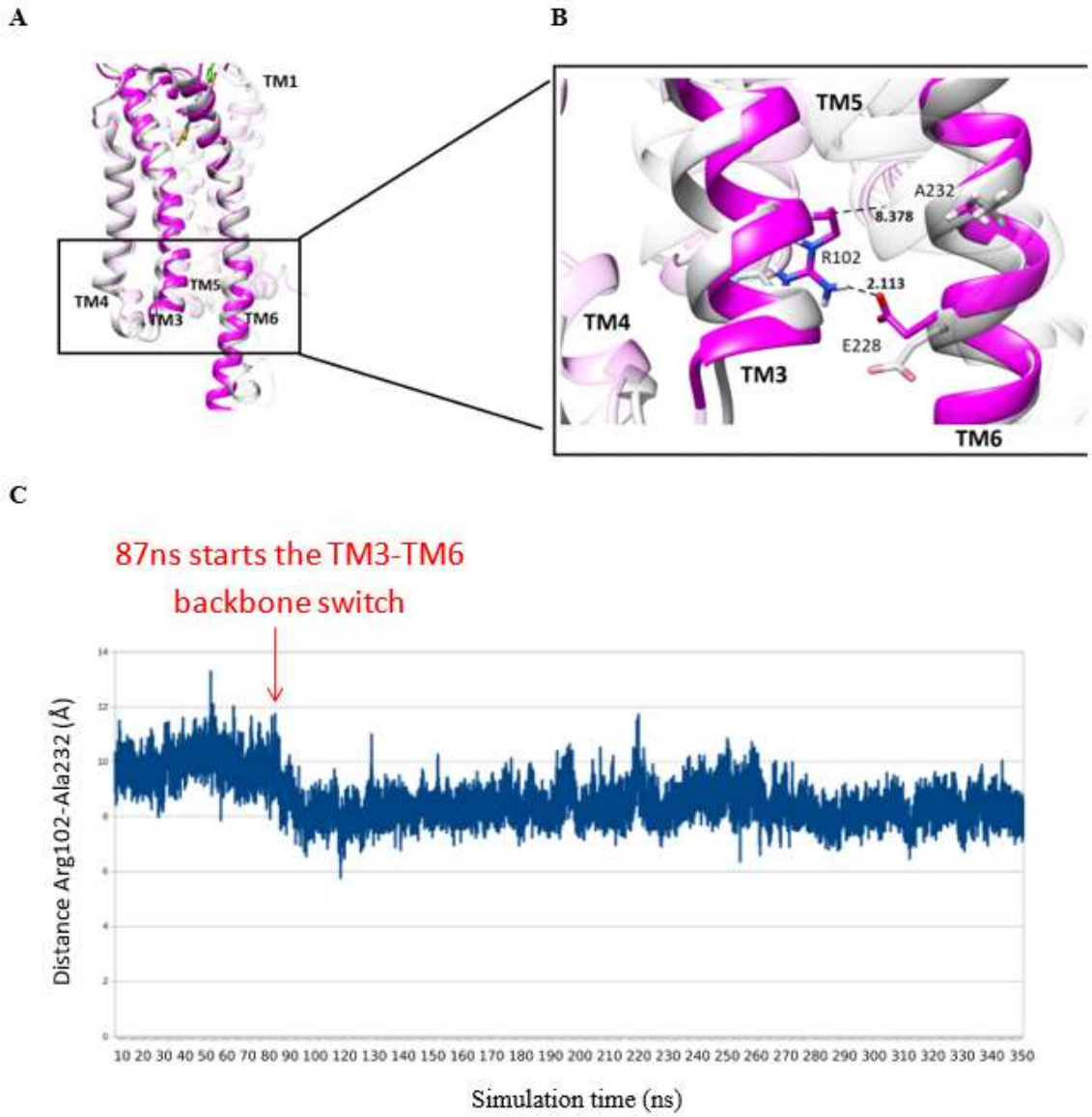

Figure 5.1 (A), (B) The decrease in the distance between TM3-TM6 caused the formation of the ionic lock between R102$^{3.50}$ and E228$^{6.30}$. (C) Separation between TM3-TM6 in the 350 ns MD simulation; the distance between R102$^{3.50}$ and A232$^{6.34}$ Cα carbons decreased from ca 11 to 7.5 Å.

5.4.2 MD simulations K18 and analogues in complex with WT A_3R

The three docking poses "up TM5, TM6", "up TM1, TM2", "down" of **K18** at WT A_3R were embedded in membrane bilayers and the stability of the complexes was investigated using MD simulations coupled with binding free energy calculations using MM-PBSA [239,303] or MM-GBSA method and mutagenesis results which describe properties of the **K18** binding conformation in the complex with A_3R investigated experimentally. The MD simulation with the "up TM5, TM6" docking pose as starting structure converges in a stable "up TM5, TM6" conformation of **K18** inside the orthosteric binding area with an $RMSD_{lig}$ of less than 2 Å compared to the starting docking pose**.** [243] Interestingly, the MD simulations show that starting from the "up TM1, TM2" docking pose, phenyl-oxazolyl and also N-O bonds are rotated producing a conformation with the dichlorophenyl oriented again towards TM5, TM6 (**Figure 5.2A**). This generated a relative binding free energy of ca $\Delta\Delta G_{eff}$ = + 3.8 kcal mol^{-1} compared to "up TM5, TM6" conformation (**Figure 5.2B**) according to both MM-PBSA and MM-GBSA calculations. Starting from "down" docking pose the MD simulation produces an unstable complex of K18 in which the ligand loses binding interactions and shifts away from the binding area (**Figure 5.2C**).

The MD simulations of "up TM5, TM6" conformation of **K18** in complex with WT human A_3R show that the most frequent contacts, i.e. >20% of the MD trajectory, involve V72$^{2.23}$, L90$^{3.32}$, F168$^{5.29}$, V169$^{5.30}$, M177$^{5.38}$, L246$^{6.51}$, I249$^{6.54}$, N250$^{6.55}$, [243] and less than 15% of the MD trajectory include interactions of the ligand with V65$^{2.16}$, I186$^{5.47}$ and L264$^{7.35}$. Van der Waals contacts between the protein binding area and **K18** are shown in the interaction plot in **Figure 5.2D**, only if the side chain of the amino acid fell within 3.6 Å from the ligand. **Figure 2B** shows that the phenyl group of the 3-phenyl-isoxazole interacts through attractive van der Waals forces with V169$^{5.30}$ and I249$^{6.54}$ and isoxazole has an aromatic π-π stacking interaction with the phenyl group of F168$^{5.29}$. Nitrogen and oxygen atoms of isoxazole are hydrogen bonded with NH groups of F168$^{5.29}$ or V169$^{5.30}$. Thiazolyl group is hydrogen bonded with N250$^{6.55}$ and has van der Waals interactions with L90$^{3.32}$, M177$^{5.38}$, L246$^{6.51}$ and V72$^{2.23}$.

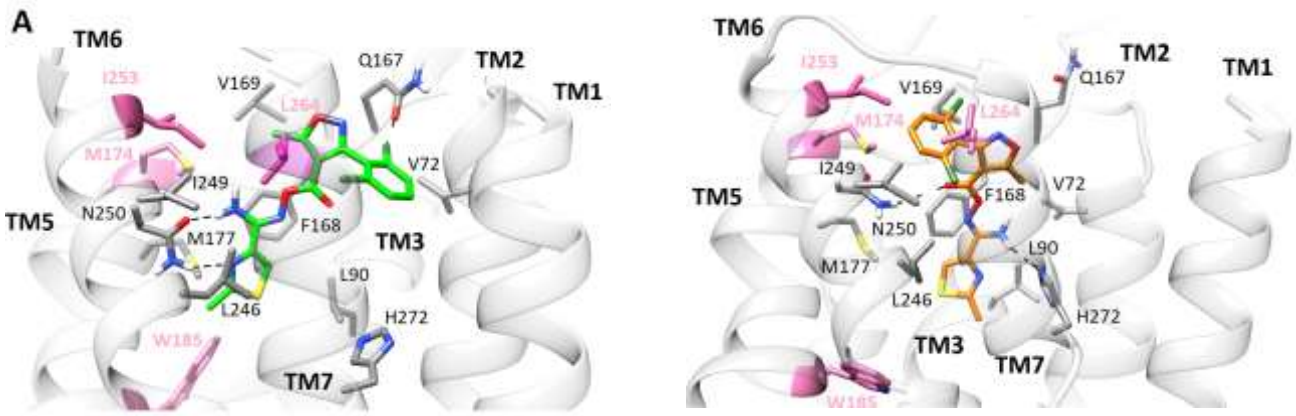

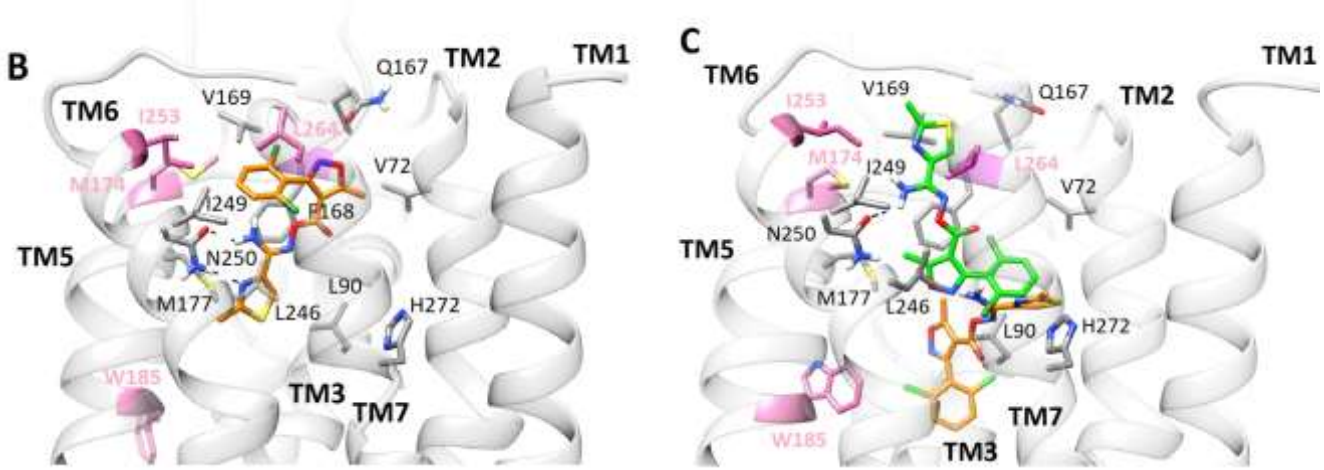
B
TM6
TM5
TM3
TM7
TM2
TM1
Q167
V169
I253
L264
M174
V72
I249
F168
N250
L90
M177
L246
H272
W185
C
TM6
TM5
TM3
TM7
TM2
TM1
V169
Q167
I253
M174
I249
L264
V72
N250
M177
L246
L90
H272
W185

D

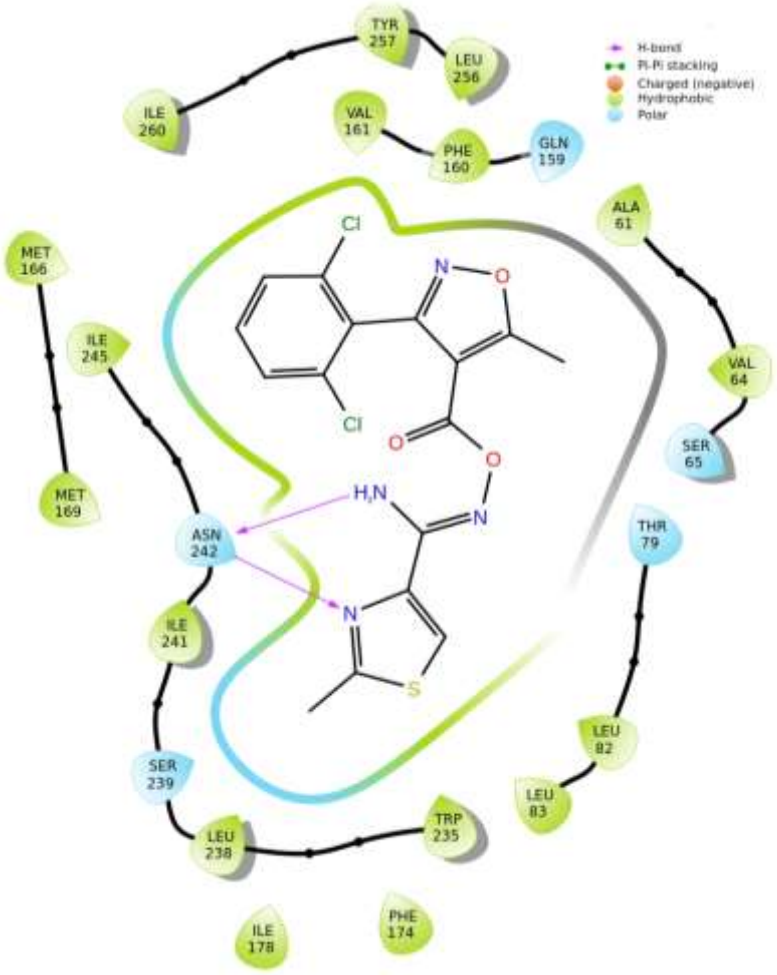
H-bond
Pi-Pi stacking
Charged (negative)
Hydrophobic
Polar
TYR 257
LEU 256
ILE 260
VAL 161
PHE 160
GLN 159
ALA 61
MET 166
ILE 245
VAL 64
SER 65
MET 169
ASN 242
THR 79
ILE 241
LEU 82
LEU 83
SER 239
TRP 235
LEU 238
PHE 174
ILE 178
Cl
Cl
N
O
O
O
N
H2N
N
S

E

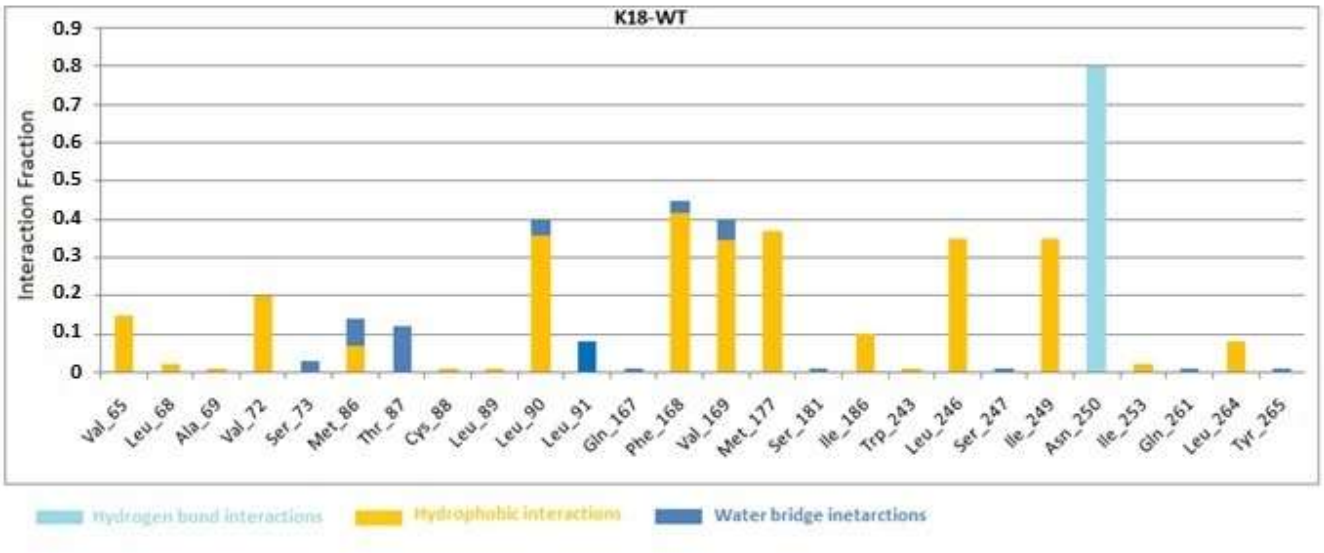

Figure 5.2 (A) (left) Starting structure of **K18** in the "up TM1, TM2" docking pose (carbon atoms in green) inside WT A_3R and (right) average structure from 100 MD simulations (carbon atoms in yellow). (B) Average structure of **K18** from 100 MD simulations in the "up TM5, TM6" conformation (carbon atoms in yellow), and (C) Starting structure of K18 in the "down" docking pose (carbon atoms in green) inside WT A_3R and average structure from 100 MD simulations showing the ligand (carbon atoms in yellow). The side chains of residues that have interaction frequency ≥ 0.2 are separated by less than 3.6 Å from the ligand and are displayed as gray sticks. Protein structure is displayed in grey ribbons. In pink residues which were mutated to alanine but are more than 4 Å apart from the ligand are displayed. Hydrogen atoms are omitted except for those involved in hydrogen bond interactions which are highlighted as black dashed lines. (D), (E) Receptor-ligand interactions and interactions histogram plot of **K18** "up TM5, TM6" conformation inside A_3R for 150 ns of MD simulations. Hydrogen bonding interactions bar is depicted in light blue, van der Waals in yellow, water bridges in blue. Bars are plotted for residues with interaction frequencies ≥ 0.2.

MM-PBSA calculations further support the "up TM5, TM6" conformation of **K18** since, as described in ref. [243], the calculated ΔG_{eff} values for **K18** and the two analogs **K17, K5,** with one or no chlorine atoms (**Scheme 5.2**), are in agreement with experimental binding affinities and antagonistic potency ranking. [243] **K17** having one chlorine atom in the phenyl ring is also a potent antagonist with a similar binding profile to **K18** shown in **Figure 5.3**; see also **Figure 5.2D**). [243] In contrast, **K5** with no chlorine atoms lacks antagonistic potency (see also **Figure 4.8**).

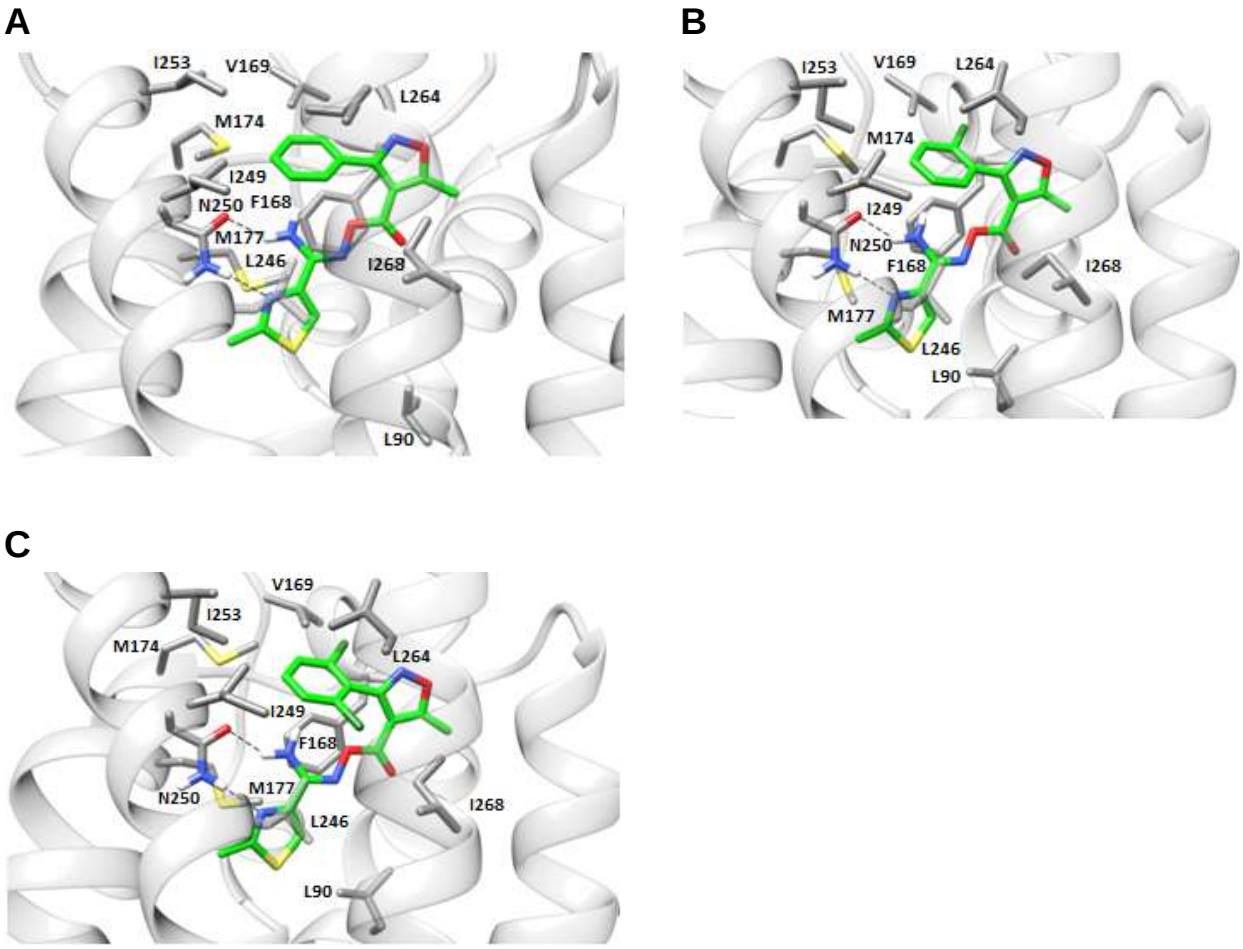

Figure 5.3 (A), (B) and (C) Average structures of **K18** (Ki=0.899 μM; pA2= 7.20), **K5** (Ki=9.45 μM; not active) and **K17** (Ki=4.16 μM; pA2= 6.35), respectively, in complex with A_3R from 100 MD simulations.

Table 5.1 Effective binding energies (ΔG_{eff}) and energy components (E_{vdW}, E_{EL}, ΔG_{solv}) in kcal mol^{-1} calculated using the MM-PBSA method for binding of **K5, K17** and **K18** to the A_3R orthosteric binding area.

	E_{vdW}[a]	E_{EL}[b]	$\Delta\Delta G_{sol}$[c]	ΔG_{eff}[d]	pK_B/pK_i[e]		
					Schild analysis[f]	***NanoBRET***[g]	***Radioligand binding***[h]
MRS 1220					10.07	9.99 ± 0.04	8.2-9.2
K5	– 42.0 ± 2.7	– 9.6 ± 5.2	30.8 ± 4.3	-20.8 ± 4.3	ND	6.06 ± 0.09	5.02
K17	– -47.0 ± 2.4	– 8.8 ± 2.7	29.8 ± 2.9	-25.9 ± 3.6	6.35	6.33 ± 0.03	5.38
K18	– 46.3 ± 2.9	– 7.5 ± 2.4	26.9 ± 3.1	-26.9 ± 2.7	7.20	6.92 ± 0.10	6.05

[a] Van der Waals energy of binding calculated using molecular mechanics with amber ff14.

[b] Electrostatic energy of binding calculated using molecular mechanics with amber ff14.

[c] Difference in solvation energy between the complex, the protein and the ligand, i.e. $\Delta\Delta G_{sol} = \Delta G^{PL}{}_{sol}$-($\Delta G^{P}{}_{sol} + \Delta G^{L}{}_{sol}$)[d] , see **equation (5.3)**.

[d] Effective binding free energy calculated as $\Delta G_{eff} = \Delta E_{MM} + \Delta\Delta G_{sol}$ in **Table 5.1**, $\Delta V_{MM} = \Delta V_{vdW}$ +

ΔV_{EL} (see **sub-section 5.1.1**).

[e] Equilibrium dissociation constant of MRS 1220, **K5, K17** and **K18** as determined through three independent experimental approaches: Schild analysis (pK_B), NanoBRET (pK_i).

[f] pK_B obtained through Schild analysis in A_3R stably expressing Flp-In CHO cells. [243]

[g] pK_i (mean ± sem) obtained in NanoBRET binding assays using Nluc-A_3R stably expressing HEK 293 cells and determined through fitting our "Kinetics of competitive binding, rapid competitor dissociation" model or in the case of MRS 1220 through fitting with the 'Kinetics of competitive binding' model with a determined K_{on} (k_3) and K_{off} (k_4) rate of 3.25 ± 0.28 x 10^8 M^{-1} min^{-1} and 0.0248 ± 0.005 min^{-1}, respectively

[h] pK_i values previously published for **K5**, **K17** and **K18** or **MRS 1220** [235,310] through radioligand binding assays

GoldScore ranking of "up TM1, TM2", "up TM5, TM6" and "down" binding poses for **K18** and ranking of "up TM5, TM6" binding pose for **K10, K11, K32** against the WT A_3R are in agreement with experimental findings (**Table S5.1**); less accurate are the ChemScore values. However, the binding poses cannot provide information about the dynamic behavior of **K18** inside the binding area. For example, the docking calculations cannot describe that the "up TM5, TM6" binding pose of **K18** is unstable and the ligand undergoes a conformational change, as described earlier.

Compounds **K11**, **K10** and **K32** are analogues of **K17** having a pyridinyl substituent, instead of 1,3-thiazolyl, which is linked with carbonyloxycarboximidamide linker through C4, C3 and C2 pyridinyl carbons, respectively. **K11, K10** and **K32** have more similar structure to K17 compared to **K18**, having only one chlorine atom in the phenyl ring (**Figure 5.4**). **K32, K10** show potent antagonistic potency while **K11** is inactive. The MD simulations show that **K32, K11, K10** can bind to A_3R through the "up TM5, TM6" conformation. The simulations suggest that compared to **K11** and **K10**, **K32** forms an additional hydrogen bond interaction between 2-pyridinyl nitrogen and $N250^{6.55}$ (**Figure 5.4C**) which is in agreement with the 2-fold higher affinity than **K10** and **K11**. **K10** forms a hydrogen bond between pyridinyl nitrogen and $S247^{6.52}$ (**Figure 5.4B**). The binding free energy values ΔG_{eff} from MM-PBSA calculations fairly agree with experimental binding affinities ranking (**Table 5.1**) which support also the "up TM5, TM6" binding conformation model for **K18**. The biological assays show that K32 and K10 are competitive antagonists with similar potencies to **K17**, but **K11** showed no antagonistic potency (below the tested concentration of 10 µM) and suggests that antagonistic potency cannot always be correlated directly with affinity [61] (**Table 5.2**).

Table 5.2 Effective binding energies (ΔG_{eff}) and energy components (E_{vdW}, E_{EL}, ΔG_{solv}) in kcal mol^{-1} calculated using the MM-PBSA method for **K10**, **K11** and **K32** binding to the A_3R orthosteric site

	E_{vdW} [a]	E_{EL} [b]	$\Delta\Delta G_{sol}$ [c]	ΔG_{eff} [d]	Schild analysis [e]	Radioligand binding [f]
			Conformation "up TM5, TM6"			
K10	– 39.7 ± 0.2	– 9.0 ± 0.2	23.7 ± 0.2	- 25.0 ± 0.2	6.39 ± 0.3	4.49
K11	– 38.7 ± 0.2	– 9.7 ± 0.1	23.9 ± 0.2	-24.4 ± 0.2	n.a.	5.15
K32	– 39.3 ± 0.2	– 6.6 ± 0.2	20.0 ± 0.2	-25.8 ± 0.2	6.77 ± 0.3	2.40

[a] Van der Waals energy of binding calculated using molecular mechanics and amber ff14.

[b] Electrostatic energy of binding calculated using molecular mechanics and amber ff14.

[c] Difference in solvation energy between the complex, the protein and the ligand, i.e. $\Delta\Delta G_{sol} = \Delta G^{PL}_{sol}$-

(ΔG^{P}_{sol} + ΔG^{L}_{sol}), see **equation (5.3)**.

[d] Effective binding free energy calculated as $\Delta G_{eff} = \Delta E_{MM} + \Delta\Delta G_{sol}$ in **Table 5.1**, $\Delta V_{MM} = \Delta V_{vdW}$ + ΔV_{EL} (see **sub-section 5.1.1**).

[e] Equilibrium dissociation constant of MRS 1220, **K5, K17** and **K18** as determined through three independent experimental approaches: Schild analysis (pK_B), NanoBRET (pK_i) (see **Table 5.1**)

[f] pK_i values previously published for **K5**, **K17** and **K18** through radioligand binding assays assays [61]

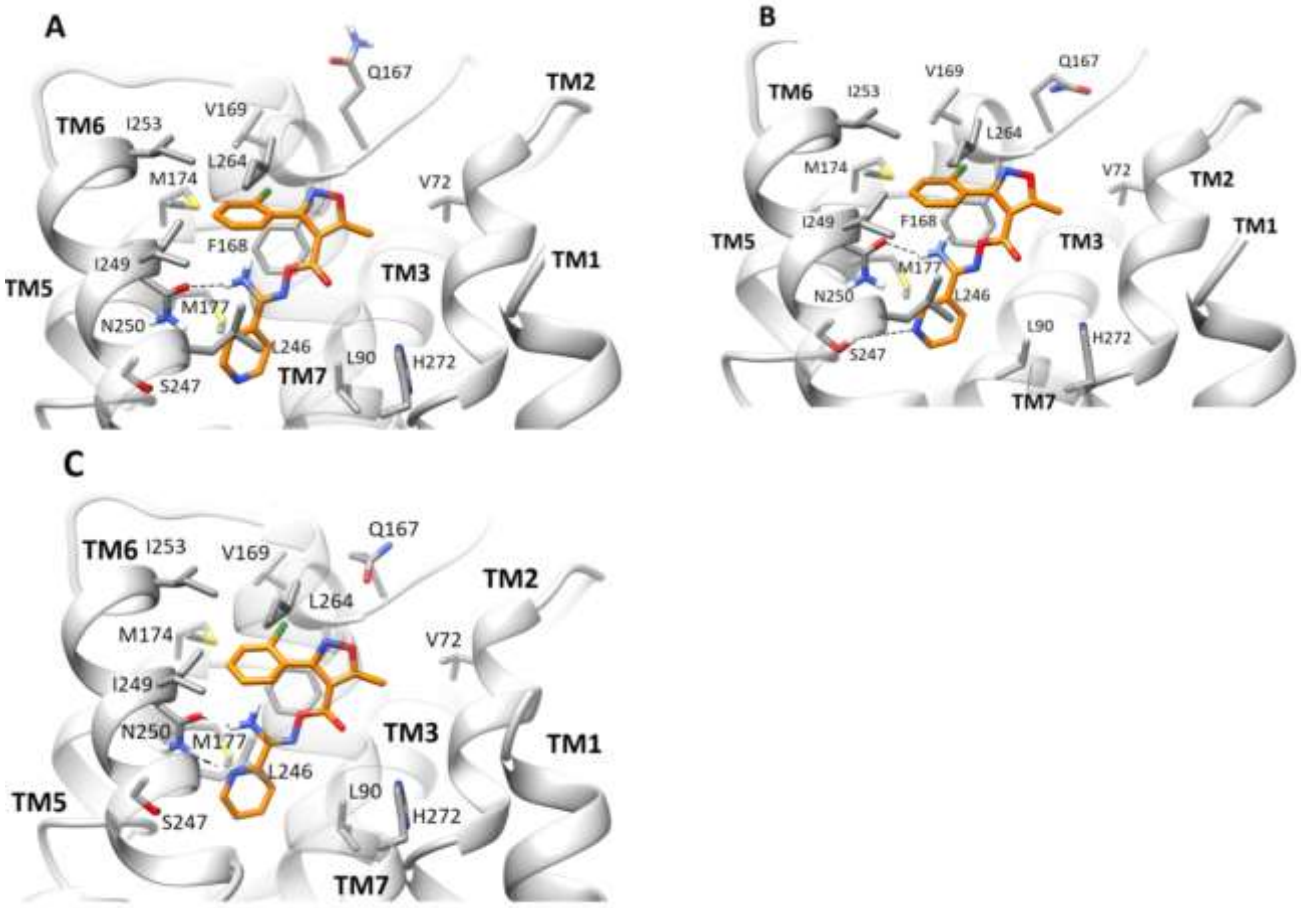

Figure 5.4 (A)-(C) Average structure of **K11, K10** and **K32** in the "up TM1, TM2" conformation inside WT A_3R from 100 MD simulations (carbon atoms in yellow). Protein structure is displayed in grey ribbons. Hydrogen atoms are omitted except for those involved in hydrogen bond interactions which are highlighted as black dashed lines.

Searching in commercial libraries using similarity-based parameters for **K18**, i.e. the TanimotoCombo [140] coefficient with a value > 0.85, we found only compounds **K40-K43** which include the chlorophenyl-5-methylisoxazole and the 2-methyl-1,3-thiazole fragments of **K17**, but connected through a different linker (**Scheme 5.3**).

We selected and tested compounds **K40-K43** which, compared to **K18**, include its two heterocyclic fragments, i.e. the chlorophenyl-5-methylisoxazole and the 2-methyl-1,3-thiazole connected through a different linker. The linker in compounds **K40-K43** connects the 4-isoxazole carbon with 2-thiazole carbon and it contains a carboxamide group connected with a piperazino-methyl group, or a phenyl group, or an

ethylene bridge in **K40, K41**, and **K42**, respectively (**Scheme 5.3**). The highly lipophilic compound **K43** was also tested.

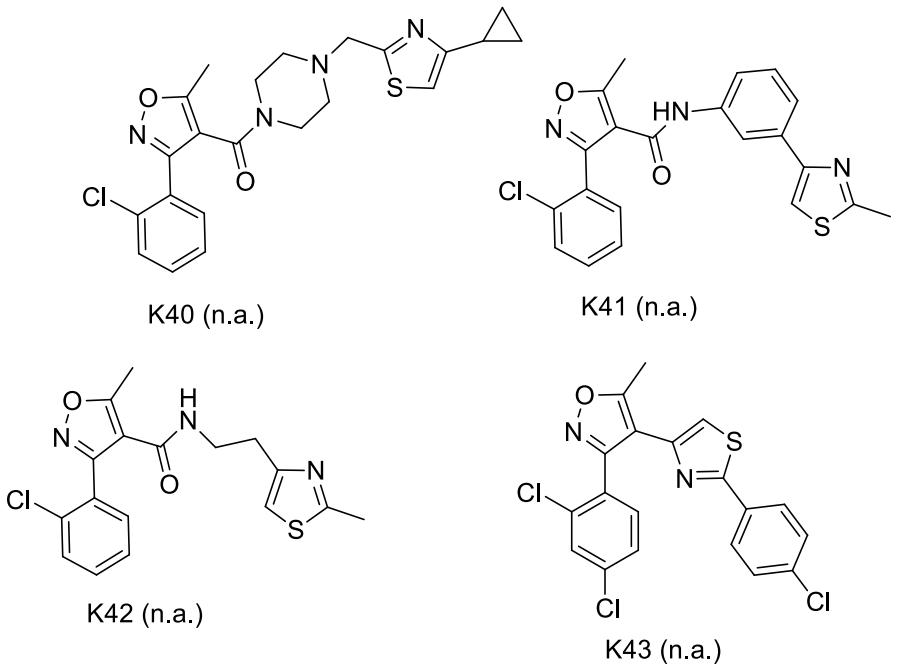

Scheme 5.3 Compounds **K40-K43**, contain similarly to **K18**, o-chlorophenyl-5-methylisoxazole and 2-methyl-1,3-thiazole fragments which are connected with a different linker in **K18**. **K40-K43** were tested and found to be inactive (n.a.) in functional assays, highlighting the importance of the carbonyloxycarboximidamide linker in **K18** for binding to A_3R.

All compounds were inactive as antagonists and consistently MD simulations show unstable binding for **K40-K43** against WT A_3R (**Figure 5.5**). The MD simulations with amber99sb showed that **K40-K43** produce unstable complexes when bound to A_3R with the chlorophenyl group is oriented either towards TM5, TM6 or TM1, TM2. With amber14sb, **K40** and **K41** remained inside the binding area with chorophenyl oriented towards TM1, TM2 (**Figure 5.5**). This binding conformation included few attractive interactions with $F168^{5.29}$, $L246^{6.51}$, $N250^{6.55}$ but lost important van der Waals interactions with $L90^{3.32}$, $V169^{5.30}$, $M177^{5.38}$, $I249^{6.54}$ which are formed through the "up TM5, TM6" conformation. The "up TM5, TM6" conformation of **K41** and **K43** is not stable probably due to the linker's short length between chlorophenyl-lisoxazole and 1,3-thiazole (**Figure 5.5A**) and in **K40** because the linker it is too long. In K42 the linker which contains two methylene groups is very flexible and the entropic cost for binding is high. None of the compounds exhibited antagonistic potency at the A_3R. In contrast in **K18** the two heterocyclic fragments are connected with the polar carbonyloxycarboximidamide linker which contributes to the stable binding inside WT A_3R through forming two hydrogen bond interactions with side chain $N250^{6.55}$.

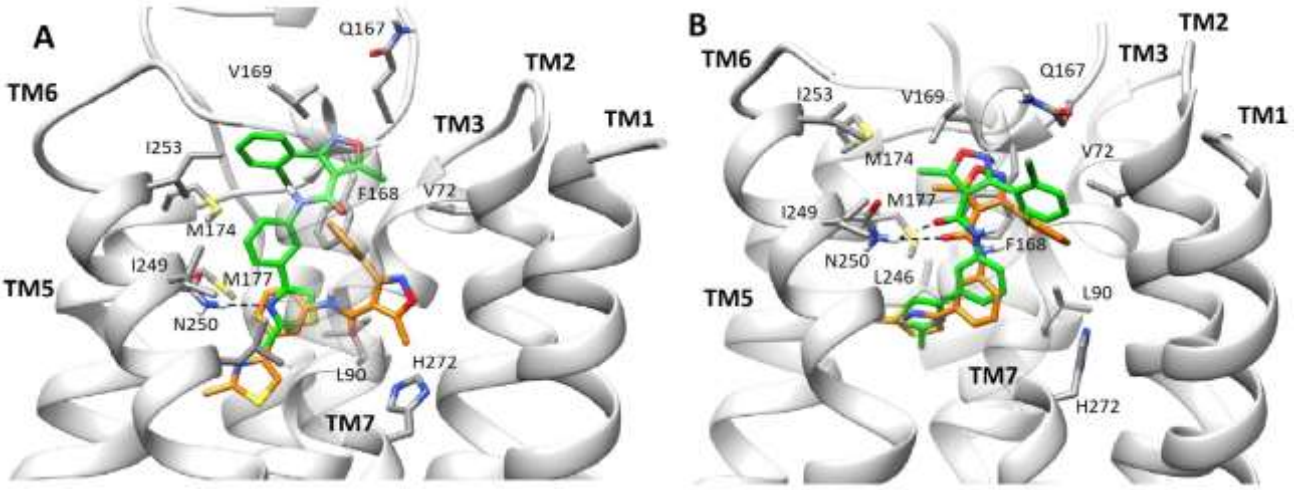

Figure 5.5 (A) Starting structure of **K41** in the "up TM5, TM6" conformation (carbon atoms in green) inside WT A_3R and average structure from 100 MD simulations using the amber14sb (carbon atoms in yellow), (B) Starting structure of **K41** in the "up TM1, TM2" conformation (carbon atoms in green) inside WT A_3R and average structure from 100 MD simulations using the amber14sb (carbon atoms in yellow). The side chains of residues involved in ligand binding, separated by 3.6 Å from the ligand and having interaction frequencies ≥ 0.2 are displayed as gray sticks. Protein structure is displayed in grey ribbons. Hydrogen atoms are omitted except for those involved in hydrogen bond interactions which are highlighted as black dashed lines.

5.4.3 Simulations of K18 in complex with mutant versions of A_3R

5.4.3.1 MM-GBSA binding free energy calculations

In order to investigate computationally the interactions for each mutant A_3R in complex with **K18,** the complexes were embedded in a hydrated POPE bilayer and were subjected to MD simulations for 150 ns (**Figure S5.1**). MM-GBSA calculations [239,303] were then performed using the MD simulation trajectories. The experimentally determined pA_2 values [243] are included in **Table 5.3** and the Schild curves are shown in **Figure 5.6.** An increase in the affinity, i.e. the pA_2 value, of **K18** for a mutant A_3R, when compared to WT A_3R, shows that **K18** has increased antagonistic potency against the mutant A_3R and a decrease in the pA_2 value indicates a reduced potency. Antagonistic potency of **K18** was determined via Schild analysis, as previously reported, [243] and presented in **Figure 5.6** for the mutant A_3RsV169$^{5.30}$E, M174$^{5.35}$A, W185$^{5.46}$A, V169$^{5.30}$A/W185$^{5.46}$A, I253$^{6.58}$A and I253$^{6.58}$E.

Table 5.3 Antagonistic potencies and relative values of MM-GBSA calculated binding free energies for K18 against mutant A_3Rs compared to WT A_3R ($\Delta\Delta G_{eff} = \Delta G_{eff,mut} - \Delta G_{eff,WT}$, in kcal mol^{-1})

Mutant A_3R	**A_3R region**	**$\Delta\Delta G_{eff}$** [a]	**pA_2** [b]	**$RMSD_{protein}$** [c]	**$RMSD_{lig}$** [d]	**Potency**
WT	-	0	7.20 ±0.1 [f]	0.63±0.1	1.67±0.26	Baseline
L90$^{3.32}$A	Low	-5.6±0.01	8.14 ±0.2	0.42±0.2	3.67±0.44	increase

F168$^{5.29}$A	Middle	+15.1±0.03	N.R.[e]	0.69±0.2	6.02±0.32	N.R.[e]
V169$^{5.30}$A	Middle	+14.1±0.1	6.81 ±0.1	0.72±0.2	4.53±0.27	decrease
V169$^{5.30}$E	Middle	+3.2±0.03	7.15 ±0.1	0.89±0.2	3.54±0.31	baseline
M174$^{5.35}$A	Middle	+12.6±0.1	6.63 ±0.2	0.48±0.1	5.14±0.67	decrease
M177$^{5.38}$A	Middle	+13.9±0.1	6.29 ±0.2	0.56±0.2	6.66±0.31	decrease
W185$^{5.46}$A	Low	+7.5±0.3	7.10 ±0.1	0.77±0.3	2.14±0.21	baseline
V169$^{5.30}$A/ W185$^{5.46}$A	Middle/ Low	+18.8±0.1	6.92 ±0.1	0.59±0.3	5.30±0.26	decrease
L246$^{6.51}$A	Middle	+15.7±0.1	N.R.[e]	0.65±0.2	6.38±0.69	N.R.[e]
I249$^{6.54}$A	Middle	+10.2±0.01	7.09 ±0.1	0.78±0.2	2.87±0.35	baseline
N250$^{6.55}$A	Middle	+1.1±0.1	N.R.[e]	0.60±0.1	5.95±0.58	N.R.[e]
I253$^{6.58}$A	Middle	+4.5±0.1	7.24 ±0.1	0.39±0.1	3.56±0.32	baseline
I253$^{6.58}$E	Middle	+3.8±0.05	7.11 ±0.1	0.56±0.1	3.63±0.21	baseline
L264$^{7.35}$A	Middle	-4.8±0.1	7.59 ±0.1	0.39±0.1	3.50±0.20	increase

[a] Relative binding free energy (kcal mol $^{-1}$) between mutant and WT receptors ($\Delta G_{\text{eff,mutant}} - \Delta G_{\text{eff, WT}}$). ΔG_{eff} is calculated from the last 50 ns of the trajectories using 50 ps intervals (i.e. 1000 frames per trajectory). See also Table S1.

[b] Antagonists potency as determined via Schild analysis as previously reported [243] or presented in **Figure 5.6** (V169$^{5.30}$E, M174$^{5.35}$A, W185$^{5.46}$A, V169$^{5.30}$A/W185$^{5.46}$A, I253$^{6.58}$A and I253$^{6.58}$E).

[c] Mean±SD (Å); Protein RMSD is calculated for the C_α atoms of the α-helices, for the last 50 ns of the trajectories. Average structure is used as reference structure.

[d] Mean±SD (Å); Ligand RMSD is calculated after superposition of each protein-ligand complex to that of the starting structure (snapshot 0) based on the C_α atoms of the protein, for the last 50ns of the trajectories.

[e] N.R.; no response, denotes no agonist activity preventing determination of K18 activity using Schild analysis

[f] Mean absolute error.

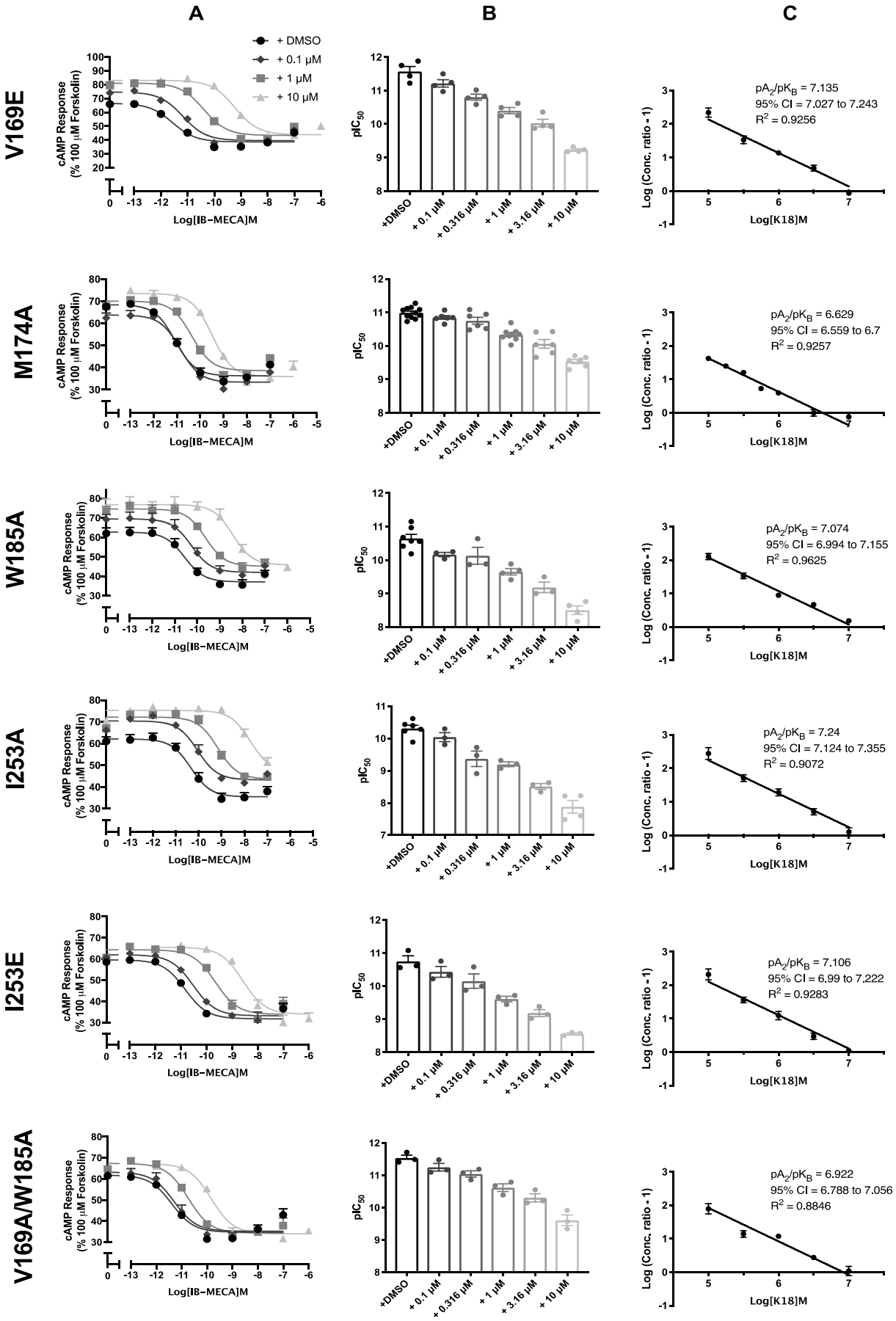
A
B
C
V169E
M174A
W185A
I253A
I253E
V169A/W185A
+ DMSO
+ 0.1 μM
+ 1 μM
+ 10 μM
cAMP Response (% 100 μM Forskolin)
Log[IB-MECA]M
pIC50
+DMSO
+ 0.1 μM
+ 0.316 μM
+ 1 μM
+ 3.16 μM
+ 10 μM
Log (Conc. ratio - 1)
Log[K18]M
pA2/pKB = 7.135
95% CI = 7.027 to 7.243
R2 = 0.9256
pA2/pKB = 6.629
95% CI = 6.559 to 6.7
R2 = 0.9257
pA2/pKB = 7.074
95% CI = 6.994 to 7.155
R2 = 0.9625
pA2/pKB = 7.24
95% CI = 7.124 to 7.355
R2 = 0.9072
pA2/pKB = 7.106
95% CI = 6.99 to 7.222
R2 = 0.9283
pA2/pKB = 6.922
95% CI = 6.788 to 7.056
R2 = 0.8846

Figure 5.6 IB-MECA stimulated cAMP inhibition at mutant A3R mutants with increasing concentrations of K18. Flp-In-CHO cells (2000 cells/well) stably expressing mutant A3R were exposed to forskolin (10 μM), IB-MECA and K18 at varying concentrations for 30 minutes and cAMP accumulation detected. A) Representative dose response curves are shown as mean ± SEM expressed as percentage maximum forskolin response (100 μM). B) pIC_{50} values for independent pIC_{50} values, conducted in duplicate, including half-log concentration are shown as mean ± SEM C) Schild analysis of data represented in A/B.

The MM-GBSA calculated effective binding free energies ΔG_{eff} (see **Table 5.3**) and the pA_2 values show a significant correlation for **K18**, r = -0.81 (95% confidence interval, -0.94 to -0.68 (n=12), $p < 0.01$) (**Figures 5.7, 5.8**). In a previous work, we showed that MM-GBSA calculated ΔG_{eff} values of agonists IB-MECA and NECA and activities for a set of mutant A_3Rs have fair correlation. [241]

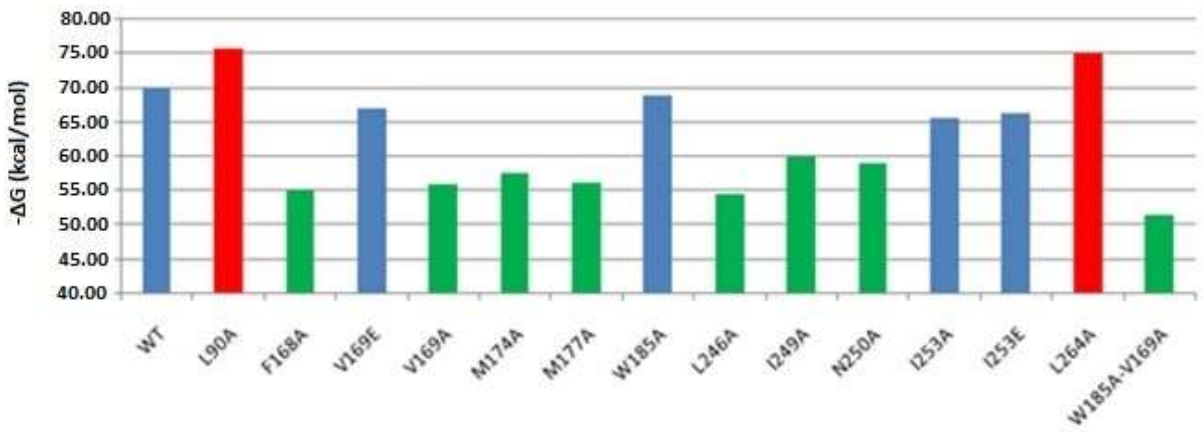

Figure 5.7 MM-PBSA binding free energy (ΔG_{eff}) results in bars, for **K18** in complex with WT and 14 mutant A_3Rs. In green color are shown the calculated energies for mutations that showed experimentally reduction or elimination of the antagonistic potency. In blue color are shown mutations where no change of the potency and in red, mutations where an increase of the **K18** antagonistic potency was experimentally observed.

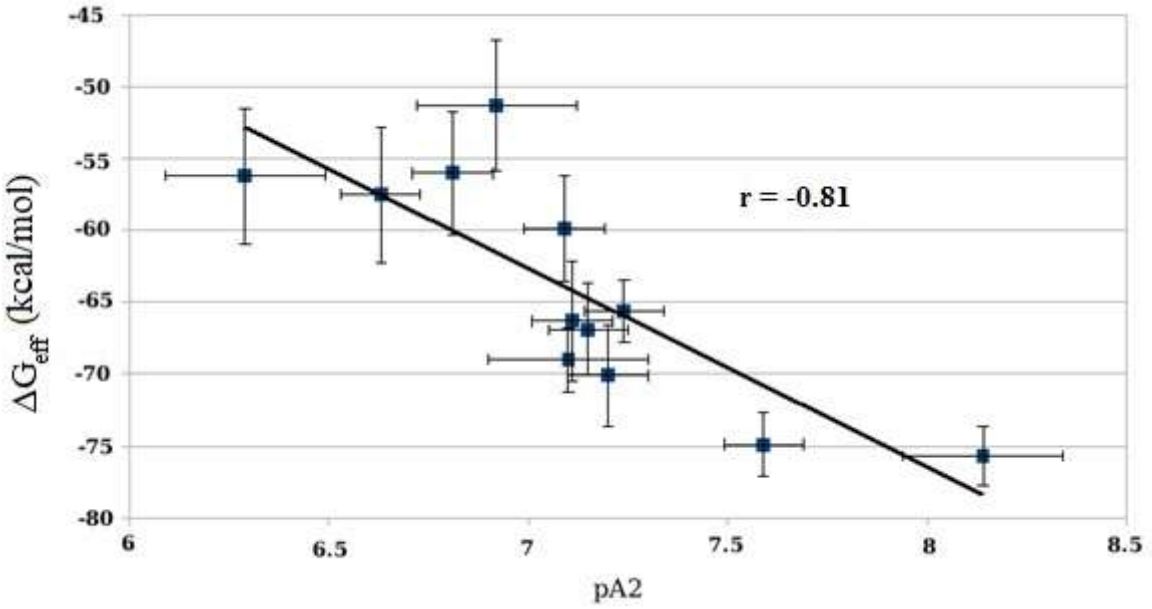

Figure 5.8 Binding free energies (ΔG_{eff}) of **K18** computed by the MM-GBSA method plotted against experimental activities (pA_2) for several mutant A_3Rs. Maximal errors in assays pA_2 and calculated ΔG_{eff} values are shown as error bars along the vertical and horizontal axes, respectively.

Mutants V169$^{5.30}$A, M174$^{5.35}$A, M177$^{5.38}$A, W185$^{5.46}$A/V169$^{5.30}$A, which lead to reduction or loss of potency of **K18**, display relative binding free energy values ($\Delta\Delta G_{eff} = \Delta G_{eff,mut} - \Delta G_{eff,WT}$) for the studied agonist greater than +10 kcal mol^{-1} compared to the WT receptor (**Table 5.3**, **Figure 5.7**). The calculations also show that the complexes of **K18** with mutant F168$^{5.29}$A, L246$^{6.51}$A, N250$^{6.55}$A A_3Rs are not favored (**Table 5.3**). The effect of mutant F168$^{5.29}$A, L246$^{6.51}$A and N250$^{6.55}$A A_3Rs cannot be explored experimentally by mutagenesis given these mutants show no agonist activity. Mutant receptors V169$^{5.30}$E, W185$^{5.46}$A, I249$^{6.54}$A, I253$^{6.58}$A, I253$^{6.58}$E that maintain activity have $\Delta\Delta G_{eff}$ in the range +1 to +4.5 kcal mol^{-1} except I249$^{6.54}$A with a $\Delta\Delta G_{eff}$ of ca +10 kcal mol^{-1} (**Table 5.3**, **Figure 5.7**). Mutants L90$^{3.32}$, L264$^{7.35}$A that increase the potency of the studied antagonist **K18** have $\Delta\Delta G_{eff}$ equal to -5.6 and -4.8 kcal mol^{-1}, respectively. The computationally demanded FEP/MD [311] can be used for the accurate calculation of the $\Delta\Delta G_{eff}$ values. However, the calculated MM-GBSA $\Delta\Delta G_{eff}$ values can distinguish the reduction, maintenance and increase of **K18** potency against the mutant A_3R receptors and are part of the computational model applied for the characterization of the effect of **K18** against A_3Rs in combination with mutagenesis results. This differentiation cannot be achieved using only the highest scores from docking calculations with GoldScore and ChemScore. All the docking calculations produce the "up TM5, TM6" docking pose and a binding free energy score with the GoldScore scoring function for all the 14 **K18**-mutant A_3R complexes. The GoldScore and ChemScore values are consistent with the change in activity of **K18** against mutant A_3Rs compared to the WT A_3R, correspondingly for only 6 or 1 out of 14 mutations (**Table S5.2**) and the correlation between GoldScore or ChemScore and pA_2 values is poor (**Figure S5.2** which shows GoldScore and ChemScore values of **K18** plotted against experimental activities (pA_2) for A_3Rs). Additionally, the docking score values are not sufficient to provide information about the binding profile for **K18** in each A_3R complex, i.e. the different interactions frequency with residues in the binding area. For example, in the case of an unstable complex the docking calculations are not able to describe if the ligand escapes binding area, or remains but critical interactions are lost.

5.4.3.2 Receptor mutations that lead to loss or reduction of antagonistic potency

Mutations of residues that are positioned in EL2, TM5, TM6, i.e. $V169^{5.30}$, $M174^{5.35}$, $M177^{5.38}$, $W185^{5.46}/V169^{5.30}$ to alanine reduce antagonistic potency compared to the WT A_3R. This result further supports the "up TM5-TM6" conformation for **K18** since the loss of the attractive van der Waals interactions with residues in TM5 and TM6, $V169^{5.30}$, $M177^{5.38}$, $I249^{6.54}$, decreases antagonistic potency. Mutations $F168^{5.29}A$, $L246^{6.51}A$ and $N250^{6.55}A$ A_3Rs produce no detecting response since the agonist is not active. Except from $M174^{5.35}$, all the other residues are in contact with the ligand (**Figure 5.2**).
From the trajectories of complexes between K18 and $F168^{5.29}A$, $L246^{6.51}A$, $N250^{6.55}A$, $M174^{5.35}A$, $M177^{5.38}A$ A_3Rs, it was clear that **K18** is unstable inside the receptor area, probably because of the significant displacement of the ligand from the starting docking pose during the MD simulations according to $RMSD_{lig}$ values between 4.5 and 7 Å and $\Delta\Delta G_{eff}$ values between +13 and +16 kcal mol^{-1} (**Table 5.3**, **Figures S5.3-S5.5**). For example, in the unstable complex of **K18** with mutant $F168^{5.29}A$ the π-π interactions between phenyl of $F168^{5.29}$ and oxazole ring of **K18** are absent and this results in the decrease of the hydrogen bond interactions with $N250^{6.55}$ and van der Waals interactions with $V169^{5.30}$ (**Figure 5.9**). During the MD simulation ligand translocates from the starting docking pose, drifts deeper in the receptor and waters enter the binding area and the loss of binding is consistent with the $\Delta\Delta G_{eff}$ of +15 kcal mol^{-1} compared to the complex **K18**-WT A_3R. In the case of **K18** in complex with $V169^{5.30}A$ or $M177^{5.38}A$ or $L246^{6.51}A$, $RMSD_{lig}$ is 4.5 Å and $\Delta\Delta G_{eff}$ is +14 kcal mol^{-1} or 6.7 Å and +14 kcal mol^{-1} or 6.4 Å and +16 kcal mol^{-1} respectively (**Figures S5.3, S5.4, S5.6**, respectively). The functional assays suggest that $M174^{5.35}$ is an important residue, [243] since its mutation to alanine lead to the reduction of antagonistic potency as is reflected by $RMSD_{lig}$ of 5 Å and $\Delta\Delta G_{eff}$ of +13 kcal mol^{-1} (**Figure S5.5**). According to the interactions plot this residue, which is in distance of 4 Å from the ligand, does not have direct interactions with **K18** but is located between $I253^{6.58}$ and $V169^{5.30}$ and seems to contribute significantly to a suitable conformation of the binding area.

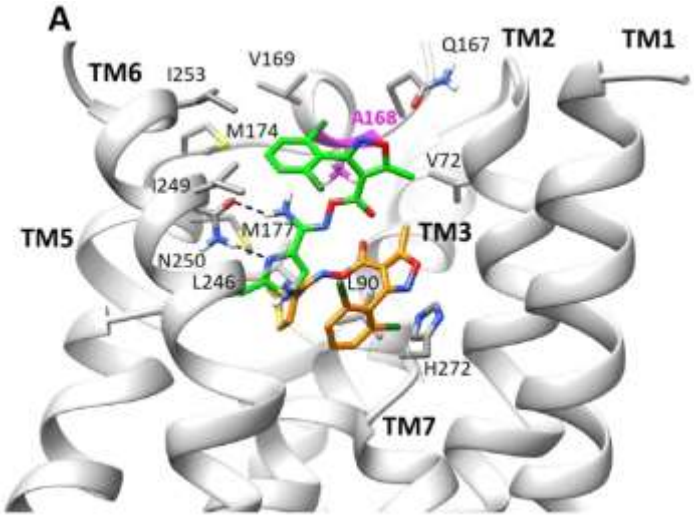

B

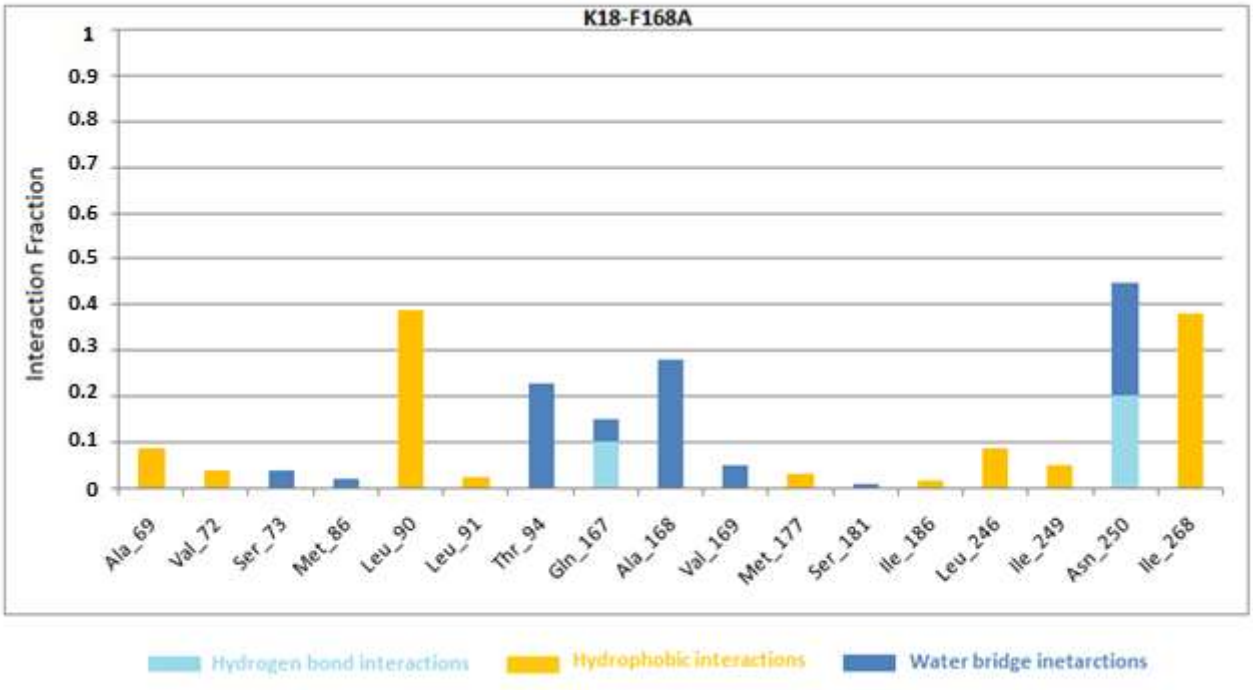

Figure 5.9 (A) Snapshots of **K18**-F168$^{5.29}$A A_3R complex from the unrestrained 100 ns MD simulation. The starting structure of the ligand is shown in green sticks. The binding conformation of the ligand after the 100 ns MD simulation is shown in yellow sticks. The side chains of residues that have interaction frequency ≥ 0.2 are separated by less than 3.6 Å from the ligand and are displayed as gray sticks. Protein structure is displayed in grey ribbons. Hydrogen atoms are omitted except for those involved in hydrogen bond interactions which are highlighted as black dashed lines. (B) Interaction histogram recorded from the 100 ns MD simulation trajectory. Hydrogen bonding interactions bar is depicted in light blue, van der Waals in yellow, water bridges in blue. Bars are plotted for residues with interaction frequencies ≥ 0.2.

5.4.3.3 Mutations that maintain antagonistic potency

K18 has a WT-like antagonistic potency for mutant W185$^{5.46}$A, I249$^{6.54}$A, I253$^{6.58}$A A_3Rs which is in agreement with $\Delta\Delta G_{eff}$ values of +1, +7.5 and +4.5 kcal mol^{-1}, respectively (**Table 5.3**). MD simulations for I253$^{6.58}$A A_3R-**K18** complex show that hydrogen bond interactions with N250$^{6.55}$ and van der Waals interactions with L90$^{3.32}$ and L246$^{6.51}$ are maintained. **K18** translocates towards TM3 and TM7 with an RMSD of 3.6 Å and as a consequence, the interaction frequency with L264$^{7.35}$ is increased, with V169$^{5.30}$ is reduced and with V72$^{2.23}$ is eliminated, compared to the complex with WT A_3R. Also a strong hydrogen bond interaction with T87$^{3.29}$ is formed (**Figure 5.10**).

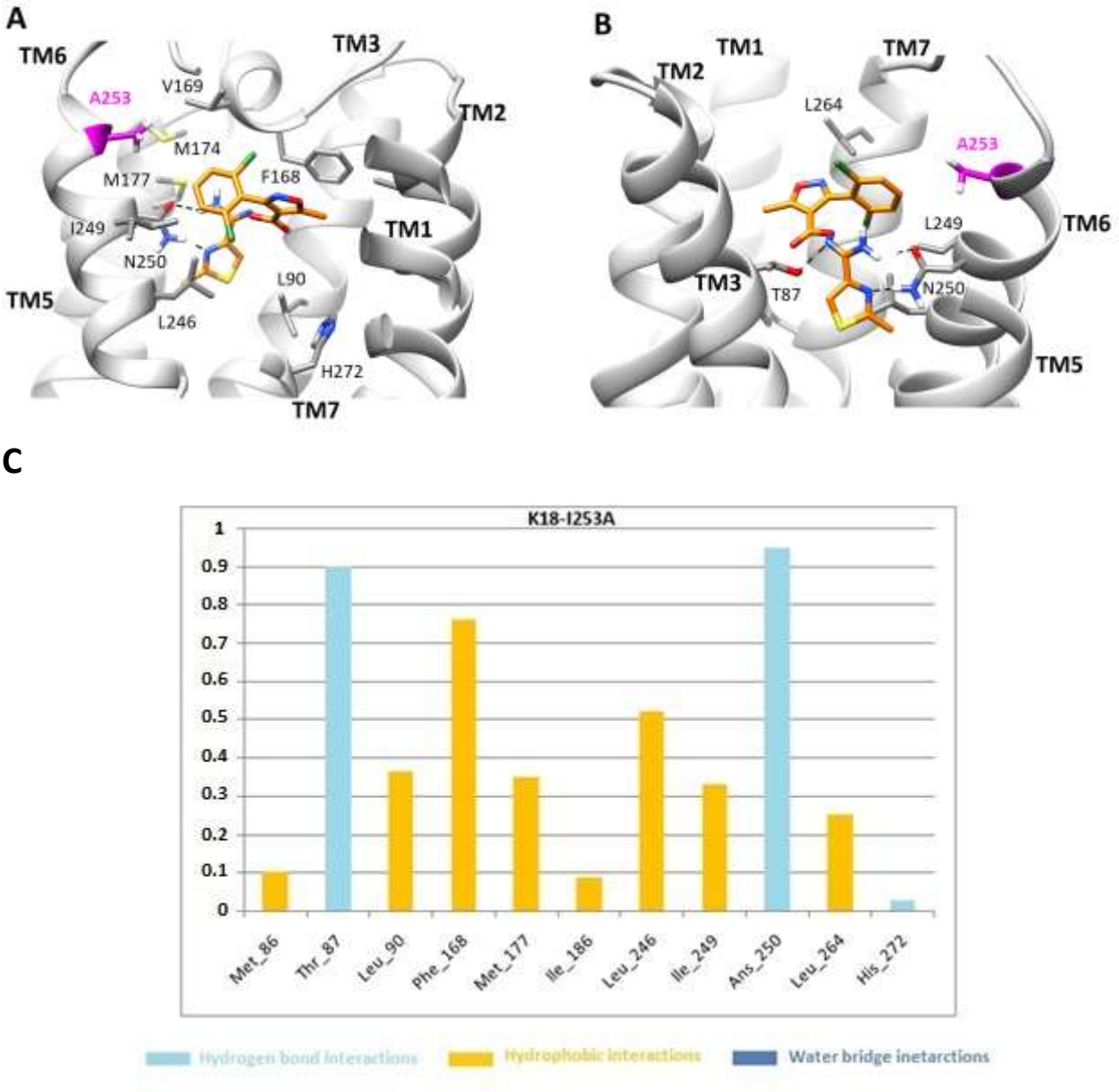

Figure 5.10 (A), (B) Two different perspectives of the average binding conformation of **K18** inside the I253$^{6.58}$A A_3R binding site from unrestrained 100 ns MD simulations (carbon atoms are depicted in yellow color). The side chains of residues that have interaction frequency ≥ 0.2 are separated by less than 3.6 Å from the ligand and are displayed as gray sticks. Protein structure is displayed in grey ribbons. Hydrogen atoms are omitted except for those involved in hydrogen bond interactions which are highlighted as black dashed lines. (C) Interaction histogram recorded from the 100 ns MD simulation trajectory. Hydrogen bonding interactions bar is depicted in light blue, van der Waals in yellow, water bridges in blue. Bars are plotted for residues with interaction frequencies ≥ 0.2.

In the case of **K18**-I249$^{6.54}$A A_3R the ligand remains close to the starting binding conformation with $RMSD_{lig}$ of 2.8 Å and $\Delta\Delta G_{eff}$ value of +10 kcal mol^{-1}. The important van der Waals interactions with V169$^{5.30}$, M177$^{5.38}$ are reduced but new interactions are formed, i.e. van der Waals interactions

with L264, Y265, I268 and water mediated interactions with the backbone amide groups of F168$^{5.29}$ (**Figure 5.11**).

A

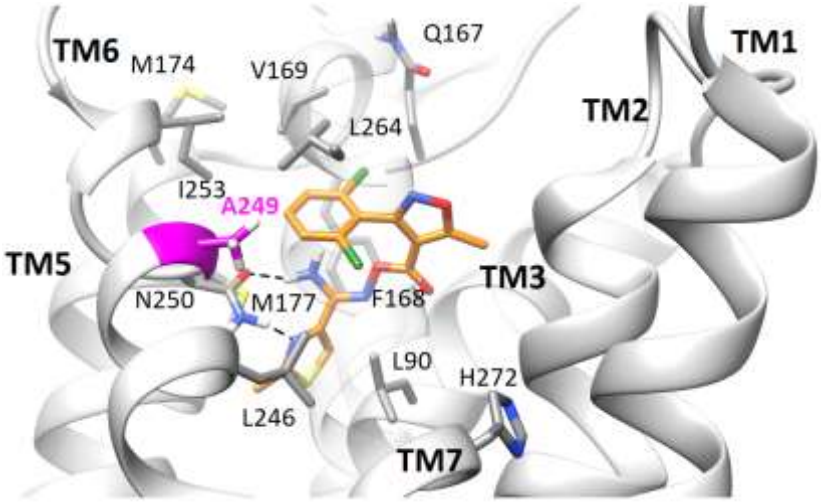

B

Figure 5.11 (A) Binding conformation of **K18** inside I249$^{6.54}$A A_3R after the unrestrained 100 ns MD simulation (shown as yellow sticks). The side chains of residues that have interaction frequency ≥ 0.2 are separated by less than 3.6 Å from the ligand and are displayed as gray sticks. Protein structure is displayed in grey ribbons. Hydrogen atoms are omitted except for those involved in hydrogen bond interactions which are highlighted as black dashed lines. (B) Interaction histogram recorded from the 100 ns MD simulation trajectory. Hydrogen bonding interactions bar is depicted in light blue, van der Waals in yellow, water bridges in blue. Bars are plotted for residues with interaction frequencies ≥ 0.2.

5.4.3.4 Mutations that increase antagonistic potency

Mutations L264$^{7.35}$A and L90$^{3.32}$A increase antagonistic potency (**Table 5.3**).[243] When compared to the K18-WT A_3R complex, the interactions of **K18** with N250$^{6.55}$, F168$^{5.29}$, L246$^{6.51}$, M177$^{5.38}$, I249$^{6.54}$ are maintained in **K18**-L90$^{3.32}$A A_3R complex. The van der Waals interaction with I249$^{6.54}$ and the interaction with F168$^{5.29}$ show increased frequency, the last due to a strong hydrogen bond interaction between the carbonyl group of **K18** and the backbone NH groups of F168$^{5.29}$, aided by the reorientation of **K18** towards TM6 (**Figure 5.12**). This reorientation resulted in an $RMSD_{lig}$ of 3.7 Å. The increase in potency is reflected by the $\Delta\Delta G_{eff}$ of -6 kcal mol^{-1}. In the case of L264$^{7.35}$A mutant receptor, **K18** maintains interactions with L90$^{3.32}$, F168$^{5.29}$, M177$^{5.38}$, L246$^{6.51}$, N250$^{6.55}$, I249$^{6.54}$. The ligand translocates with $RMSD_{lig}$ of 3.5 Å, the interactions frequency with L90$^{3.32}$, L246$^{6.51}$and I268$^{7.39}$ are increased and a new hydrogen bond interaction with T87$^{3.29}$ appears (**Figure 5.13**). The increase of this complex potency is in agreement with $\Delta\Delta G_{eff}$ of -5 kcal mol^{-1} (**Table 5.3**).

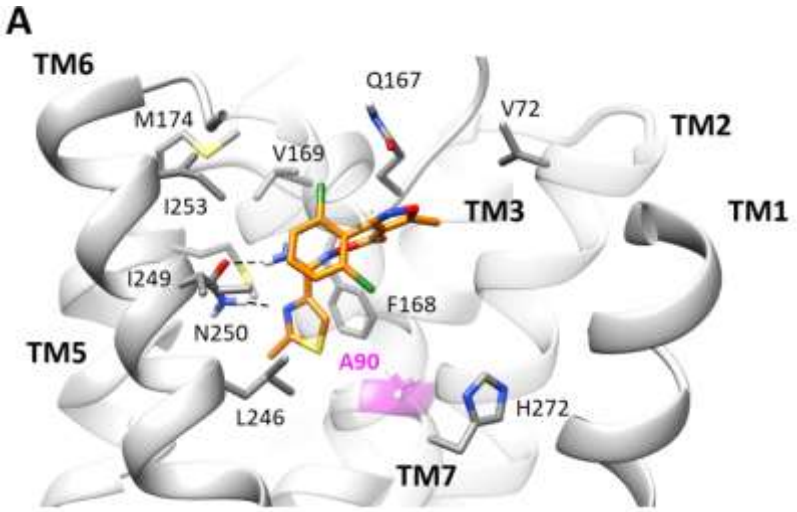

B

Figure 5.12 (A) Average binding conformation of K18 inside the L90$^{3.32}$A A_3R binding site from the unrestrained 100 ns MD simulation (carbon atoms are depicted in yellow color). The side chains of residues that have interaction frequency ≥ 0.2 are separated by less than 3.6 Å from the ligand and are displayed as gray sticks. Protein structure is displayed in grey ribbons. Hydrogen atoms are omitted except for those involved in hydrogen bond interactions which are highlighted as black dashed lines. (B) Interaction histogram recorded from the 100 ns MD simulation trajectory. Hydrogen bonding interactions bar is depicted in light blue, van der Waals in yellow, water bridges in blue. Bars are plotted for residues with interaction frequencies ≥ 0.2.

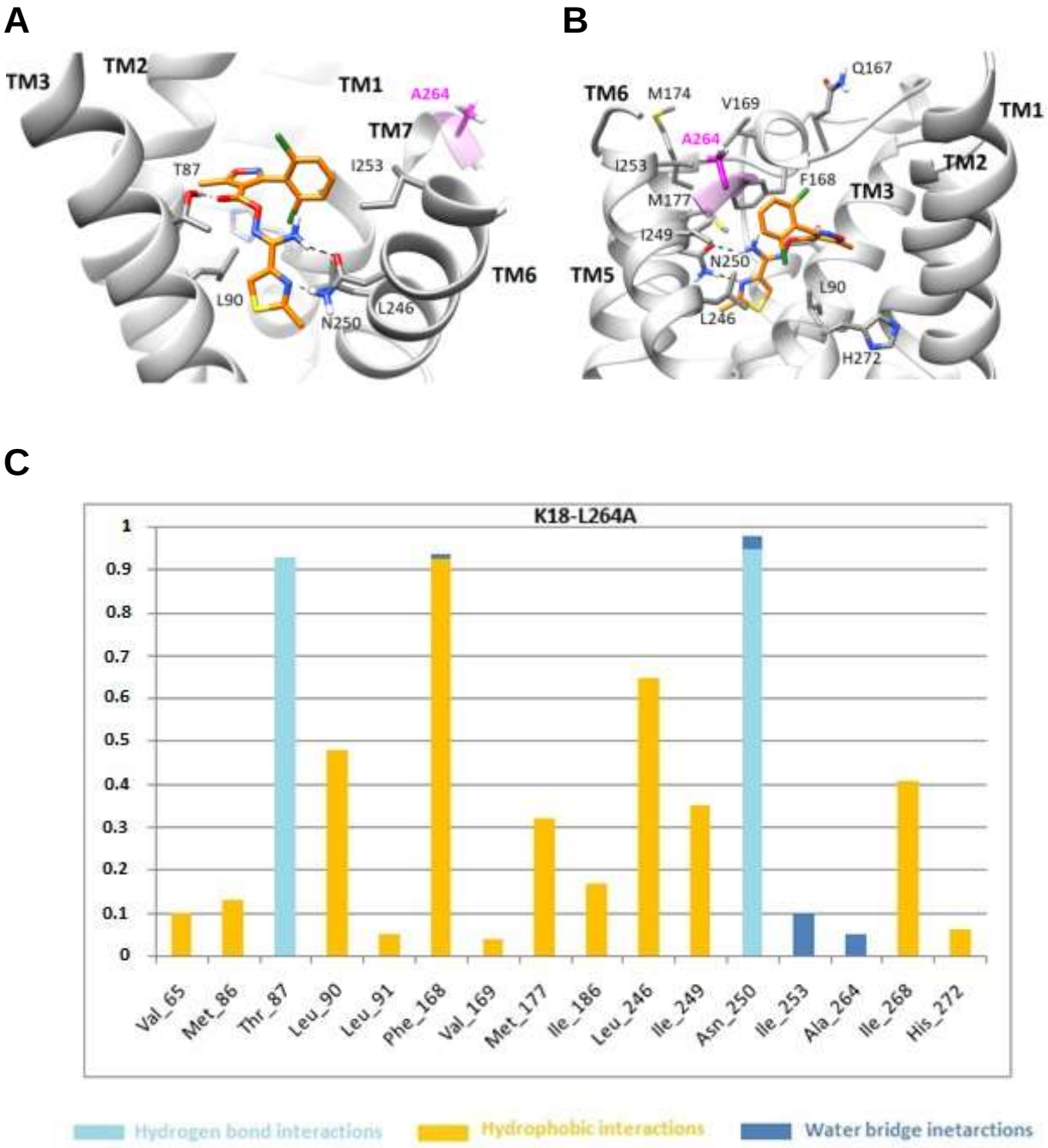

Figure 5.13 (A), (B) Two different perspectives of the average binding conformation of K18 inside the L264$^{7.35}$A A_3R binding site from the unrestrained 100 ns MD simulation (carbon atoms are depicted in yellow color). The side chains of residues that have interaction frequency ≥ 0.2 are separated by less than 3.6 Å from the ligand and are displayed as gray sticks. Protein structure is displayed in grey ribbons. Hydrogen atoms are omitted except for those involved in hydrogen bond interactions which are highlighted as black dashed lines. (C) Interaction histogram recorded from the 100 ns MD simulation trajectory. Hydrogen bonding interactions bar is depicted in light blue, van der Waals in yellow, water bridges in blue. Bars are plotted for residues with interaction frequencies ≥ 0.2.

5.4.3.5 Mutations to glutamate acid

It has been suggested that residue 5.30 may contribute to the subtype-selectivity of antagonists and its correct modeling can be used in drug design for the identification of new selective antagonists. **K18** in the "up TM5 TM6" conformation has the dichlorophenyl group oriented close to the EL2. Residue I253$^{6.58}$ also lies in this area, but in contrast to V169$^{5.30}$, does not interact directly with K18 according to the MD simulation (**Figure 5.2B,D**). Seeking to verify the significance of these residues, we mutated V169$^{5.30}$ and the remote I253$^{6.58}$ to glutamate and expected a reduced binding affinity and receptor's signaling (**Figure 5.2D**). However, complexes of **K18** with I253$^{6.58}$E and V169$^{5.30}$E A_3Rs show maintenance of potency (**Table 5.3**).
MD simulations show that binding of **K18** is stabilized inside the orthosteric binding area by avoiding interactions between the lipophilic dichlorophenyl and glutamate groups. This can be realized through a 180º rotation of the bond connecting oxazolyl and CO which relocates dichlorophenyl group away from E$^{5.30}$ and towards the empty space between TM2, TM1 and TM7 with $RMSD_{lig}$ of 3.5 Å (**Figures 5.14**, **Figure S5.7**). This orientation of dichlorophenyl group facing TM1, TM2 for **K18** inside the WT A_3R is not favored according to the calculations (**see Figures 5.2A-C**). The interactions plot show that hydrogen bond interaction between the amino group of the K18 and N250$^{6.55}$, π-π stacking interaction with phenyl group of F168$^{5.29}$ and van der Waals interaction with M177$^{5.38}$, L246$^{6.51}$ are maintained. New frequent hydrophobic interactions with W185$^{5.46}$, L264$^{7.35}$, Y265$^{7.36}$ and I268$^{7.39}$ appear and a new strong hydrogen bond is formed between the amino group of the ligand and E253$^{6.58}$ carboxylate mediated by a water molecule (**Figure 5.14**).
For **K18** binding inside I253$^{6.58}$E A_3R, trajectory analysis show binding interactions, some of which include N250$^{6.55}$, F168$^{5.29}$, L246$^{6.51}$, W185$^{5.46}$, L264$^{7.35}$, Y265$^{7.36}$ while additional hydrogen bond interactions are formed with Q253$^{6.58}$ and backbone of F168$^{5.29}$ **(Figure S11).**

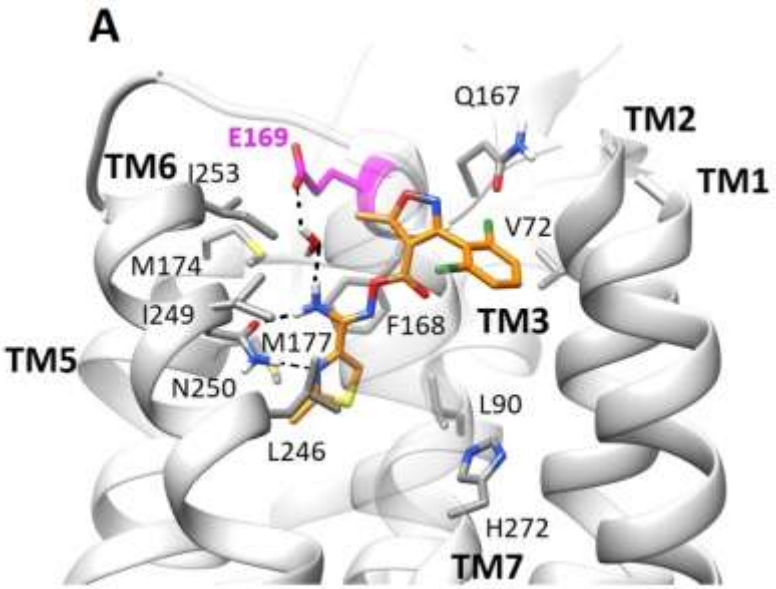

B

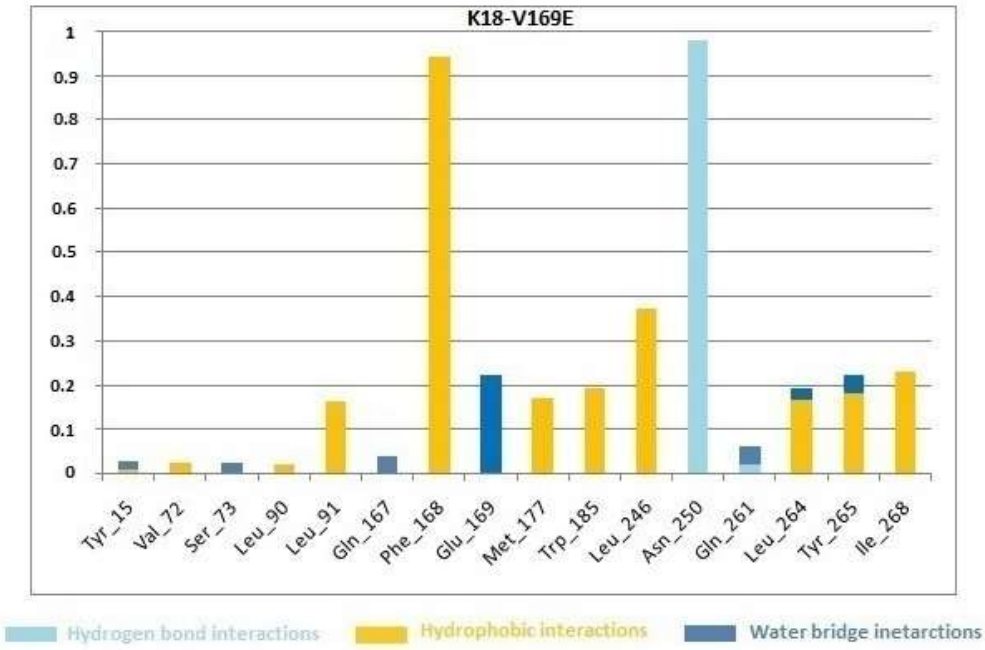

Figure 5.14 (A) Average binding conformation of K18 inside $V169^{5.30}E$ A_3R binding site from unrestrained 100 ns MD simulation. (B) Receptor-ligand interaction histogram inside $V169^{5.30}E$ A_3R orthosteric binding area, recorded from the 100 ns MD simulation trajectory. Hydrogen bonding interactions bar is depicted in light blue, van der Waals in yellow, water bridges in blue. Bars are plotted for residues with interaction frequencies ≥ 0.2.

Since in A_1R and $A_{2A}R$ there is a glutamate acid in position 5.30, MD simulations were also performed for the complexes of **K18** with A_1R and $A_{2A}R$ in order to investigate computationally why **K18** does not bind these AR subtypes. The MD simulations show that K18 fails to bind with the "up TM5,TM6" conformation due to the repulsions with $E169^{5.30}$ but also with "up TM1,TM2" conformation possibly because of the more polar area close to TM1, TM2 in A_1R and $A_{2A}R$ (compared to A_3R) which may cause repulsion with dichlorophenyl group (**Figure 5.15**). Thus, in A_1R and $A_{2A}R$ the repulsion between dichlorophenyl and glutamate groups cannot be relieved in a similar way to A_3R.

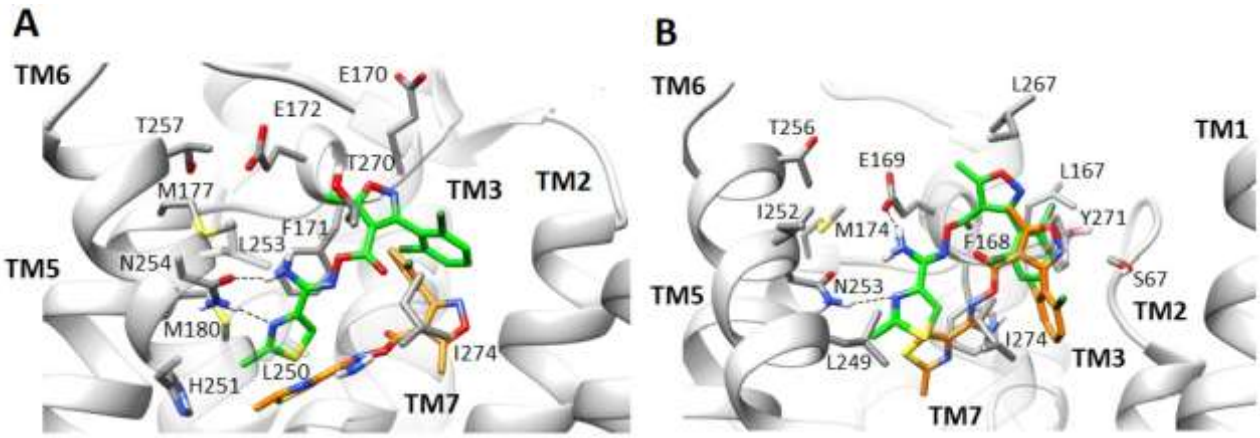

Figure 5.15 (A), (B) Snapshots of K18 inside the A_1R and $A_{2A}R$ binding site respectively from unrestrained 100 ns MD simulations. The starting structure of the ligand is shown in green sticks. The binding conformation of the ligand after the 100 ns MD simulation is shown in yellow sticks. The side chains of residues that have interaction frequency ≥ 0.2 are separated by less than 3.6 Å from the ligand and are displayed as gray sticks. Hydrogen atoms are omitted except for those involved in hydrogen bond interactions which are highlighted as black dashed lines.

5.5 Conclusions

The A_3R is currently an important drug target,[86,312] and there is a lack of available structures. In this work using experimental pA_2 values from mutagenesis experiments, a computational model for the description of a specific antagonist binding with orthosteric binding area of A_3R is approved. In particular, the computational model used: (a) A homology model of A_3R in complex and the most likely binding conformation of **K18** inside WT A_3R orthosteric binding area which was investigated using MD simulations with amber99sb and MM-PBSA or MM-GBSA calculations. (b) The effect of point-mutations of residues in the orthosteric binding area to **K18** activity.

In a previous study, [241] it was found experimentally and confirmed computationally using the same model that critical interactions for IB-MECA activity to A_3R include residues at the TM5, TM6 and EL2. These are $F168^{5.29}$, $L246^{6.51}$, $V169^{5.30}$, $N250^{6.55}$ forming direct interactions with agonist and $M177^{5.38}$, $L90^{3.32}$ at the bottom of the orthosteric binding area which include indirect interactions. Other critical direct interactions for IB-MECA activity include the additional residues at the bottom of the binding area, $T94^{3.36}$, $S271^{7.42}$, $H272^{7.43}$ and $I268^{7.39}$. [241] According to our computational model the competitive antagonist **K18** is stabilized inside the A_3R orthosteric binding area through an "up TM5, TM6" conformer which interacts directly with some common residues with the agonist. It forms a π-π interaction with $F168^{5.29}$, van der Waals interactions with $L90^{3.32}$, $V169^{5.30}$, $L246^{6.51}$, and hydrogen bond interactions with $N250^{6.55}$. In the middle region of the A_3R, K18 makes contacts with residues $M177^{5.38}$, $I249^{6.54}$ which are not in contact with IB-MECA. To add further contrast, IB-MECA contacts residue $W185^{5.46}$ whereas **K18** does not. From these residues $M177^{5.38}$ causes a negation of both agonists and antagonist potency activity when mutated to alanine. [241] $L90^{3.32}$ is a residue in contact with **K18** but not in contact with the agonists suggesting that **K18** sits higher in the orthosteric binding region. $L90^{3.32}$A mutation causes correspondingly an increase in the potency of **K18** and a reduction in the potency of agonists. [241] Our calculations describe why the majority of mutated residues to alanine, which are in contact with K18 antagonist in the WT receptor, reduce or eliminate potency, i.e. correspondingly $V169^{5.30}$, $M177^{5.38}$ or $L246^{6.51}$, $F168^{5.29}$, $N250^{6.55}$. Additionally, the computational model shows that the selectivity of **K18** is not only due to direct interactions with the binding area residues. Remote residues which are positioned at the edges of the binding area in EL2, TM5 and TM6, like $M174^{5.35}$ at 4 Å may act by modulating the structure of the pocket. Residue $M174^{5.35}$ is important for NECA and **K18** activity since its mutation to alanine reduce potency. The results produced experimental pA_2 values which were used as experimental probes [241,243] for MD simulations and binding free energy MM-GBSA calculations for of **K18** in complex with 14 mutant A_3Rs. Using the MM-GBSA calculated ΔG_{eff} values it was possible to distinguish three sets of mutant receptors, i.e. those that reduce or negate **K18** potency at the A_3R, those that bind stably and maintain potency and those that increase potency compared to WT A_3R. The calculated ΔG_{eff} values for **K18** and experimentally determined pA_2 values displayed very good correlation, with r = -0.81. In our previous work investigating IB-MECA and NECA agonists binding to A_3R, the correlation between calculated ΔG_{eff} values and experimental pIC_{50} values was also fair (correspondingly r = -0.69 and r = -0.76). [241]

The characterization of the area TM6-EL2-TM5 in A_3R which includes lipophilic residues is very important for structure-based drug design of selective ligands. Although this area is considered to be occupied from the lipophilic groups of selective ligands, like the iodo-benzyl group in IB-MECA, the experimental results show and the computational model supports [241] that the mutation $V169^{5.30}E$ causes an increase in IB-MECA and NECA activity, rather than the expected reduction, and that $I253^{6.58}$ is not an important residue of this region. We also showed that $I253^{6.58}$ and $V169^{5.30}E$ maintains **K18** antagonistic potency.[243] It is also interesting that the potency of **K18** is enhanced by the mutations of $L90^{3.32}A$ in the low region or $L264^{7.35}A$ in the middle/upper region which are directly interacting residues with **K18**, suggesting an empty space in the orthosteric area available for increasing antagonist potency. These findings could have significant impact on the design of potent and selective ligands targeting A_3R.

References

1. Hanson MA, Stevens RC. Discovery of New GPCR Biology: One Receptor Structure at a Time. *Structure*. 2009;17(1):8-14. doi:10.1016/j.str.2008.12.003
2. Tyndall J, Sandilya R. GPCR Agonists and Antagonists in the Clinic. *Med Chem (Los Angeles)*. 2005;1(4):405-421. doi:10.2174/1573406054368675
3. Lagerström MC, Schiöth HB. Structural diversity of G protein-coupled receptors and significance for drug discovery. *Nat Rev Drug Discov*. 2008;7(4):339-357. doi:10.1038/nrd2518
4. Katritch V, Kufareva I, Abagyan R. Structure based prediction of subtype-selectivity for adenosine receptor antagonists. *Neuropharmacology*. 2011;60(1):108-115. doi:10.1016/j.neuropharm.2010.07.009
5. Overington JP, Al-Lazikani B, Hopkins AL. How many drug targets are there? *Nat Rev Drug Discov*. 2006;5(12):993-996. doi:10.1038/nrd2199
6. Lefkowitz RJ. Historical review: A brief history and personal retrospective of seven-transmembrane receptors. *Trends Pharmacol Sci*. 2004;25(8):413-422. doi:10.1016/j.tips.2004.06.006
7. Tian S, Wang X, Li L, et al. Discovery of Novel and Selective Adenosine A 2A Receptor Antagonists for Treating Parkinson's Disease through Comparative Structure-Based Virtual Screening. *J Chem Inf Model*. 2017;57(6):1474-1487. doi:10.1021/acs.jcim.7b00188
8. Laporte SA, Oakley RH, Holt JA, Barak LS, Caron MG. The interaction of β-arrestin with the AP-2 adaptor is required for the clustering of β2-adrenergic receptor into clathrin-coated pits. *J Biol Chem*. 2000;275(30):23120-23126. doi:10.1074/jbc.M002581200
9. Laporte SA, Oakley RH, Zhang J, et al. The β2-adrenergic receptor/βarrestin complex recruits the clathrin adaptor AP-2 during endocytosis. *Proc Natl Acad Sci U S A*. 1999;96(7):3712-3717. doi:10.1073/pnas.96.7.3712
10. Sutherland EW, Rall TW. Fractionation and characterization of a cyclic adenine ribonucleotide formed by tissue particles. *J Biol Chem*. 1958;232(2):1077-1091. http://www.ncbi.nlm.nih.gov/pubmed/13549488.
11. Taussig R, Tang WJ, Hepler JR, Gilman AG. Distinct patterns of bidirectional regulation of mammalian adenylyl cyclases. *J Biol Chem*. 1994;269(8):6093-6100.
12. Fredholm BB, IJzerman AP, Jacobson KA, Linden J, Muller CE. International Union of Basic and Clinical Pharmacology. LXXXI. Nomenclature and Classification of Adenosine Receptors--An Update. *Pharmacol Rev*. 2011;63(1):1-34. doi:10.1124/pr.110.003285
13. Lebon G, Edwards PC, Leslie AGW, Tate CG. Molecular determinants of CGS21680 binding to the human adenosine A2A receptor. *Mol Pharmacol*. 2015. doi:10.1124/mol.114.097360
14. Lebon G, Warne T, Edwards PC, et al. Agonist-bound adenosine A2A receptor structures reveal common features of GPCR activation. *Nature*. 2011;474(7352):521-525. doi:10.1038/nature10136
15. Xu F, Wu H, Katritch V, et al. Structure of an Agonist-Bound Human A2A Adenosine Receptor. *Science (80-)*. 2011;332(6027):322-327. doi:10.1126/science.1202793
16. Carpenter B, Nehmé R, Warne T, Leslie AGW, Tate CG. Structure of the adenosine A2A receptor bound to an engineered G protein. *Nature*. 2016. doi:10.1038/nature18966
17. García-Nafría J, Lee Y, Bai X, Carpenter B, Tate CG. Cryo-EM structure of the adenosine A2Areceptor coupled to an engineered heterotrimeric G protein. *Elife*. 2018;7:e35946:1-19. doi:10.7554/eLife.35946.001
18. Rasmussen SGF, DeVree BT, Zou Y, et al. Crystal structure of the β2 adrenergic receptor–Gs protein complex. *Nature*. 2011;477(7366):549-555. doi:10.1038/nature10361
19. Cherezov V, Rosenbaum DM, Hanson MA, et al. High-resolution crystal structure of an engineered human β2-adrenergic G protein-coupled receptor. *Science (80-)*. 2007;318(5854):1258-1265. doi:10.1126/science.1150577
20. Jaakola VP, Griffith MT, Hanson MA, et al. The 2.6 angstrom crystal structure of a human A2A adenosine receptor bound to an antagonist. *Science (80-)*. 2008;322(5905):1211–1217. doi:10.1126/science.1164772
21. Rasmussen SGF, Choi H-J, Rosenbaum DM, et al. Crystal structure of the human β2 adrenergic G-protein-coupled receptor. *Nature*. 2007;450(7168):383-387. doi:10.1038/nature06325

22. Rosenbaum P, Paneth N, Leviton A, Goldstein M, Bax M. A report: the definition and classification of cerebral palsy April 2006. *Dev Med Child Neurol*. 2007;49:8-14. doi:10.1111/j.1469-8749.2007.tb12610.x
23. Warne T, Serrano-Vega MJ, Baker JG, et al. Structure of a β1-adrenergic G-protein-coupled receptor. *Nature*. 2008;454(7203):486-491. doi:10.1038/nature07101
24. Hanson MA, Roth CB, Jo E, et al. Crystal structure of a lipid G protein-coupled receptor. *Science (80-)*. 2012;335(6070):851-855. doi:10.1126/science.1215904
25. Fredriksson R, Lagerström MC, Lundin LG, Schiöth HB. The G-protein-coupled receptors in the human genome form five main families. Phylogenetic analysis, paralogon groups, and fingerprints. *Mol Pharmacol*. 2003;63(6):1256-1272. doi:10.1124/mol.63.6.1256
26. Carlsson J, Yoo L, Gao Z, Irwin J, Shoichet B, Jacobson K. Structure-Based Discovery of A(2A) Adenosine Receptor Ligands. *J Med Chem*. 2010;53(9):3748-3755. doi:10.1021/jm100240h
27. Katritch V, Jaakola VP, Lane JR, et al. Structure-based discovery of novel chemotypes for adenosine A2Areceptor antagonists. *J Med Chem*. 2010;53:1799–1809. doi:10.1021/jm901647p
28. van der Horst E, van der Pijl R, Mulder-Krieger T, Bender A, Ijzerman AP. Substructure-based virtual screening for adenosine A2A receptor ligands. *ChemMedChem*. 2011;6(12):2302-2311. doi:10.1002/cmdc.201100369
29. Chen J-F, Eltzschig HK, Fredholm BB. Adenosine receptors as drug targets—what are the challenges? *Nat Rev Drug Discov*. 2013;12(4):265-286. doi:10.1038/nrd3955
30. Congreve M, Andrews SP, Dore AS, et al. Discovery of 1,2,4-Triazine Derivatives as Adenosine A. 2012;55(5):1898-1903.
31. Rodríguez D, Gao Z-G, Moss SM, Jacobson KA, Carlsson J. Molecular Docking Screening Using Agonist-Bound GPCR Structures: Probing the A 2A Adenosine Receptor. *J Chem Inf Model*. 2015;55(3):550-563. doi:10.1021/ci500639g
32. Glukhova A, Thal DM, Nguyen AT, et al. Structure of the Adenosine A1 Receptor Reveals the Basis for Subtype Selectivity. *Cell*. 2017;168(5):867-877. doi:10.1016/j.cell.2017.01.042
33. Weis F, Menting JG, Margetts MB, et al. The signalling conformation of the insulin receptor ectodomain. *Nat Commun*. 2018;9(1):4420. doi:10.1038/s41467-018-06826-6
34. Liu W, Chun E, Thompson AA, et al. Structural Basis for Allosteric Regulation of GPCRs by Sodium Ions. *Science*. 2012;337(6091):232-236. doi:10.1126/science.1219218
35. Cheng RKY, Segala E, Robertson N, et al. Structures of Human A1 and A2A Adenosine Receptors with Xanthines Reveal Determinants of Selectivity. *Structure*. 2017;25(8):1275-1285. doi:10.1016/j.str.2017.06.012
36. Okada T, Sugihara M, Bondar A-N, Elstner M, Entel P, Buss V. The Retinal Conformation and its Environment in Rhodopsin in Light of a New 2.2Å Crystal Structure. *J Mol Biol*. 2004;342(2):571-583. doi:10.1016/j.jmb.2004.07.044
37. Palczewski K, Kumasaka T, Hori T, et al. Crystal Structure of Rhodopsin: A G Protein-Coupled Receptor. *Science (80-)*. 2000;289(5480):739-745. doi:10.1126/science.289.5480.739
38. Vogel R, Mahalingam M, Lüdeke S, Huber T, Siebert F, Sakmar TP. Functional Role of the "Ionic Lock"—An Interhelical Hydrogen-Bond Network in Family A Heptahelical Receptors. *J Mol Biol*. 2008;380(4):648-655. doi:10.1016/j.jmb.2008.05.022
39. Drury AN, Szent-Györgyi A. The physiological activity of adenine compounds with especial reference to their action upon the mammalian heart. *J Physiol*. 1929;68(3):213-237. doi:10.1113/jphysiol.1929.sp002608
40. Wilbur SL, Marchlinski FE. Adenosine as an Antiarrhythmic Agent. *Am J Cardiol*. 1997;79(12):30-37. doi:10.1016/S0002-9149(97)00261-0
41. Müller CE, Jacobson KA. Recent developments in adenosine receptor ligands and their potential as novel drugs. *Biochim Biophys Acta - Biomembr*. 2011;1808(5):1290-1308. doi:10.1016/j.bbamem.2010.12.017
42. Jacobson KA, Merighi S, Varani K, et al. A 3 Adenosine Receptors as Modulators of Inflammation: From Medicinal Chemistry to Therapy. *Med Res Rev*. 2017;38(4):1031-1072. doi:10.1002/med.21456
43. Fredholm BB, IJzerman AP, Jacobson KA, Klotz K-N, Linden J. International Union of Pharmacology. XXV. Nomenclature and classification of adenosine receptors. *Pharmacol Rev*.

2001;53(4):527-552.
44. Fredholm BB, IJzerman AP, Jacobson KA, Linden J, Müller CE. International union of basic and clinical pharmacology. LXXXI. Nomenclature and classification of adenosine receptors - An update. *Pharmacol Rev*. 2011. doi:10.1124/pr.110.003285
45. Schulte G, Fredholm BB. Signaling Pathway from the Human Adenosine A 3 Receptor Expressed in Chinese Hamster Ovary Cells to the Extracellular Signal-Regulated Kinase 1/2. *Mol Pharmacol*. 2002;62(5):1137-1146. doi:10.1124/mol.62.5.1137
46. Ji XD, Jacobson KA. Use of the triazolotriazine [3H]ZM 241385 as a radioligand at recombinant human A(2B) adenosine receptors. *Drug Des Discov*. 1999;16(3):217-226.
47. Carpenter B, Nehmé R, Warne T, Leslie AGW, Tate CG. Structure of the adenosine A2Areceptor bound to an engineered G protein. *Nature*. 2016;536:104-107. doi:10.1038/nature18966
48. García-Nafría J, Lee Y, Bai X, Carpenter B, Tate CG. Cryo-EM structure of the adenosine A2A receptor coupled to an engineered heterotrimeric G protein. *Elife*. 2018. doi:10.7554/eLife.35946.001
49. White KL, Eddy MT, Gao Z-G, et al. Structural Connection between Activation Microswitch and Allosteric Sodium Site in GPCR Signaling. *Structure*. 2018;26(2):259-269. doi:10.1016/j.str.2017.12.013
50. Draper-Joyce CJ, Khoshouei M, Thal DM, et al. Structure of the adenosine-bound human adenosine A1 receptor–Gi complex. *Nature*. 2018;558(7711):559-563. doi:10.1038/s41586-018-0236-6
51. Sun B, Bachhawat P, Chu ML-H, et al. Crystal structure of the adenosine A 2A receptor bound to an antagonist reveals a potential allosteric pocket. *Proc Natl Acad Sci*. 2017;114(8):2066–2071. doi:10.1073/pnas.1621423114
52. Doré AS, Robertson N, Errey JC, et al. Structure of the adenosine A 2A receptor in complex with ZM241385 and the xanthines XAC and caffeine. *Structure*. 2011;19(9):1283-1293. doi:10.1016/j.str.2011.06.014
53. Cheng RKY, Segala E, Robertson N, et al. Structures of Human A1and A2AAdenosine Receptors with Xanthines Reveal Determinants of Selectivity. *Structure*. 2017;25(8):1275–1285. doi:10.1016/j.str.2017.06.012
54. Draper-Joyce CJ, Khoshouei M, Thal DM, et al. Structure of the adenosine-bound human adenosine A1 receptor-Gi complex. *Nature*. 2018. doi:10.1038/s41586-018-0236-6
55. Massotte D, Kieffer BL. The second extracellular loop: a damper for G protein–coupled receptors? *Nat Struct Mol Biol*. 2005;12(4):287-288. doi:10.1038/nsmb0405-287
56. Nguyen ATN, Vecchio EA, Thomas T, et al. Role of the Second Extracellular Loop of the Adenosine A 1 Receptor on Allosteric Modulator Binding, Signaling, and Cooperativity. *Mol Pharmacol*. 2016;90(6):715-725. doi:10.1124/mol.116.105015
57. Schiedel AC, Hinz S, Thimm D, et al. The four cysteine residues in the second extracellular loop of the human adenosine A 2B receptor: Role in ligand binding and receptor function. *Biochem Pharmacol*. 2011;82(4):389-399. doi:10.1016/j.bcp.2011.05.008
58. Chen JF, Eltzschig HK, Fredholm BB. Adenosine receptors as drug targets-what are the challenges? *Nat Rev Drug Discov*. 2013. doi:10.1038/nrd3955
59. Valls MD, Cronstein BN, Montesinos MC. Adenosine receptor agonists for promotion of dermal wound healing. *Biochem Pharmacol*. 2009;77(7):1117-1124. doi:10.1016/j.bcp.2008.11.002
60. de Lera Ruiz M, Lim Y-H, Zheng J. Adenosine A 2A Receptor as a Drug Discovery Target. *J Med Chem*. 2014;57(9):3623-3650. doi:10.1021/jm4011669
61. Lagarias P, Vrontaki E, Lambrinidis G, et al. Discovery of Novel Adenosine Receptor Antagonists through a Combined Structure- and Ligand-Based Approach Followed by Molecular Dynamics Investigation of Ligand Binding Mode. *J Chem Inf Model*. 2018;58(4):794–815. doi:10.1021/acs.jcim.7b00455
62. Gessi S, Varani K, Merighi S, et al. Pharmacological and biochemical characterization of A3 adenosine receptors in Jurkat T cells. *Br J Pharmacol*. 2001;134(1):116-126.
63. Madi L, Ochaion A, Rath-Wolfson L, et al. The A3 Adenosine Receptor Is Highly Expressed in Tumor versus Normal Cells. *Clin Cancer Res*. 2004;10(13):4472-4479. doi:10.1158/1078-0432.CCR-03-0651
64. Borea PA, Varani K, Vincenzi F, et al. The a3 adenosine receptor: History and perspectives.

Pharmacol Rev. 2015;67(1):74-102. doi:10.1124/pr.113.008540
65. Yao Y, Sei Y, Abbracchio MP, Jiang J-L, Kim Y-C, Jacobson KA. Adenosine A3 receptor agonists protect HL-60 and U-937 cells from apoptosis induced by A3 antagonists. *Biochem Biophys Res Commun*. 1997;232(2):317-322. doi:10.1006/bbrc.1997.6290
66. Trincavelli ML, Tuscano D, Marroni M, et al. A3 adenosine receptors in human astrocytoma cells: agonist-mediated desensitization, internalization, and down-regulation. *Mol Pharmacol*. 2002;62(6):1373-1384.
67. Merighi S, Varani K, Gessi S, et al. Pharmacological and biochemical characterization of adenosine receptors in the human malignant melanoma A375 cell line. *Br J Pharmacol*. 2001;134(6):1215-1226.
68. Suh B-C, Kim T-D, Lee J-U, Seong J-K, Kim K-T. Pharmacological characterization of adenosine receptors in PGT-β mouse pineal gland tumour cells. *Br J Pharmacol*. 2001;134(1):132-142.
69. Morello S, Petrella A, Festa M, et al. Cl-IB-MECA inhibits human thyroid cancer cell proliferation independently of A3 adenosine receptor activation. *Cancer Biol Ther*. 2008;7(2):278-284.
70. Yan L, Burbiel JC, Maaß A, Müller CE. Adenosine receptor agonists: from basic medicinal chemistry to clinical development. *Expert Opin Emerg Drugs*. 2003;8(2):537-576. doi:10.1517/14728214.8.2.537
71. Jacobson KA, Gao ZG. Adenosine receptors as therapeutic targets. *Nat Rev Drug Discov*. 2006;5(3):247-264. doi:10.1038/nrd1983
72. Jacobson KA. Introduction to adenosine receptors as therapeutic targets. *Handb Exp Pharmacol*. 2009. doi:10.1007/978-3-540-89615-9_1
73. Chen J-F, Eltzschig HK, Fredholm BB. Adenosine receptors as drug targets — what are the challenges? *Nat Rev Drug Discov*. 2013;12(4):265-286. doi:10.1038/nrd3955
74. Layland J, Carrick D, Lee M, Oldroyd K, Berry C. Adenosine: physiology, pharmacology, and clinical applications. *JACC Cardiovasc Interv*. 2014;7(6):581-591.
75. Kim HO, Ji X, Siddiqi SM, Olah ME, Stiles GL, Jacobson KA. 2-Substitution of N6-benzyladenosine-5'-uronamides enhances selectivity for A3 adenosine receptors. *J Med Chem*. 1994;37(21):3614-3621.
76. Deninno MP, Masamune H, Chenard LK, et al. 3 '-Aminoadenosine-5 '-uronamides: discovery of the first highly selective agonist at the human adenosine A3 receptor. *J Med Chem*. 2003;46(3):353-355.
77. Jeong LS, Jin DZ, Kim HO, et al. N6-Substituted D-4'-Thioadenosine-5'-methyluronamides: Potent and Selective Agonists at the Human A3 Adenosine Receptor. *J Med Chem*. 2003;46(18):3775-3777. doi:10.1021/jm034098e
78. Volpini R, Costanzi S, Lambertucci C, et al. N 6-Alkyl-2-alkynyl derivatives of adenosine as potent and selective agonists at the human adenosine A3 receptor and a starting point for searching A2B ligands. *J Med Chem*. 2002;45(15):3271-3279.
79. Melman A, Wang B, Joshi B V, et al. Selective A3 adenosine receptor antagonists derived from nucleosides containing a bicyclo[3.1.0]hexane ring system. *Bioorg Med Chem*. 2008;16(18):8546-8556. doi:10.1016/j.bmc.2008.08.007
80. Tchilibon S, Joshi B V, Kim S-K, Duong HT, Gao Z-G, Jacobson KA. (N)-Methanocarba 2, N6-disubstituted adenine nucleosides as highly potent and selective A3 adenosine receptor agonists. *J Med Chem*. 2005;48(6):1745-1758. doi:10.1021/jm049580r
81. Fishman P, Bar-Yehuda S, Liang BT, Jacobson KA. Pharmacological and therapeutic effects of A3 adenosine receptor agonists. *Drug Discov Today*. 2012;17(7-8):359-366.
82. Jacobson KA, Tosh DK, Jain S, Gao Z-G. Historical and Current Adenosine Receptor Agonists in Preclinical and Clinical Development. *Front Cell Neurosci*. 2019;13:1-17. doi:10.3389/fncel.2019.00124
83. Salvatore CA, Tilley SL, Latour AM, Fletcher DS, Koller BH, Jacobson MA. Disruption of the A 3 Adenosine Receptor Gene in Mice and Its Effect on Stimulated Inflammatory Cells. *J Biol Chem*. 2000;275(6):4429-4434. doi:10.1074/jbc.275.6.4429
84. Kreckler LM. Adenosine Inhibits Tumor Necrosis Factor- Release from Mouse Peritoneal Macrophages via A2A and A2B but Not the A3 Adenosine Receptor. *J Pharmacol Exp Ther*. 2006;317(1):172-180. doi:10.1124/jpet.105.096016

85. Blackburn MR, Vance CO, Morschl E, Wilson CN. Adenosine receptors and inflammation. In: Wilson C, Mustafa S, eds. *Adenosine Receptors in Health and Disease. Handbook of Experimental Pharmacology*. Springer, Berlin, Heidelberg; 2009:215-269. doi:10.1007/978-3-540-89615-9_8
86. Okamura T, Kurogi Y, Hashimoto K, et al. Structure–activity relationships of adenosine A 3 receptor ligands: new potential therapy for the treatment of glaucoma. *Bioorg Med Chem Lett*. 2004;14(14):3775-3779. doi:10.1016/j.bmcl.2004.04.099
87. Gessi S, Merighi S, Varani K, Leung E, Mac Lennan S, Borea PA. The A3 adenosine receptor: An enigmatic player in cell biology. *Pharmacol Ther*. 2008;117(1):123-140. doi:10.1016/j.pharmthera.2007.09.002
88. Melman A, Gao Z-G, Kumar D, et al. Design of (N)-methanocarba adenosine 5′-uronamides as species-independent A3 receptor-selective agonists. *Bioorg Med Chem Lett*. 2008;18(9):2813-2819. doi:10.1016/j.bmcl.2008.04.001
89. Lengauer T, Rarey M. Computational methods for biomolecular docking. *Curr Opin Struct Biol*. 1996;6(3):402-406. doi:10.1016/S0959-440X(96)80061-3
90. Kitchen DB, Decornez H, Furr JR, Bajorath J. Docking and scoring in virtual screening for drug discovery: Methods and applications. *Nat Rev Drug Discov*. 2004;3(11):935-949. doi:10.1038/nrd1549
91. Jorgensen WL. Rusting of the lock and key model for protein-ligand binding. *Science (80-)*. 1991;254(5034):954-955. doi:10.1126/science.1719636
92. Wei BQ, Weaver LH, Ferrari AM, Matthews BW, Shoichet BK. Testing a Flexible-receptor Docking Algorithm in a Model Binding Site. *J Mol Biol*. 2004;337(5):1161-1182. doi:10.1016/j.jmb.2004.02.015
93. GOLD Suite, Version 5.2; Cambridge Crystallographic Data Centre: Cambridge, U. K. http://www.ccdc.cam.ac.uk. :5.
94. Lensink MF, Méndez R, Wodak SJ. Docking and scoring protein complexes: CAPRI 3rd Edition. *Proteins Struct Funct Bioinforma*. 2007;69(4):704-718. doi:10.1002/prot.21804
95. Robertson TA, Varani G. An all-atom, distance-dependent scoring function for the prediction of protein-DNA interactions from structure. *Proteins Struct Funct Bioinforma*. 2007;66(2):359-374. doi:10.1002/prot.21162
96. Ajay, Murcko MA. Computational Methods to Predict Binding Free Energy in Ligand-Receptor Complexes. *J Med Chem*. 1995;38(26):4953-4967. doi:10.1021/jm00026a001
97. Engel T. Basic overview of chemoinformatics. *J Chem Inf Model*. 2006;46(6):2267-2277. doi:10.1021/ci600234z
98. Gasteiger J, Engel T. *Chemoinformatics: A Textbook*. Wiley; 2003. doi:10.1002/3527601643
99. Varnek A, Baskin II. Chemoinformatics as a Theoretical Chemistry Discipline. *Mol Inform*. 2011;30(1):20-32. doi:10.1002/minf.201000100
100. Brown FK. Chapter 35. Chemoinformatics: What is it and How does it Impact Drug Discovery. In: *Annual Reports in Medicinal Chemistry*. ; 1998:375–384. doi:10.1016/S0065-7743(08)61100-8
101. Brown F. Editorial opinion: Chemoinformatics - A ten year update. *Curr Opin Drug Discov Dev*. 2005;8(3):298-302.
102. Fernández-De Gortari E, García-Jacas CR, Martinez-Mayorga K, Medina-Franco JL. Database fingerprint (DFP): an approach to represent molecular databases. *J Cheminform*. 2017. doi:10.1186/s13321-017-0195-1
103. Duan J, Dixon SL, Lowrie JF, Sherman W. Analysis and comparison of 2D fingerprints: Insights into database screening performance using eight fingerprint methods. *J Mol Graph Model*. 2010;29(2):157-170. doi:10.1016/j.jmgm.2010.05.008
104. Hert J, Willett P, Wilton DJ, et al. Comparison of topological descriptors for similarity-based virtual screening using multiple bioactive reference structures. *Org Biomol Chem*. 2004;2(22):3256-3266. doi:10.1039/b409865j
105. Hu Y, Lounkine E, Bajorath J. Improving the search performance of extended connectivity fingerprints through activity-oriented feature filtering and application of a bit-density-dependent similarity function. *ChemMedChem*. 2009;4(4):540-548. doi:10.1002/cmdc.200800408
106. Yuriev E, Ramsland PA. Latest developments in molecular docking: 2010-2011 in review. *J Mol*

Recognit. 2013;26(5):215-239. doi:10.1002/jmr.2266
107. Kollman PA, Massova I, Reyes C, et al. Calculating structures and free energies of complex molecules: Combining molecular mechanics and continuum models. *Acc Chem Res*. 2000;33(12):889-897. doi:10.1021/ar000033j
108. Homeyer N, Stoll F, Hillisch A, Gohlke H. Binding free energy calculations for lead optimization: Assessment of their accuracy in an industrial drug design context. *J Chem Theory Comput*. 2014;10(8):3331-3344. doi:10.1021/ct5000296
109. Zhang X, Wong SE, Lightstone FC. Toward fully automated high performance computing drug discovery: A massively parallel virtual screening pipeline for docking and molecular mechanics/generalized born surface area rescoring to improve enrichment. *J Chem Inf Model*. 2014;54(1):324-337. doi:10.1021/ci4005145
110. Feig M, Onufriev A, Lee MS, Im W, Case DA, Brooks CL. Performance Comparison of Generalized Born and Poisson Methods in the Calculation of Electrostatic Solvation Energies for Protein Structures. *J Comput Chem*. 2004;25(2):265-284. doi:10.1002/jcc.10378
111. Chen D, Ranganathan A, Ijzerman AP, Siegal G, Carlsson J. Complementarity between in silico and biophysical screening approaches in fragment-based lead discovery against the A2A adenosine receptor. *J Chem Inf Model*. 2013. doi:10.1021/ci4003156
112. Li Y, Liu Z, Wang R. Test MM-PB/SA on True Conformational Ensembles of Protein−Ligand Complexes. *J Chem Inf Model*. 2010;50(9):1682-1692. doi:10.1021/ci100036a
113. Huanga D, Caflischa A. Library screening by fragment-based docking. *J Mol Recognit*. 2010;23(2):183-193. doi:10.1002/jmr.981
114. Davenport AP, Russell FD. Radioligand Binding Assays: Theory and Practice. In: *Current Directions in Radiopharmaceutical Research and Development*. Dordrecht: Springer Netherlands; 1996:169-179. doi:10.1007/978-94-009-1768-2_11
115. Klotz KN, Hessling J, Hegler J, et al. Comparative pharmacology of human adenosine receptor subtypes - Characterization of stably transfected receptors in CHO cells. *Naunyn Schmiedebergs Arch Pharmacol*. 1997;357(1):1-9. doi:10.1007/PL00005131
116. Börner S, Schwede F, Schlipp A, et al. FRET measurements of intracellular cAMP concentrations and cAMP analog permeability in intact cells. *Nat Protoc*. 2011;6(4):427-438. doi:10.1038/nprot.2010.198
117. Post SR, Ostrom RS, Insel PA. Biochemical Methods for Detection and Measurement of Cyclic AMP and Adenylyl Cyclase Activity. In: *Adrenergic Receptor Protocols*. New Jersey: Humana Press; 2000:363-374. doi:10.1385/1-59259-684-3:363
118. Ballesteros JA, Weinstein H. Integrated methods for the construction of three-dimensional models and computational probing of structure-function relations in G protein-coupled receptors. *Methods Neurosci*. 1995. doi:10.1016/S1043-9471(05)80049-7
119. Alnouri MW, Jepards S, Casari A, Schiedel AC, Hinz S, Müller CE. Selectivity is species-dependent: Characterization of standard agonists and antagonists at human, rat, and mouse adenosine receptors. *Purinergic Signal*. 2015;11(3):389-407. doi:10.1007/s11302-015-9460-9
120. Katritch V, Jaakola V-P, Lane JR, et al. Structure-based discovery of novel chemotypes for adenosine A(2A) receptor antagonists. *J Med Chem*. 2010;53(4):1799-1809. doi:10.1021/jm901647p
121. Langmead CJ, Andrews SP, Congreve M, et al. Identification of Novel Adenosine A2A Receptor Antagonists by Virtual Screening. *J Med Chem*. 2012;55(5):1904-1909. doi:10.1021/jm201455y
122. Jazayeri A, Andrews SP, Marshall FH. Structurally Enabled Discovery of Adenosine A 2A Receptor Antagonists. *Chem Rev*. 2016;117(1):21-37. doi:10.1021/acs.chemrev.6b00119
123. Lenselink EB, Beuming T, van Veen C, et al. In search of novel ligands using a structure-based approach: a case study on the adenosine A2A receptor. *J Comput Aided Mol Des*. 2016;30(10):863-874. doi:10.1007/s10822-016-9963-7
124. Chen D, Ranganathan A, IJzerman AP, Siegal G, Carlsson J. Complementarity between in silico and biophysical screening approaches in fragment-based lead discovery against the A(2A) adenosine receptor. *J Chem Inf Model*. 2013;53(10):2701-2714. doi:10.1021/ci4003156
125. Kolb P, Phan K, Gao Z-G, Marko AC, Sali A, Jacobson K a. Limits of ligand selectivity from docking to models: in silico screening for A(1) adenosine receptor antagonists. *PLoS One*.

2012;7(11):e49910. doi:10.1371/journal.pone.0049910
126. Ranganathan A, Stoddart LA, Hill SJ, Carlsson J. Fragment-Based Discovery of Subtype-Selective Adenosine Receptor Ligands from Homology Models. *J Med Chem*. 2015;58(24):9578-9590. doi:10.1021/acs.jmedchem.5b01120
127. Kim J, Wess J, van Rhee AM, Schöneberg T, Jacobson KA. Site-directed Mutagenesis Identifies Residues Involved in Ligand Recognition in the Human A Adenosine Receptor. *J Biol Chem*. 1995;270(23):13987–13997. doi:10.1074/jbc.270.23.13987
128. Gao Z, Chen A, Barak D, Kim S, Mu CE, Jacobson KA. Identification by Site-directed Mutagenesis of Residues Involved in Ligand Recognition and Activation of the Human A 3 Adenosine Receptor *. *J Biol Chem*. 2002;277(21):19056-19063. doi:10.1074/jbc.M110960200
129. Ballesteros JA, Weinstein H. *Receptor Molecular Biology*. Vol 25.; 1995. doi:10.1016/S1043-9471(05)80049-7
130. Li Y, Liu Z, Wang R. Test MM-PB / SA on True Conformational Ensembles of Protein - Ligand Complexes. 2010:1682-1692.
131. Lavecchia A, Di Giovanni C. Virtual Screening Strategies in Drug Discovery: A Critical Review. *Curr Med Chem*. 2013;20(23):2839-2860. doi:10.2174/09298673113209990001
132. Schrödinger, LLC, New York N. LigPrep, version 2.5. Suite 2012.
133. Hawkins PCD, Skillman AG, Warren GL, Ellingson BA, Stahl MT. Conformer generation with OMEGA: Algorithm and validation using high quality structures from the protein databank and cambridge structural database. *J Chem Inf Model*. 2010;50(4):572-584. doi:10.1021/ci100031x
134. Hawkins PCD, Nicholls A. the Analysis of Failures. 2012.
135. Maestro, version 10.5; Schrodinger, Inc.: New York, NY, 2015.
136. Jones G, Willett P, Glen RC, Leach AR, Taylor R. Development and validation of a genetic algorithm for flexible docking. *J Mol Biol*. 1997;267(3):727-748. doi:10.1006/jmbi.1996.0897
137. Verdonk ML, Chessari G, Cole JC, et al. Modeling Water Molecules in Protein−Ligand Docking Using GOLD. *J Med Chem*. 2005;48(20):6504-6515. doi:10.1021/jm050543p
138. Eldridge MD, Murray CW, Auton TR, Paolini G V, Mee RP. Empirical scoring functions: I. The development of a fast empirical scoring function to estimate the binding affinity of ligands in receptor complexes. *J Comput Aided Mol Des*. 1997;11(5):425-445. doi:Doi 10.1023/A:1007996124545
139. Korb O, Stützle T, Exner TE. Empirical scoring functions for advanced Protein-Ligand docking with PLANTS. *J Chem Inf Model*. 2009;49(1):84-96. doi:10.1021/ci800298z
140. Hawkins PCD, Skillman AG, Nicholls A. Comparison of shape-matching and docking as virtual screening tools. *J Med Chem*. 2007;50(1):74-82. doi:10.1021/jm0603365
141. Sastry M, Lowrie JF, Dixon SL, Sherman W. Large-Scale Systematic Analysis of 2D Fingerprint Methods and Parameters to Improve Virtual Screening Enrichments. *J Chem Inf Model*. 2010;50(5):771-784. doi:10.1021/ci100062n
142. Gaulton A, Bellis LJ, Bento AP, et al. ChEMBL: A large-scale bioactivity database for drug discovery. *Nucleic Acids Res*. 2012;40(Database issue):D1100-7. doi:10.1093/nar/gkr777
143. Bento AP, Gaulton A, Hersey A, et al. The ChEMBL bioactivity database: An update. *Nucleic Acids Res*. 2014;42((Database issue)):D1083-D1090. doi:10.1093/nar/gkt1031
144. Brooks BR, Bruccoleri RE, Olafson BD, States DJ, Swaminathan S, Karplus M. CHARMM: A program for macromolecular energy, minimization, and dynamics calculations. *J Comput Chem*. 1983;4(2):187-217. doi:10.1002/jcc.540040211
145. Brooks BR, Brooks CL, Mackerell AD, et al. CHARMM: The biomolecular simulation program. *J Comput Chem*. 2009;30(10):1545–1614. doi:10.1002/jcc.21287
146. Kolb P, Caflisch A. Automatic and efficient decomposition of two-dimensional structures of small molecules for fragment-based high-throughput docking. *J Med Chem*. 2006;49(25):7384-7392. doi:10.1021/jm060838i
147. Warwicker J, Watson HC. Calculation of the Electric Potential in the Active due to a-Helix Dipoles Site Cleft. *J Mol Biol*. 1982;157(4):671-679. doi:10.1016/0022-2836(82)90505-8
148. Im W, Beglov D, Roux B. Continuum solvation model: computation of electrostatic forces from numerical solutions to the Poisson-Boltzmann equation. *Comput Phys Commun*. 1998;111(1-3):59-75.

149. Kent RS, De Lean A, Lefkowitz RJ. A quantitative analysis of beta-adrenergic receptor interactions: resolution of high and low affinity states of the receptor by computer modeling of ligand binding data. *Mol Pharmacol*. 1980;17(1):14-23.
150. GraphPad Software Inc. GraphPad Statistics Guide. *GraphPad*. 2012.
151. Klotz KN, Cristalli G, Grifantini M. Photoaffinity labeling of A1-adenosine receptors. *J Biol Chem*. 1985;260(27):14659-14664.
152. Dal Ben D, Lambertucci C, Marucci G, Volpini R, Cristalli G. Adenosine receptor modeling: What does the A2A crystal structure tell us? *Curr Top Med Chem*. 2010;10(10):993-1018. doi:10.2174/156802610791293145
153. Ivanov A, Barak D, Jacobson K. Evaluation of homology modeling of G protein-coupled receptors in light of the A2A adenosine receptor crystallographic structure. *J Med Chem*. 2009;52(10):3284-3292.
154. Jazayeri A, Dias JM, Marshall FH. From G protein-coupled receptor structure resolution to rational drug design. *J Biol Chem*. 2015;290(32):19489-19495. doi:10.1074/jbc.R115.668251
155. Wu J-P, Fleck R, Brickwood J, et al. The discovery of thienopyridine analogues as potent IkappaB kinase beta inhibitors. Part II. *Bioorg Med Chem Lett*. 2009;19(19):5547-5551. doi:10.1016/j.bmcl.2009.08.054
156. Lebon G, Warne T, Edwards PC, et al. Agonist-bound adenosine A2A receptor structures reveal common features of GPCR activation. *Nature*. 2011. doi:10.1038/nature10136
157. Hawkins PCD, Nicholls A. Conformer generation with OMEGA: Learning from the data set and the analysis of failures. *J Chem Inf Model*. 2012. doi:10.1021/ci300314k
158. Tuccinardi T, Nuti E, Ortore G, Rossello A, Avramova SI, Martinelli A. Development of a receptor-based 3D-QSAR study for the analysis of MMP2, MMP3, and MMP9 inhibitors. *Bioorg Med Chem*. 2008;16(16):7749-7758. doi:10.1016/j.bmc.2008.07.004
159. Frisch M, Trucks G, Schlegel H, Scuseria G. Gaussian 03, revision C. 02; Gaussian, Inc.: Wallingford, CT, 2004. *There is no Corresp*. 2013.
160. Carlsson J, Tosh DK, Phan K, Gao ZG, Jacobson KA. Structure-activity relationships and molecular modeling of 1,2,4-triazoles as adenosine receptor antagonists. *ACS Med Chem Lett*. 2012;3(9):715-720. doi:10.1021/ml300097g
161. Allen MP. *Introduction to Molecular Dynamics Simulation Michael.*; 1995. doi:10.1006/cbir.1995.1007
162. Desmond Molecular Dynamics System, version 3.0, D.E. Shaw Research: New York, 2011. *Desmond Mol Dyn Syst version 30; DE Shaw Res New York, 2011; Maest Interoperability Tools, 31; Schrodinger Res New York, 2012*.
163. Maestro-Desmond.pdf.
164. Jorgensen WL, Maxwell DS, Tirado-Rives J. Development and Testing of the OLPS All-Atom Force Field on Conformational Energetics and Properties of Organic Liquids. *J Am Chem Soc*. 1996;118(15):11225-11236. doi:10.1021/ja9621760
165. Kaminski G, Friesner R, Tirado-rives J, Jorgensen WL. Comparison with Accurate Quantum Chemical Calculations on Peptides. *J Phys Chem B*. 2001;105(28):6474-6487. doi:10.1021/jp003919d
166. Shivakumar D, Williams J, Wu YJ, Damm W, Shelley J, Sherman W. Prediction of Absolute Solvation Free Energies using Molecular Dynamics Free Energy Perturbation and the OPLS Force Field. *J Chem Theory Comput*. 2010;6(5):1509-1519. doi:10.1021/ct900587b
167. Case DA, Berryman JT, Betz RM, Cai Q, Cerutti DS, Cheatham TE III, Darden TA, Duke RE, Gohlke H, Goetz AW, Gusarov S, Homeyer N, Janowski P, Kaus J, Kolossváry I, Kovalenko A, Lee TS, LeGrand S, Luchko T, Luo R, Madej B. The Amber Molecular Dynamics Package. *AMBER 14, Univ California, San Fr*. 2014.
168. Maier JA, Martinez C, Kasavajhala K, Wickstrom L, Hauser KE, Simmerling C. ff14SB: Improving the Accuracy of Protein Side Chain and Backbone Parameters from ff99SB. *J Chem Theory Comput*. 2015;11(8):3696-3713. doi:10.1021/acs.jctc.5b00255
169. Sali A, Blundell TL. Comparative protein modelling by satisfaction of spatial restraints. *J Mol Biol*. 1993;234(3):779-815. doi:10.1006/jmbi.1993.1626
170. Fiser A, Do RK, Šali A. Modeling of loops in protein structures. *Protein Sci*. 2000;9(9):1753-1773.

doi:10.1110/ps.9.9.1753
171. Floris M, Sabbadin D, Medda R, Bulfone A, Moro S. Adenosiland: Walking through adenosine receptors landscape. *Eur J Med Chem*. 2012. doi:10.1016/j.ejmech.2012.10.022
172. Halgren TA. Merck molecular force field. I. Basis, form, scope, parameterization, and performance of MMFF94. *J Comput Chem*. 1996;17:490-519. doi:10.1002/(SICI)1096-987X(199604)17:5/6<490::AID-JCC1>3.0.CO;2-P
173. Halgren TA. MMFF VII. Characterization of MMFF94, MMFF94s, and other widely available force fields for conformational energies and for intermolecular-interaction energies and geometries. *J Comput Chem*. 1999;20(7):720–729. doi:10.1002/(SICI)1096-987X(199905)20:7<730::AID-JCC8>3.0.CO;2-T
174. Pettersen EF, Goddard TD, Huang CC, et al. UCSF Chimera?A visualization system for exploratory research and analysis. *J Comput Chem*. 2004;25(13):1605-1612. doi:10.1002/jcc.20084
175. Lomize MA, Lomize AL, Pogozheva ID, Mosberg HI. OPM: Orientations of Proteins in Membranes database. *Bioinformatics*. 2006;22(5):623-625. doi:10.1093/bioinformatics/btk023
176. Jorgensen WL, Chandrasekhar J, Madura JD, Impey RW, Klein ML. Comparison of simple potential functions for simulating liquid water. *J Chem Phys*. 1983;79(2):926-929. doi:10.1063/1.445869
177. Kaminski GA, Friesner RA, Tirado-rives J, Jorgensen WL. Comparison with Accurate Quantum Chemical Calculations on Peptides †. *Quantum*. 2001.
178. Darden T, York D, Pedersen L. Particle mesh Ewald: An N·log(N) method for Ewald sums in large systems. *J Chem Phys*. 1993;98(12):10089-10092. doi:10.1063/1.464397
179. Essmann U, Perera L, Berkowitz ML, Darden T, Lee H, Pedersen LG. A smooth particle mesh Ewald method. *J Chem Phys*. 1995;103(19):8577-85779. doi:10.1063/1.470117
180. Martyna GJ, Tobias DJ, Klein ML. Constant pressure molecular dynamics algorithms. *J Chem Phys*. 1994;101(5):4177-4189. doi:10.1063/1.467468
181. Humphreys DD, Friesner RA, Berne BJ. A multiple-time-step Molecular Dynamics algorithm for macromolecules. *J Phys Chem*. 1994;98(27):6885-6892. doi:10.1021/j100078a035
182. Koynova R, Caffrey M. Phases and phase transitions of the phosphatidylcholines. *Biochim Biophys Acta - Rev Biomembr*. 1998;1376(1):91-145. doi:10.1016/S0304-4157(98)00006-9
183. Dickson CJ, Madej BD, Skjevik ÅA, et al. Lipid14: The amber lipid force field. *J Chem Theory Comput*. 2014;10(2):865–879. doi:10.1021/ct4010307
184. Wang J, Wolf RM, Caldwell JW, Kollman PA, Case DA. Development and testing of a general amber force field. *J Comput Chem*. 2004;25(9):1157-1174. doi:10.1002/jcc.20035
185. Dupradeau FY, Pigache A, Zaffran T, et al. The R.E.D. tools: Advances in RESP and ESP charge derivation and force field library building. *Phys Chem Chem Phys*. 2010;12(28):7821-7839. doi:10.1039/c0cp00111b
186. Zgarbová M, Otyepka M, Šponer J, et al. Refinement of the Cornell et al. Nucleic Acids Force Field Based on Reference Quantum Chemical Calculations of Glycosidic Torsion Profiles. *J Chem Theory Comput*. 2011;7(9):2886-2902. doi:10.1021/ct200162x
187. Lzaguirre JA, Catarello DP, Wozniak JM, Skeel RD. Langevin stabilization of molecular dynamics. *J Chem Phys*. 2001;114(5):2090-2098. doi:10.1063/1.1332996
188. Berendsen HJC, Postma JPM, Van Gunsteren WF, Dinola A, Haak JR. Molecular dynamics with coupling to an external bath. *J Chem Phys*. 1984;81(8):3684-3690. doi:10.1063/1.448118
189. Ryckaert J-P, Ciccotti G, Berendsen HJ. Numerical integration of the cartesian equations of motion of a system with constraints: molecular dynamics of n-alkanes. *J Comput Phys*. 1977;23(3):327-341. doi:10.1016/0021-9991(77)90098-5
190. Mori T, Ogushi F, Sugita Y. Analysis of lipid surface area in protein-membrane systems combining voronoi tessellation and monte carlo integration methods. *J Comput Chem*. 2012;33(3):286-293. doi:10.1002/jcc.21973
191. Isgro T, Phillips JC, Sotomayor M, Villa E. VMD NAMD Tutorial. *VMD Tutor*. 2009.
192. Bruns RF, Fergus JH. Allosteric enhancement of adenosine A1 receptor binding and function by 2-amino-3-benzoylthiophenes. *Mol Pharmacol*. 1990;38(6):939-949.
193. Kourounakis A, Visser C, De Groote M, IJzerman AP. Differential effects of the allosteric enhancer (2-amino-4,5-dimethyl-trienyl)[3-(trifluoromethyl) phenyl]methanone (PD81,723) on agonist and

antagonist binding and function at the human wild-type and a mutant (T277A) adenosine A1 receptor. *Biochem Pharmacol*. 2001;61(2):137-144. doi:10.1016/S0006-2952(00)00536-0
194. Nikolakopoulos G, Figler H, Linden J, Scammells PJ. 2-Aminothiophene-3-carboxylates and carboxamides as adenosine A1 receptor allosteric enhancers. *Bioorg Med Chem*. 2006;14(7):2358-2365. doi:10.1016/j.bmc.2005.11.018
195. Romagnoli R, Baraldi PG, Moorman AR, Borea PA, Varani K. Current status of A 1 adenosine receptor allosteric enhancers. *Future Med Chem*. 2015;7(10):1247-1259. doi:10.4155/fmc.15.65
196. Valant C, Aurelio L, Devine SM, et al. Synthesis and characterization of novel 2-amino-3-benzoylthiophene derivatives as biased allosteric agonists and modulators of the adenosine A 1 receptor. *J Med Chem*. 2012;55(5):2367-2375. doi:10.1021/jm201600e
197. Tranberg CE, Zickgraf A, Giunta BN, et al. 2-Amino-3-aroyl-4,5-alkylthiophenes: Agonist allosteric enhancers at human a1 adenosine receptors. *J Med Chem*. 2002;45(2):382-389. doi:10.1021/jm010081p
198. Ferguson GN, Valant C, Horne J, et al. 2-Aminothienopyridazines as novel adenosine A1 receptor allosteric modulators and antagonists. *J Med Chem*. 2008;51(19):6165-6172. doi:10.1021/jm800557d
199. Yaziji V, Rodríguez D, Gutiérrez-De-Terán H, et al. Pyrimidine derivatives as potent and selective A3 adenosine receptor antagonists. *J Med Chem*. 2011;54(2):457-471. doi:10.1021/jm100843z
200. Van Muijlwijk-Koezen JE, Timmerman H, Link R, Van der Goot H, Ijzerman AP. A novel class of adenosine A3 receptor ligands. 1. 3-(2- pyridinyl)isoquinoline derivatives. *J Med Chem*. 1998;41(21):3987-3993. doi:10.1021/jm980036q
201. Eastwood P, Gonzalez J, Paredes S, et al. Discovery of N-(5,6-diarylpyridin-2-yl)amide derivatives as potent and selective A2B adenosine receptor antagonists. *Bioorganic Med Chem Lett*. 2010;20(5):1697-1700. doi:10.1016/j.bmcl.2010.01.045
202. Eastwood P, Esteve C, González J, et al. Discovery of LAS101057: A Potent, Selective, and Orally Efficacious A 2BAdenosine Receptor Antagonist. *ACS Med Chem Lett*. 2011;2(3):213-218. doi:10.1021/ml100249e
203. Carlsson J, Tosh DK, Phan K, Gao Z-G, Jacobson KA. Structure-activity relationships and molecular modeling of 1,2,4-triazoles as adenosine receptor antagonists. *ACS Med Chem Lett*. 2012;3(9):715-720. doi:10.1021/ml300097g
204. Receveur J-M, Bjurling E, Ulven T, Little PB, Nørregaard PK, Högberg T. 4-Acylamino-and 4-ureidobenzamides as melanin-concentrating hormone (MCH) receptor 1 antagonists. *Bioorg Med Chem Lett*. 2004;14(20):5075-5080. doi:10.1016/j.bmcl.2004.07.077
205. Baell JB, Holloway GA. New substructure filters for removal of pan assay interference compounds (PAINS) from screening libraries and for their exclusion in bioassays. *J Med Chem*. 2010;53(7):2719-2740. doi:10.1021/jm901137j
206. Capuzzi SJ, Muratov EN, Tropsha A. Phantom PAINS: Problems with the Utility of Alerts for P an-A ssay IN terference Compound S. *J Chem Inf Model*. 2017;57(3):417-427. doi:10.1021/acs.jcim.6b00465
207. Jasial S, Hu Y, Bajorath J. How Frequently Are Pan Assay Interference Compounds Active? Large-Scale Analysis of Screening Data Reveals Diverse Activity Profiles, Low Global Hit Frequency, and Many Consistently Inactive Compounds. *J Med Chem*. 2017;60(9):3879-3886. doi:10.1021/acs.jmedchem.7b00154
208. Kiss LE, Ferreira HS, Torrão L, et al. Discovery of a long-acting, peripherally selective inhibitor of catechol-O-methyltransferase. *J Med Chem*. 2010;53(8):3396-3411. doi:10.1021/jm1001524
209. Http://www.cbligand.org/PAINS/. PAINS. doi:http://www.cbligand.org/PAINS/
210. Shoichet BK. Screening in a spirit haunted world. *Drug Discov Today*. 2006;11(13-14):607-615. doi:10.1016/j.drudis.2006.05.014
211. Sabbadin D, Ciancetta A, Moro S, Modeling M, Mms S, Padova U. Bridging Molecular Docking to Membrane Molecular Dynamics To Investigate GPCR − Ligand Recognition: The Human A. 2014.
212. Tarcsay Á, Paragi G, Vass M, Jójárt B, Bogár F, Keserű GM. The Impact of Molecular Dynamics Sampling on the Performance of Virtual Screening against GPCRs. *J Chem Inf Model*. 2013;53(11):2990-2999. doi:10.1021/ci400087b
213. Ng HW, Laughton CA, Doughty SW. Molecular Dynamics Simulations of the Adenosine A2a

Receptor in. 2014;(1).
214. Ng HW, Laughton CA, Doughty SW. Molecular Dynamics Simulations of the Adenosine A2a Receptor: Structural Stability, Sampling, and Convergence. *J Chem Inf Model*. 2013;53(5):1168-1178. doi:10.1021/ci300610w
215. Li J, Jonsson AL, Beuming T, Shelley JC, Voth G a. Ligand-dependent activation and deactivation of the human adenosine A(2A) receptor. *J Am Chem Soc*. 2013;135(23):8749-8759. doi:10.1021/ja404391q
216. Sabbadin D, Ciancetta A, Deganutti G, Cuzzolin A, Moro S. Exploring the recognition pathway at the human A 2A adenosine receptor of the endogenous agonist adenosine using supervised molecular dynamics simulations. *Med Chem Commun*. 2015;6(15):1081-1085. doi:10.1039/C5MD00016E
217. Dickson CJ, Rosso L, Betz RM, Walker RC, Gould IR. GAFFlipid: A General Amber Force Field for the accurate molecular dynamics simulation of phospholipid. *Soft Matter*. 2012;8:9617-9627. doi:10.1039/c2sm26007g
218. Cheng PC. The contrast formation in optical microscopy. In: *Handbook of Biological Confocal Microscopy: Third Edition*. ; 2006:162-206. doi:10.1007/978-0-387-45524-2_8
219. Euro-Bioimaging Interim Web-Access Portal. http://www.eurobioimaging-interim.eu/fret.html. Accessed January 11, 2020.
220. Harris DC. Applications of Spectrophotometry. *Quant Chem Anal*. 2010.
221. Zheng J. Spectroscopy-Based Quantitative Fluorescence Resonance Energy Transfer Analysis. In: *Ion Channels*. Totowa, NJ: Humana Press; 2006:65-77. doi:10.1385/1-59745-095-2:65
222. Stoddart LA, Vernall AJ, Denman JL, Briddon SJ, Kellam B, Hill SJ. Fragment Screening at Adenosine-A3 Receptors in Living Cells Using a Fluorescence-Based Binding Assay. *Chem Biol*. 2012;19(9):1105-1115. doi:10.1016/j.chembiol.2012.07.014
223. Klein MT, Vinson PN, Niswender CM. Approaches for probing allosteric interactions at 7 transmembrane spanning receptors. *Prog Mol Biol Transl Sci*. 2013;115:1-59. doi:10.1016/B978-0-12-394587-7.00001-4
224. Degorce F, Card A, Soh S, Trinquet E, Knapik GP, Xie B. HTRF: A technology tailored for drug discovery - A review of theoretical aspects and recent applications. *Curr Chem Genomics*. 2009;3:22-32. doi:10.2174/1875397300903010022
225. Ayoub MA, Trebaux J, Vallaghe J, et al. Homogeneous time-resolved fluorescence-based assay to monitor extracellular signal-regulated kinase signaling in a high-throughput format. *Front Endocrinol (Lausanne)*. 2014;5:94. doi:10.3389/fendo.2014.00094
226. Miwatashi S, Arikawa Y, Matsumoto T, et al. Synthesis and Biological Activities of 4-Phenyl-5-pyridyl-1,3-thiazole Derivatives as Selective Adenosine A3 Antagonists. *Chem Pharm Bull (Tokyo)*. 2008;56(8):1126-1137. doi:10.1248/cpb.56.1126
227. Haeusler D, Grassinger L, Fuchshuber F, et al. Hide and seek: A Comparative Autoradiographic In Vitro Investigation of the Adenosine A3 Receptor. *Eur J Nucl Med Mol Imaging*. 2015;42(6):928-939. doi:10.1007/s00259-014-2985-2
228. Yaziji V, Rodríguez D, Coelho A, et al. Selective and potent adenosine A3 receptor antagonists by methoxyaryl substitution on the N-(2,6-diarylpyrimidin-4-yl)acetamide scaffold. *Eur J Med Chem*. 2013;59:235-242. doi:10.1016/j.ejmech.2012.11.010
229. Areias F, Correia C, Rocha A, et al. 2-Aryladenine derivatives as a potent scaffold for A1, A3 and dual A1/A3 adenosine receptor antagonists: Synthesis and structure-activity relationships. *Bioorganic Med Chem*. 2019;27(19):3551-3558. doi:10.1016/j.bmc.2019.06.034
230. Sexton PM, Christopoulos A. To Bind or Not to Bind: Unravelling GPCR Polypharmacology. *Cell*. 2018. doi:10.1016/j.cell.2018.01.018
231. Zhang G, Liu Y, Ruoho AE, Hurley JH. Structure of the adenylyl cyclase catalytic core. *Nature*. 1997;386(6622):247-253. doi:10.1038/386247a0
232. Knight A, Hemmings JL, Winfield I, et al. Discovery of Novel Adenosine Receptor Agonists That Exhibit Subtype Selectivity. *J Med Chem*. 2016;59(3):947-964. doi:10.1021/acs.jmedchem.5b01402
233. Motulsky HJ, Mahan LC. The kinetics of competitive radioligand binding predicted by the law of mass action. *Mol Pharmacol*. 1984;25(1):1-9. doi:10.1124/mol.114.11er14
234. Regression with Prism 8: 'Ambiguous'Title. http://www.graphpad.com/guides/prism/8/curve-

fitting/reg_analysischeck_nonlin_ambiguous.htm.
235. Stoddart LA, Johnstone EKM, Wheal AJ, et al. Application of BRET to monitor ligand binding to GPCRs. *Nat Methods*. 2015;12(7):661-663. doi:10.1038/nmeth.3398
236. Motulsky HJ. Interpreting the extra sum-of squares F test. https://www.graphpad.com/guides/prism/7/curve-fitting/index.htm?reg_interpreting_comparison_of_mod_2.htm%0A. Published 2019.
237. Schild HO. pA, A new scale for the measurement of drug antagonism. *Br J Pharmacol Chemother*. 1947;2(3):189-206. doi:10.1111/j.1476-5381.1947.tb00336.x
238. Curtis MJ, Alexander S, Cirino G, et al. Experimental design and analysis and their reporting II: updated and simplified guidance for authors and peer reviewers. *Br J Pharmacol*. 2018;175(7):987-993. doi:10.1111/bph.14153
239. Massova I, Kollman PA. Combined molecular mechanical and continuum solvent approach (MM-PBSA/GBSA) to predict ligand binding. *Perspect Drug Discov Des*. 2000;18:113-135. doi:10.1023/A:1008763014207
240. Homeyer N, Gohlke H. FEW: A workflow tool for free energy calculations of ligand binding. *J Comput Chem*. 2013;34(11):965-973. doi:10.1002/jcc.23218
241. Stamatis D, Lagarias P, Barkan K, Vrontaki E, Ladds G, Kolocouris A. Structural Characterization of Agonist Binding to an A 3 Adenosine Receptor through Biomolecular Simulations and Mutagenesis Experiments. *J Med Chem*. 2019;62(19):8831-8846. doi:10.1021/acs.jmedchem.9b01164
242. Stoddart LA, Kilpatrick LE, Hill SJ. NanoBRET Approaches to Study Ligand Binding to GPCRs and RTKs. *Trends Pharmacol Sci*. 2018;39(2):136-147. doi:10.1016/j.tips.2017.10.006
243. Barkan K, Lagarias P, Stamatis D, Vrontaki E, Klotz KL, Kolocouris A, Ladds G. Pharmacological Characterisation of Novel Adenosine Receptor A3AR Antagonists. *bioRxiv, doi.org/101101/693796*. 2019.
244. Cheng YC, Prusoff WH. Relationship between the inhibition constant (KI) and the concentration of inhibitor which causes 50 per cent inhibition (I50) of an enzymatic reaction. *Biochem Pharmacol*. 1973;22(23):3099-3108. doi:10.1016/0006-2952(73)90196-2
245. Meng X-Y, Zhang H-X, Mezei M, Cui M. Molecular Docking: A Powerful Approach for Structure-Based Drug Discovery. *Curr Comput Aided-Drug Des*. 2011;7(2):146-157. doi:10.2174/157340911795677602
246. Giraldo J, Serra J, Roche D, Rovira X. Assessing Receptor Affinity for Inverse Agonists: Schild and Cheng-Prusoff Methods Revisited. *Curr Drug Targets*. 2006;8(1):197-202. doi:10.2174/138945007779315687
247. Tunçer S, Gurbanov R, Sheraj I, Solel E, Esenturk O, Banerjee S. Low dose dimethyl sulfoxide driven gross molecular changes have the potential to interfere with various cellular processes. *Sci Rep*. 2018;8(1):14828. doi:10.1038/s41598-018-33234-z
248. Arruda MA, Stoddart LA, Gherbi K, Briddon SJ, Kellam B, Hill SJ. A Non-imaging High Throughput Approach to Chemical Library Screening at the Unmodified Adenosine-A3 Receptor in Living Cells. *Front Pharmacol*. 2017;8. doi:10.3389/fphar.2017.00908
249. Gao Z-G, Kim S-K, Biadatti T, et al. Structural determinants of A3 adenosine receptor activation: nucleoside ligands at the agonist/antagonist boundary. *J Med Chem*. 2002;45(20):4471-4484.
250. May LT, Bridge LJ, Stoddart LA, Briddon SJ, Hill SJ. Allosteric interactions across native adenosine-A 3 receptor homodimers: quantification using single-cell ligand-binding kinetics. *FASEB J*. 2011;25(10):3465-3476. doi:10.1096/fj.11-186296
251. Straatsma TP, McCammon JA. Computational Alchemy. *Annu Rev Phys Chem*. 1992;43(1):407-435. doi:10.1146/annurev.pc.43.100192.002203
252. Walker R, Steinbrecher T, McGee T, Miller B III JS. AMBER ADVANCED TUTORIALS. TUTORIAL 3: MM-PBSA. http://ambermd.org/tutorials/advanced/tutorial3/. Published 2006. Accessed January 11, 2020.
253. Homeyer N, Gohlke H. Free energy calculations by the Molecular Mechanics Poisson-Boltzmann Surface Area method. *Mol Inform*. 2012;31(1):114-122. doi:10.1002/minf.201100135
254. Baker NA, Sept D, Joseph S, Holst MJ, McCammon JA. Electrostatics of nanosystems: Application to microtubules and the ribosome. *Proc Natl Acad Sci*. 2001;98(18):10037-10041.

doi:10.1073/pnas.181342398
255. Boschitsch AH, Fenley MO. A fast and robust Poisson-Boltzmann solver based on adaptive Cartesian grids. *J Chem Theory Comput*. 2011;7(5):1524-1540. doi:10.1021/ct1006983
256. Wang N, Zhou S, Kekenes-Huskey PM, Li B, McCammon JA. Poisson-Boltzmann versus size-modified Poisson-Boltzmann electrostatics applied to lipid bilayers. *J Phys Chem B*. 2014. doi:10.1021/jp511702w
257. Li C, Li L, Petukh M, Alexov E. Progress in developing Poisson-Boltzmann equation solvers. *Comput Math Biophys*. 2013;1:42-62. doi:10.2478/mlbmb-2013-0002
258. Wang J, Tan C, Chanco E, Luo R. Quantitative analysis of Poisson–Boltzmann implicit solvent in molecular dynamics. *Phys Chem Chem Phys*. 2010;12(5):1194-1202. doi:10.1039/B917775B
259. Salomon-Ferrer R, Case DA, Walker RC. An overview of the Amber biomolecular simulation package. *Wiley Interdiscip Rev Comput Mol Sci*. 2013;3(2):198-210. doi:10.1002/wcms.1121
260. Prabhu N V., Zhu P, Sharp KA. Implementation and testing of stable, fast implicit solvation in molecular dynamics using the smooth-permittivity finite difference Poisson-Boltzmann method. *J Comput Chem*. 2004;25(16):2049-2064. doi:10.1002/jcc.20138
261. Li L, Li C, Sarkar S, et al. DelPhi: a comprehensive suite for DelPhi software and associated resources. *BMC Biophys*. 2012;5(1):9. doi:10.1186/2046-1682-5-9
262. Qi R, Botello-Smith WM, Luo R. Acceleration of Linear Finite-Difference Poisson–Boltzmann Methods on Graphics Processing Units. *J Chem Theory Comput*. 2017;13(7):3378-3387. doi:10.1021/acs.jctc.7b00336
263. Constanciel R, Contreras R. Self consistent field theory of solvent effects representation by continuum models: Introduction of desolvation contribution. *Theor Chim Acta*. 1984;65:1–11. doi:10.1007/BF02427575
264. Clark Still W, Tempczyk A, Hawley RC, Hendrickson T. Semianalytical Treatment of Solvation for Molecular Mechanics and Dynamics. *J Am Chem Soc*. 1990;112(16):6127–6129. doi:10.1021/ja00172a038
265. Qiu D, Shenkin PS, Hollinger FP, Still WC. The GB/SA Continuum Model for Solvation. A Fast Analytical Method for the Calculation of Approximate Born Radii. *J Phys Chem A*. 1997;101(16):3005-3014. doi:10.1021/jp961992r
266. Hawkins GD, Cramer CJ, Truhlar DG. Parametrized models of aqueous free energies of solvation based on pairwise descreening of solute atomic charges from a dielectric medium. *J Phys Chem*. 1996;100(51):19824-19839. doi:10.1021/jp961710n
267. Tsui V, Case DA. Theory and applications of the Generalized Born solvation model in macromolecular simulations. *Biopolymers*. 2000;56(4):275-291. doi:10.1002/1097-0282(2000)56:4<275::AID-BIP10024>3.0.CO;2-E
268. Onufriev A, Bashford D, Case DA. Exploring protein native states and large-scale conformational changes with a modified generalized born model. *Proteins Struct Funct Bioinforma*. 2004;55(2):383-394. doi:10.1002/prot.20033
269. Roe DR, Okur A, Wickstrom L, Hornak V, Simmerling C. Secondary Structure Bias in Generalized Born Solvent Models: Comparison of Conformational Ensembles and Free Energy of Solvent Polarization from Explicit and Implicit Solvation. *J Phys Chem B*. 2007;111(7):1846-1857. doi:10.1021/jp066831u
270. Lee MS, Feig M, Salsbury FR, Brooks CL. New analytic approximation to the standard molecular volume definition and its application to generalized born calculations. *J Comput Chem*. 2003;24(11):1348-1356. doi:10.1002/jcc.10272
271. Sun H, Li Y, Tian S, Xu L, Hou T. Assessing the performance of MM/PBSA and MM/GBSA methods. 4. Accuracies of MM/PBSA and MM/GBSA methodologies evaluated by various simulation protocols using PDBbind data set. *Phys Chem Chem Phys*. 2014;16(31):16719-16729. doi:10.1039/C4CP01388C
272. Hou T, Wang J, Li Y, Wang W. Assessing the performance of the MM/PBSA and MM/GBSA methods. 1. The accuracy of binding free energy calculations based on molecular dynamics simulations. *J Chem Inf Model*. 2011;51(1):69-82. doi:10.1021/ci100275a
273. Zhu K, Shirts MR, Friesner RA. Improved Methods for Side Chain and Loop Predictions via the

Protein Local Optimization Program: Variable Dielectric Model for Implicitly Improving the Treatment of Polarization Effects. *J Chem Theory Comput*. 2007;3(6):2108-2119. doi:10.1021/ct700166f

274. Li J, Abel R, Zhu K, Cao Y, Zhao S, Friesner RA. The VSGB 2.0 model: A next generation energy model for high resolution protein structure modeling. *Proteins Struct Funct Bioinforma*. 2011;79(10):2794-8120. doi:10.1002/prot.23106
275. Tan C, Tan Y-H, Luo R. Implicit Nonpolar Solvent Models. *J Phys Chem B*. 2007;111(42):12263-12274. doi:10.1021/jp073399n
276. Wong S, Amaro RE, McCammon JA. MM-PBSA Captures Key Role of Intercalating Water Molecules at a Protein−Protein Interface. *J Chem Theory Comput*. 2009;5(2):422-429. doi:10.1021/ct8003707
277. Genheden S, Mikulskis P, Hu L, Kongsted J, Söderhjelm P, Ryde U. Accurate predictions of nonpolar solvation free energies require explicit consideration of binding-site hydration. *J Am Chem Soc*. 2011;133(33):13081-13092. doi:10.1021/ja202972m
278. Mikulskis P, Genheden S, Ryde U. Effect of explicit water molecules on ligand-binding affinities calculated with the MM/GBSA approach. *J Mol Model*. 2014;20(6):2273. doi:10.1007/s00894-014-2273-x
279. Genheden S, Ryde U. The MM/PBSA and MM/GBSA methods to estimate ligand-binding affinities. *Expert Opin Drug Discov*. 2015;10(5):449-461. doi:10.1517/17460441.2015.1032936
280. Greenidge PA, Kramer C, Mozziconacci JC, Wolf RM. MM/GBSA binding energy prediction on the PDBbind data set: Successes, failures, and directions for further improvement. *J Chem Inf Model*. 2013;53(1):201-209. doi:10.1021/ci300425v
281. Cappel D, Sherman W, Beuming T. Calculating Water Thermodynamics in the Binding Site of Proteins – Applications of WaterMap to Drug Discovery. *Curr Top Med Chem*. 2017;17(23):2586-2598. doi:10.2174/1568026617666170414141452
282. Homeyer N, Ioannidis H, Kolarov F, et al. Interpreting Thermodynamic Profiles of Aminoadamantane Compounds Inhibiting the M2 Proton Channel of Influenza A by Free Energy Calculations. *J Chem Inf Model*. 2016;56(1):110-126. doi:10.1021/acs.jcim.5b00467
283. Matricon P, Ranganathan A, Warnick E, et al. Fragment optimization for GPCRs by molecular dynamics free energy calculations: Probing druggable subpockets of the A 2A adenosine receptor binding site. *Sci Rep*. 2017;7(1):6398. doi:10.1038/s41598-017-04905-0
284. Gkeka P, Eleftheratos S, Kolocouris A, Cournia Z. Free Energy Calculations Reveal the Origin of Binding Preference for Aminoadamantane Blockers of Influenza A/M2TM Pore. *J Chem Theory Comput*. 2013;9(2):1272-1281. doi:10.1021/ct300899n
285. Ioannidis H, Drakopoulos A, Tzitzoglaki C, et al. Alchemical Free Energy Calculations and Isothermal Titration Calorimetry Measurements of Aminoadamantanes Bound to the Closed State of Influenza A/M2TM. *J Chem Inf Model*. 2016;56(5):862-876. doi:10.1021/acs.jcim.6b00079
286. Miller BR, McGee TD, Swails JM, Homeyer N, Gohlke H, Roitberg AE. MMPBSA.py : An Efficient Program for End-State Free Energy Calculations. *J Chem Theory Comput*. 2012;8(9):3314-3321. doi:10.1021/ct300418h
287. Hou T, Wang J, Li Y, Wang W. Assessing the performance of the molecular mechanics/Poisson Boltzmann surface area and molecular mechanics/generalized Born surface area methods. II. the accuracy of ranking poses generated from docking. *J Comput Chem*. 2011;32(5):866-877. doi:10.1002/jcc.21666
288. Carlsson J, Yoo L, Gao ZG, Irwin JJ, Shoichet BK, Jacobson KA. Structure-based discovery of A2Aadenosine receptor ligands. *J Med Chem*. 2010;53(9):3748-3755. doi:10.1021/jm100240h
289. Protein Preparation Wizard, Epik Version 2.2, Impact Version 5.7, Prime Version 3.0, Schrödinger, LLC., New York, NY. *Protein Prep Wizard 2015-2; Epik version 24, Schrödinger, LLC, New York, NY, 2015; Impact version 59, Schrödinger, LLC, New York, NY, 2015; Prime version 32, Schrödinger, LLC, New York, NY, 2015*. 2011.
290. Kaminski GA, Friesner RA, Tirado-Rives J, Jorgensen WL. Evaluation and reparametrization of the OPLS-AA force field for proteins via comparison with accurate quantum chemical calculations on peptides. *J Phys Chem B*. 2001;105(22):6474-6487. doi:10.1021/jp003919d

291. Schrödinger Release 2017-1: Maestro, Schrödinger, LLC, New York, NY, 2017.
292. GOLD Suite, version 5.2; Cambridge Crystallographic Data Centre: Cambridge, U.K., 2015. *GOLD Suite, version 52; Cambridge Crystallogr Data Cent Cambridge, UK, 2015*.
293. Verdonk ML, Chessari G, Cole JC, et al. Modeling water molecules in protein- ligand docking using GOLD. *J Med Chem*. 2005;48(20):6504-6515.
294. Schrödinger Llc New York Ny. Glide, version 5.7. *Glid Schrödinger LLC NY*. 2011.
295. Maestro-Desmond Interoperability Tools, version 3.1; Schrodinger: New York, 2012.
296. Bowers KJ, Chow E, Xu H, et al. Scalable algorithms for molecular dynamics simulations on commodity clusters. In: *Proceedings of the 2006 ACM/IEEE Conference on Supercomputing, SC'06*. ; 2006:43-43. doi:10.1145/1188455.1188544
297. Wang J, Cieplak P, Kollman PA. How well does a restrained electrostatic potential (RESP) model perform in calculating conformational energies of organic and biological molecules? *J Comput Chem*. 2000;21(12):1049-1074. doi:10.1002/1096-987X(200009)21:12<1049::AID-JCC3>3.0.CO;2-F
298. Hornak V, Abel R, Okur A, Strockbine B, Roitberg A, Simmerling C. Comparison of multiple amber force fields and development of improved protein backbone parameters. *Proteins Struct Funct Genet*. 2006;65(3):712-725. doi:10.1002/prot.21123
299. Martyna GJ, Klein ML, Tuckerman M. Nosé–Hoover chains: The canonical ensemble via continuous dynamics. *J Chem Phys*. 1992;97(4):2635-2643.
300. Bayly CI, Cieplak P, Cornell WD, Kollman PA. A well-behaved electrostatic potential based method using charge restraints for deriving atomic charges: The RESP model. *J Phys Chem*. 1993;97(40):10269–10280. doi:10.1021/j100142a004
301. Frisch, M. J.; Trucks, G.W.; Schlegel, H. B.; Scuseria, G. E.; Robb, M. A.; Cheeseman, J. R.; Scalmani, G.; Barone, V.;Mennucci, B.; Petersson, G. A.; Nakatsuji, H.; Caricato, M.; Li, X.; Hratchian, H. P.; Izmaylov, A. F.; Bloino, J.; Zheng, G.; Sonnenber DJ. Gaussian 09. *Gaussian, Inc Wallingford CT*. 2009. doi:111
302. Humphrey W, Dalke A, Schulten K. VMD: Visual molecular dynamics. *J Mol Graph*. 1996;14(1):28-33. doi:10.1016/0263-7855(96)00018-5
303. Gohlke H, Case DA. Converging Free Energy Estimates: MM-PB(GB)SA Studies on the Protein-Protein Complex Ras-Raf. *J Comput Chem*. 2004;25(2):238-250. doi:10.1002/jcc.10379
304. Tikhonova IG, Selvam B, Ivetac A, Wereszczynski J, McCammon JA. Simulations of Biased Agonists in the β 2 Adrenergic Receptor with Accelerated Molecular Dynamics. *Biochemistry*. 2013;52(33):5593-5603. doi:10.1021/bi400499n
305. Fleetwood O, Matricon P, Carlsson J, Delemotte L. Energy Landscapes Reveal Agonist Control of G Protein-Coupled Receptor Activation via Microswitches. *Biochemistry*. 2020;59:880-891. doi:10.1021/acs.biochem.9b00842
306. Dror RO, Pan AC, Arlow DH, et al. Pathway and mechanism of drug binding to G-protein-coupled receptors. *Proc Natl Acad Sci*. 2011;108(32):13118-13123. doi:10.1073/pnas.1104614108
307. Guo D, Pan AC, Dror RO, et al. Molecular Basis of Ligand Dissociation from the Adenosine A2A Receptor. *Mol Pharmacol*. 2016;89(5):485-491. doi:10.1124/mol.115.102657
308. Lee S, Nivedha AK, Tate CG, Vaidehi N. Dynamic Role of the G Protein in Stabilizing the Active State of the Adenosine A2A Receptor. *Structure*. 2019;27(4):703-712.e3. doi:10.1016/j.str.2018.12.007
309. Latorraca NR, Venkatakrishnan AJ, Dror RO. GPCR Dynamics : Structures in Motion. *Chem Rev*. 2017;117(1):139-155. doi:10.1021/acs.chemrev.6b00177
310. Stoddart LA, Kilpatrick LE, Briddon SJ, Hill SJ. Probing the pharmacology of G protein-coupled receptors with fluorescent ligands. *Neuropharmacology*. 2015;98:48-57. doi:10.1016/j.neuropharm.2015.04.033
311. Keränen H, Åqvist J, Gutiérrez-De-Terán H. Free energy calculations of A2Aadenosine receptor mutation effects on agonist binding. *Chem Commun*. 2015;51(17):3522-3525. doi:10.1039/c4cc09517k
312. Liang BT, Jacobson KA. A physiological role of the adenosine A3 receptor: Sustained cardioprotection. *Proc Natl Acad Sci*. 2002;95(12):6995-6999. doi:10.1073/pnas.95.12.6995

APPENDIX

Table S5.1 GoldScore and Chemscore values for binding poses of **K18** and ranking of **K10, K11, K32**

	GoldScore	ChemScore	Schild analysis[a]	Radioligand binding[a]
K10	54.8	31.8	6.39 ± 0.3	4.49
K11	55.2	30.0	n.a.	5.15
K32	56.4	31.1	6.77 ± 0.3	2.40

	GoldScore	ChemScore	Schild analysis[a]	Radioligand binding[a]
"up TM1, TM2"	69.0	33.0	7.20 ± 0.3	0.899
"up TM5, TM6"	68.1	33.7		
"down"	55.9	29.0		

[a]see **Table 5.4** for definition

Table S5.2 (a) Highest GoldScore values of the "up TM5, TM6" docking pose for K18 in complex with WT and mutant A_3Rs. (b) MM-GBSA binding free energies (ΔG_{eff} in kcal mol^{-1}) for the complexes of K18 with WT and mutant A_3Rs; these were calculated using the trajectories of the MD simulations from the embedded docking poses of the complexes in fully hydrated POPE bilayers. (c) $\Delta\Delta G_= \Delta G_{mut}$ - ΔG_{WT}, in kcal mol^{-1}. In blue or red are shown $\Delta\Delta G$ values which are in agreement or not with biological results.

No	mutant	GoldScore	ΔG_{bind}[b] (ChemScore)	ΔG_{eff}[a] (MM-GBSA)	Potency[a]
1	WT	68.0	30.1	-70.1±3.5	baseline
2	L90$^{3.32}$A	66.3	30.0	-75.7±2.1	increase
3	V169$^{5.30}$A	56.6	27.9	-56.0±4.3	N.R.[c]
4	F168$^{5.29}$A	64.4	32.1	-55.0±3.1	decrease
5	V169$^{5.30}$E	67.9	32.8	-66.9±3.1	baseline
6	M174$^{5.35}$A	66.3	32.0	-57.5±4.7	decrease
7	M177$^{5.38}$A	61.0	32.0	-56.2±4.7	decrease
8	W185$^{5.46}$A	65.7	32.8	-69.0±2.2	baseline
9	V169$^{5.30}$A/W185$^{5.46}$A	66.6	29.9	-51.3±4.6	decrease
10	L246$^{6.51}$A	62.1	30.5	-54.4±5.2	N.R.[c]
11	I249$^{6.54}$A	63.5	32.3	-59.9±3.7	baseline
12	N250$^{6.55}$A	67.7	30.4	-68.9±5.2	N.R.[c]
13	I253$^{6.58}$A	61.6	27.6	-65.6±2.2	baseline
14	I253$^{6.58}$E	64.6	28.8	-66.3±4.2	baseline
15	L264$^{7.35}$A	61.4	30.9	-74.9±2.2	increase

[a] see **Table 5.2** for definition; [b] ΔG_{bind} is the Chemscore value; [c] No response Mutants

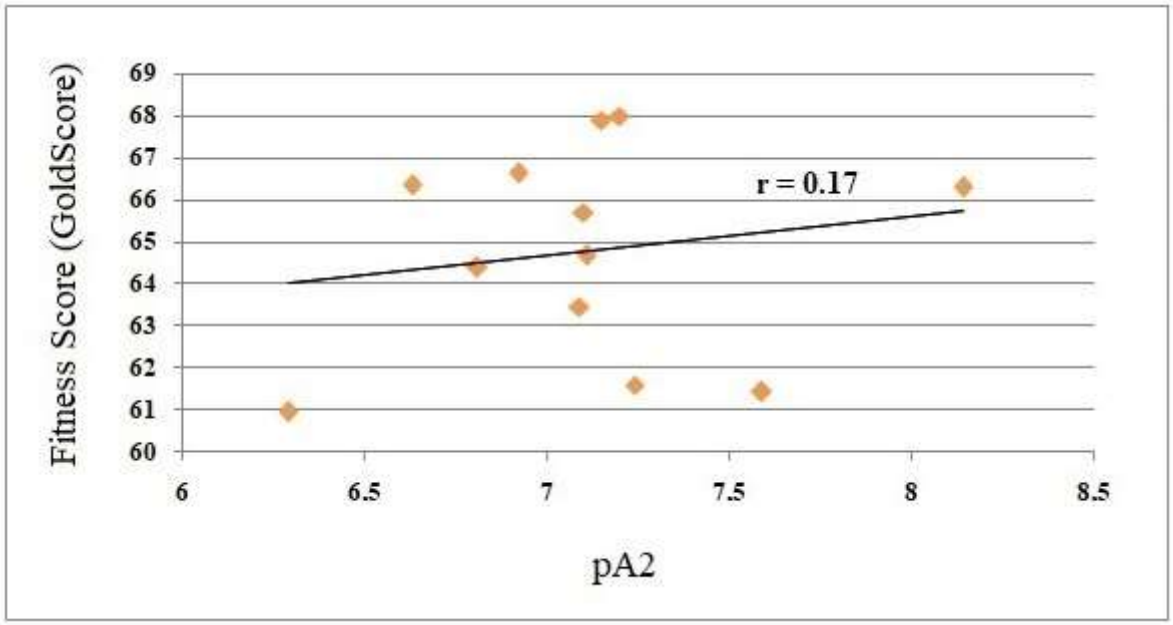

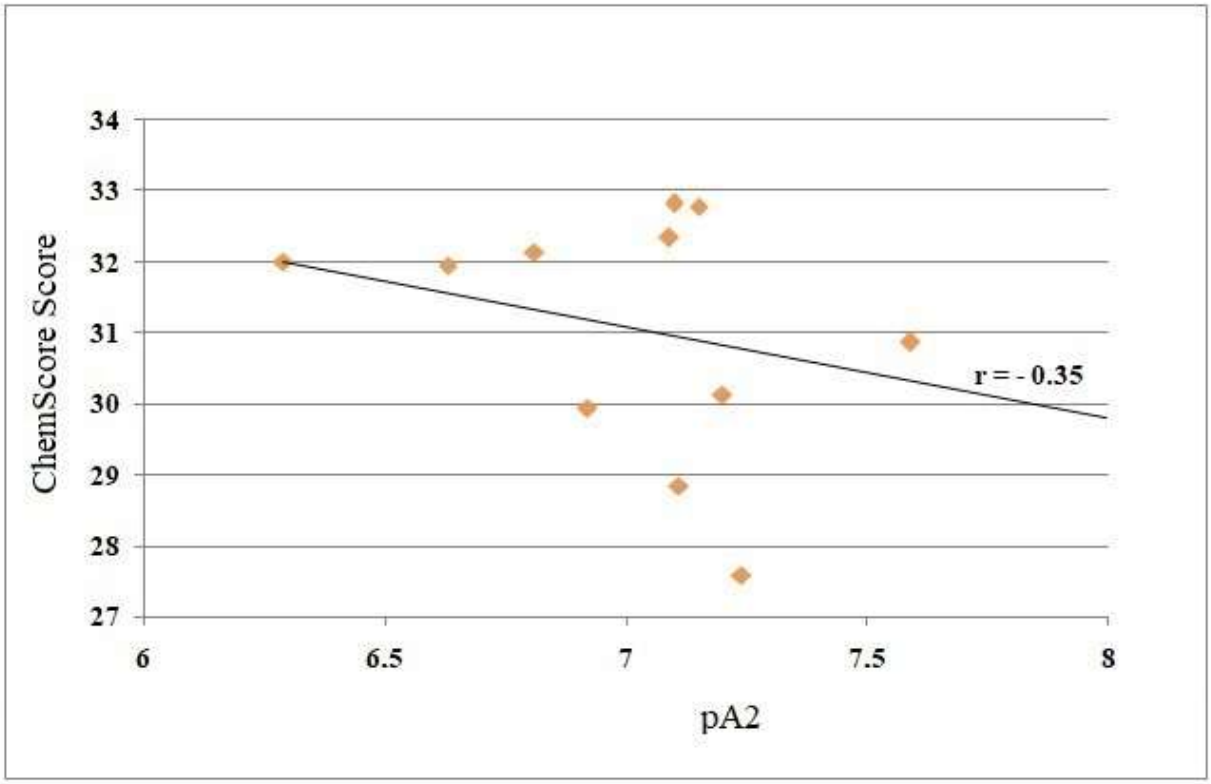

Figure S5.1(Top) GoldScore and (bottom) ChemScore values of **K18** plotted against experimental activities (pA2) for A_3Rs.

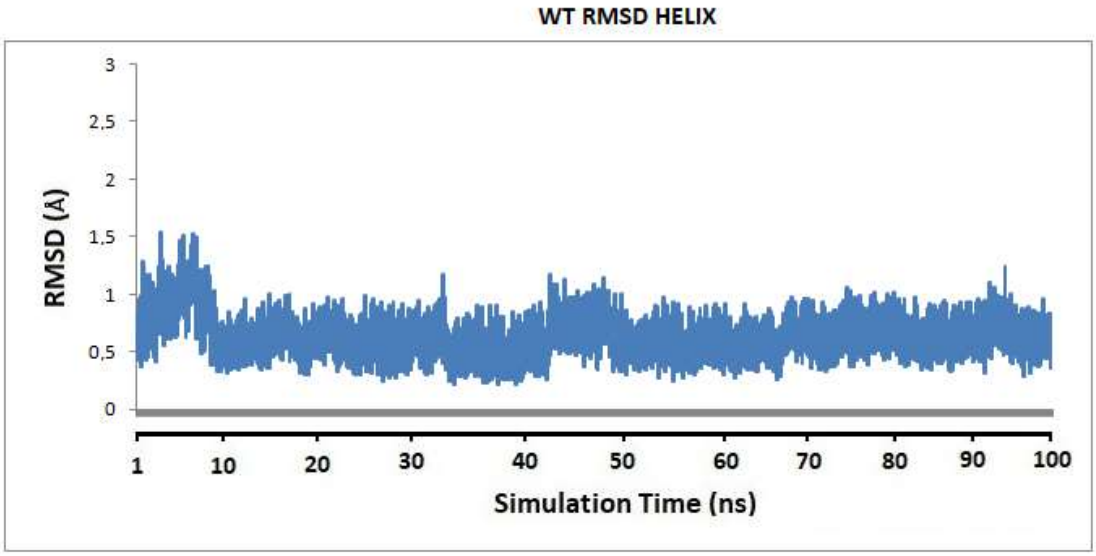
WT RMSD HELIX
RMSD (Å)
3
2,5
2
1,5
1
0,5
0
1
10
20
30
40
50
60
70
80
90
100
Simulation Time (ns)

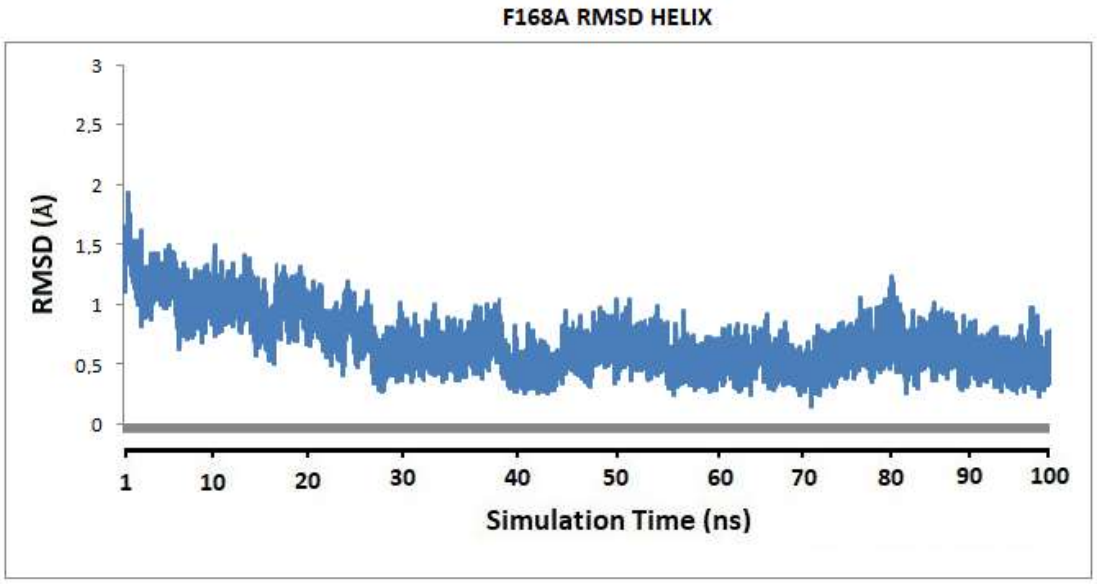
F168A RMSD HELIX
RMSD (Å)
3
2,5
2
1,5
1
0,5
0
1
10
20
30
40
50
60
70
80
90
100
Simulation Time (ns)

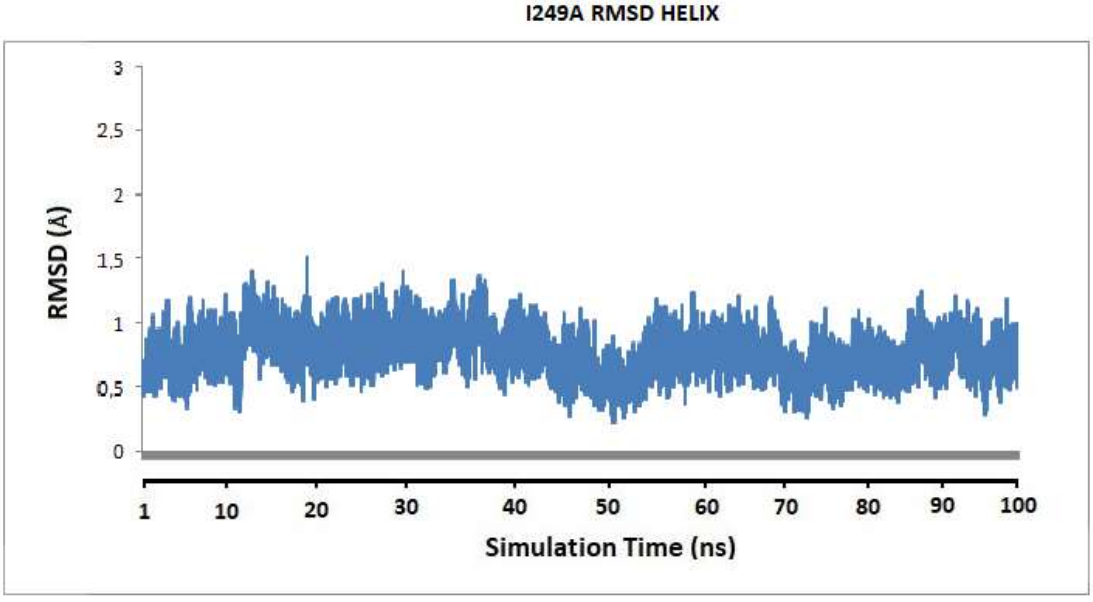
I249A RMSD HELIX
RMSD (Å)
3
2,5
2
1,5
1
0,5
0
1
10
20
30
40
50
60
70
80
90
100
Simulation Time (ns)

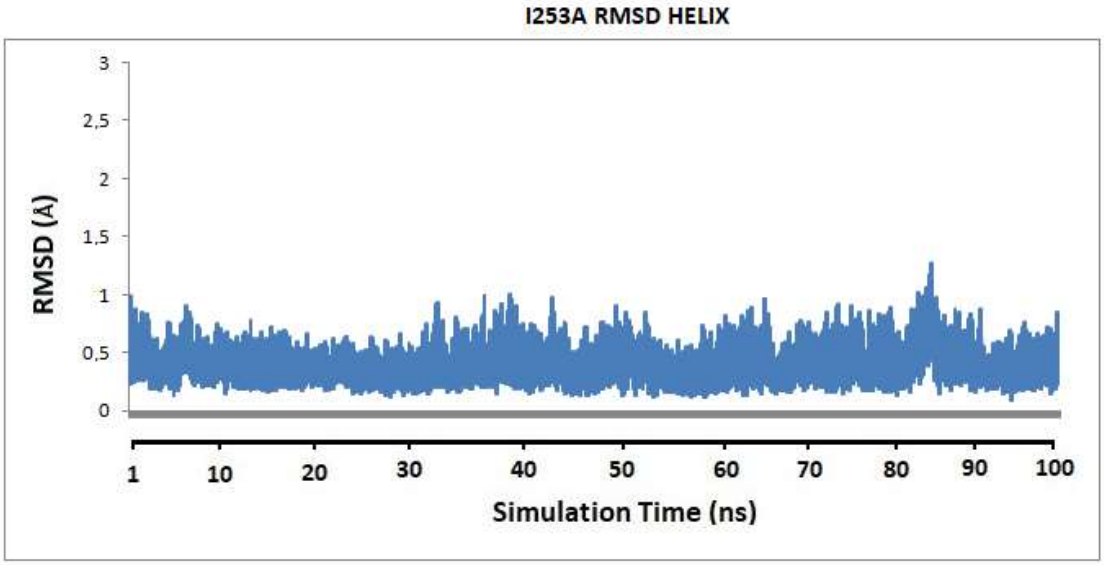
I253A RMSD HELIX
RMSD (Å)
3
2,5
2
1,5
1
0,5
0
1
10
20
30
40
50
60
70
80
90
100
Simulation Time (ns)

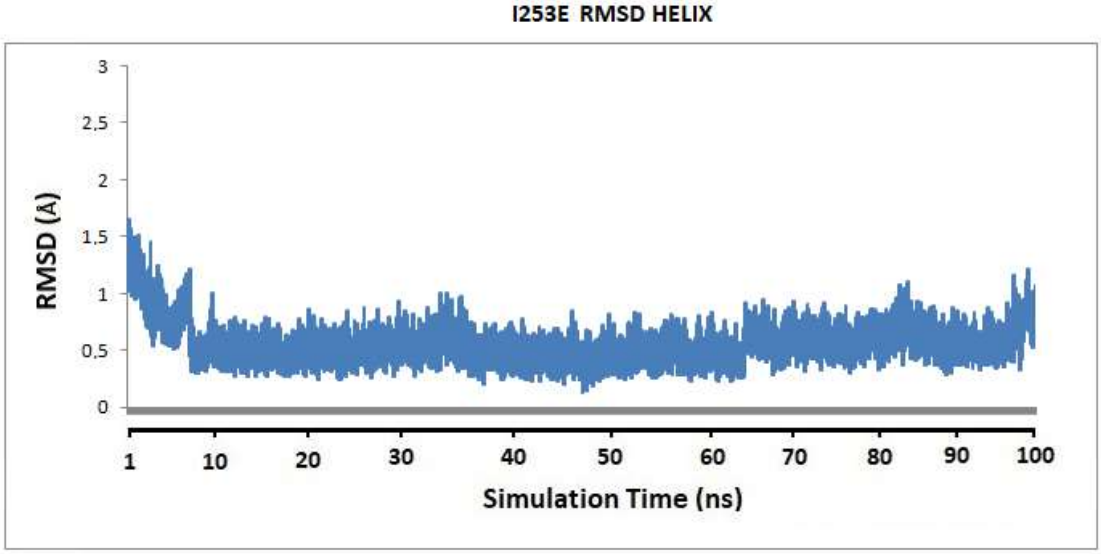
I253E RMSD HELIX
RMSD (Å)
3
2,5
2
1,5
1
0,5
0
1
10
20
30
40
50
60
70
80
90
100
Simulation Time (ns)

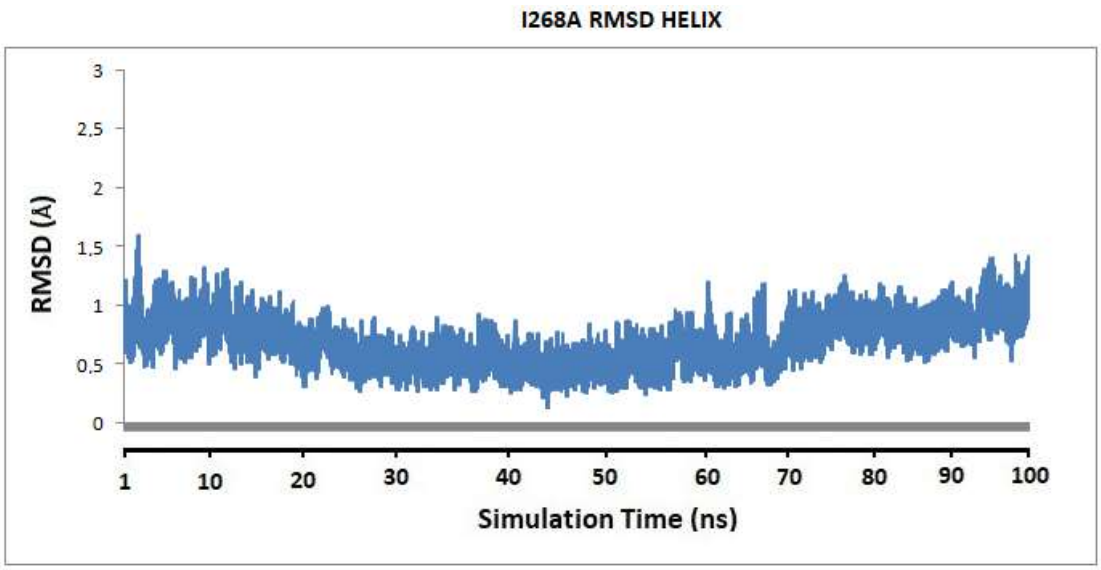
I268A RMSD HELIX
RMSD (Å)
3
2,5
2
1,5
1
0,5
0
1
10
20
30
40
50
60
70
80
90
100
Simulation Time (ns)

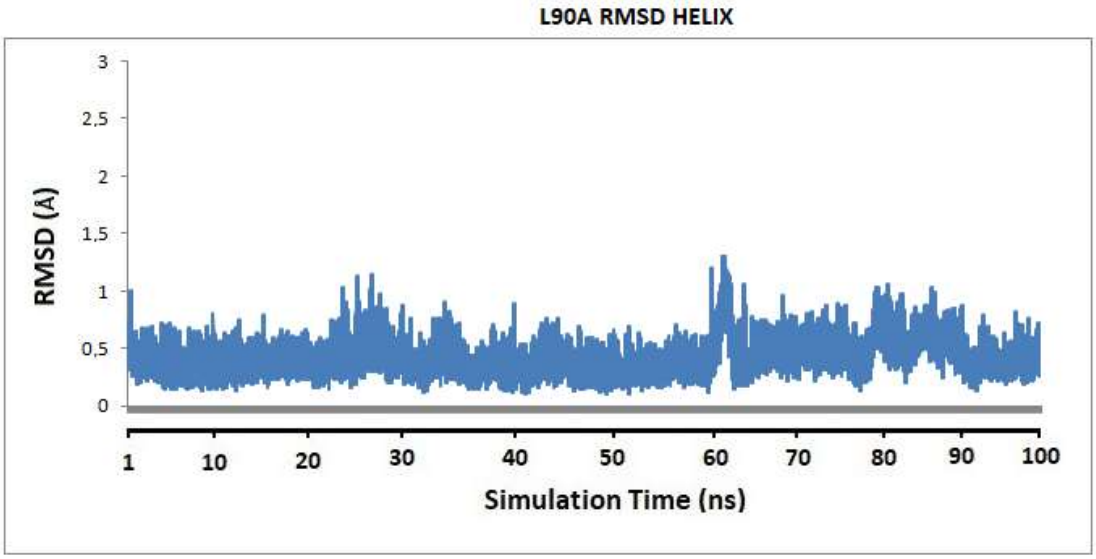
L90A RMSD HELIX
RMSD (Å)
3
2,5
2
1,5
1
0,5
0
1
10
20
30
40
50
60
70
80
90
100
Simulation Time (ns)

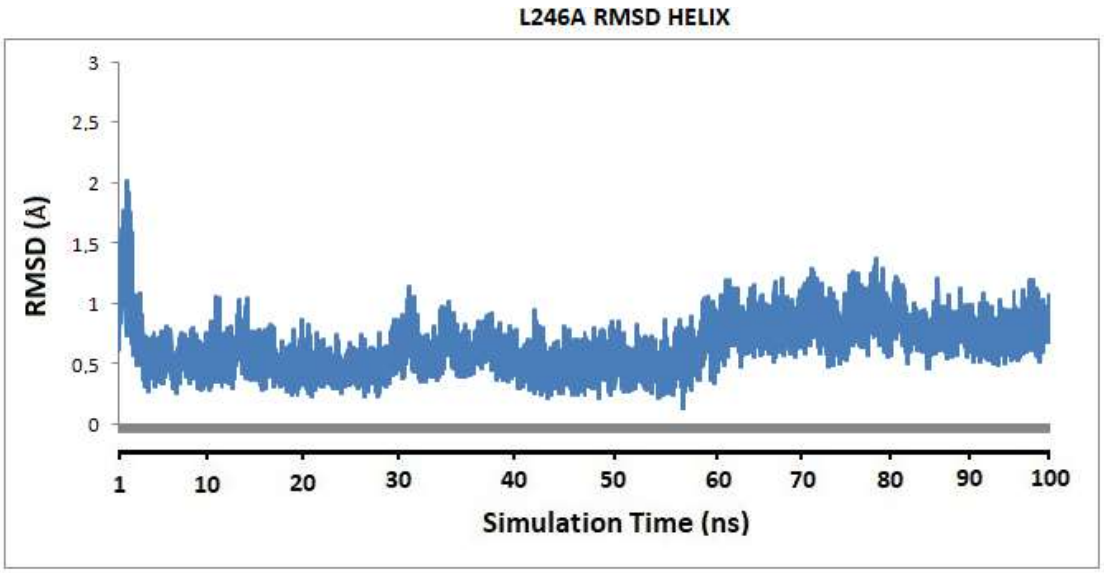
L246A RMSD HELIX
RMSD (Å)
3
2,5
2
1,5
1
0,5
0
1
10
20
30
40
50
60
70
80
90
100
Simulation Time (ns)

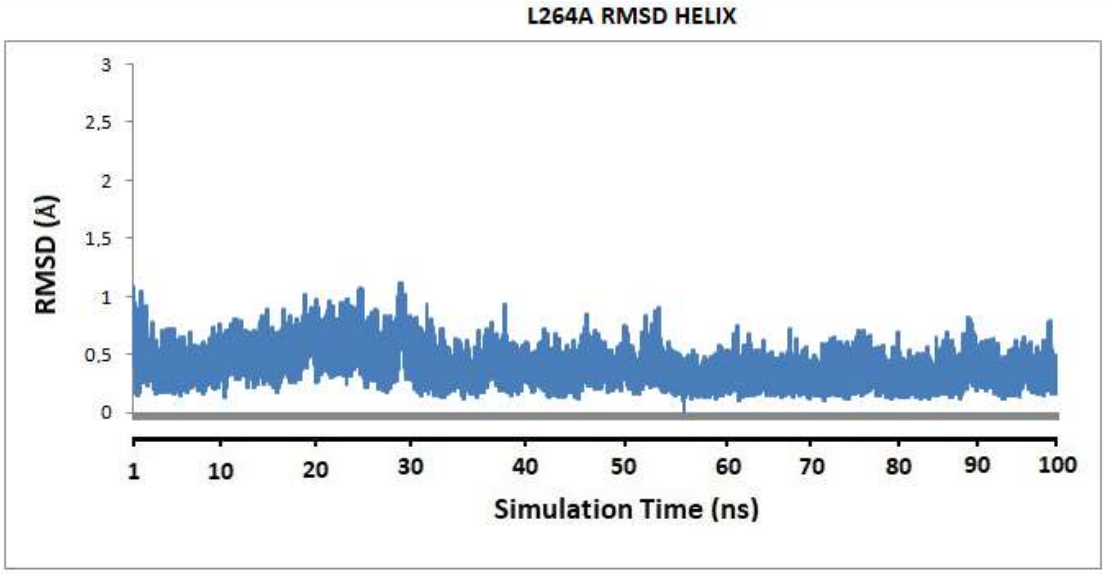
L264A RMSD HELIX
RMSD (Å)
3
2,5
2
1,5
1
0,5
0
1
10
20
30
40
50
60
70
80
90
100
Simulation Time (ns)

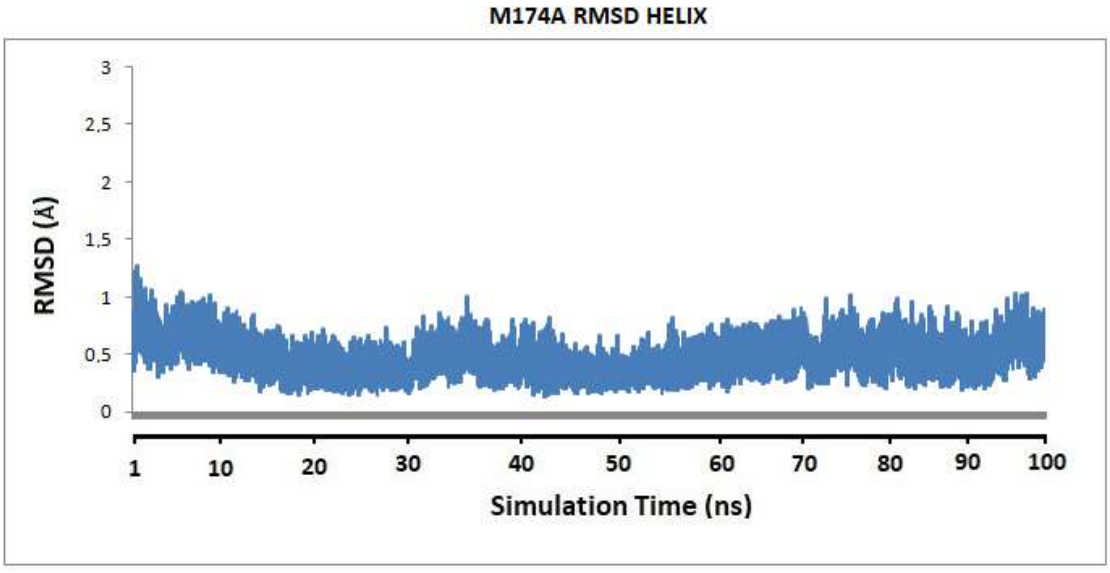
M174A RMSD HELIX
RMSD (Å)
3
2,5
2
1,5
1
0,5
0
1
10
20
30
40
50
60
70
80
90
100
Simulation Time (ns)

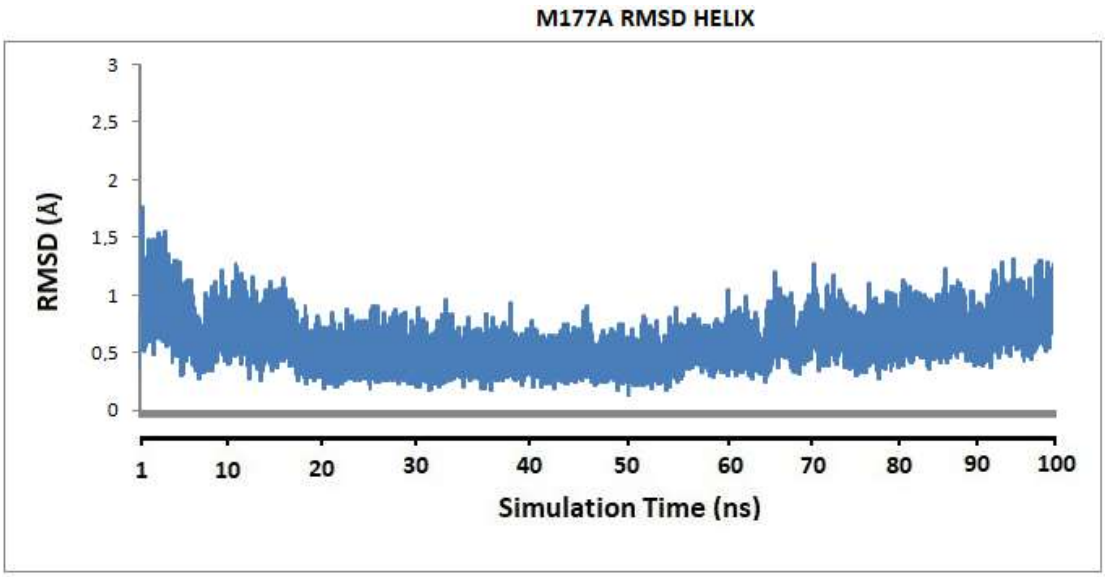
M177A RMSD HELIX
RMSD (Å)
3
2,5
2
1,5
1
0,5
0
1
10
20
30
40
50
60
70
80
90
100
Simulation Time (ns)

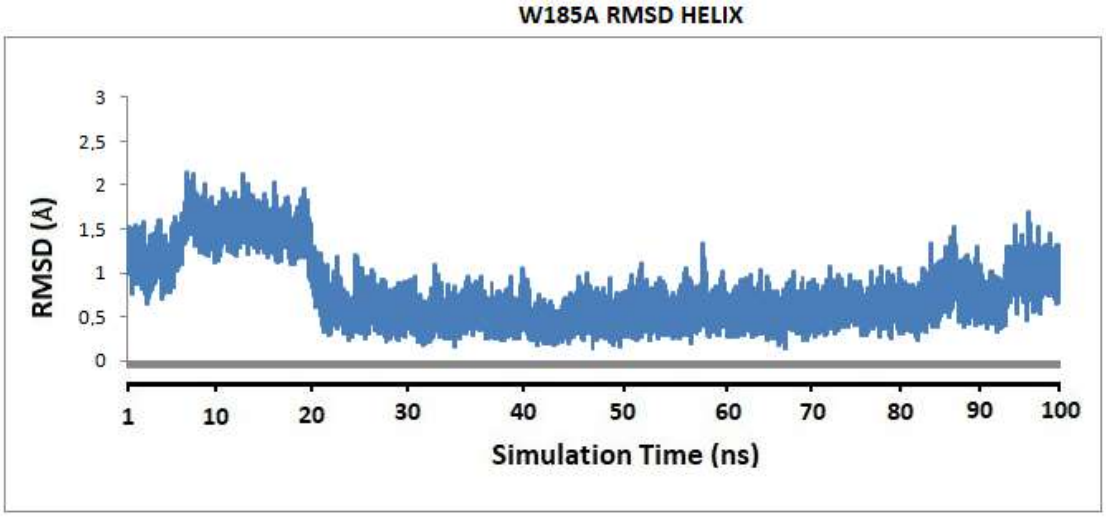
W185A RMSD HELIX
RMSD (Å)
3
2,5
2
1,5
1
0,5
0
1
10
20
30
40
50
60
70
80
90
100
Simulation Time (ns)

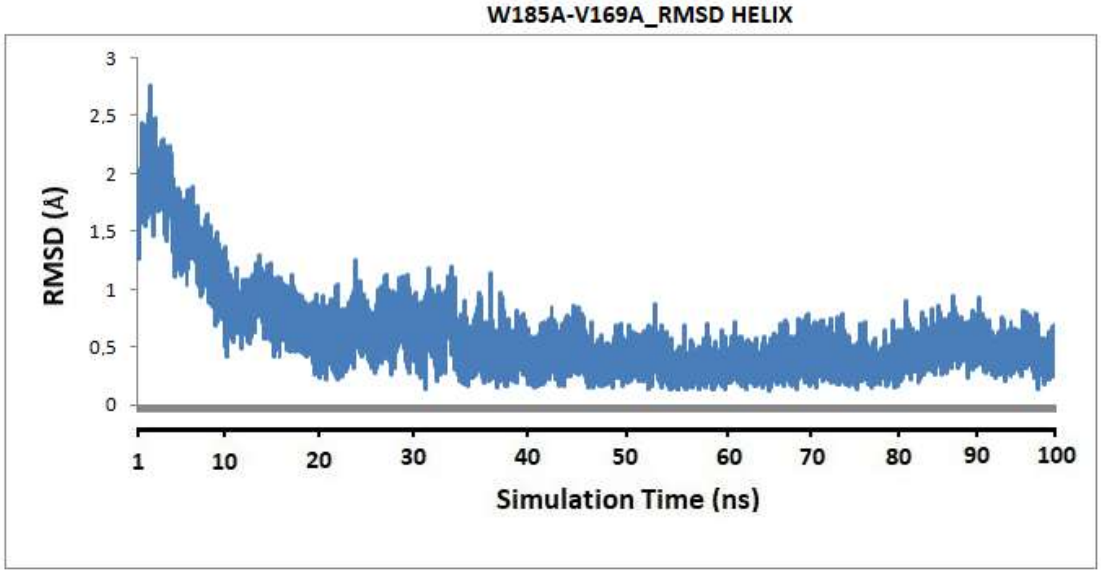
W185A-V169A_RMSD HELIX
RMSD (Å)
3
2,5
2
1,5
1
0,5
0
1
10
20
30
40
50
60
70
80
90
100
Simulation Time (ns)

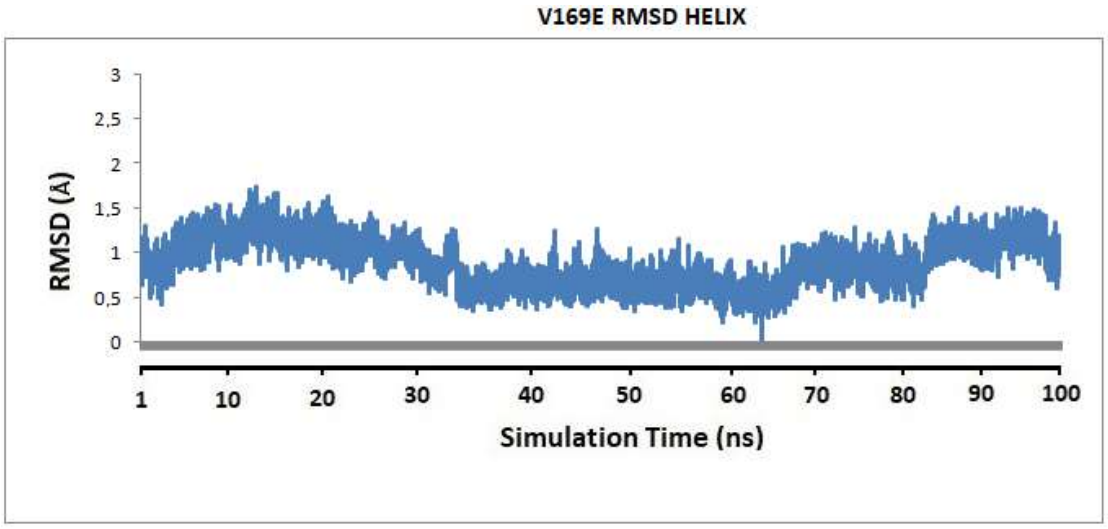
V169E RMSD HELIX
RMSD (Å)
3
2,5
2
1,5
1
0,5
0
1
10
20
30
40
50
60
70
80
90
100
Simulation Time (ns)

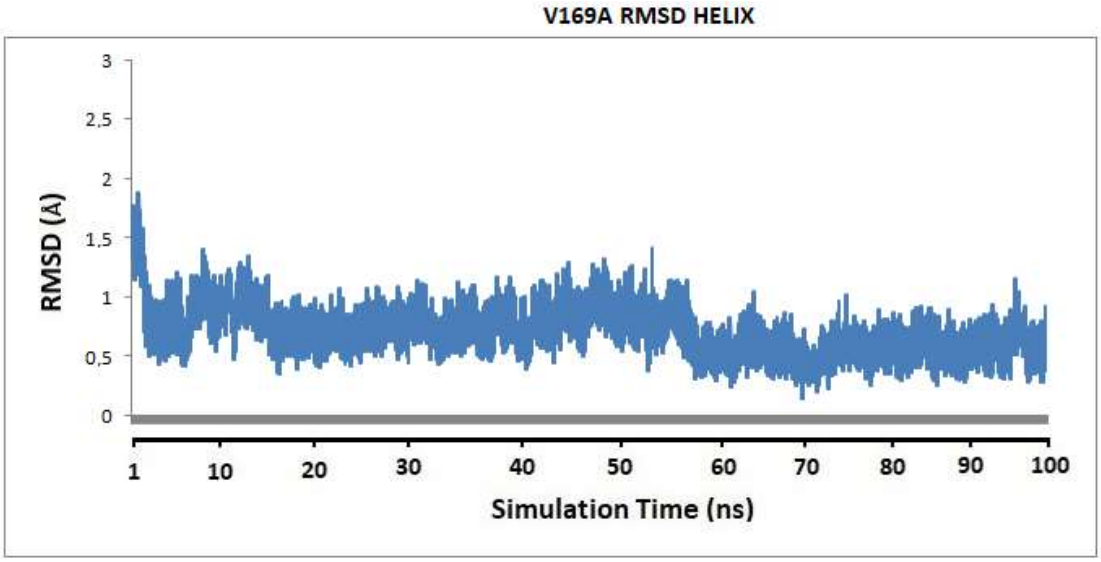
V169A RMSD HELIX
RMSD (Å)
3
2,5
2
1,5
1
0,5
0
1
10
20
30
40
50
60
70
80
90
100
Simulation Time (ns)

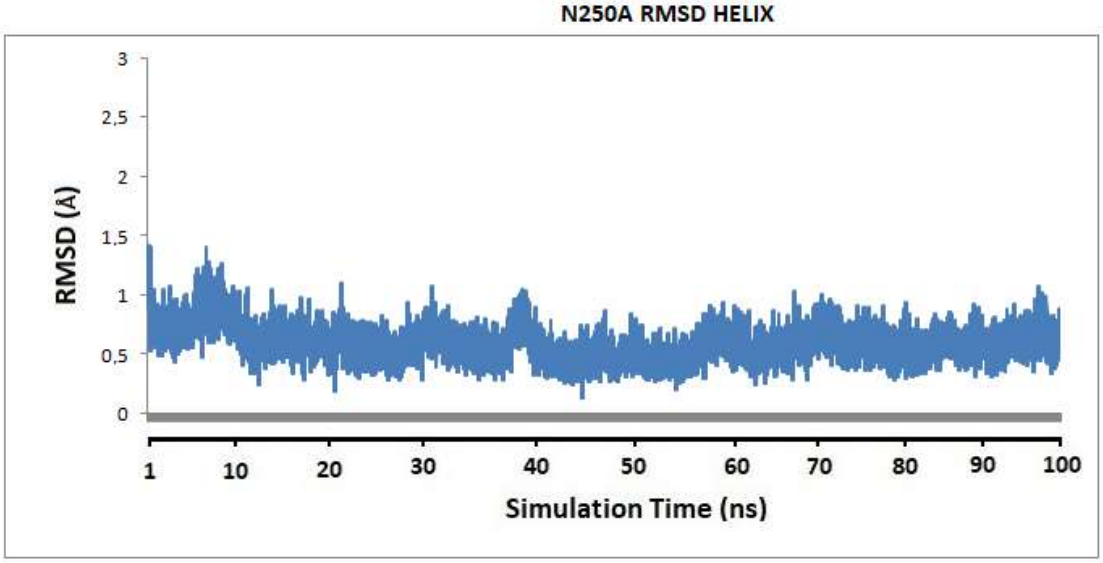
N250A RMSD HELIX
RMSD (Å)
3
2,5
2
1,5
1
0,5
0
1
10
20
30
40
50
60
70
80
90
100
Simulation Time (ns)

Figure S5.2 RMSD plots of Cα-carbons of TM helices relative the average structure for each mutant A_3R-**K18** complex after 100ns MD simulations.

A

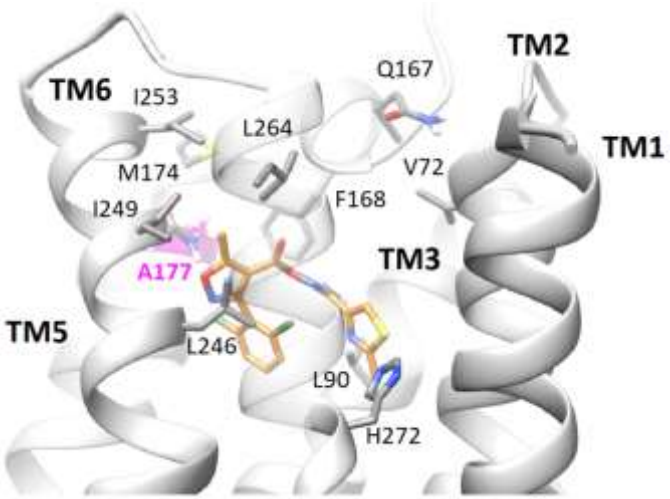

B

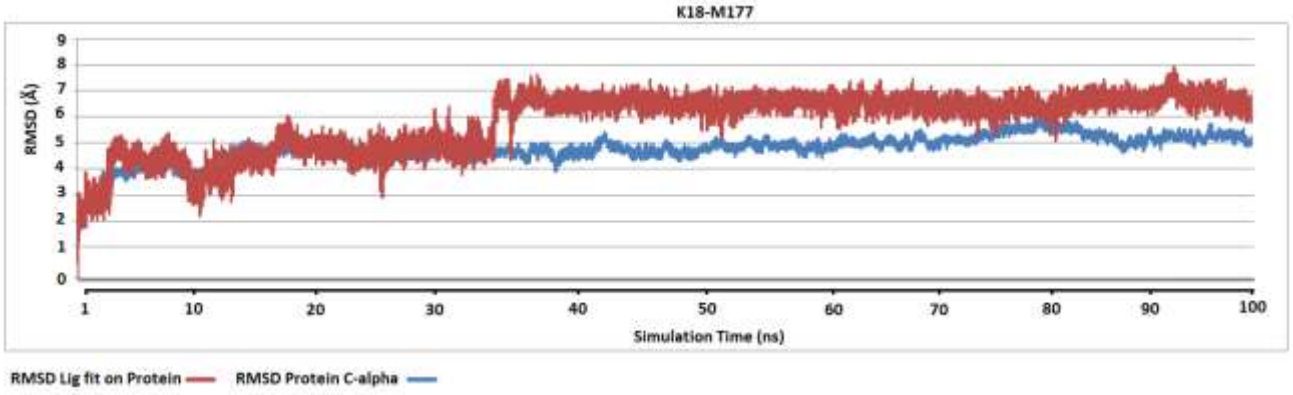

C

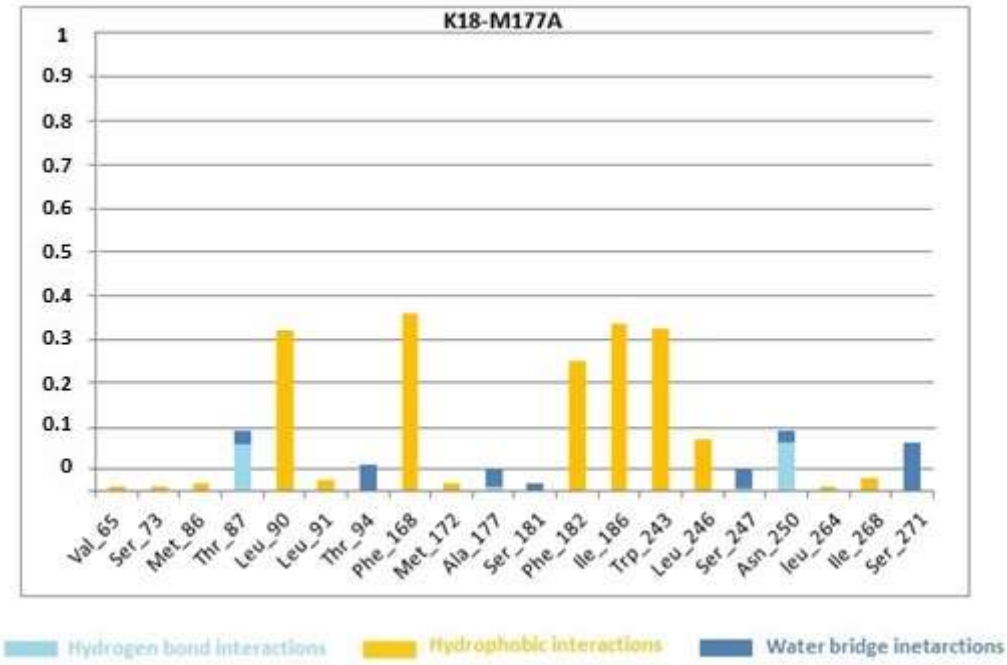

Figure S5.3 (A) Average binding orientation recorded from 100 ns MD simulation, (B) RMSD plot of the proteins Ca (in blue) and RMSD plot of the ligand displacement (in red) and (C) receptor-ligand interaction histogram for M177$^{5.38}$A A_3R.

A

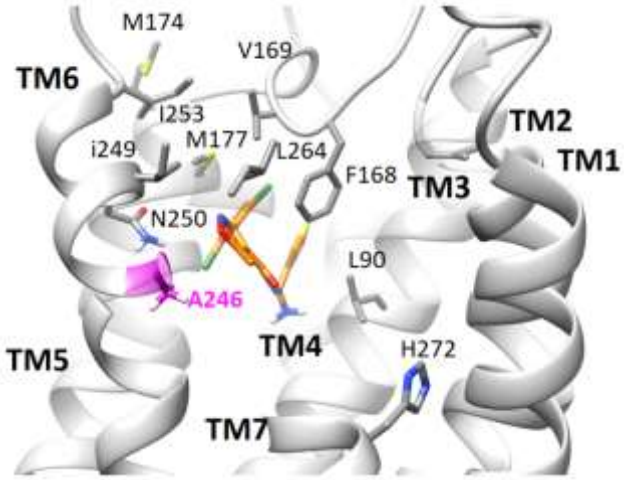

B

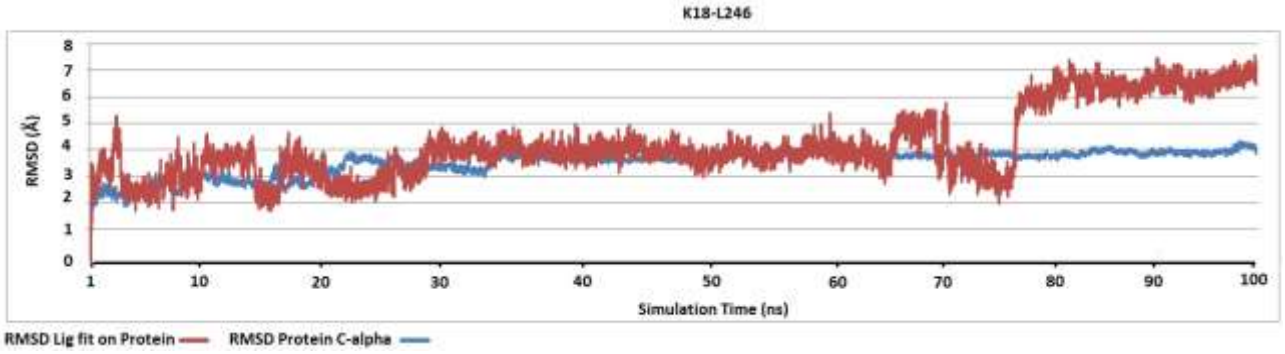

C

Figure S5.4 (A) Average binding orientation recorded from 100 ns MD simulation, (B) RMSD plot of the proteins Ca (in blue) and RMSD plot of the ligand displacement (in red) and (C) receptor-ligand interaction histogram for L246$^{6.51}$A A_3R.

A

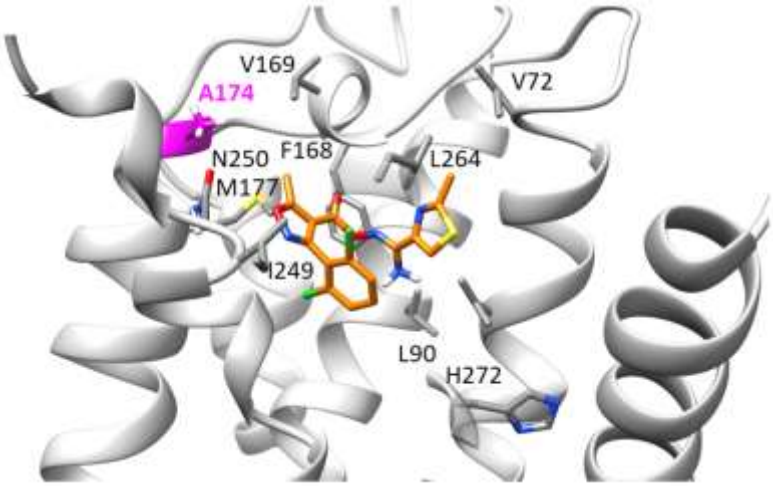
V169
A174
V72
N250
F168
L264
M177
I249
L90
H272

B

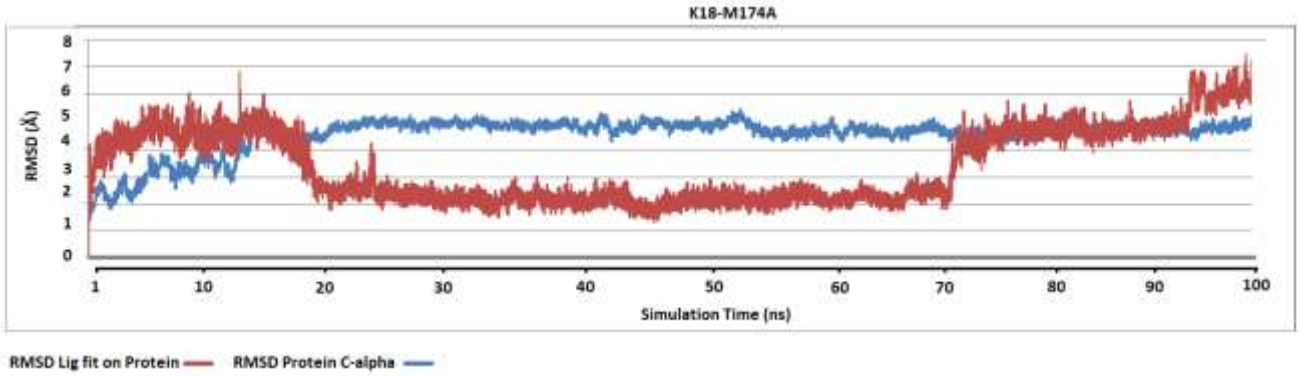
K18-M174A
RMSD (Å)
0
1
2
3
4
5
6
7
8
1
10
20
30
40
50
60
70
80
90
100
Simulation Time (ns)
RMSD Lig fit on Protein
RMSD Protein C-alpha

C

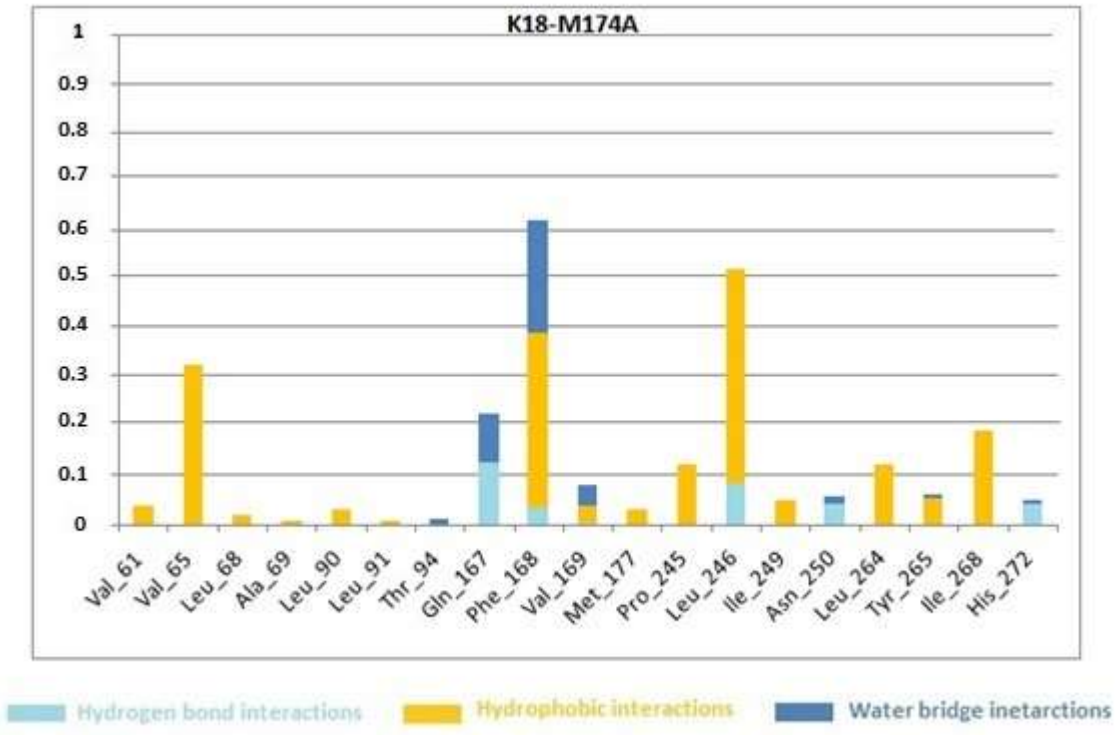

Figure S5.5 (A) Average binding orientation recorded from 100 ns MD simulation, (B) RMSD plot of the proteins Ca (in blue) and RMSD plot of the ligand displacement (in red) and (C) receptor-ligand interaction histogram for $M174^{5.35}A$ A_3R.

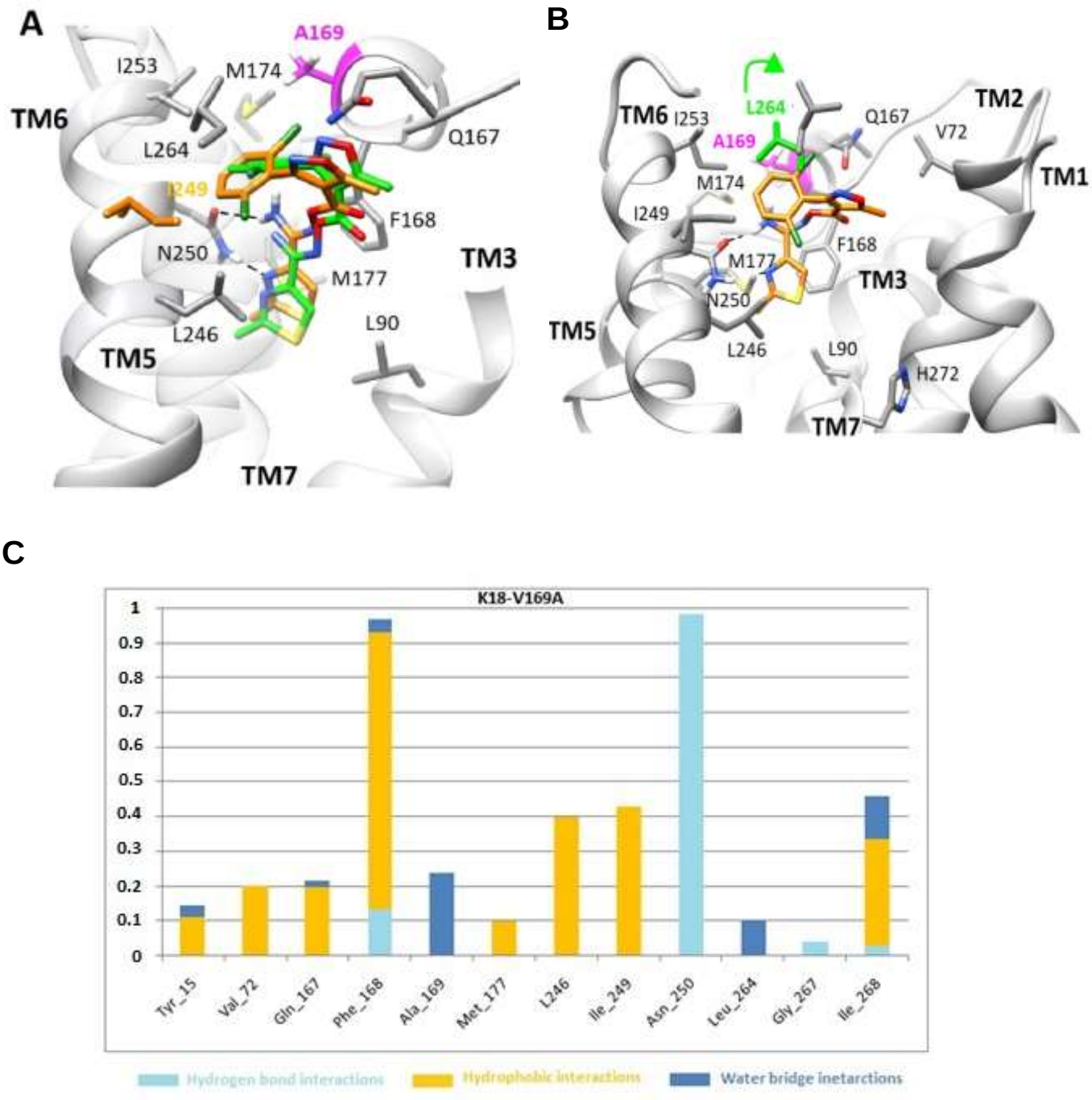

Figure S5.6. Snapshots of **K18**-V169$^{5.30}$A A_3R complex from the unrestrained 100 ns MD simulation. (A) The starting structure of the ligand is shown in green sticks. The binding conformation of the ligand after the 100 ns MD simulation is shown in yellow sticks. The side chains of residues involved in ligand binding, separated by 3.6 Å from the ligand and having interaction frequencies ≥ 0.2 are displayed as gray sticks. Protein structure is displayed in grey ribbons. Hydrogen atoms are omitted except for those involved in hydrogen bond interactions which are highlighted as black dashed lines. (B) Change in the conformation of L264 in order to accommodate the ligand observed after the 100 ns MD simulation. (C) Interaction histogram recorded from the 100 ns MD simulation trajectory. Hydrogen bonding interactions bar is depicted in green, van der Waals in purple, water bridges in blue. Bars are plotted for residues with interaction frequencies ≥ 0.2.

The MD simulation for the K18-V169$^{5.30}$A A_3R (**Figure S5.6**) showed that the antagonist maintained π-π interaction with F168$^{5.29}$, the van der Waals contacts with L246$^{6.51}$, I249$^{6.54}$ and hydrogen bonding with N250$^{6.55}$A. The loss of the attractive van der Waals interactions with V169$^{5.30}$ and the decrease of antagonistic potency supports the "up TM5-TM6" conformation of **K18**. Additionally, due to the mutation of A169$^{5.30}$, the interactions with L90$^{3.32}$, deeper in the receptor but also with M177$^{5.38}$ in the upper part of the binding area disappeared or significantly reduced, respectively, and the dichlorophenyl group of K18 was positioned closer to TM7 towards L264$^{7.35}$ and I268$^{7.39}$ to establish new hydrophobic contact. This re-orientation of the ligand can't balance the stabilizing interactions inside the WT A_3R resulting in the reduced potency which can be detected computationally by the $\Delta\Delta G_{eff}$ of ca +16 kcal mol^{-1}.

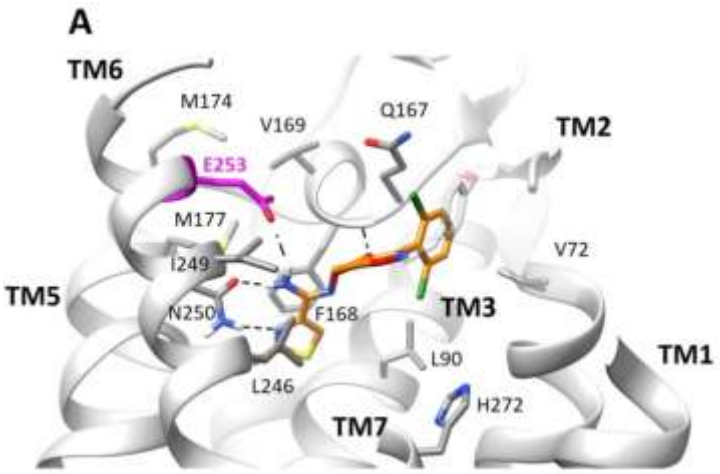

B

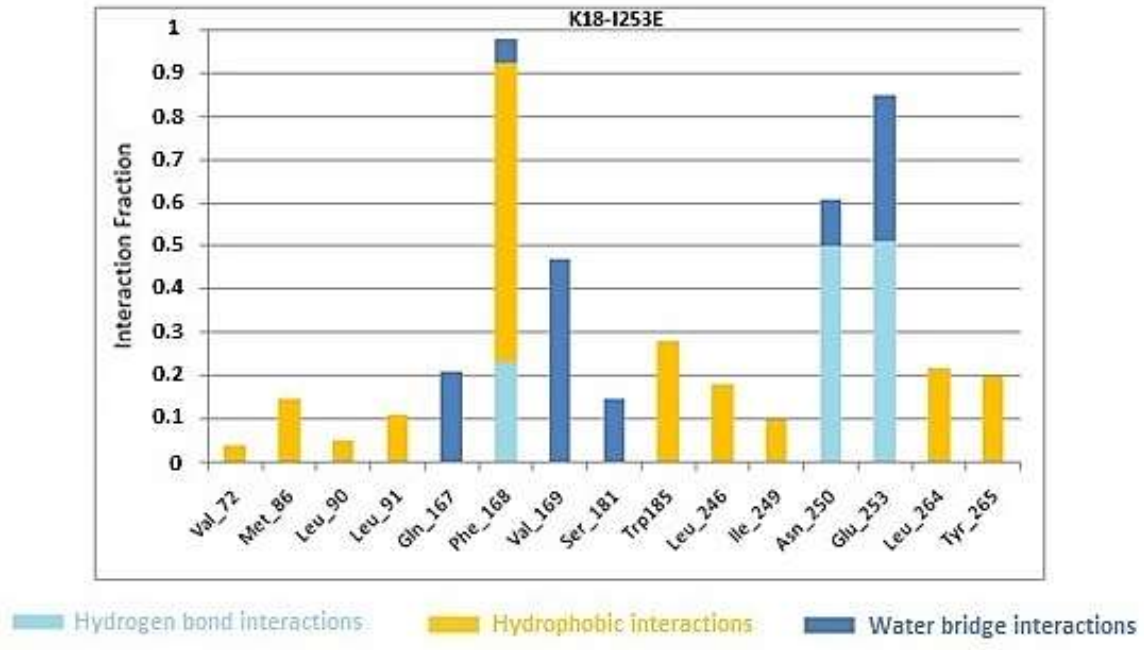

C

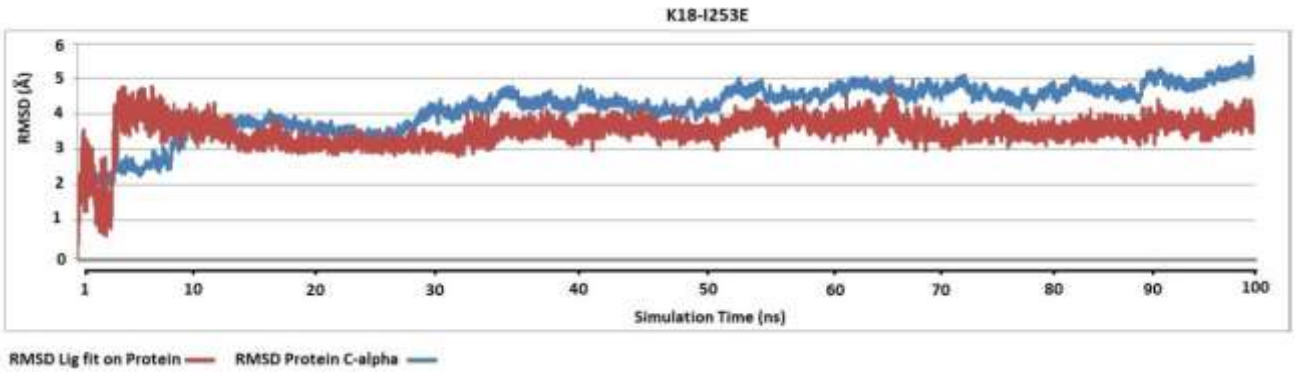

Figure S5.7 (A) Average binding orientation recorded from 100 ns MD simulation, (B) RMSD plot of the proteins Ca (in blue) and RMSD plot of the ligand displacement (in red) and (C) receptor-ligand interaction histogram for $I253^{6.58}E$ A_3R.